A Comprehensive Investigation of the Unimolecular Decomposition of Guaiacol and Its Derivatives: A Comparison of Neutral, Protonated, and Radical Cation Forms

SANDESH GONDARRY

A thesis submitted to the University of Ottawa
in partial fulfillment of the requirements for the
Doctorate in Philosophy degree in Chemistry

Department of Chemistry and Biomolecular Sciences
Faculty of Science
University of Ottawa

Dedicated to my parents. This journey was only possible because of your sacrifices, and this achievement wouldn't be mine without your support. This success belongs to both of us - we did it!

"Find a job you enjoy doing, and you will never have to work a day in your life."
— Mark Twain

ABSTRACT

This research addresses a critical knowledge gap regarding the atmospheric fate of methoxyphenols (guaiacols), semi-volatile aromatic oxygenated compounds derived primarily from biomass pyrolysis that serve as precursors to secondary organic aerosol formation. The research objective is to elucidate the unimolecular dissociation mechanisms of guaiacol and its derivatives through a direct comparison of their behaviour across three key environmental forms: the neutral molecule (dominant in the gas phase), the protonated species (relevant to aqueous media like cloud/fog droplets), and the radical cation (relevant to high-energy combustion and photoionization). This work integrates a multifaceted methodology combining tandem mass spectrometry (using electrospray ionization) and density functional theory (DFT) for the protonated ions, mass-analyzed ion kinetic energy (MIKE) spectrometry and high-resolution imaging photoelectron photoion coincidence spectroscopy (iPEPICO) combined with RRKM (Rice-Ramsperger-Kassel-Marcus) kinetic modelling for the radical cations, and systematic low-pressure SiC microreactor pyrolysis coupled with iPEPICO for the neutral molecules.

In Chapter 4, the thermal decomposition of neutral 4-ethylguaiacol and eugenol was probed using a low-pressure pyrolysis SiC microreactor at an approximation of 1000 ºC coupled to iPEPICO spectroscopy. Pyrolysis products were identified using photoion mass-selected threshold photoelectron spectroscopy (ms-TPES) based on their *m*/*z* values, supported by ionization energy calculations and Franck–Condon simulations. DFT calculations were conducted to elucidate the detailed reaction mechanisms of the thermal degradation pathways, and microcanonical unimolecular rate constants were evaluated using RRKM theory to assess competing reaction channels. In contrast to prior investigations conducted at atmospheric pressure and lower temperatures, which predominantly invoked free-radical mechanisms, these findings under low-pressure conditions indicate that dissociation can also occur via the loss of closed-shell species. The results establish a mechanistic framework for neutral dissociation in alkylated guaiacols and provide fundamental insight into the thermal behaviour of lignin model compounds under high-temperature, low-pressure conditions.

Chapter 5 explores the dissociation of the protonated ions of guaiacol and its substituted derivatives (creosol, 4-ethylguaiacol, 4-vinylguaiacol, eugenol, and vanillin) and hence,

potentially, their atmospheric fate. Owing to their volatility, guaiacol and its derivatives can interact with atmospheric water, forming protonated methoxyphenols via proton transfer. Tandem mass spectrometry (ESI-MS/MS) was employed to analyze the unimolecular dissociation of the protonated forms of these methoxyphenols. DFT calculations were applied to determine the observed minimum energy reaction pathways, and reliable energetics were acquired using CBS-QB3 single-point energy calculations. All the protonated ions, except for vanillin, exhibit the loss of CH_3OH via a series of hydrogen transfers, followed by ring contraction to lose CO. In contrast, vanillin first exhibits the loss of CO, followed by sequential losses of CH_3OH and CO to generate a cyclopentadienyl ion. Altogether, the protonated ions primarily lose CH_3OH and CO as neutral molecules, generating a cyclopentadienyl ion as a dissociation product.

Chapter 6 assesses the gas-phase acid-mediated degradation of guaiacol using reactive tandem mass spectrometry. The ion-molecule reactions between HSO_4^- and NO_3^- with neutral guaiacol vapour were studied in a modified triple quadrupole mass spectrometer. In both cases, an exothermic reaction was observed, forming neutral benzene and $HSO_4(HCOOH)^-$ and $NO_3(HCOOH)^-$. Also observed were the formate anion, deprotonated guaiacol and the deprotonated guaiacol dimer ion. Deuterium-exchange experiments demonstrated intracluster hydrogen transfer, supporting a mechanism that proceeds via a stabilized encounter complex rather than direct deprotonation. Density functional theory calculations of the reaction pathways demonstrated exothermic reactions in each case. These results establish a mechanistically viable, acid-guided route for the C−O bond cleavage in methoxyphenols under low-solvation, acid-mediated conditions. The study demonstrates that strong Brønsted-like centers can facilitate the catalytic extraction of oxygen as small oxygenates (formic acid) while preserving the aromatic hydrocarbon ring, a finding highly relevant to understanding the role of acidity in bio-oil upgrading catalysts.

Chapter 7 investigates the ion chemistry of radical cations to determine structural and mechanistic similarities with neutral thermal degradation. MIKE spectrometry was employed to investigate the unimolecular dissociation of radical cations, complemented by DFT calculations to elucidate the minimum energy reaction pathways. All the radical cations, apart from vanillin, exhibit the loss of a methyl radical ($^{\bullet}CH_3$). Methanol (CH_3OH) loss is also observed in selected guaiacol derivatives,

with the relative intensities of the methanol-loss fragment ions being lower than that for $^{\bullet}CH_3$ loss. Conversely, vanillin only displayed CO loss. The observed radical cation chemistry of guaiacol correlates well with previous studies of its neutral thermal decomposition, suggesting that the dissociation of the radical cations of the derivatives may also be analogous to their neutral thermal degradation.

Chapter 8 explores the dissociative ionization pathways of 4-ethylguaiacol and eugenol using iPEPICO spectroscopy and RRKM modelling. Threshold photoelectron spectra (TPES) for both species were recorded and analyzed with Franck–Condon simulations. Breakdown diagrams were analyzed using RRKM theory. 4-Ethylguaiacol dominantly loses a $^{\bullet}CH_3$ group at low energies, consistent with our prior MIKE study (Chapter 7), although traces of methanol loss are also seen. Nonetheless, the discrepancy between the RRKM-fitted methyl-loss E_0 of 1.88 eV and the previously proposed theoretical value (2.15 eV) led us to find a new reaction pathway involving sequential hydrogen shifts and structural rearrangements consistent with the experimental results. The eugenol radical cation was found to dissociate by the loss of $^{\bullet}CH_3$ and CH_3OH, in agreement with MIKE results. The energy barriers derived from the RRKM analysis (1.60 eV and 1.52 eV) were again significantly lower than the previous computational reaction barriers of 2.63 eV and 3.21 eV, respectively. Alternative, lower-energy, isomerization–fragmentation mechanisms, analogous to those of 4-ethylguaiacol, were found to be active. This study highlights the critical role of experimental techniques in validating and refining computational models and demonstrates how quantitative spectroscopic data can uncover previously unidentified reaction mechanisms.

ACKNOWLEDGEMENTS

I wish to begin by expressing my deepest gratitude to my family, whose unwavering support made this journey possible. Mom, Dad, although the specifics of my research may have remained a mystery, you have always supported me in every decision I have made and never once questioned my choice to pursue science as a career. Your sacrifices and love are what have helped me reach this point today. So, a big THANK YOU! My thanks also extend to my wider family for their frequent check-ins and support. A special shout-out to Uncle Kiran; your hospitality and the comfort of home-cooked meals made my transition to Canada feel like coming home, easing the weight of homesickness more than words can express.

At the heart of my academic journey is my supervisor and mentor, Dr. Paul Mayer. I am profoundly grateful that he took a chance on a student from Mauritius and welcomed me into his research group. I could not have hoped for someone better than him. He is one of the kindest, most knowledgeable, and humble individuals I have had the privilege to meet in my life. I was never hesitant to ask him questions — trust me, I was often bothering him — with even the simplest or most trivial doubts, and he always responded enthusiastically. I am truly grateful for everything he has done for me throughout my PhD. This opportunity means the world to me, and I am honoured to have completed this journey under his guidance.

During my time with the Mayer group, I have been fortunate to meet and work with amazing individuals, forming meaningful friendships that will carry long after this PhD. I am grateful to the entire group, both past and present. Special thanks to Dr. Sharon for her vibrant spirit and passion for chemistry, and to Dr. Sander for his valuable experience and expertise. My journey was made all the better by my fellow labmates: Dr. Malick for his constant helpfulness, Edgar (soon to be Dr. Edgar) for being my adventure buddy, Angela for her endless patience in enduring my pranks and quirks, as well as Reshmi, Peace, Nick, and Dr. Vijanaka. Each of you has uniquely contributed to my growth and learning, making the lab a place of both academic pursuit and enjoyment. I also want to thank Dr. Andras Bodi and Dr. Maxi Burgos-Paci for all their contributions.

TABLE OF CONTENTS

LIST OF FIGURES

LIST OF TABLES

LIST OF ABBREVIATIONS

$\langle S^2 \rangle$ - expectation value of the S^2 operator

2FFR - second field-free region

aqSOA - aqueous secondary organic aerosol

BrC - Brown Carbon

CBS - Complete Basis Set

CBS-QB3 - Complete Basis Set-quadratic Becke3

CCCBDB - NIST Computational Chemistry Comparison and Benchmark Database

cc-pVTZ - correlation-consistent polarized valence triple-zeta

CCSDT - coupled cluster with single, double, and perturbative triple excitations

CID - collision-induced dissociation

DC - direct current

DDO - direct deoxygenation

DFT - density functional theory

E_0 - 0 K appearance energy

EFs - emission factors

EI - electron ionization

E_{lab} - lab-frame kinetic energy

E_{com} - center-of-mass frame energy

ESA - electrostatic analyzer

ESI-MS - electrospray ionization mass spectrometry

ESI-MS/MS - electrospray ionization mass spectrometry with tandem mass spectrometry

eV - electronvolts

FC - Franck-Condon

FWHM - full width at half maximum

Gn - Gaussian-n

GTO - Gaussian-type orbitals

GUA + H^+ - protonated guaiacol

$GUA^{+\bullet}$ - guaiacol radical cation

GUA^0 - neutral guaiacol

HDO - hydrodeoxygenation

HF - Hartree-Fock

HLC - higher level correction

HPLC - high-performance liquid chromatography

HYD - hydrogenation–deoxygenation

IE - ionization energy

IE_a / IE_{ad} - adiabatic ionization energy

IE_v - vertical ionization energy

iPEPICO - imaging photoelectron photoion coincidence spectroscopy

IR - infrared spectroscopy

IRC - intrinsic reaction coordinate

IVR - intramolecular vibrational energy redistribution

k(E) - internal energy-dependent rate constant

k(T) - temperature-based canonical rate constant

LCAO - linear combination of atomic orbitals

m/z - mass-to-charge ratio

MERP - minimum energy reaction pathway

MIKES - mass-analyzed ion kinetic energy spectrometry
ms-TPES - mass-selected threshold photoelectron spectroscopy
MO - molecular orbital
PES - potential energy surface
PIMS - photoionization time-of-flight mass spectroscopy
$PM_{2.5}$ - fine particulate matter
POA - primary organic aerosol
RF - radio-frequency
RRK - Rice-Ramsperger-Kassel
RRKM - Rice-Ramsperger-Kassel-Marcus
sccm - standard cubic centimetres per minute
SIA - secondary inorganic aerosol
SLS - Swiss Light Source
SOA - secondary organic aerosol
STQN - synchronous transit-guided quasi-Newton
TD-DFT - time-dependent density functional theory
TOF - time-of-flight
TPEPICO - threshold photoelectron photoion spectroscopy
TPES - threshold photoelectron spectrum
TST - transition state theory
VMI - velocity map imaged
VOCs - volatile organic compounds
VUV - vacuum ultraviolet
ZPE - zero-point energy
OVGF - Outer-Valence Green's Function
PAH - polycyclic aromatic hydrocarbon
PEPICO - photoelectron photoion coincidence spectroscopy

ZPVE - zero-point vibrational energy
MPn - Møller–Plesset perturbation theory
$\Delta^{\ddagger}S$ - effective activation entropy

CHAPTER 1: INTRODUCTION

1.1 Global energy transition: Renewable resources and the role of bioenergy

1.1.1 Policy drivers and energy transition

The global energy system is undergoing a rapid and consequential transition driven by both policy imperatives and the finite nature of fossil resources.[1] The historic COP21 Paris Agreement in 2015 established a coordinated international framework to substantially reduce greenhouse gas emissions and to limit the increase in the global average temperature to well below 2 ºC above pre-industrial levels, while actively pursuing efforts to limit it to 1.5 ºC.[2] This commitment, combined with declining recoverable reserves of oil, gas, and coal, has led to stringent climate policies that necessitate a large-scale reorientation toward low-carbon energy sources.[3] Meeting the ambitious 1.5 ºC objective imposes fundamental constraints on the utilization of energy resources. Current model assessments indicate that a substantial fraction of known fossil fuel reserves, specifically 65% of oil and gas and 90% of coal[4], must remain unexploited.[3] This inherent constraint necessitates the immediate scaling of renewable energy capacity and a swift global phase-down of fossil fuels.[3] Major industrialized economies are responding with ambitious mandates; for example, Germany has committed to achieving Net Zero emissions by 2045[5,6] and Canada has legislated a 2050 Net Zero commitment[7]. This structural transformation drives accelerated deployment of renewables and systemic changes across industry and infrastructure, and also validates the necessity of extensive research into all aspects of renewable energy production, including the environmental consequences of derived fuel sources.

1.1.2 Biomass as a sustainable energy resource

Bioenergy, derived from organic biomass, is one of the largest sources of renewable energy globally, accounting for almost 55% of the total renewable energy supply and over 6% of the world's overall energy demand.[8] The perceived sustainability of bioenergy rests on the assumption of macroscopic carbon neutrality, based on the principle that the carbon dioxide released during combustion is counterbalanced by an equivalent amount absorbed by plants during photosynthesis.[8–10] Global momentum, evidenced by dedicated support policies in major regions

including Europe, China and the United States, supports the continued expansion of biomass-derived fuels, with the use of modern bioenergy increased on average by about 4% per year between 2010 and 2023 and continuing an upward trend (**Figure 1-1**[11]).[11,12]

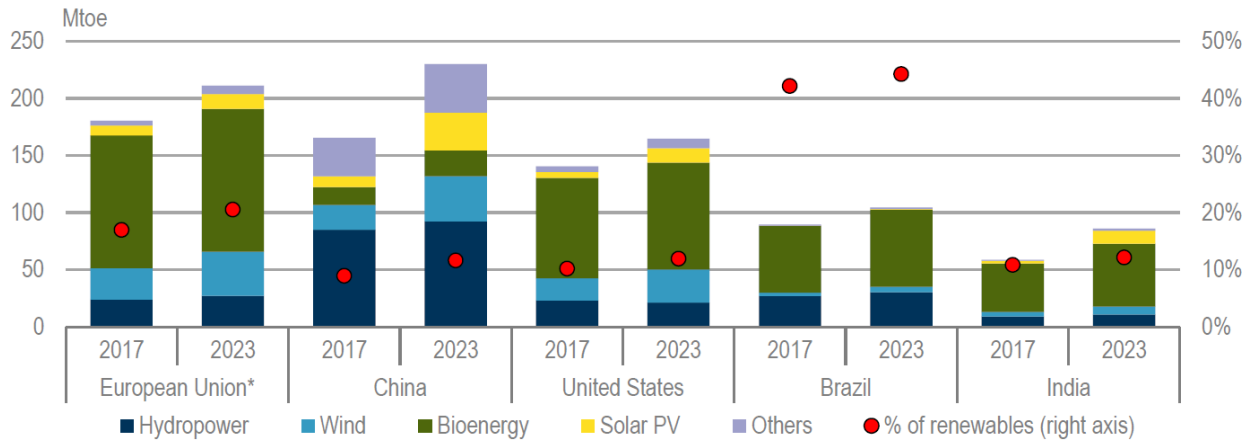

Figure 1-1. Renewable energy consumption in major markets in 2017 and projections for 2023 for five major markets. Note: Mtoe stands for mega tonnes of oil equivalent. (Reproduced from ref 11. Licensed under CC BY 4.0 https://creativecommons.org/licenses/by/4.0/)[11]

Nonetheless, the increasing use of biomass, particularly through large-scale thermal conversion processes such as pyrolysis and combustion, introduces significant environmental trade-offs. While the global energy transition aims for macroscopic carbon neutrality, this policy objective is fundamentally decoupled from air quality effects, due to increased local emissions of reactive organic species and secondary pollutants.[13] The classification of bioenergy as a "near-zero emissions" source is environmentally unsustainable without rigorous characterization of these local emissions. Quantitative assessments of pollution burdens reveal a critical disparity;[14,15] energy facilities in the United States that burn biomass may release, on average, up to 2.8 times the amount of health-harming pollutants and particulates per unit energy generated compared to their non-biomass counterparts (fossil fuels).[15] This research suggests that replacing fossil fuels with biomass, particularly in frontline communities already facing disproportionate exposure, constitutes replacing one dangerous fuel source with a potentially even more polluting one.[15] Consequently, the net environmental benefit of bioenergy depends critically on addressing the air quality and public health impact of the biomass decomposition products.[13,16] This link between

energy policy and molecular chemistry of biomass decomposition products underscores the need for accurate atmospheric modelling to validate the true sustainability of large-scale bioenergy utilization. Specifically, methoxyphenols, including guaiacol (2-methoxyphenol) and its derivatives, emerge as key products of biomass combustion that serve as precursors to these secondary pollutants.[17,18]

1.2 Lignin pyrolysis and methoxyphenol formation: A critical environmental byproduct

1.2.1 Thermal degradation of lignin and aromatic compound formation

Lignocellulosic biomass, the principal structural component of woody plant tissue, consists primarily of the polysaccharides cellulose and hemicellulose, along with the alkyl-aromatic heteropolymer lignin (**Figure 1-2**[19]).[20,21] Lignin is a structurally complex, cross-linked biopolymer that imparts mechanical strength and rigidity to plant cell walls, and is principally aromatic in character.[22] It is synthesized from three basic building blocks, known as monolignols, which differ in their degree of methoxylation: p-coumaryl alcohol (zero methoxy group), coniferyl alcohol (one methoxy group), and sinapyl alcohol (two methoxy groups).[21,22] These monomers are interconnected via various C−O and C−C linkages, resulting in a heterogeneous, three-dimensional structure.[23]

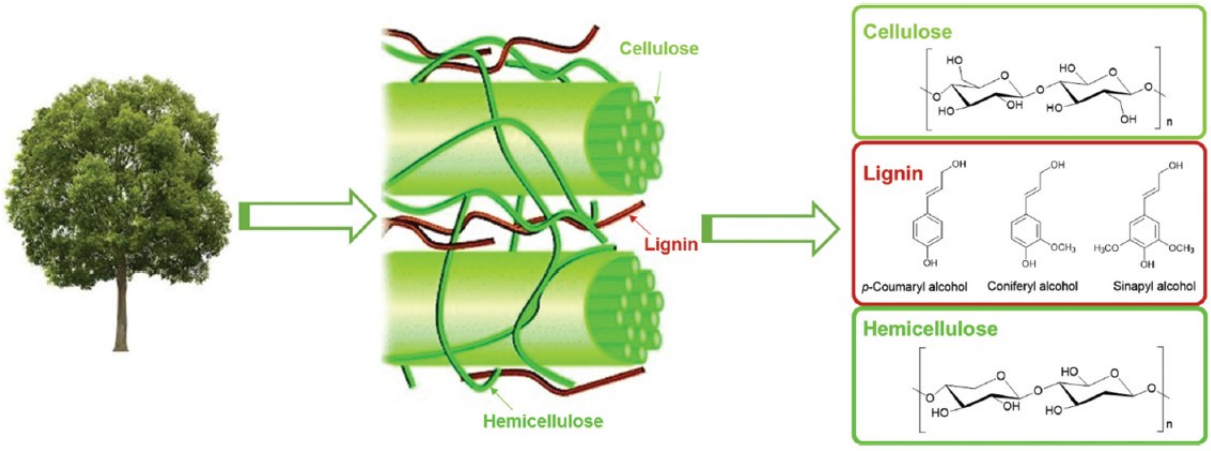

Figure 1-2. The structure of lignocellulosic biomass with cellulose strands surrounded by hemicellulose and lignin. Also shown is the structure of the three main monolignol monomer species of lignin. (Adapted with permission from ref 19. Copyright 2016)[19]

Under thermal conversion conditions such as fast pyrolysis, thermally labile inter-unit linkages in lignin cleave, yielding smaller, primarily single-ring aromatic products, predominantly methoxy-substituted phenols.[24] The release of these methoxyphenols is governed by the cleavage of the weakest linkages in the polymer backbone, predominantly the β-O-4 ether bond (**Figure 1-3**[25]), which is most susceptible to disruption during thermal degradation.[26] This bond cleavage dictates the high concentration of methoxy-substituted phenols, with guaiacol (derived from coniferyl alcohol) and syringol derivatives emerging as the abundant primary compounds.[27] Softwood-derived lignin tends to produce predominantly guaiacol derivatives, while hardwood-derived lignin generates both guaiacyl and syringyl products.[27] A study by Kjällstrand et al.[28] investigated methoxyphenols emitted from plant material burning and reported that methoxyphenols are emitted in substantial quantities, in some cases exceeding emissions of common volatile organic compounds like methane or ethane. Within the overall methoxyphenol pool, the results show that alkenyl phenols, such as 4-vinylguaiacol, often account for a significant fraction, typically 40-50% of the total methoxyphenols, while vanillin represents a major carbonyl-containing compound, constituting 10-20% of the recorded 2-methoxyphenols.[28]

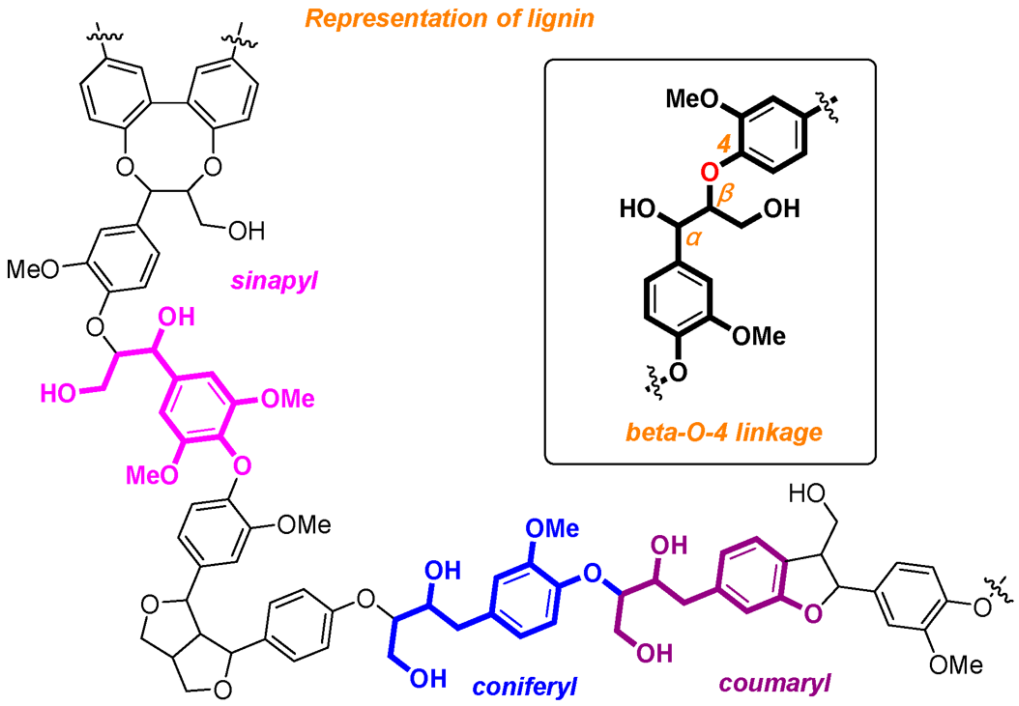

Figure 1-3. Structural representation of lignin and the β-O-4 linkage. (Reproduced from ref 25. Licensed under CC BY 4.0 https://creativecommons.org/licenses/by/4.0/)[25]

The studied derivatives - creosol, 4-ethylguaiacol, 4-vinylguaiacol, eugenol, and vanillin - are formed via complex thermal decomposition pathways that involve side-chain cleavage, demethoxylation, oxidation, and reduction reactions occurring alongside the primary depolymerization of lignin.[23] Consequently, guaiacol and its derivatives, owing to their abundance and atmospheric relevance, especially during residential heating and open biomass burning[29] serve as model compounds for understanding the atmospheric and thermal fate of methoxyphenols originating from biomass-burning emissions.

1.2.2 Guaiacol and its derivatives as atmospheric tracers: Emission factors and aging

Biomass burning, encompassing both wildfires and controlled fires, has emerged as a significant global source of atmospheric pollutants, contributing to substantial levels of particulate matter and volatile organic compounds (VOCs).[17,18] Aerosol from biomass combustion has been estimated to account for 90% of all primary organic carbon emitted by combustion sources worldwide.[17] Studies have shown that methoxyphenols, including guaiacol and its derivatives, represent a substantial fraction of wood-smoke particulate matter, accounting for 45% by mass of total

aerosol.[17] Emission yields of methoxyphenols vary widely with fuel type, with reported values spanning 1 to 10 000 mg kg^{-1} fuel burnt.[29] Due to their abundance in wood smoke, these methoxyphenols are widely used as molecular markers of wood combustion and as biomarkers of human exposure.[17,18] They play a central role in source appointment studies aimed at identifying and quantifying biomass burning's contribution to ambient particulate matter.

Emission factors (EFs) are essential for quantifying the environmental impact. A recent study conducted by Zhang and coworkers[30] demonstrated the substantial atmospheric loading of guaiacol; the EFs for guaiacol in fresh $PM_{2.5}$ (fine particulate matter) emitted from biomass burning ranged from 3.80 ± 0.44 to 26.2 ± 5.40 mg kg^{-1} fuel burnt. This range significantly exceeds the EFs found in coal combustion, which spanned from 0.03 ± 0.01 to 1.42 ± 0.28 mg kg^{-1}. Beyond mere emission, atmospheric aging profoundly affects how these molecules contribute to aerosol burdens, necessitating a distinction between primary and secondary aerosol formation potential. Guaiacol, traditionally employed as a wood combustion marker, can be identified as a primary organic aerosol (POA) tracer due to its low aged-to-fresh ratio, ranging from 0.21 to 0.97. This low ratio (less than 1) indicates that guaiacol itself is rapidly decomposed during oxidation, thereby being consumed rapidly during aging. In contrast, its substituted derivatives such as creosol, 4-ethylguaiacol and eugenol can be identified as prominent secondary organic aerosol (SOA) tracers, exhibiting higher aged-to-fresh ratios (between 1.90 and 4.20), indicative of formation during atmospheric aging.[30] This crucial difference in atmospheric fate necessitates that comprehensive research must investigate not only the primary parent compound (guaiacol), but also its key substituted derivatives to accurately address both immediate thermal emission or decomposition (POA precursors) and the subsequent atmospheric transformation steps leading to SOA formation (SOA tracers).

1.2.3 Atmospheric impact: Methoxyphenols as Secondary Organic Aerosol (SOA) and Brown Carbon (BrC) precursors

The high atmospheric loading of methoxyphenols is a significant environmental concern due to their high propensity to react with atmospheric oxidants, forming toxic products.[17,23,29] Laboratory and modelling studies have demonstrated the high SOA-forming potential of methoxyphenols, contributing to an estimated global SOA yield from biomass burning emissions of 8-26 Tg yr^{-1}.[31,32]

The rapid atmospheric degradation of guaiacol and its derivatives, driven by their semi-volatile nature and high chemical reactivity, renders them important precursors for SOA formation.[17,23,32] SOA formation has significant implications for climate forcing and human health.[33,34] SOA represents a substantial fraction of $PM_{2.5}$, and its presence has been strongly associated with adverse health effects.[33] Exposure to SOA has been linked to increased risk of cardiovascular and respiratory diseases and neurological impairments, effects largely attributed to the induction of oxidative stress in biological systems.[33,34]

Guaiacol exhibits significant gas-phase SOA potential, with chamber experiments demonstrating average mass yields in the range of 44-50% under low NO_x conditions following $^{\bullet}OH$ radical photooxidation.[17] This conversion produces aerosol with extremely high oxygenation levels (O:C ratios approaching 0.9), comparable to highly aged atmospheric organic aerosols, indicative of rapid conversion to low-volatility products that promote particle growth.[17] Under high NO_x conditions, oxidation favours the formation of nitrophenols, which contribute to light-absorbing organic aerosols known as Brown Carbon (BrC).[17,35] Furthermore, eugenol has been shown to exhibit significantly enhanced reactivity towards oxidants such as the $^{\bullet}OH$ radical and O_3, with reported atmospheric lifetimes of 4.70 h and 0.72 h, respectively.[36] The short lifetimes are indicative of quick oxidation and degradation leading to immediate and localized SOA formation, and validate the focus on short timescale unimolecular decay mechanisms. These rapid primary chemical events are foundational for accurately predicting the overall atmospheric budget, the fate, and the SOA contributions of methoxyphenols.[36,37]

Upon emission, these methoxyphenols predominantly partition into the gas phase owing to their relatively high vapour pressure at ambient temperature.[23,38,39] Nonetheless, in the presence of atmospheric water (in the form of cloud or fog droplets), aqueous-borne species facilitate the solubilization of these compounds, thereby promoting aqueous phase chemistry.[23,32] Consequently, the atmospheric fate of these compounds is governed by multiphase processes and requires characterization of both gas- and aqueous-phase reaction mechanisms (**Figure 1-4**). In the aqueous phase, these semi-volatile methoxyphenols can also undergo rapid dissolution and form aqueous SOA (aqSOA).[32] This aqueous processing can proceed on time scales comparable to or shorter than those of gas-phase reactions, and may yield greater SOA contributions.[40] Aqueous SOA

formation is driven by reactive oxidant molecules in the aqueous phase, such as •OH radical, singlet molecular oxygen ($^1O_2$*) and triplet excited states of organics (^3C*), forming aqSOA with high mass yields and elevated oxygenation (high O:C ratios).[40–43] The increased oxygenation enhances hygroscopicity and cloud-nucleating potential, thereby influencing cloud formation and aerosol-climate interactions.[40,44] Additionally, aqueous reactions can generate light-absorbing species that contribute to BrC, defined as organic aerosols that absorb radiation in the near-UV (300-400 nm) and visible spectral regions.[40,45,46] Aqueous-phase photooxidation of methoxyphenols, often mediated by inorganic nitrate (NO_3) photolysis, leads to the formation of nitrophenols like 4-nitroguaiacol and 4,6-dinitroguaiacol, species identified as prominent BrC constituents.[23,45] BrC significantly influences the climate radiative budget due to its ability to absorb solar radiation and influence cloud formation,[45,47] and also contributes to adverse air pollution effects such as reduced visibility and the formation of pollutants and irritants.[48]

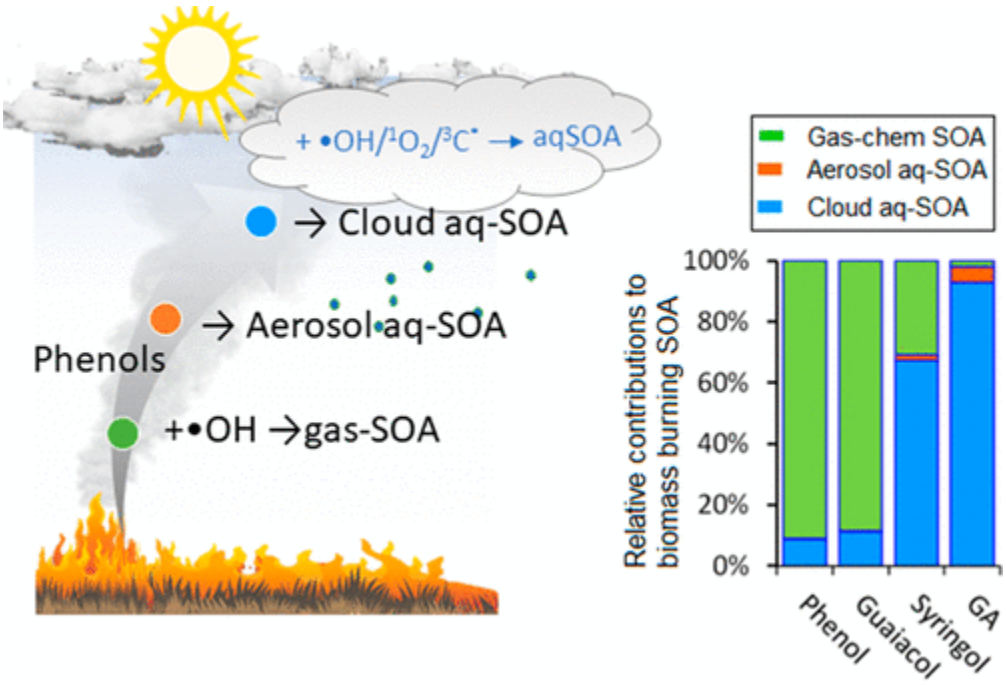

Figure 1-4. The principal multiphase processes leading to gasSOA and aqSOA formation. (Adapted with permission from ref 32. Copyright 2024)[32]

1.3 The multiphase, multiform chemical complexity of guaiacol degradation

The necessity of distinguishing between the chemical behaviours of neutral, protonated and radical cationic species exemplifies a central challenge in atmospheric chemistry: characterizing trace pollutants across multiple phases and energy regimes. Guaiacol and its derivatives serve as well-suited model compounds for investigating the atmospheric behaviour of methoxyphenols emitted from biomass burning. A comprehensive understanding of guaiacol chemistry, therefore, requires comparative studies across different molecular forms, since charge state fundamentally dictates intrinsic chemical reactivity, product distributions and mechanistic decomposition pathways. As distinct molecular forms correspond to different, often concurrent environmental conditions, comparative analysis is indispensable.[49–51]

This thesis focuses on the neutral (GUA^0), protonated ($GUA + H^+$) and radical cation ($GUA^{+\bullet}$) forms of guaiacol and selected derivatives (**Figure 1-5**). The neutral form dominates in the gas phase at ambient temperatures and undergoes thermal, photochemical and radical-driven unimolecular decomposition reactions.[52] The protonated form becomes highly relevant in aqueous media, where proton transfer and aqueous-phase reactions occur.[53] The radical cation form is conventionally generated under high-energy conditions, specifically under high-temperature pyrolysis or photoionization experiments, which are vital for characterizing emissions and identifying molecular structures.[54,55] Investigating these three forms bridges a critical gap in understanding how the same molecular backbone responds to diverse atmospheric and thermal environments. Consequently, elucidating the gas-phase unimolecular and radical-induced reaction pathways is essential not only for understanding SOA formation but also for predicting the generation of other climatically and toxicologically significant pollutants.

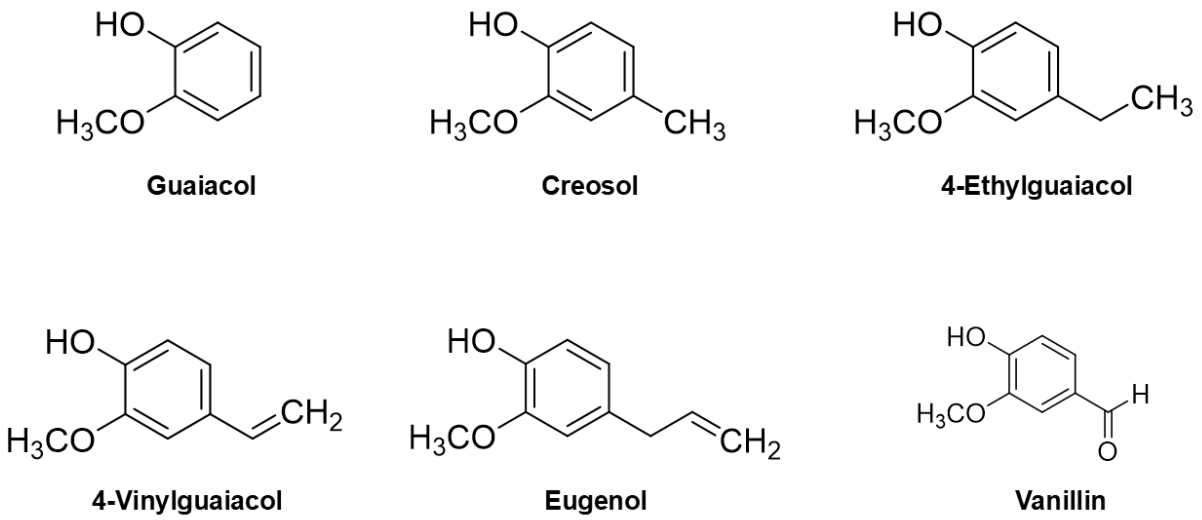

Figure 1-5. Structures of guaiacol and derivatives studied in this thesis.

1.3.1 Neutral form, (GUA^0): Thermal processes

The neutral form of these methoxyphenols is the predominant species emitted directly into the atmosphere during thermal processes and serves as the principal reactant in subsequent gas-phase oxidation reactions.[56–60] Once in the ambient atmosphere, these neutral molecules undergo thermal, photochemical and radical-driven unimolecular decomposition.[61] Investigating the unimolecular degradation of neutral guaiacol and its derivatives, therefore, provides critical insight into both combustion kinetics and the intrinsic thermal stability of these compounds.[52]

Under pyrolysis and high-temperature oxidation environments, degradation proceeds primarily via unimolecular O−C bond scission, generating a hydroxyphenoxy radical intermediate through methyl radical ($^{\bullet}CH_3$) loss.[52,59,60,62,63] Additionally, in the atmosphere, the neutral species may also undergo bimolecular radical reactions with oxidants, contributing to SOA formation.[17,32,37,40,64] Understanding the competition between thermal fragmentation (unimolecular) and atmospheric radical attack (bimolecular) is crucial for defining key chemical precursors and for accurately predicting SOA yields, product distributions, and the broader climatic and health impacts of combustion-derived methoxyphenols.

1.3.2 Protonated form, (GUA + H^+): Aqueous ion chemistry

The protonated form is particularly relevant in aqueous media, such as cloud or fog droplets. Owing to their polarity and semi-volatility, these methoxyphenols are susceptible to rapid dissolution in atmospheric water bodies, where they can undergo proton transfer, especially under acidic (low pH) conditions.[65] This shift to the ionic form facilitates distinct aqueous-phase chemistry, leading to enhanced aqSOA formation as discussed previously.[32]

In this charged protonated state, the unimolecular dissociation pathways are expected to differ from those of the neutral species. These guaiacols possess multiple potential protonation sites, including the oxygen atoms of the hydroxyl and methoxy groups, and carbon atoms of both the aromatic ring and the side chain. Studies on related organic molecules have established that the site of protonation determines the thermodynamic stability of the resulting protomer and, essentially, the subsequent degradation outcome.[66] The fragmentation reactions observed experimentally depend directly on which protomer is significantly populated.[66,67] Knowledge of product distributions and the energetics of the unimolecular degradation of protonated guaiacol and its derivatives is essential for accurately modelling complex aqueous and acidic atmospheric processing mechanisms that lead to aqSOA formation.[32]

1.3.2.1 Acid-mediated reaction

Atmospheric aerosols, whether primary (formed by wind action) or secondary, play a critical role in climate and air quality, with fine aerosols (radius less than 1 μm) predominantly formed by the condensation of precursor gases.[68] While sulfuric acid is a well-established precursor typically formed via sulphur dioxide oxidation,[68–70] nitric acid is a significantly more abundant tropospheric inorganic acid, often reaching concentrations four to seven orders of magnitude higher.[70] Due to their strong acidity and high oxidizing power,[70] these acids drive the formation of secondary inorganic aerosol (SIA) and SOA through acid-catalyzed reactions of organic precursors.[71]

Paralleling these atmospheric processes, the catalytic upgrading of lignocellulosic biomass relies heavily on similar acid functionality.[72,73] Bio-oil produced from pyrolysis requires hydrodeoxygenation (HDO) to reduce its oxygen content, a process often studied using guaiacol as a representative model compound.[72] Thus, investigating the gas-phase, acid-mediated reaction

of guaiacol with bisulphate (HSO_4^-) and nitrate (NO_3^-) anions provides a productive bridge between atmospheric multiphase chemistry and catalytic upgrading. It serves as a fundamental probe of the intrinsic mechanisms of catalytic deoxygenation in biomass valorization while simultaneously providing a predictive model of acid-driven degradation of organic matter in the atmosphere.

1.3.3 Radical cation, ($GUA^{+\bullet}$): High-energy processes

Radical cations are conventionally generated by high-energy processes, such as photoionization (via UV irradiation) and combustion.[74] Possessing both a positive charge and an unpaired electron, these species undergo distinctive radical-driven fragmentation pathways that are fundamentally distinct from those of the closed-shell neutral and protonated species and are central to understanding the chemistry in high-energy environments.[75] Experimental evidence suggests that guaiacol pyrolysis proceeds via free-radical chemistry, initiated by the loss of a methyl radical ($^{\bullet}CH_3$).[76] Similarly, Scheer et al.,[77] using photoionization time-of-flight mass spectroscopy (PIMS), also identified methyl radical loss as the initial high-temperature decomposition step, producing the hydroxyphenoxy radical intermediate. Additional pyrolysis products observed include acetylene and substituted alkynes, which can be subsequently oxidized by $^{\bullet}OH$ or NO_3, contributing to SOA formation.[77,78] Thus, studying the radical cationic forms links high-energy ionization chemistry with atmospheric radical processes, providing a comprehensive framework for understanding the formation, transformation and fate of radical intermediates.

Table 1. Comparison of the environmental contexts and mechanistic significance of guaiacol and its derivatives across distinct charge states.

Molecular form	Primary environmental context	Mechanistic significance
Neutral	Thermal processes: Emitted directly into the atmosphere during thermal events (pyrolysis); acts as the principal reactant in gas-phase oxidation.	➢ Critical for defining chemical precursors, predicting SOA formation and assessing climatic and health impacts. ➢ Provides insight into combustion kinetics and intrinsic thermal stability.
Protonated	Aqueous media: Occurrence in cloud or fog droplets, formed via dissolution and proton transfer under acidic conditions.	➢ Essential for modelling complex aqueous and acidic processing mechanisms leading to aqSOA formation.
Radical cation	High-energy processes: Photoionization; combustion	➢ Links high-energy ionization chemistry with low-energy atmospheric radical processes. ➢ Provides a framework for understanding the formation of radical intermediates.

1.4 Research objectives: Quantifying unimolecular chemistry across charge regimes

1.4.1 The critical data gap in unimolecular kinetics and atmospheric modelling

Although the atmospheric prevalence and general reactivity of guaiacol and several of its derivatives are well established, a detailed molecular-level understanding of their degradation mechanisms across diverse environmental interfaces remains incomplete. As highlighted in prior studies, these methoxyphenols do not persist in a single chemical state; rather, they undergo transformation through neutral gas-phase oxidation,[52,59,60,62,63] protonated aqueous-phase reactions[65] and radical-cationic high-energy degradation pathways.[76,77] Despite advances in characterizing bulk reaction rates, the fundamental thermodynamic and kinetic parameters governing unimolecular decay across these distinct regimes are often lacking or inferred from theoretical approximations.[61,79]

The lack of experimentally constrained thermochemical and kinetic data – notably accurate appearance energies and energy-dependent branching ratios for competing degradation channels – represents a critical bottleneck. Without accurate dissociation rates, branching ratios, and energetics for the short-lived transient intermediates, atmospheric models cannot reliably predict the formation of SOA and BrC pollutants, both of which exert significant climatic and public health impacts.[61,80] Current models often fail to account for complex molecular rearrangement mechanisms or charge-specific reaction pathways, leading to the critical uncertainties highlighted in BrC radiative forcing predictions.[81]

1.4.2 Aims and experimental strategy: A comparative mass spectrometry approach

The central rationale for this thesis is that the degradation chemistry of guaiacol and its derivatives is not governed by a single mechanism but is highly dependent on molecular charge state. This thesis seeks to address this gap by conducting a comparative investigation of the unimolecular decomposition of guaiacol and its derivatives across three distinct charge regimes: neutral (GUA^0), protonated ($GUA + H^+$) and radical-cationic ($GUA^{+\bullet}$).

To probe the distinct fragmentation behaviours associated with each charge state, complementary mass-spectrometric techniques are employed, each optimally selected for the specific molecular form and kinetic regime:

***Neutral species**: imaging photoelectron photoion coincidence (iPEPICO)*
The use of iPEPICO is uniquely suited to this task as it provides optimal energy resolution and sensitivity. It provides precise internal energy selection for the molecular ion, enabling determination of the 0 K appearance energy (E_0) for specific fragmentation channels. This energy threshold data, coupled with statistical RRKM modelling, is essential for obtaining microsecond-timescale rate constants.

***Protonated species**: electrospray ionization mass spectrometry (ESI-MS)*
ESI generates stable, solvent-free protonated ions, which can then undergo collision-induced dissociation (CID) to simulate energy deposition relevant to aqueous phase processing. This approach helps in characterizing the distinct, charge-driven rearrangement and fragmentation pathways of specific protomers, providing essential data for modelling aqSOA formation mechanisms.

***Radical cations**: mass-analyzed ion kinetic energy spectrometry (MIKES) and iPEPICO*
MIKES is utilized to identify metastable ion dissociations occurring on the microsecond timescale.

By integrating energy-resolved experimental mass spectrometric data with statistical modelling (RRKM theory), this thesis aims to advance the molecular-level understanding of guaiacols degradation and provide the quantitative framework for improved atmospheric models. The specific objectives are:
1) Mechanistic elucidation – Determine the unimolecular fragmentation pathways and product distributions characteristic of each charge state.
2) Thermochemical and kinetic characterization – Obtain accurate appearance energies and rate constants for the reaction intermediates and transient species.
3) Model integration – Provide the fundamental physical chemistry data required to enhance the predictive accuracy of atmospheric models for SOA and related combustion-derived pollutants.

CHAPTER 2: INSTRUMENTATION

2.1 Mass-analyzed ion kinetic energy spectrometry (MIKES)

Mass-analyzed ion kinetic energy (MIKE) spectrometry was performed on a VG ZAB mass spectrometer. A schematic representation of the VG ZAB mass spectrometer is shown below (**Figure 2-1**).[82] Basically, ions are produced by electron ionization (EI) and directed towards the magnetic analyzer, where separation is based on momentum. Once the ions of interest are selected, they travel through the second field-free region (2FFR), where metastable dissociation occurs. The resulting fragment ions are then analyzed by the electrostatic analyzer (ESA) according to their kinetic energies.

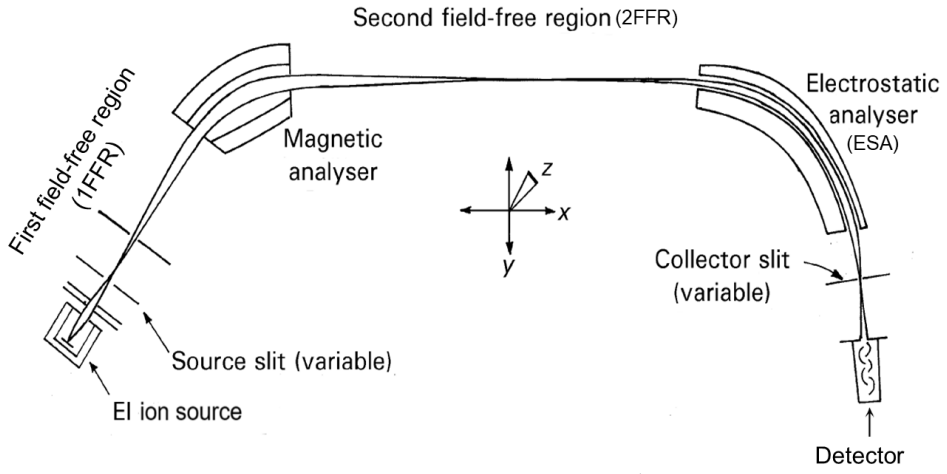

Figure 2-1. Schematic representation of the VG ZAB instrument. (Reproduced from ref 82. Licensed under CC BY 4.0 https://creativecommons.org/licenses/by/4.0/).[82]

2.1.1 Electron Ionization (EI)

Electron ionization (EI), or electron impact ionization, is a technique in which high-energy electrons collide with neutral gas-phase molecules, resulting in ion formation and the respective ejected electron. The term “electron impact ionization" is somewhat misleading, given the electron’s small size in molecular terms, and thus would have difficulty “hitting” any part of an atomic target. A more accurate description is to think of the electron as passing close to or even through the atomic target. In quantum mechanical terms, the electron’s wavefunction interacts with

and distorts the electric field of the atomic system.[83] Upon interaction with a high-energy electron possessing tens of electronvolts (eV) of kinetic energy, part of the electron's energy may be transferred to the neutral molecule. If the energy transfer is sufficiently efficient to surpass the ionization energy (IE) of the neutral, ionization occurs via electron ejection, producing a molecular ion, a positive radical ion (cation):[84]

$$M + e^- \rightarrow M^{+\bullet} + 2e^-$$

A schematic layout of the ion source is shown below (**Figure 2-2**), consisting of an ion source block, filament, repeller electrode, trap electrode, acceleration region, and focusing lens. Depending on their physical state at room temperature, neutral molecules are introduced using one of two methods. Liquid samples, which were most common, were introduced via a liquid inlet, while a heated solid probe was utilized for solid samples. The analyte molecule is ionized by electrons that are ejected through thermal emission from a filament and collected at the trap electrode. The resulting electron beam carries an energy of approximately 80 eV, closely matching the optimal ionization efficiency typically observed at 70 eV.[85] To minimize ion losses due to neutralizing collisions with the walls, a small voltage is applied to the repeller electrode to push out the newly formed ions immediately after generation.[84] The ions are accelerated to the operating kinetic energy of the instrument (6, 7 or 8 kV, depending on the timescale desired for the experiment). A series of ion lenses guides the ion beam towards the mass analyzer.

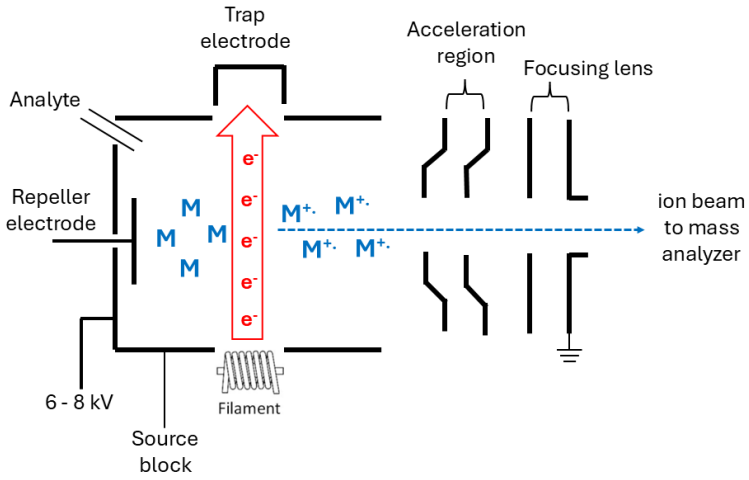

Figure 2-2. Schematic diagram of an electron impact ion source.

Ionization by energetic electrons does not result in the deposition of a fixed amount of energy into the target molecule. For example, a 10 eV electron beam may transfer anywhere between 0 and 10 eV of energy. Consequently, electron ionization sources typically employ higher-energy electron beams. An energy of approximately 70 eV is commonly used in most analytical instruments, as this energy value has been shown to yield the maximum ionization efficiency for most organic molecules.[85]

2.1.2 Magnetic analyzer (magnetic sector)

After ion formation, they are accelerated to 8 keV through a first field-free region before entering the magnetic sector, in which the magnetic field is applied perpendicular to the ion beam trajectory.[85,86] Ion selection within the magnetic sector is based on momentum, which is governed by the applied magnetic field. The sector consists of two parallel electromagnets surrounding an iron core, and the relationship between ion momentum (mv) and magnetic field strength is described by the following equation:

$$mv = rBze \qquad \textbf{(eq. 1)}$$

where r denotes the radius of curvature of the ion's path, m is the ion's mass, v is its velocity, B is the magnetic field strength, z represents the number of charges on the ion, and e is the elementary charge unit. Most instruments are designed with a fixed value for the radius of curvature, r, and

ion selection is achieved by tuning the magnetic field (*B)*. This allows only ions of specific values of momentum, mv, through the magnetic sector. Thus, the magnetic sector fundamentally selects ions based on their momentum rather than their mass.

Magnetic sector instruments typically operate with ion sources held at a potential of 6-10 kV, resulting in ions with translational kinetic energies on the order of several keV. The ion velocity (v) is directly related to the acceleration voltage (V), as described by the following expression:

$$zeV = \frac{1}{2}mv^2 \qquad \textbf{(eq. 2)}$$

Consequently, the mass-to-charge ratio (m/z) of the selected ion can be determined by combining **equations 1** and **2**,

$$m/z = \frac{B^2r^2e}{2V} \qquad \textbf{(eq. 3)}$$

In essence, selective transmission of ions with a given mass-to-charge ratio (m/z) through the magnetic sector can be achieved by adjusting the acceleration voltage (V) and magnetic field strength (B); though, in typical operation, V is fixed, and ion selection is accomplished by varying B.[85]

2.1.3 Second field-free region (2FFR)

The momentum-selected ions travel through the second field-free region (2FFR) of the instrument prior to reaching the electrostatic analyzer. Within this region, dissociation of metastable ions takes place. These metastable ions have acquired sufficient internal energy from the ion source to fragment without external stimulation; that is, by virtue of energy acquired from the source and not from collisions. These ions dissociate on the microsecond timescale with typical rates ranging between 10^4 and 10^6 s^{-1} (**Figure 2-3**[84] below).[84,85]

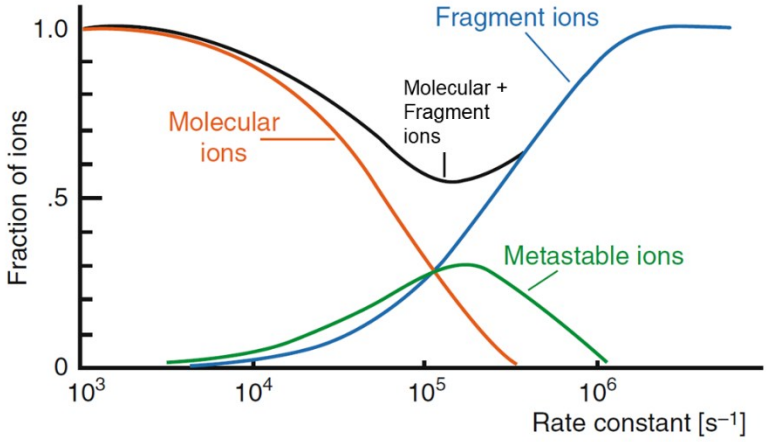

Figure 2-3. Relationship between rate constants of ion dissociations. (Adapted with permission from ref 84. Copyright Springer International Publishing AG 2017)[84]

2.1.4 Electrostatic analyzer (ESA)

The electrostatic analyzer comprises two curved parallel plates across which a potential difference is applied, generating an electric field of strength E. Ion separation is achieved by varying the potential across the ESA plates, allowing ions with specific translational kinetic energies to pass through and be focused onto the detector. The transmission of ions through the analyzer is described by the following equation:

$$\frac{1}{2}mv^2 = zeV = \frac{1}{2}zeEr \qquad \textbf{(eq. 4)}$$

Rearranging this equation allows for the characterization of the ion based on its *m*/*z* value

$$m/z = \frac{eEr}{v^2} \qquad \textbf{(eq. 5)}$$

The electric field can be configured either as a constant field, enabling the ESA to act as a mass selector, or as a variable field, allowing it to function as a mass filter.[85]

2.1.5 Photomultiplier detector

The detector represents the final component of the sector instrument. In the VG-ZAB system, ion detection is accomplished using a photomultiplier, as illustrated in **Figure 2-4** below**:**

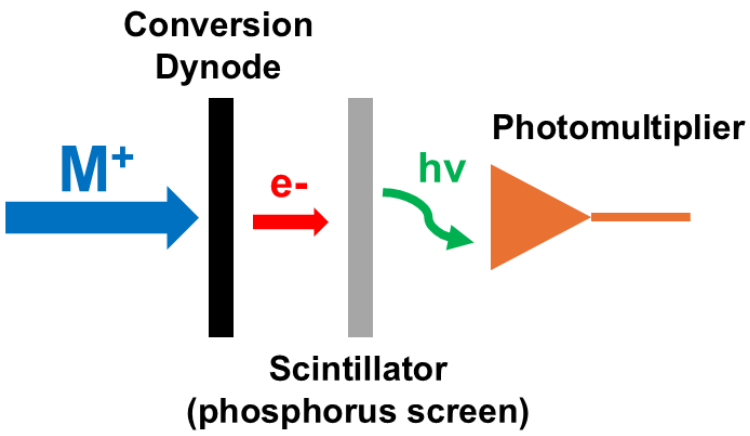

Figure 2-4. Schematic representation of a photomultiplier detector.

Ions striking the conversion dynode result in the emission of an electron. The emitted electron interacts with a scintillator, which absorbs its energy and emits a photon. This photon is transmitted to a photomultiplier tube, where the resulting signal is amplified via multiple dynodes. The processed electrical signal is relayed to the data acquisition system of the mass spectrometer, where it is digitized and recorded. This signal reflects the intensity of emitted photons, which is directly proportional to the number of ions reaching the detector. The recorded data is processed to produce a mass spectrum, showing the ion intensities detected at different mass-to-charge ratios (*m*/*z*).

2.1.6 Mass-analyzed ion kinetic energy spectrometry (MIKES)

Following acceleration to keV translational kinetic energies and selection by the magnetic sector based on *m*/*z*, ions arrive at the second field-free region (2FFR) of the instrument in several microseconds, a timescale during which metastable ions dissociate. Due to the conservation of energy and momentum, the unimolecular decomposition products A^+ and $B^\bullet$ (originating from the mass-selected metastable ion $AB^{+\bullet}$) possess lower kinetic energy, T, than their precursor:

$$T_{A^+} = \frac{1}{2} m_{A^+} v^2 \qquad T_{B^\bullet} = \frac{1}{2} m_{B^\bullet} v^2 \qquad T_{AB^{+\bullet}} = \frac{1}{2} m_{AB^{+\bullet}} v^2$$

By rearranging,

$$T_{\mathrm{A}^+} = \frac{m_{A^+}}{m_{AB^{+\bullet}}} T_{AB^{+\bullet}} \qquad \textbf{(eq. 6)}$$

Thus, using the relationships outlined above, the final ion abundance kinetic energy spectrum is transformed to the ion abundance fragment *m*/*z* spectrum.[85]

2.2 Electrospray ionization mass spectrometry (ESI-MS)

The dissociation of protonated guaiacol and its derivatives was studied using a Waters Micromass Quattro Ultima Pt triple quadrupole mass spectrometer. A schematic diagram of the instrument is shown below (**Figure 2-5**).[87] Conventional triple quadrupole mass spectrometers employ three sequential quadrupole mass filters to isolate, fragment and quantify target analytes. However, in our configuration, the system features two quadrupoles in conjunction with an ion tunnel, which serves as the collision cell. Essentially, protonated ions were generated using an electrospray source, and the precursor protonated ions were selected based on their *m*/*z* using the first quadrupole and directed into the ion tunnel collision cell, where they undergo collision-induced dissociation (CID) with argon gas. The resulting product ions were detected using the second quadrupole analyzer and the detector.

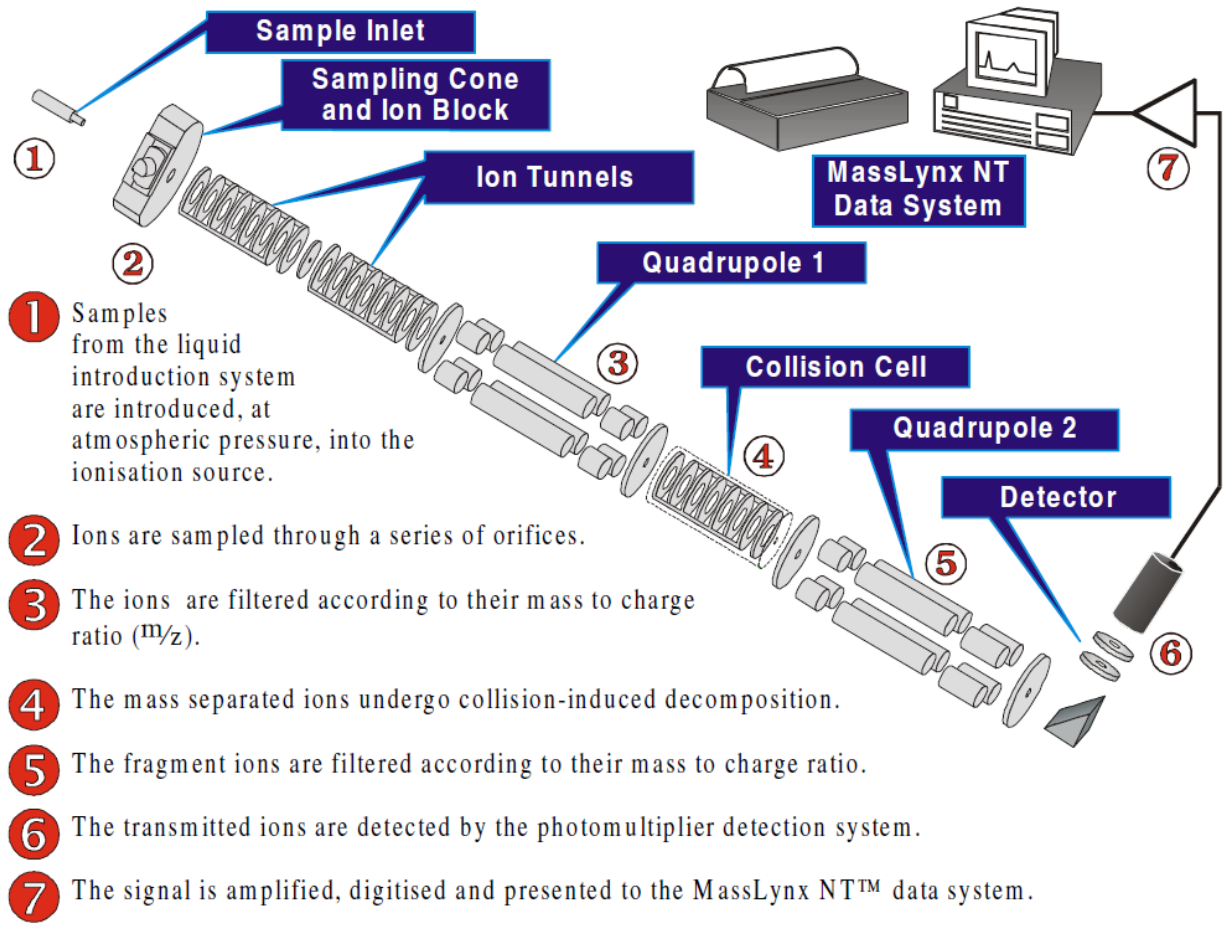

Figure 2-5. Experimental setup of the Waters Micromass Quattro Ultima Pt triple quadrupole mass spectrometer. (Reproduced from ref 87. Licensed under CC BY 4.0 https://creativecommons.org/licenses/by/4.0/)[87]

2.2.1 Electrospray ionization process (ESI)

Electrospray ionization (ESI) uses electrical energy to assist the transition of analyte ions from the liquid to the gas phase for mass spectrometric detection. Neutral molecules are ionized either by addition ($[M+H]^+$) or abstraction ($[M-H]^-$) of a proton. Operated at atmospheric pressure, ESI proceeds through three principal stages (**Figure 2-6**):[86] 1) generation of charged droplets, 2) solvent evaporation, and 3) ion ejection from the highly charged droplets. Within the ESI source, a continuous stream of analyte solution is delivered through a metal capillary held at 2-6 kV. The solution at the capillary tip is distorted into a Taylor cone that emits a fine mist of charged droplets. This spraying process is assisted by a nebulizing gas, primarily nitrogen. As these droplets move

along a pressure and potential gradient toward the mass analyzer, they undergo rapid solvent evaporation, often assisted by heating of the ESI source. The charged droplets are continuously reduced in size, leading to an increase in surface charge density and a decrease in the droplet radius. Finally, when coulombic repulsion overcomes surface tension, ions at the surface of the droplets are ejected into the gas phase, pass through a skimmer cone, and are accelerated into the mass analyzer.[88,89]

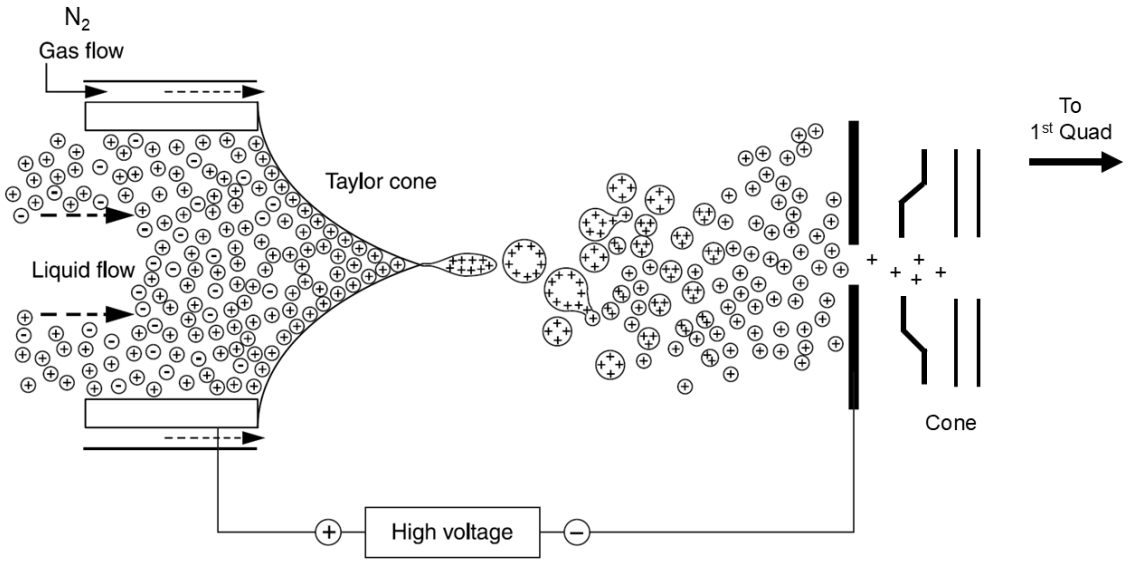

Figure 2-6. Electrospray ionization in positive mode. The sample solution is delivered through a positively charged capillary. The combination of applied potential and nebulizing nitrogen gas produces charged microdroplets. Solvent evaporation (assisted by heat) progressively reduces droplet size until coulombic repulsion induces droplet fission, transferring positive charge to the analyte and yielding gas-phase ions. (Adapted with permission from ref 86. Copyright 2009 John Wiley & Sons, Inc.)[86]

2.2.2 Quadrupole mass analyzer

The quadrupole mass analyzer consists of four parallel rod electrodes, either hyperbolically or cylindrically in cross-section, arranged in a square configuration in the xy-plane and extending along the z-direction (**Figure 2-7**).[84] Each pair of opposite rods is held at the same potential, which is composed of a DC (direct current) and an AC (alternating current) component. As an ion travels through the quadrupole along the z-direction, an attractive force is exerted on it by one of the rods

with its charge opposite to the ionic charge. If the applied voltage is periodic, attraction and repulsion in both the x- and y-directions will alternate in time.[84] The applied potential Φ_0 is a combination of a DC (direct current) potential, U and an RF (radio-frequency) potential, $V\cos\omega t$, given by[84,85]

$$\Phi_0 = U + V\cos\omega t \qquad \textbf{(eq. 7)}$$

The equations of motion within such a field are as follows:[85]

$$\frac{d^2x}{dt^2} + \frac{e}{mr_0^2}(U - V\cos\omega t)x = 0$$
$$\frac{d^2y}{dt^2} + \frac{e}{mr_0^2}(U - V\cos\omega t)y = 0 \qquad \textbf{(eq. 8)}$$

Here, r_0 denotes the radial distance from the trap center to the electrodes, and e is the electron charge. Ion motion travelling in the quadrupole field follows the Mathieu equation.[86]

Expressing **equation 8** in its dimensionless form results in:[84,90]

$$\frac{d^2x}{d\xi^2} + (a_x + 2q_x\,cos2\xi)x = 0$$
$$\frac{d^2y}{d\xi^2} + \left(a_y + 2q_y\,cos2\xi\right)y = 0 \qquad \textbf{(eq. 9)}$$

Now, the following three substitutions can be applied:[85]

$$a_x = -a_y = \frac{8eU}{m\omega^2 r_0^2} \qquad q_x = -q_y = \frac{8eV}{m\omega^2 r_0^2} \qquad \xi = \frac{\omega t}{2}$$

Accordingly, the outcome is expressed in the general form of the Mathieu equation:[85,91]

$$\frac{d^2u}{d\xi^2} + (a_u - 2q_u cos2\xi)u = 0 \qquad \textbf{(eq. 10)}$$

The Mathieu equation (**equation 10**) describes the ion motion in the quadrupole field (where u can be either x or y). Its stable, bounded solutions delineate the conditions under which ion trajectories remain confined within the quadrupole. **Figure 2-8**[92] depicts the stability diagram for the stable solutions to the equations for both the x- and y-axes. The stability region is unique for a given m/z.[85] For a specified combination of the DC (U), and RF potentials (V) and frequency, ω, only ions whose m/z range fall within the narrow stability window have stable trajectories through the quadrupole. This window is governed by the magnitude of the RF voltage and by the ratio of the DC and RF potentials (U/V). Any ion whose m/z lies outside this region follows an unstable trajectory, collides with the rods and does not make it further.[86] The operating line, which intersects the apex of each m/z region, defines the DC (U) and RF (V) settings required for selective ion transmission. The ratio of U to V is a constant along the operating line. By varying the slope of the operating line, one can tune the resolution of the quadrupole. A steeper slope results in greater ion separation, but at the expense of sensitivity.

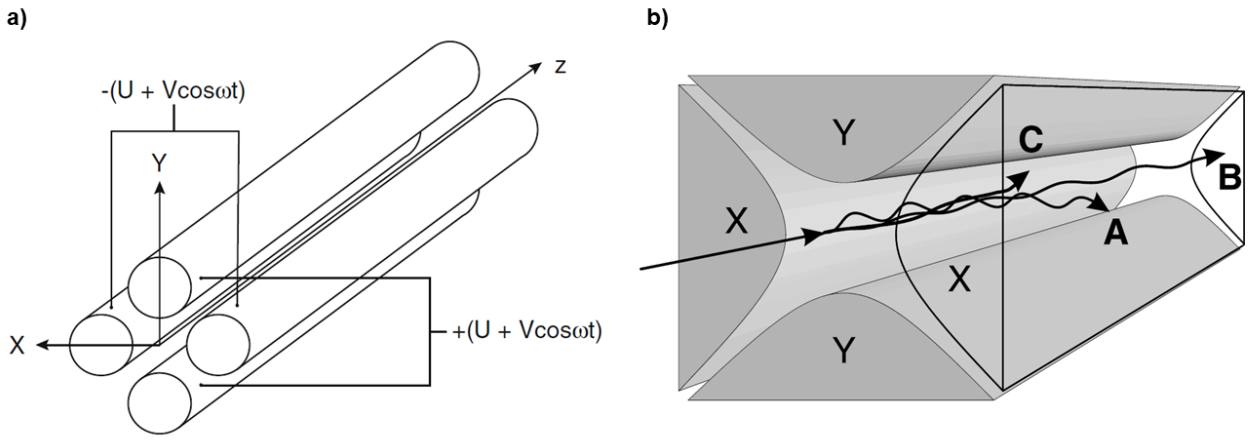

Figure 2-7. a) Schematic diagram of the quadrupole mass analyzer. b) Operating principle of the quadrupole mass analyzer. The x-direction pair of rods acts like a high-pass filter (excluding low m/z ions), so ion C (with low m/z) is not allowed through, and the y-direction pair of rods acts like a low-pass filter (excluding high m/z ions) and takes care of ion A (with high m/z). Only ions with m/z values that satisfy both stability conditions (ion B) traverse the quadrupole and reach the detector. (Adapted with permission from ref 84. Copyright Springer International Publishing AG 2017)[84]

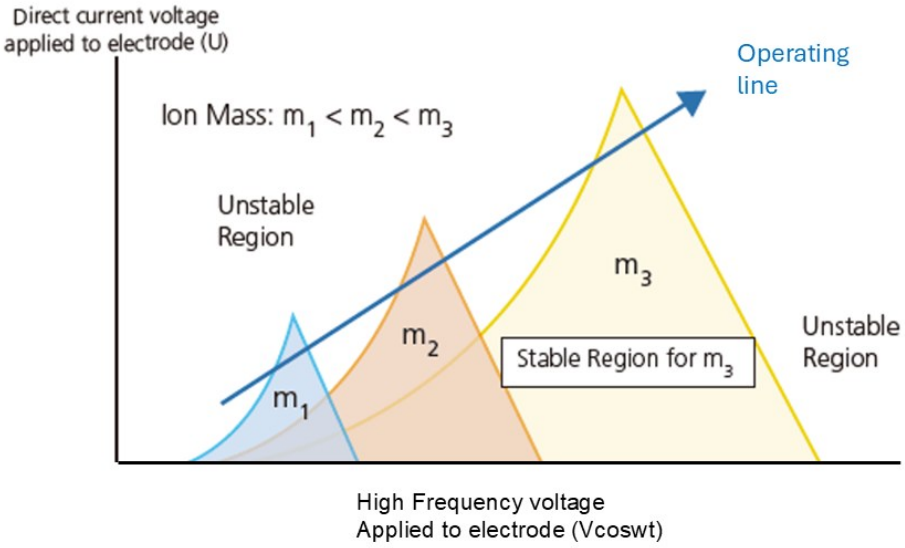

Figure 2-8. Mathieu stability diagram showing stable regions for different ion masses in a quadrupole mass filter. Each ion mass (m_1, m_2, m_3) occupies a distinct stability region. When the RF and DC voltages are scaled together so that their ratio remains constant, the resulting operating (scan) line traverses the stability regions for successive masses. Ions whose stability regions intersect the scan line are transmitted in sequence ($m_1 \rightarrow m_2 \rightarrow m_3$), producing a mass spectrum that scans from low to high *m*/*z*. (Reproduced from ref 92. Licensed under CC BY 4.0 https://creativecommons.org/licenses/by/4.0/)[92]

2.2.3 Collision-induced dissociation (CID)

Collision-induced dissociation (CID) is a fundamental mass spectrometry technique for fragmenting selected precursor ions through collisions with neutral gas atoms or molecules. After selection by the first quadrupole, the precursor ions are accelerated by the electric field between a grounded plate and the collision cell, before colliding with an inert gas, such as argon. The kinetic energy imparted to the ion molecules, referred to as lab-frame kinetic energy (E_{lab}) in electron volts (eV), can be tuned to regulate the extent of fragmentation. During inelastic collisions with argon atoms, part of the ion's total kinetic energy is internalized and distributed among its vibrational and rotational modes. Once the internal vibrational energy surpasses bond dissociation thresholds, the bonds irreversibly stretch and break, generating fragment ions and neutral species (**Figure 2-9**).[93]

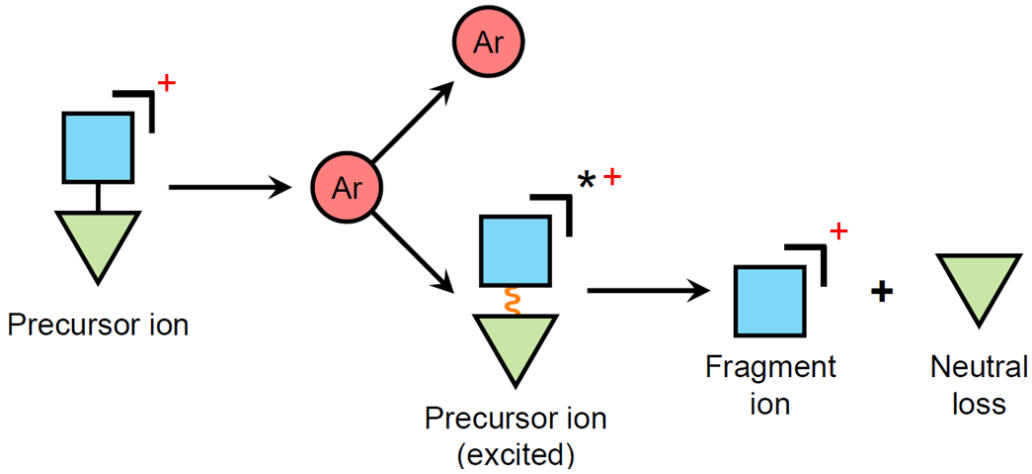

Figure 2-9. Collision-induced dissociation process. As the accelerated precursor ion collides with an argon atom, part of its translational kinetic energy is converted into internal energy (vibrational and rotational excitation). If the resulting internal energy exceeds the relevant dissociation or isomerization thresholds, the ion undergoes bond cleavage or unimolecular fragmentation. (Reproduced from ref 93. Licensed under CC BY 4.0 https://creativecommons.org/licenses/by/4.0/)[93]

To relate fragmentation efficiency to collision energy, the center-of-mass frame energy (E_{com}) is used as an approximation. E_{com}, calculated via **equation 11**,[94] represents the amount of lab-frame energy that can be internalized, taking into account the relative mass difference between the precursor ion (M_{ion}) and that of the collision gas (M_{Ar}).[84,93]

$$E_{com} = E_{lab}\left(\frac{M_{Ar}}{M_{Ar} + M_{ion}}\right) \qquad \textbf{(eq. 11)}$$

2.3 Imaging photoelectron photoion coincidence spectroscopy (iPEPICO)

The imaging photoelectron photoion coincidence (iPEPICO) apparatus, used for unimolecular radical cation dissociation and pyrolysis studies of 4-ethylguaiacol and eugenol, is located at the vacuum ultraviolet beamline of the Swiss Light Source (SLS), a third-generation synchrotron light source.

2.3.1 Photoionization process

To initiate photoionization and generate both ionic and neutral species, a high-energy radiation source is required to excite valence-shell electrons. Synchrotron radiation, produced by accelerating electrons at relativistic speeds through magnetic fields in particle accelerators, serves as an ideal source due to its broad spectral range and high brilliance. Unlike conventional discharge lamps, synchrotron light offers superior tunability via diffraction gratings and significantly enhances ionization efficiency, enabling more precise and sensitive spectroscopic measurements.[95] Upon photon absorption, an isolated gas-phase molecule can be excited across its translational, rotational, vibrational and electronic modes. Electronic and vibrational excitations occur at discrete energy levels and are frequently accompanied by rotational level transitions, collectively known as rovibrational transitions. Translational energy levels, by contrast, are so densely spaced that they can be treated as a continuum, and the effect of the photon's momentum on the molecule is effectively negligible.[95]

When a generic molecule AB absorbs a photon, *hv*, ionization predominantly proceeds via direct ionization and autoionization mechanisms.[95,96]

$$AB + h\nu \rightarrow AB^+ + e^- \quad \text{Ionization}$$

$$AB + h\nu \rightarrow AB^* \rightarrow AB^+ + e^- \quad \text{Autoionization}$$

$$AB + h\nu \rightarrow AB^* \rightarrow AB^+ + e^- \rightarrow A^+ + B + e^- \quad \text{Dissociative photoionization}$$

The key distinction between direct ionization and autoionization lies in the origin of the transition probability: in direct ionization, it is governed by the ionization continuum, whereas in autoionization, it is determined by the transition to the excited neutral state, AB^*. In the PEPICO

(photoelectron photoion coincidence spectroscopy) experiment, the decay of autoionizing resonances directly impacts the ability to isolate electrons at precise kinetic energies. By exploiting autoionization, ions can be generated within Franck-Condon (FC) gap regions – areas where direct ionization is inherently weak due to low FC factors – that are otherwise inaccessible via direct photon excitation from either the neutral or ionic ground state. These phenomena are investigated in this thesis using threshold photoelectron photoion spectroscopy (TPEPICO).[95,96]

2.3.2 Principle of energy selection

When a molecule absorbs a vacuum ultraviolet (VUV) photon with an energy ($h\nu$) exceeding the binding energy of an electron, ionization occurs at a threshold known as the ionization energy (*IE*) and two types of *IE* are generally reported: 1) Adiabatic ionization energy: the minimum energy required to remove an electron and form the ion in its ground electronic and zero-point vibrational state ($v = 0$ to $v^+ = 0$). It represents the lowest *IE* for the transition to a particular ion electronic state. 2) Vertical ionization energy: it represents the energy associated with the most intense peak within the vibrational progression of the photoelectron spectrum, typically reflecting the most probable transition, which may or may not correspond to ionization to the $v^+ = 0$ level, depending on the geometric similarity between the neutral and ionic states. This distinction arises because electron excitation leads to a redistribution of the electronic charge, which in turn influences the Coulombic interactions experienced by the nuclei. This change can induce nuclear motion, resulting in enhanced vibration (phenomena known as vibronic transitions).[95,96]

Upon photon absorption, the ejected electron can have energy that ranges from 0 to IE-$h\nu$.[96] Consequently, the kinetic energy of the electron is given by[95]

$$h\nu = IE + E_{ion} + KE_{ion} + KE_{e^-} \qquad \textbf{(eq. 12)}$$

IE denotes the adiabatic ionization energy, E_{ion} represents the ion's internal energy, KE_{ion} the ion's kinetic energy, and KE_{e^-} the electron's kinetic energy. By conservation of momentum, most of this excess energy is partitioned into the electron kinetic energy (being the lighter fragment), leaving the much heavier cation with negligible recoil velocity. Thus, the ion's kinetic energy term can be disregarded, and the expression simplifies to[95]

$$h\nu = IE + E_{ion} + KE_{e^-} \qquad \textbf{(eq. 13)}$$

Equation 13 shows that an ion of internal energy E_{ion} corresponds directly to an electron with a specific kinetic energy. Therefore, by detecting ions in coincidence with an electron of a specified kinetic energy, it is possible to selectively analyze ions corresponding to defined internal energies.[96]

In TPEPICO, "threshold" refers to the detection of electrons with initially zero kinetic energy. Thus, TPEPICO involves the measurement of internal energy-selected ions alongside their close to zero-energy (threshold) ejected electron.

The internal energy of the ion E_{int} (M^+) is as follows:

$$E_{int}(M^+) = E_{int}(M) + h\nu - IE_{ad} \qquad \textbf{(eq. 14)}$$

where $h\nu$ is the photon energy, $E_{int}(M)$ denotes the internal energy of the neutral, and IE_{ad} represents the adiabatic ionization energy.

Threshold electron detection, which selectively records electrons with negligible kinetic energy, offers several advantages over conventional PEPICO techniques. The fact that threshold electrons are effectively stationary within the ionization region, whereas energetic electrons are mobile, this difference can be exploited experimentally. Absorption of a photon promotes a neutral molecule to a high-lying neutral electronic state, AB^*, typically a Rydberg state, in which the ion core is left with the excited electron in an orbital with a high principal quantum number. As the electron possesses virtually no kinetic energy, once in a Rydberg orbital, it spends most of its time at large distances from the core, treating the core as a point charge.[95,97] A dense series of these Rydberg states converges upon each ion state. During autoionization, the Rydberg state can couple to a lower-energy ion state, producing a vibrationally or rotationally excited ion and the corresponding ejected threshold electron.[95,98] As a result, additional spectral features can be identified in the TPES (threshold photoelectron spectra) within Franck-Condon gap regions, where there is no direct

overlap between the states involved in the transition (**Figure 2-10**).[95] Additionally, threshold detection achieves superior electron resolution, typically below 1 meV, eliminating the need for dispersive electron analyzers, as only threshold electrons are selected. This method also achieves higher sensitivity because nearly all threshold electrons are collected (higher collection efficiency), improving signal-to-noise ratios and minimizing false coincidences.[96]

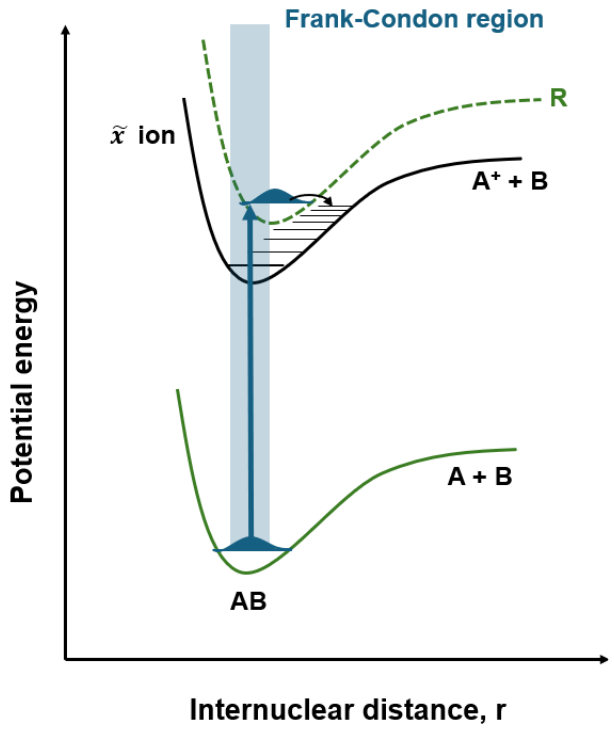

Figure 2-10. Potential energy curves demonstrating autoionization. The neutral molecule is excited to the Rydberg state, R, which can cross over to the ionic ground state, $\tilde{x}$, leading to the formation of an ion and a neutral fragment. (Reproduced from ref 95. Licensed under CC BY 4.0 https://creativecommons.org/licenses/by/4.0/)[95]

2.3.3 Experimental setup

Samples of 4-ethylguaiacol and eugenol are effusively introduced into the endstation (**Figure 2-11**) via a continuous argon flow. The resulting vapour-argon mixture expands through an orifice to generate a molecular beam, which is directed into a SiC microreactor (also known as a heating tube, **Figure 2-12a**). A surrounding water-cooled chamber protects the optics and vacuum components from radiative heating. For radical cation unimolecular dissociation studies, the microreactor is maintained at ambient temperature, allowing the neutral molecular beam to be

skimmed directly into the iPEPICO ionization chamber. Conversely, for neutral pyrolysis experiments, the microreactor is resistively heated (**Figure 2-12b**) to thermally decompose the samples, and the resulting molecular beam of neutral pyrolysis products is then introduced into the ionization chamber.

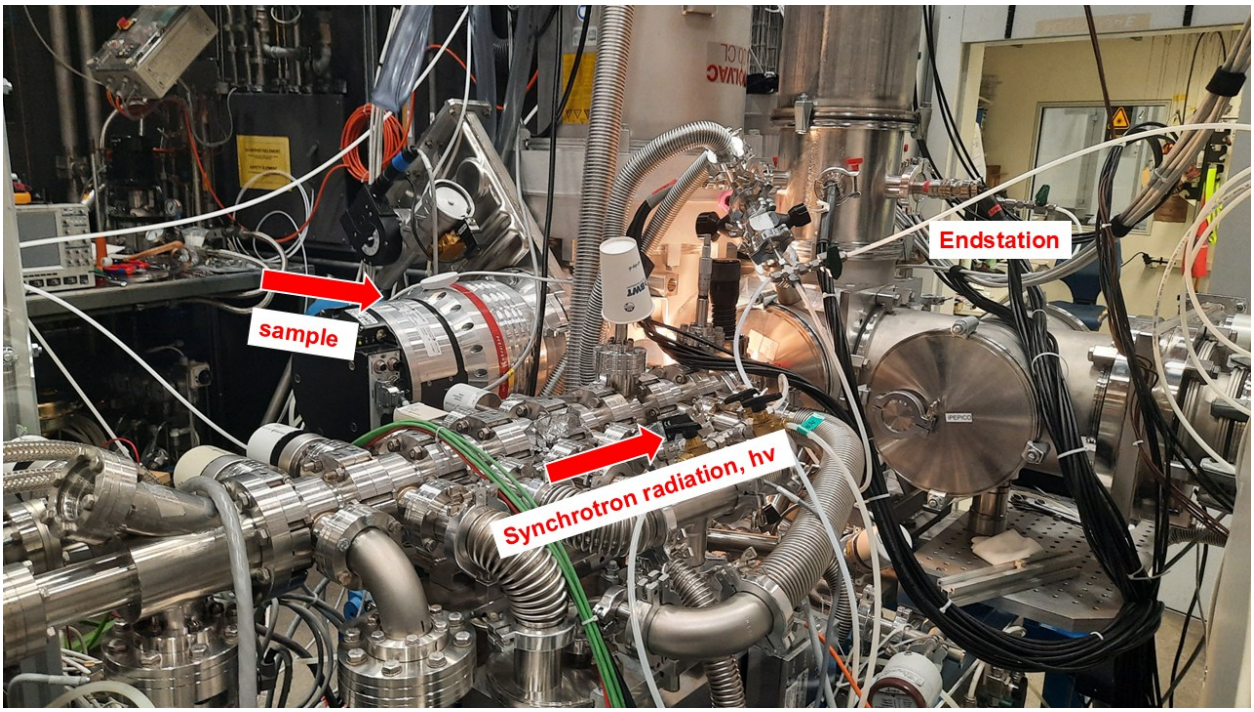

Figure 2-11. The iPEPICO endstation at SLS.

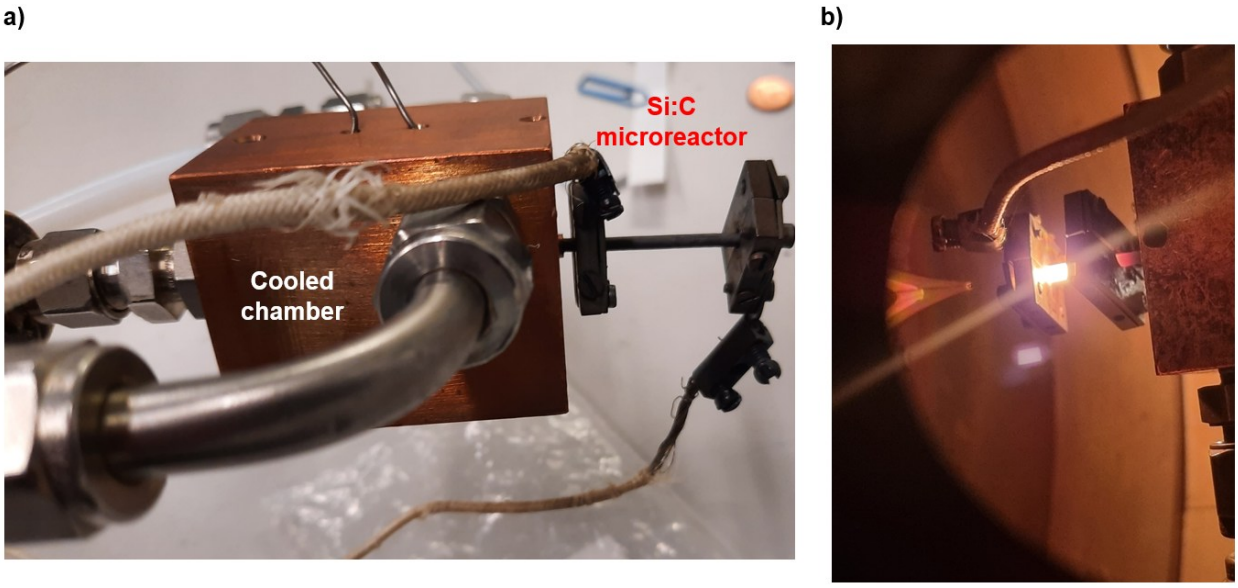

Figure 2-12. a) Cooling chamber and SiC microreactor pictured at SLS. b) SiC microreactor heated for pyrolysis.

The sample is ionized using monochromatic VUV synchrotron radiation, dispersed by a grazing incidence monochromator.[99] Following photoionization, electrons and ions are accelerated in opposite directions toward their respective detectors by a constant extraction field of 20-120 V/cm applied across the ionization region (**Figure 2-13**).[100] As electrons are orders of magnitude lighter than ions, they reach the detector substantially earlier and initiate the time-of-flight (TOF) measurement. The ejected electrons are velocity map imaged (VMI) onto a 40 x 40 mm DLD40 Roentdek position sensitive delay-line detector (**Figure 2-14a**).[95] The advantage of VMI is that electrons with similar initial velocity (and by consequence, same kinetic energy) are focused to the same area of the detector regardless of their point of origin of formation in the ionization region.[101] Threshold electrons are focused directly onto the centre of the detector (**Figure 2-14b**). Nonetheless, electrons are also produced, which initially possess kinetic energy (referred to as "hot" electrons) and are focused around the central threshold electron spot.[100] However, a subset of these hot electrons may have velocity vectors directed toward the centre of the detector, leading to contamination of the true threshold signal. Thus, during data analysis, the hot electron contamination of the threshold signal is accounted for by a simple subtraction process introduced by Sztáray and Baer[102], in which the hot electron signal, represented as a small ring around the central spot, is subtracted from the central threshold signal (**Figure 2-14c**).

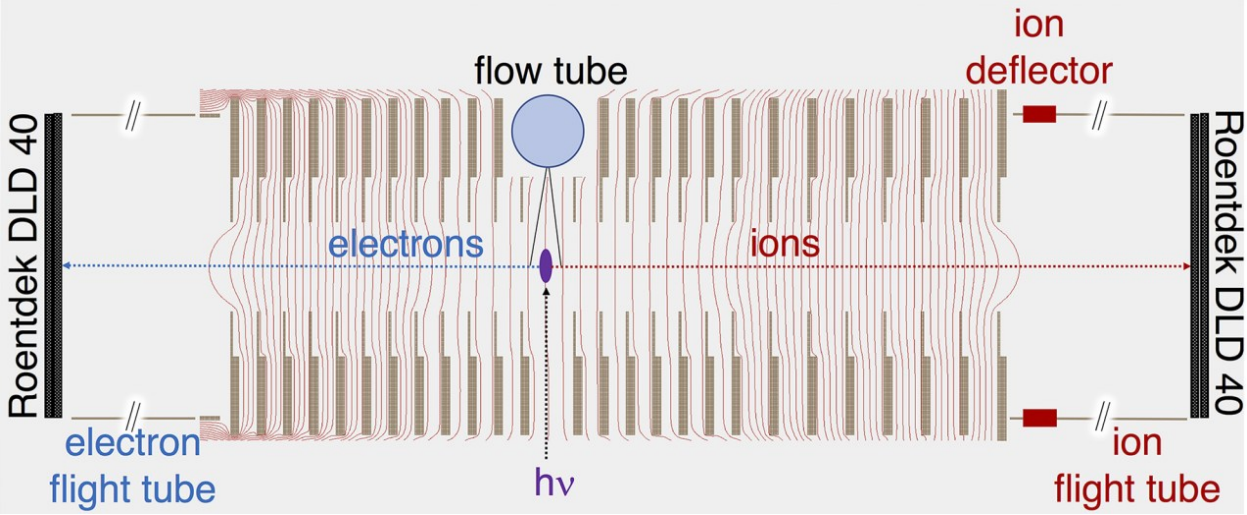

Figure 2-13. Schematic of the iPEPICO endstation interior, showing the principal components and illustrating the photoionization process within the vacuum chamber. (Adapted with permission from ref 100. Copyright 2017)[100]

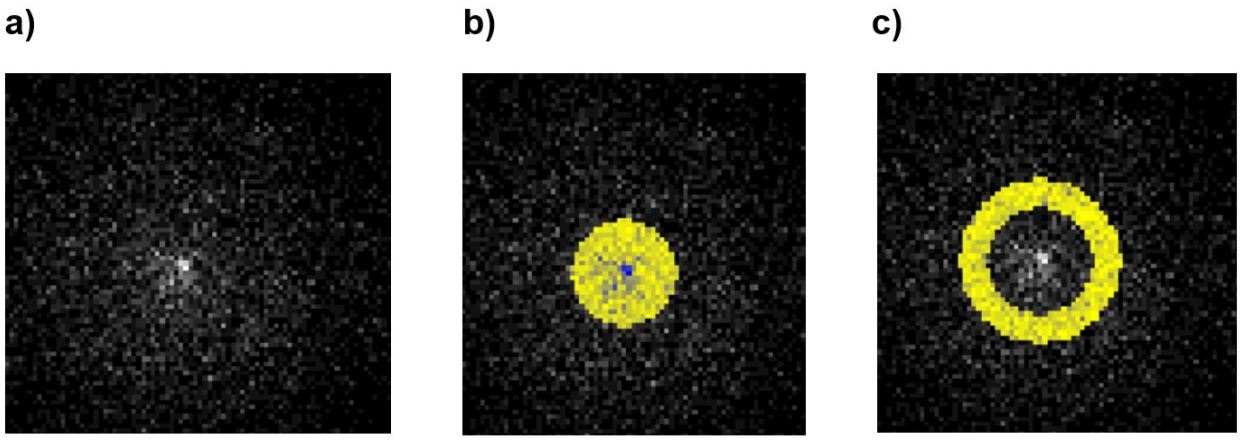

Figure 2-14. a) The electron signal image of 4-ethylguaiacol radical cation at 8.0022 eV as captured by the DLD40 Roentdek detector. b) The circle area for the threshold electron signal. c) The ring area accounting for hot electrons.

After acceleration through a 5 cm long 120 V/cm primary acceleration region, the ions are further accelerated to -1800 V to establish the required space-focusing conditions.[99] This configuration follows the standard Wiley-McLaren geometry[103], making the arrival time of ions with the same *m*/*z* effectively independent of their point of ionization within the ionization region. All ions receive the same net kinetic energy during acceleration, so their velocity depends only on *m*/*z*, not

on where they were generated. Ions generated closer to the first electrode (near the electron detector) originate at a more positive potential, and therefore experience a different potential drop than those formed closer to the ion detector. The first-stage and second-stage fields are chosen so that ions created at the front of the source gain a somewhat larger initial velocity but travel a slightly longer effective distance; ions created at the back gain a smaller initial velocity but travel a slightly shorter effective distance. These two effects offset each other at the detector, such that both populations reach the ion detector nearly simultaneously and define the lower and upper limits of the TOF distribution (earliest and latest possible arrival times of ions with the same m/z).[103,104] Detection of the ion terminates the time-of-flight measurement.

2.3.4 Experimental results and data processing

The primary experimental outputs consist of the electron signal from the central spot and ring correction, ion TOF distributions obtained in coincidence with electron events from the central spot (circle) and the ring, acquisition times and photon energy. The initial processing step is accounting for the hot electron contamination. This is accomplished by scaling the ring signal by a multiplication factor (typically 0.6 or 0.7, the ratio of the ring-to-circle area) and subtracting the scaled ring contribution from the threshold central spot signal. Plotting the corrected threshold electron intensity as a function of photon energy yields the TPES, while a plot of the integrated absolute ion intensities versus photon energy produces the mass-selected TPES (ms-TPES). Plotting the integrated relative ion intensities (fractional ion abundance) as a function of photon energy results in a breakdown diagram.

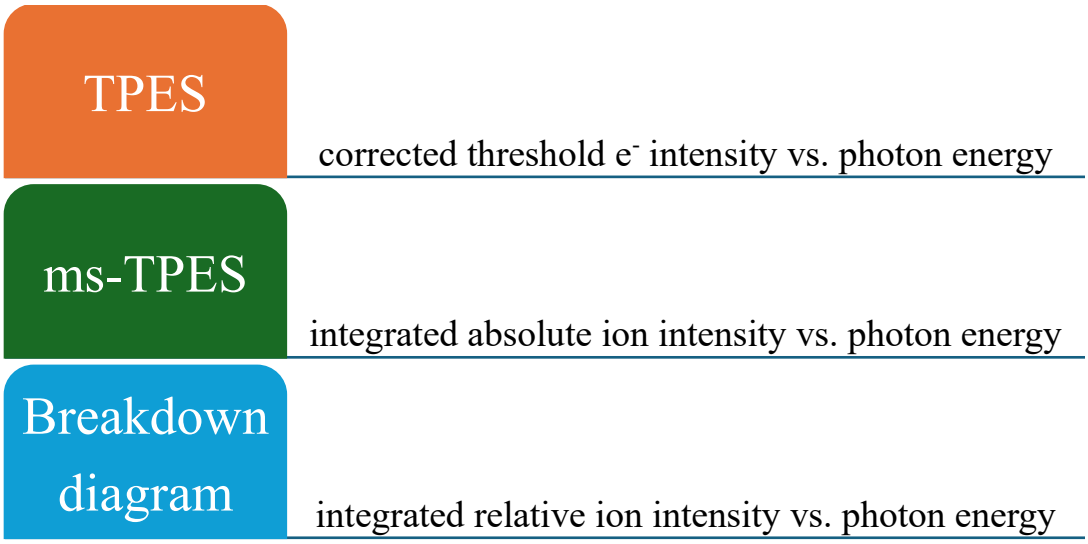

Figure 2-15. iPEPICO data processing workflow

2.3.5 Vibrational structure, FC simulation

Vibronic transitions observed in TPES and ms-TPES are a combination of electronic, vibrational, and rotational transitions that arise when an electronic transition occurs from the neutral to the ionized molecule. The probability of an observable transition is given by the Franck-Condon (FC) principle[105] and is based on the Born-Oppenheimer approximation: because nuclei are much heavier than electrons, electronic promotion occurs on a significantly shorter timescale than nuclear motion, so the nuclei may be considered fixed during the transition. Consequently, ionization proceeds as a vertical transition.[105] FC factors can be used to determine the probability of transitions to different vibrational levels, while taking into account the change in geometry between the ion and the neutral.[95,105] Transitions with a high probability involve a transition from lower vibrational states to upper vibrational states, where the vibrational wavefunctions exhibit maximal overlap and manifest themselves as intense peaks in the TPES (**Figure 2-16**)[95] and ms-TPES, whereas transitions with poor overlap appear as weaker features within the same band.[95,106] FC simulations calculated using the Gaussian software can be overlaid on experimental TPES and ms-TPES to assign and visualize the contributing vibrational transitions.

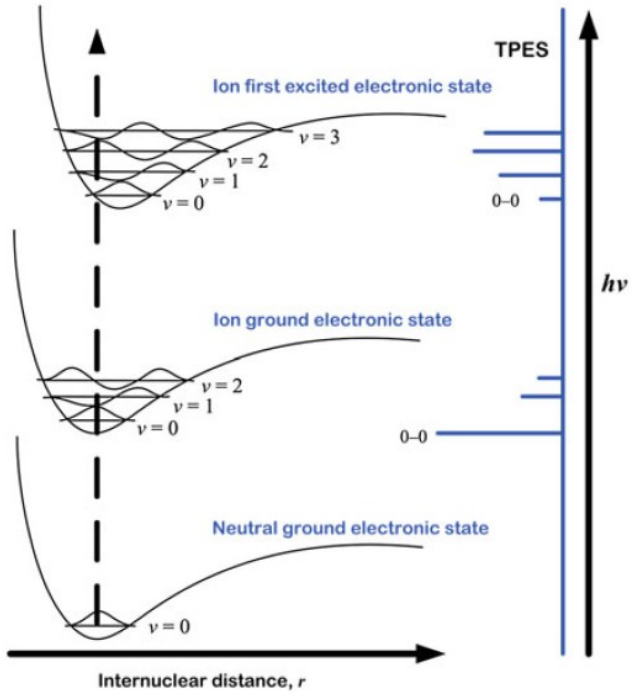

Figure 2-16. Potential energy curves with an overlaid stick TPES illustrating the Franck–Condon principle. The dashed line denotes the vertical electronic transition. Intense TPES peaks correspond to vibrational levels with maximum overlap between the neutral and ionic vibrational wavefunctions. (Reproduced from ref 95. Licensed under CC BY 4.0 https://creativecommons.org/licenses/by/4.0/)[95]

2.3.6 Statistical modelling, minimalpepico software

Accurate thermochemical and kinetic parameters from PEPICO experimental data require careful modelling in terms of energy distributions and dissociation rates. For this thesis, the unimolecular radical-cation dissociation was modelled using the minimalpepico program.[107] The program incorporates the physical parameters of the ion optics in the iPEPICO experiment, the parent ion internal energy distribution (derived by shifting the neutral thermal distribution by the photon energy minus the adiabatic ionization energy), and statistical rate constants for each dissociation channel.[107] From these inputs, minimalpepico computes theoretical branching ratios and time-of-flight distributions for direct comparison with experimental results.[107]

The program executes the following steps:

1) Generate the thermal energy distribution of the neutral precursor.

The first step is to determine the energy distribution of the neutral precursor molecule at the experimental temperature. Molecular rotations are treated using a classical density of states function ρ(*E*)[107,108] and the vibrational density of states are convoluted with the rotational states using the direct-count method (Beyer and Swinehart direct-count algorithm).[109] The energy distribution of the neutral molecule *P*(*E*) at temperature *T* is then determined by the Boltzmann expression:[107]

$$P(E) = \frac{\rho(E)e^{-E/k_BT}}{\int_0^\infty \rho(E)e^{-E/k_BT}} \qquad \textbf{(eq. 15)}$$

*2) Generate the internal energy distribution of the molecular ion using the neutral precursor's density of states and photon energy (**Figure 2-17**).*

The energy distribution of the neutral molecule is directly transposed onto the ground electronic state of the ionic manifold, and the molecular ion's internal energy can be obtained by **equation 14** (refer to section 2.3.2):

$$E_{int}^{M^+} = E_{int}^{M} + h\nu - IE_{ad} \qquad \textbf{(eq. 14)}$$

where $E_{int}^{M^+}$ represents the internal energy of the molecular ion, E_{int}^{M} is the internal energy of the neutral, $h\nu$ denotes the photon energy and IE_{ad} the adiabatic ionization energy. This direct transposition of the neutral energy distribution upon ionization is widely validated across many systems,[110,111] and it has been found that the approximation generally improves for larger molecules.[107]

3) Calculate the dissociation rates, k(E), as a function of the ion's internal energy using RRKM theory (refer to section 3.5).

4) Generate a theoretical breakdown diagram using the energy distributions and dissociation rates.

5) Compute TOF distributions using experimental rate information.

6) Comparison of the calculated breakdown curve and TOF spectra with the experimental data to assess agreement.

7) Adjust the model parameters, E_0 and $\Delta^{\ddagger}S$, and repeat steps 1-6 iteratively until the simulated and experimental results converge.

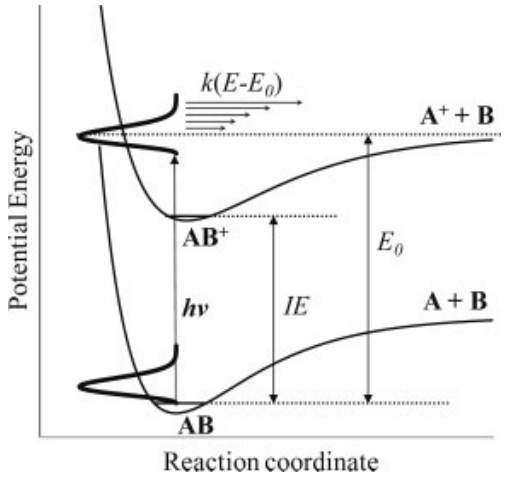

Figure 2-17. The dissociative threshold photoionization process. The neutral's internal energy distribution is transposed onto the ion manifold upon threshold ionization. The shift between the neutral and ionic origin energies equals the photon energy, *hv*; the adiabatic ionization energy (*IE*) is the energy difference between the neutral and ionic ground states; the 0 K appearance energy (E_0) is the energy difference between the ionic dissociation limit and the neutral ground state. (Adapted with permission from ref 107. Copyright 2010 John Wiley & Sons, Ltd.)[107]

CHAPTER 3: COMPUTATIONAL METHODS

This chapter describes the computational approaches employed to support and interpret the experimental data. Investigating guaiacol and its derivatives across their neutral, protonated, and radical-cationic states requires a rigorous, multi-level computational strategy to resolve dissociation dynamics, determine reliable thermochemical values, and map the relevant potential energy surfaces (PES). Density Functional Theory (DFT), as implemented in the Gaussian 16 software suite,[112] served as the primary tool for geometry optimizations, vibrational frequency analyses, and minimum energy reaction pathway (MERP) mapping. These foundational DFT calculations were subsequently augmented by high-accuracy composite methods (CBS-QB3) to obtain refined thermochemical and kinetic parameters. This chapter outlines the fundamental principles underlying these methodologies and outlines the specific computational protocols applied to study the different molecular forms.

3.1 Density functional theory (DFT)

DFT provides a computationally efficient and scalable framework for determining the electronic structure of molecular systems, offering a practical compromise between accuracy and computational cost.[113,114] Unlike traditional ab initio methods that solve the complex, multi-electron Schrödinger equation for both the energy and the wavefunction, DFT reformulates the problem in terms of electron density ($\rho(x,y,z)$), which is a function of position only, that is, it only depends on three variables (x,y,z).[115] By contrast, the many-electron wavefunction of an n-electron molecule is a function of $4n$ variables (three spatial coordinates and one spin coordinate, for each electron), which greatly increases computational complexity. DFT methods were built on concepts from Hartree-Fock (HF) theory, which treats electrons as moving in an average potential generated by all the other electrons, without accounting for the dynamic electron correlation.[114] In contrast, DFT employs the Kohn-Sham approach, which is based on the Hohenberg-Kohn theorems,[116,117] which states that the total energy of the system is a unique functional of the total electron density. The practical implementation involves solving the Kohn-Sham single-electron equations, which map the interacting system with noninteracting system (electrons). The complexity of electron-electron interactions is then approximated within the exchange-correlation functional.[115]

Time-dependent density functional theory (TD-DFT) was employed to investigate the excited state properties and optimize the geometries of molecules in their excited states (for example, the first singlet excited state, S_1). While ground state DFT relies on the Hohenberg-Kohn theorems, TD-DFT is founded on the Runge-Gross theorem, which establishes that for a system evolving from a fixed initial state, there is a one-to-one mapping between the time-dependent external potential and the time-dependent electron density.[118] In practical applications, this formalism enables the determination of vertical excitation state energies and the subsequent optimization of excited-state geometries. To achieve the latter, analytic gradients of the TD-DFT energy are calculated. These gradients allow for the iterative exploration of the excited state potential energy surface to locate stationary points, such as local minima, representing the equilibrium nuclear configuration of the molecule in its excited state.[119]

3.1.1 B3LYP and M06 functionals

DFT approximates the exchange–correlation energy through the use of functionals that map the electron density to a scalar energy contribution. A good functional handles not only exchange and correlation errors but also self-repulsion and kinetic energy errors.[115] B3LYP and M06 are the two functionals employed in this thesis. Functionals are typically partitioned into an exchange term and a correlation term. B3LYP is a widely popular functional known for its balance between computational efficiency and accuracy, particularly for predicting molecular geometries and thermochemistry.[115,120] B3LYP is classified as a hybrid functional as it integrates a portion of the Hartree-Fock exact exchange with density functional exchange and correlation components.[112] In B3LYP, B3 denotes the Becke 3-parameter exchange functional[121] and LYP the Lee, Yang, Parr correlation functional[122].

M06, developed by the Truhlar group[123], is part of the Minnesota family of functionals. Unlike standard hybrid functionals that rely solely on electron density, M06 also incorporates the kinetic energy density of the Kohn-Sham orbitals, allowing for a more flexible and accurate modelling of complex electronic environments. The M06 functional was specifically parameterized to correct deficiencies often found in earlier methods, particularly regarding non-covalent interactions (such as Van der Waal forces and π-π stacking) and transition metal chemistry.[115,123]

3.1.2 Basis set

In computational quantum chemistry, the electronic wavefunction is mathematically described using a basis set, which is a collection of mathematical functions (basis functions) used to approximate atomic orbitals within a molecule. Following the linear combination of atomic orbitals (LCAO) approximation, molecular orbitals are built as linear combinations of these individual basis functions.[115] Quantum-chemistry packages like Gaussian 16 commonly employ Gaussian-type orbitals (GTO) as Gaussian integrals can be evaluated far more rapidly than integrals over alternative primitive functions.[115,124] The choice of basis set is consequential; larger, more flexible basis sets impose fewer constraints on the electrons and generally yield more accurate results, but at a significantly higher computational cost.[115]

The electronic structure calculations presented in this thesis were performed using the Pople-type split-valence basis sets 6-31G(d) and 6-311+G(d,p). The 6-311+G(d,p) basis set is a split-valence triple-zeta basis set, which offers greater mathematical flexibility for the valence electrons compared to the double-zeta basis set of 6-31G(d).[95] The specific architectural components of these basis sets are detailed as follows:

- **6-311 (split-valence notation)**: Within this framework, the core orbitals of each atom are represented by one basis function, each composed of six Gaussians (hence the "6"). The 311 represents a split-valence set with each valence atomic orbital split into three shells; the first one (3) is composed of a linear combination of 3 Gaussian functions, and the second and third (11) are a linear combination of individual Gaussian functions. This triple split allows the valence orbitals to expand or contract more dynamically to accommodate the specific electronic environment of the molecule.[115,125,126]
- **+ (diffuse function)**: Lone-pairs of electrons are relatively weakly bound and, on average, at a larger distance from the nuclei than core electrons or electrons engaged in bonding, which are relatively tightly bound to the molecular nuclear framework. To accurately represent these spatially extended electron distributions, diffuse functions (denoted by the plus sign) are incorporated. These functions augment the non-hydrogen heavy atoms with diffuse s and p orbitals, which improve the description of anions and weak interactions by allowing the electron density to extend further from the nucleus.[115,127]

- **G(d,p) (polarization function)**: These are used to account for the distortion of atomic orbitals within a molecule caused by the interaction with neighbouring atoms. In this convention, d-type functions (orbitals) are added to the heavy atoms (2^{nd} row atoms) and p functions added to the hydrogens. This provides the necessary angular flexibility to atomic orbitals, thereby improving the representation of orbital deformation induced by bonding and the molecular environment.[115,128]

3.2 Composite methods

While standard DFT provides a versatile tool for molecular modelling, achieving chemical accuracy (typically defined as errors less than 1 kcal/mol) often requires methods that account for electron correlation more rigorously, such as Coupled Cluster theory.[115] Direct application of such high-level methods with large basis sets is computationally prohibitive for most systems. Composite methods mitigate this computational cost by performing a sequence of smaller, high-level calculations and combining the results using an additive scheme. This approach assumes that the effects of improving the basis set and the treatment of electron correlation are approximately additive, allowing the program to estimate the energy of a high-level calculation at a fraction of the cost.[129,130] A central element of composite methods is the extrapolation of the basis set to an infinite limit (to completion).[115]

3.2.1 CBS-QB3 method

The CBS-QB3 (Complete Basis Set-quadratic Becke3), developed by Petersson and coworkers, is a multi-step model chemistry that approximates a high-level calculation (such as Coupled Cluster theory with a large basis set) by combining a series of computationally efficient lower-level calculations and applying empirical corrections.[129,130] The power of CBS-QB3 lies in its ability to extrapolate the electron correlation energy to the Complete Basis Set (CBS) limit. It is widely used in computational kinetics and thermodynamics because it provides a more reliable energy value than single-step DFT methods, which can sometimes struggle with specific electronic environments or large basis set requirements.[115,131]

The CBS-QB3 method does not solve for the energy in a single step. Instead, it performs a series of calculations at different levels of theory and combines them. The CBS-QB3 protocol follows a predefined sequence of steps:[129,130]

1. Zero-Point Vibrational Energy (ZPVE)

The molecular structure is first optimized at the B3LYP/6−311G(d,p) level, followed by a frequency calculation. This generates the ZPVE, which is scaled by a factor (typically 0.99) to account for anharmonicity.

2. Single-point calculations at MP2 and MP4 Levels

A single-point calculation is an energy evaluation performed at a fixed molecular geometry. Unlike in a geometry optimization, the atoms do not move (fixed); the program simply calculates the electronic energy for that specific set of coordinates.[132,133] In CBS-QB3, several single-point calculations are performed:

- MP2/CBSB3 and MP4/CBSB4: These steps utilize Møller–Plesset perturbation theory (MPn)[134], which improves upon Hartree-Fock theory by accounting for electron correlation.
    - MP2 handles the majority of the correlation energy, while MP4 captures higher-order effects.
    - The suffixes CBSB3 and CBSB4 refer to the specific, internal basis sets chosen by the CBS protocol to be used with these specific MP levels to ensure the data is compatible for the final extrapolation.[134,135]

3. CCSD(T) and perturbative excitations

The most critical step for accuracy is the CCSD(T) calculation. This method, "Coupled Cluster with Single, Double, and Perturbative Triple excitations," is often called the "gold standard" of quantum chemistry.

- In a full CCSDT calculation, the simultaneous movement of three electrons (triple excitations) is calculated iteratively, which is computationally demanding and slow. In CCSD(T), the triple excitations are treated perturbatively. This means they are calculated as a mathematical correction (using perturbation theory) rather than

through the full iterative process. This provides nearly the same accuracy as a full triple calculation but at a fraction of the time and cost.[136]

4. Extrapolation to the Complete Basis Set (CBS) limit and final correction

The core "trick" of the CBS methods is the final extrapolation. Because even a large basis set cannot perfectly describe an electron cloud, the results from the MP2 steps are used to mathematically estimate what the energy would be if an infinitely large (complete) basis set were used, and the corrections from the MP4 and CCSD(T) steps are added.[137] Finally, an empirical Higher Level Correction (HLC) and a correction for spin contamination are added to calculate the reaction energetics for the species optimized at the B3LYP level.[129]

3.2.2 The Gaussian-n (Gn) series: G2, G3 and G4

The Gaussian-n (Gn) methods, developed by Curtiss, Raghavachari and Pople, consist of a series of high-accuracy composite protocols designed to determine the total electronic energies of molecular systems. In this thesis, the Gn series was employed in conjunction with CBS-QB3 to determine the adiabatic ionization energies of molecules where experimental literature values are currently unavailable.

3.2.2.1 Gaussian-2 (G2) method

G2 theory was developed as a refinement of the original G1 method to better account for basis set deficiencies. The protocol initiates with a geometry optimization and subsequent frequency analysis at the MP2/6-31G(d) level. The total energy is then estimated through a series of single-point evaluations, including MP4 and QCISD(T) (Quadratic Configuration Interaction with Single, Double, and Perturbative Triple excitations). These steps are designed to treat electron correlation more rigorously than standard HF or DFT methods. The final energy includes an empirical HLC, which is parameterized based on the number of valence electrons to account for residual deficiencies in the correlation treatment.[138]

3.2.2.2 Gaussian-3 (G3) method

The G3 method was introduced to enhance the performance of G2 by implementing an expanded basis set and a refined HLC. A key innovation in G3 theory is the utilization of MP2-based basis

set extensions to estimate the effects of larger basis sets. This modification significantly improves computational efficiency, enabling the study of larger molecular systems without sacrificing the accuracy of thermochemical properties, such as enthalpies of formation and ionization potentials. G3 generally provides a more consistent description of 3rd row elements compared to its predecessor.[139]

3.2.2.3 Gaussian-4 (G4) method

G4 theory represents the most sophisticated and computationally refined iteration of the Gn series. While G2 and G3 rely on MP2-derived geometries, G4 utilizes B3LYP/6-31G(2df,p) for structural optimization and frequency calculations. This transition to a DFT-based geometry often provides a more reliable starting point for complex electronic environments. Significant advancements in the G4 protocol include:[140]

- An expanded basis set scheme is used for the MP2 level extrapolation to the complete basis set limit.
- The inclusion of spin-orbit coupling and scalar relativistic corrections for accurate energetic predictions of systems containing heavier atoms.
- An optimized HLC that was parametrized against a much larger and more diverse collection of experimental data, ensuring broader applicability across the periodic table.

3.3 Outer-Valence Green's Function (OVGF)

The Outer-Valence Green's Function (OVGF) method belongs to a family of quantum mechanical approaches known as electron propagator methods. Unlike methods that primarily target finding the total energy of a stable molecule, OVGF is specifically designed to describe the process of changing the number of electrons in a system (processes like ionization or electron affinity). It is a technique designed to bridge the gap between simple orbital theories and the complex reality of electron removal.[141,142]

In standard DFT or ab initio calculations, the ionization energy is typically obtained by performing two separate calculations: one for the neutral molecule (E_M) and one for the cation (E_{M^+}). The ionization energy is then the difference between two ($\Delta E = E_{M^+} - E_M$). In contrast, OVGF treats

the ionization energy as a single physical event: instead of calculating two total energies, it solves a single equation where the solutions represent the energy required to remove an electron from specific orbitals.[143] The core basis of the OVGF method lies in a mathematical term called the self-energy, which accounts for the energetic shift that occurs when an electron is removed from the outer-valence shell. The self-energy is a dynamic correction factor which incorporates orbital relaxation and electron correlation energies and calculates these two effects simultaneously. By incorporating this correction into the initial orbital energy, OVGF yields ionization energies that are significantly more accurate than simple-model estimates, which assume that the other electrons stay "frozen" in place.[144]

The OVGF method, combined with the cc-pVTZ basis set, was used to calculate vertical outer valence orbital ionization energies. The cc-pVTZ (correlation-consistent polarized valence triple-zeta) basis set, developed by Dunning and coworkers, is optimized for correlated electronic-structure methods that go beyond the Hartree-Fock approximation. The prefix 'cc' denotes correlation-consistent, 'p' indicates the inclusion of polarization functions, 'V' refers to valence and 'TZ' stands for triple zeta, which signifies that three distinct basis functions are used to represent each valence atomic orbital, thereby improving the flexibility and accuracy of the valence description.[115,145]

3.4 Equilibrium and transition state structure optimization

To elucidate the reaction mechanisms and energetic landscapes explored in this thesis, electronic structure calculations were carried out using DFT as implemented in the Gaussian 16 software package[112]. DFT served as the primary computational framework for the geometric optimization of neutral precursors and fragments, molecular ions and transition states. The optimization process proceeds via a gradient-based algorithm in which an initial structural guess is iteratively refined by small coordinate adjustments until a stationary point on the potential energy surface is reached, corresponding to an energy minimum.[146]

The mathematical nature of these stationary points is confirmed through the calculation of harmonic vibrational frequencies. A stable equilibrium structure (local or global minimum) is

confirmed by the absence of imaginary frequencies (read as negative values). Conversely, a transition state corresponds to a first-order saddle point, that is, a maximum along the reaction coordinate but a minimum in all other directions (**Figure 3-1**).[147] Consequently, a valid transition state is characterized by exactly one imaginary frequency. The presence of multiple imaginary frequencies suggests a higher-order saddle point, indicating that the structure has not converged to a chemically relevant transition state.[146]

Locating these saddle points was achieved using Synchronous Transit-guided Quasi-Newton (STQN) methods, specifically the QST2 and QST3 protocols integrated into the Gaussian computational suite.[148,149] Unlike conventional transition state methods which often require a highly accurate initial guess derived from constrained optimization scans, QST2 uses the optimized structures of the reactants and products to guide the search. The QST3 variant provides further refinement by incorporating a rough estimate of the transition state geometry to facilitate convergence. Once a transition state is successfully identified, it is validated using the Intrinsic Reaction Coordinate (IRC) method.[150,151] By following the path of the imaginary vibrational mode in both forward and reverse directions, IRC ensures that the transition state correctly links the intended reactants to the designated products.

Finally, all reported internal energies were adjusted to include zero-point energy (ZPE) corrections. To account for basis set dependency and anharmonic effects,[152] raw ZPE values were adjusted using scaling factors from the NIST Computational Chemistry Comparison and Benchmark Database (CCCBDB).[153] The final internal energy for each species was determined by adding the scaled ZPE to the total electronic energy, providing the precise thermochemical data required in subsequent kinetic and mechanistic evaluations.

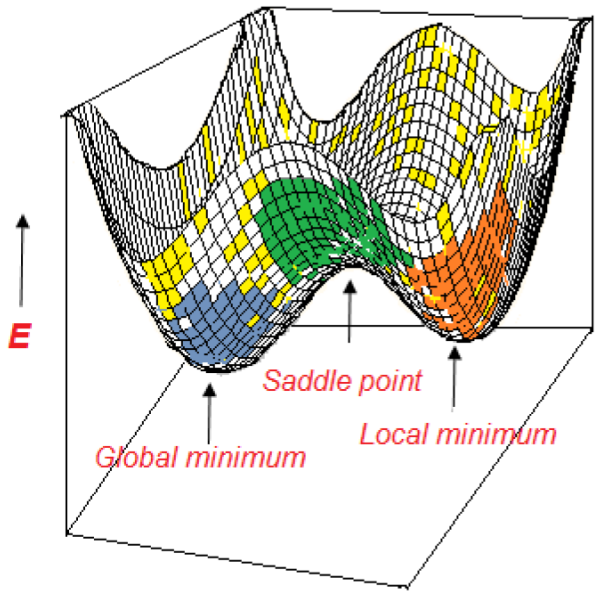

Figure 3-1. Representative potential energy surface showing the reactant (global minimum), the transition state (first-order saddle point) and the product (local minimum). (Reproduced from ref 147. Licensed under CC BY 4.0 https://creativecommons.org/licenses/by/4.0/)[147]

3.5 Unimolecular rate theory: Rice-Ramsperger-Kassel-Marcus (RRKM) theory

In the gas-phase systems investigated throughout this thesis, the primary reactions of interest are unimolecular dissociations occurring under high-vacuum conditions, typically at pressures below 10^{-6} mbar. Within this collisionless regime, the timescale of molecular collisions is significantly longer than the microsecond timescale of the dissociation events. Consequently, the ions do not maintain a thermal Boltzmann distribution, rendering standard temperature-based canonical rate constants ($k(T)$) inapplicable. Instead, the system is treated as a microcanonical ensemble, in which the reaction kinetics are dictated by the internal energy (E) of the individual ion. This necessitates the application of RRKM (Rice-Ramsperger-Kassel-Marcus) theory to determine the internal energy-dependent rate constant, $k(E)$.[154,155]

RRKM theory represents a significant advancement over the preceding RRK (Rice-Ramsperger-Kassel) model. While RRK theory simplified the molecular dynamics by treating the system as a collection of identical, degenerate harmonic oscillators, RRKM theory treats each vibrational

mode individually. RRKM incorporates the vibrational frequencies and rotational constants derived from DFT optimizations (refer to section 3.4) to account for the discrete distribution of energy among the internal modes of the molecule. This mode-specific treatment recognizes that energy is partitioned across distinct vibrational and rotational degrees of freedom rather than residing in a single averaged oscillator.[156]

Within the RRKM framework, it is assumed that the reaction rate is determined by the number of ways the internal energy can be distributed among the various degrees of freedom of the reactant and the transition state. Dissociation occurs when a sufficient amount of energy – the critical energy (E_0) – is localized in the critical oscillator, which corresponds to the motion along the reaction coordinate.[157] A central assumption of RRKM is rapid intramolecular vibrational energy redistribution (IVR), in which the energy must be randomized among all vibrational and rotational modes on a timescale much shorter than that of bond breaking. This fast energy randomization ensures that the energy gets redistributed among all the available modes before finding the critical oscillator. If IVR is slower compared to the dissociation rate, the reaction becomes non-statistical, and RRKM theory is no longer applicable.[158]

A distinguishing feature of RRKM theory is its integration of transition state theory (TST). A key assumption is that once the reaction reaches the transition state, it proceeds irreversibly to products without recrossing. Under this no-recrossing approximation, the microcanonical rate constant is expressed as:[112,129]

$$k(E) = \frac{\sigma N^{\ddagger}(E - E_0)}{h\rho(E)} \qquad \textbf{(eq. 16)}$$

where σ denotes the reaction degeneracy; h represents Planck's constant; E_0, the 0 K activation energy; $N^{\ddagger}(E - E_0)$ corresponds to the sum of states for the transition state at internal energy $E - E_0$. It represents the total number of quantum states available for the system to pass through the transition state and proceed to the products. Consequently, a higher $N^{\ddagger}$ directly correlates to an increased rate constant *k(E)*; $\rho(E)$ is the density of states for the reactant ion at internal energy E. This reflects the number of ways the total internal energy can be distributed among the vibrational

and rotational degrees of freedom of the reactant molecule. A higher density of states leads to a slower reaction rate, as there are statistically more ways for the energy to be distributed away from the critical oscillator.[157] The relationship between the ion internal energy E and the activation (threshold) energy E_0 is shown in **Figure 3-2**.[157]

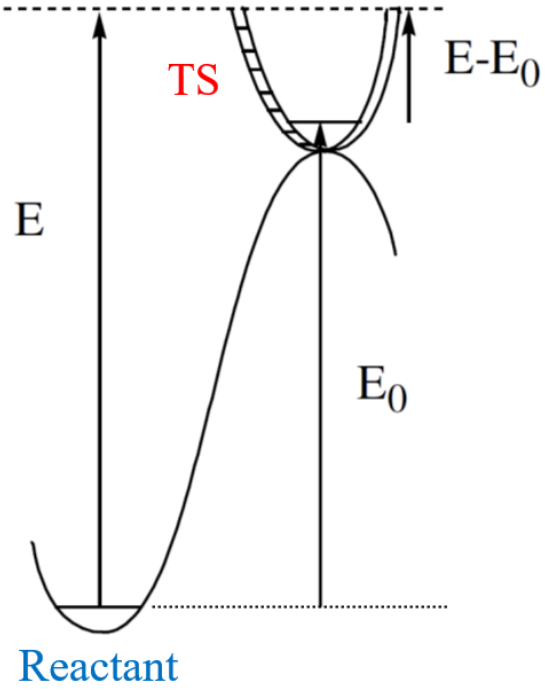

Figure 3-2. Energy level diagram illustrating the relationship between E (ion energy) and E_0 (activation energy); TS denotes the transition state. (Adapted with permission from ref 157. Copyright 1997 Published by Elsevier B.V.)[157]

In this thesis, the density of states, $\rho(E)$, for the reactant and the sum of states, $N^{\ddagger}(E - E_0)$, for the transition state, were calculated using the vibrational frequencies and rotational constants obtained from the optimized structures (section 3.4) using the Beyer and Swinehart direct count algorithm.[109] RRKM theory was subsequently applied to determine the competition between diverging reaction pathways and to model the theoretical breakdown diagram generated from the TPEPICO data, providing a comprehensive description of the unimolecular dissociation rates.

Chapter 4: Exploring the competition between the radical-initiated and closed-shell degradation pathways of 4-ethylguaiacol and eugenol using iPEPICO spectroscopy

The contents of Chapter 4 are being prepared for publication.

Author contributions:
Sandesh Gondarry: Writing – original draft, experimental data processing for the iPEPICO data, DFT calculations.
Paul M. Mayer: Conceptualization, methodology, supervision, experimental work at Swiss Light Source (SLS), writing – review & editing.
Andras Bodi: assisted experimental work at SLS, writing – review & editing.
Maxi A. Burgos-Paci: writing – review & editing

4.1 Introduction

A key constituent of plant biomass, lignin is recognized as a cost-effective and sustainable resource that can be harnessed for chemical synthesis, fuel production, and electrical power generation.[60,159–161] Pyrolysis offers an economically viable method for transforming lignocellulosic biomass into high-demand global products.[162] Due to its structural complexity and compositional diversity, lignin is characterized by diverse functional groups such as hydroxyl, methoxy, carbonyl, and aldehyde substituents distributed across the aromatic ring and alkyl side chains of its monomers.[163,164] This complexity has led researchers to investigate simple lignin model compounds in order to better understand the pyrolysis mechanism. Numerous studies in the literature have investigated the pyrolysis of model lignin compounds, such as phenol[165–167] and guaiacol,[52,56,168] to gain deeper insight into the pyrolytic pathways of lignin.

4-Ethylguaiacol and eugenol, both substituted guaiacols, are established primary pyrolysis products of lignin.[169–173] However, their thermal decomposition mechanisms remain relatively underexplored, with only a limited number of studies available in the literature.[60,62,63,174] Existing investigations have typically been conducted at atmospheric pressure and relatively low

temperatures (below 1000 ºC) and have consistently suggested free-radical reaction pathways. Mullery et al.[63] examined the thermal decomposition of 4-ethylguaiacol using a laminar-flow reactor operating at atmospheric pressure over a temperature range of 300-900 ºC and proposed that the primary decomposition mechanism involves free-radical intermediates. Similarly, Ledesma et al.[60,174] studied the pyrolysis of eugenol using a non-isothermal laminar-flow reactor under comparable conditions (1 atm and 300–900 ºC) and reached the same conclusion. Shen et al.[62] further supported this mechanism by employing synchrotron photoionization mass spectrometry to investigate eugenol pyrolysis between 450 and 750 ºC, also attributing the observed decomposition products to free-radical processes; however, detailed reaction pathway calculations were not carried out to support these hypotheses.

In the present study, the thermal decomposition of 4-ethylguaiacol and eugenol was explored using a low-pressure pyrolysis SiC microreactor at 1017 ºC coupled to imaging photoelectron photoion coincidence (iPEPICO) spectroscopy.[100] Pyrolysis products were identified using photoion mass-selected threshold photoelectron spectroscopy (ms-TPES), supported by Franck–Condon simulations of photoelectron spectra for molecular species corresponding to the observed m/z values. The potential energy surface of the neutral was explored computationally to elucidate detailed reaction mechanisms for the thermal degradation pathways.

4.2 Experimental Procedures

4-Ethylguaiacol and eugenol were purchased from Sigma-Aldrich (>98%, Sigma-Aldrich, Oakville, Ontario, CA) and used without further purification.

The experiments were conducted at the Swiss Light Source (SLS, Paul Scherrer Institut, Villigen, Switzerland) employing the imaging photoelectron photoion coincidence endstation (CRF-PEPICO) at the VUV beamline, the details of which have been thoroughly described elsewhere.[100,175] Detailed accounts of the experimental setup and data acquisition process have been published by Bodi et al.[176]. Pyrolysis was performed using the high-temperature pyrolysis microreactor previously reported for this endstation.[177] A 150 grooves per mm grating was used to disperse the synchrotron radiation, providing an energy resolution of 5 meV. Higher order

harmonics were filtered out with a differentially pumped gas filter operating with a Ne:Ar mixture at 9 mbar across a 10 cm optical path. The resulting monochromatic VUV radiation photoionized molecules within a 2 × 2 mm^2 interaction zone. Both photoelectrons and photoions were velocity map imaged on RoentDek delay line detectors. The electrons were time- and position-stamped at the detector, and the delayed, coincident photoion signal was measured to obtain the time-of-flight mass spectrum. Threshold electrons were mapped at the center of the electron detector, while non-zero kinetic energy ("hot") electrons were detected off-axis based on their momentum in the detection plane. Hot electrons without an initial lateral momentum component can also be imaged in the centre. The mass spectrum based on electrons detected in a ring around the centre spot was used to subtract the hot electron contamination from the centre signal and acquire the threshold photoionization mass spectrum.[102] The photoion mass-selected TPES (ms-TPES) is generated by plotting the normalized signal intensity of a designated *m*/*z* peak from the threshold ionization mass spectra as a function of photon energy.[178]

4-Ethylguaiacol and eugenol were soaked onto glass wool and placed inside a 200 μm molecular beam nozzle. Argon carrier gas, at a flow rate of 30 standard cubic centimetres per minute (sccm), was passed over the sample through the molecular beam nozzle into the 3 cm long, 1 mm internal diameter, resistively heated SiC pyrolysis microreactor.

The reactor surface temperatures were determined using a previously established power dependence, measured in an identical pyrolysis setup with a type C thermocouple:

$$T / °C = P / W \times 14.27 + 303$$

where T represents the reactor temperature, and P is the heating power. The reactor temperature is considered to be representative of the gas temperature inside the reactor to within 100 ºC.[179] The reactor pressure is dropping constantly from the inlet nozzle to the reactor aperture to vacuum and is estimated to be 10–40 mbar in the sweet spot where most chemistry is expected to take place, with a residence time lower than 100 μs.[179,180] The reactor is mounted in the source vacuum chamber, in which the background pressure was about 5×10^{-5} mbar during measurements. The molecular beam emerging from the pyrolysis reactor is directed through a 2 mm diameter skimmer

into the detection chamber, which was maintained at a pressure of 10^{-6} mbar during measurements. The reactor, which was heated to 1000 ºC, enabled the investigation of pyrolysis product distributions of 4-ethylguaiacol and eugenol.

The pre-expansion pressure at the reactor nozzle of 1 mm is rather low, which limits the number of collisions in the expansion.[179] This suppresses rovibrational cooling achieved in the expansion, and the effective rovibrational temperatures of methane and phenyl chloride measured in dissociative photoionization agreed with the reactor temperatures within 100 °C.[181] However, there is always a signal component, which experiences a number of wall collisions prior to ionization, and could be shown to be fully thermalized at room temperature. Thus, the total signal is the sum of the commensurate beam and rethermalized components, leading to an intermediate "effective temperature."

Pyrolysis microreactors can be used to study unimolecular and bimolecular reactions, as well.[182] Bimolecular processes require high sample concentrations and are rarely observed at less than 0.5% precursor concentrations.[183,184] However, if the pyrolysis products are highly reactive, such as in benzaldehyde[184] and acetone[185] pyrolysis, a significant contribution may be observed from bimolecular reactions. In previous studies on methyl formate, ethyl formate, and methyl chloroformate pyrolysis, no significant evidence of bimolecular reaction pathways was observed.[186–188]

4.3 Computational Procedures

Geometry optimizations (equilibrium and transition state structures) were carried out at the B3LYP/6-311+G(d,p)[121,122] level of density functional theory (DFT) employing the Gaussian 16 software suite.[112] CBS-QB3[129] single-point energy calculations (without geometry optimizations) were applied to key DFT geometries to obtain more accurate reaction energetics. Intrinsic reaction coordinate (IRC) calculations were performed on the transition states to verify that they accurately connect the designated reactants and products. Franck–Condon (FC) simulations were performed at the optimized geometries of the pyrolysis products using Gaussian 16. Simulations were carried out at a vibrational temperature of 500 K, and spectral transitions were convolved with a Gaussian

with a half-width at half-maximum of 100 cm^{-1} to take the experimental energy resolution and the rotational envelope into account. Rice–Ramsperger–Kassel–Marcus (RRKM) theory was employed to calculate microcanonical unimolecular reaction rates, $k(E)$, as defined by the equation:[108,157]

$$k(E) = \frac{\sigma N^{\ddagger}(E - E_0)}{h\rho(E)}$$

where σ denotes the reaction degeneracy, h represents Planck's constant, E_0, the 0 K activation energy, $N^{\ddagger}(E - E_0)$ corresponds to the number of internal states for the transition state at internal energy $E - E_0$, and $\rho(E)$ is the density of states for the reactant ion at internal energy E as calculated via the Beyer and Swinehart direct count algorithm within the harmonic approximation.[109] State functions were calculated based on geometries and harmonic frequencies obtained at the B3LYP/6-311+G(d,p) level in the RRKM calculation that employed a home-written code.[157]

4.4 Results and Discussion

4.4.1 4-Ethylguaiacol

Figure 4-1 shows the ms-TPES for the products generated during 4-ethylguaiacol pyrolysis. The origin transitions in Franck–Condon (FC) simulations were aligned using literature ionization energy values (**Table A4-1**, Appendix). Comparison of the intensities in the ms-TPES indicates that *m*/*z* 94 seems to correspond to the main pyrolysis product, peaks attributable to phenol or its isomers, 2,4-cyclohexadienone or 2,5-cyclohexadienone. The ionization energies of 2,4- and 2,5-cyclohexadienone are not known experimentally, and the origin transitions in their FC simulations were shifted to the mean adiabatic ionization energies (9.12 eV and 9.29 eV, respectively) calculated using the G2[138], G3[139], G4[140], and CBS-QB3[129] computational methods (**Table A4-1**, Appendix). While the FC simulations for these isomers do not perfectly match the ms-TPES, they reproduce the overall spectral shape reasonably well. Pan et al.[189] reported a second band in the phenol ms-TPES just above 9 eV, which is comparable in intensity to the ground-state band. However, this feature was not observed in our measurements, possibly because of the intense

contributions from 2,4- or 2,5-cyclohexadienone dominating the mass-selected signal. Consequently, the dominant thermal degradation pathway of 4-ethylguaiacol involves the formation of phenol as well as its cyclohexadienone isomers. The other products identified through FC simulations are benzene/fulvene (*m/z* 78), 1,3-cyclopentadiene (*m/z* 66), the cyclopentadienyl radical (*m/z* 65), 1-buten-3-yne (*m/z* 52), the propargyl radical (*m/z* 39), formaldehyde (*m/z* 30), and the methyl radical (*m/z* 15). Additionally, *m/z* 122 was also observed, which can potentially be formed directly from 4-ethylguaiacol, as confirmed by the presence of the corresponding *m/z* 30 signal (formaldehyde).

Mullery et al.[63] investigated the degradation of 4-ethylguaiacol under fast pyrolysis and gasification conditions, and identified 4-ethylphenol as one of the primary oxygen-containing products. Formation of 4-ethylphenol from 4-ethylguaiacol involves the loss of formaldehyde, but the FC simulation of 4-ethylphenol does not reproduce the experimental ms-TPES of *m/z* 122. A better spectral match for the *m/z* 122 ms-TPES was found with bicyclo[2.2.2]oct-5-ene-2-one, a product also potentially formed via formaldehyde elimination. Alternatively, *m/z* 122 could correspond to benzoic acid, whose FC simulation shows good agreement with one part of the experimental ms-TPES. Nonetheless, the formation of benzoic acid from 4-ethylguaiacol would not be accompanied by formaldehyde, but rather by ethane elimination, a product also reported by Mullery et al. as a major species in 4-ethylguaiacol pyrolysis.[63] However, at the ionization energy of ethane (12 eV),[190–192] no TPES signal was detected in coincidence with *m/z* 30 ions corresponding to $C_2H_6^{+\bullet}$. This absence may be attributed to ethane's intrinsically broad photoelectron spectrum, resulting from Jahn–Teller effects and vibrational coupling,[193] which means, at most, there is very little ethane formed in the pyrolysis reactions.

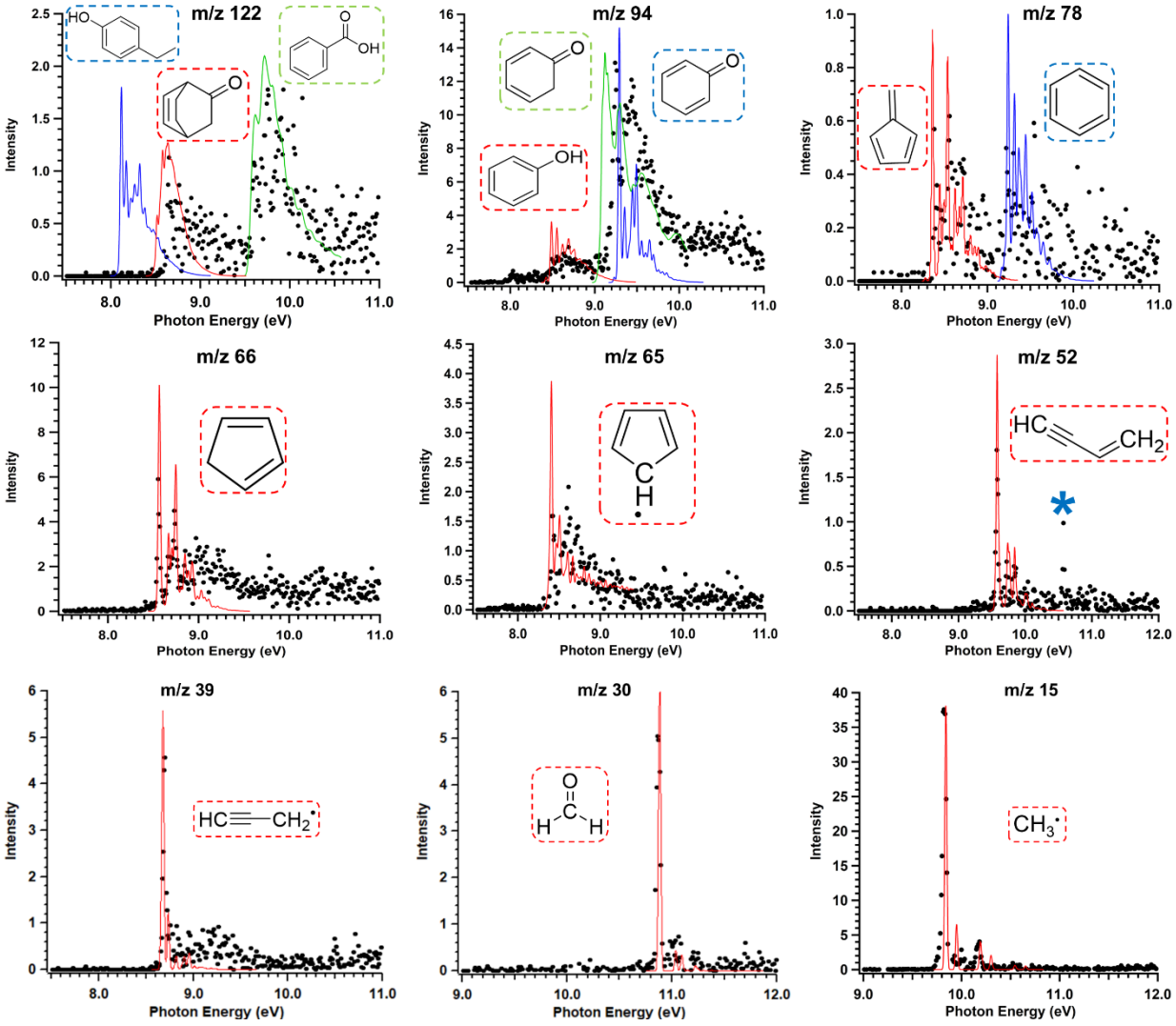

Figure 4-1. ms-TPES for all species observed from 4-ethylguaiacol pyrolysis. FC-simulations, overlaid in solid lines, have been adjusted to match the experimentally measured and computationally derived IEs listed in **Table A4-1** of the Appendix. The asterisk (*) denotes the excited-state feature of *m/z* 52 as reported by Buenger et al.[194].

There are two potential routes to phenol and its isomers. The first involves cleavage of the O–CH_3 bond to form the ethyl-substituted hydroxyphenoxyl radical with 137 Da and $^{\bullet}CH_3$ radical. Although no ms-TPES signal corresponding to *m/z* 137 was detected in our experiment (**Figure 4-2**), the methyl radical was observed among the pyrolysis products (**Figure 4-1**). The other involves a closed-shell pathway forming phenol (and its isomers 2,5-cyclohexadienone and 2,4-cyclohexadienone) plus acetone. While we did observe an ms-TPES for *m/z* 58 corresponding to

acetone in the experiment, it was found to be a background contaminant present throughout the experiments conducted during the beamtime, and so we cannot definitively assign it as a pyrolysis product.

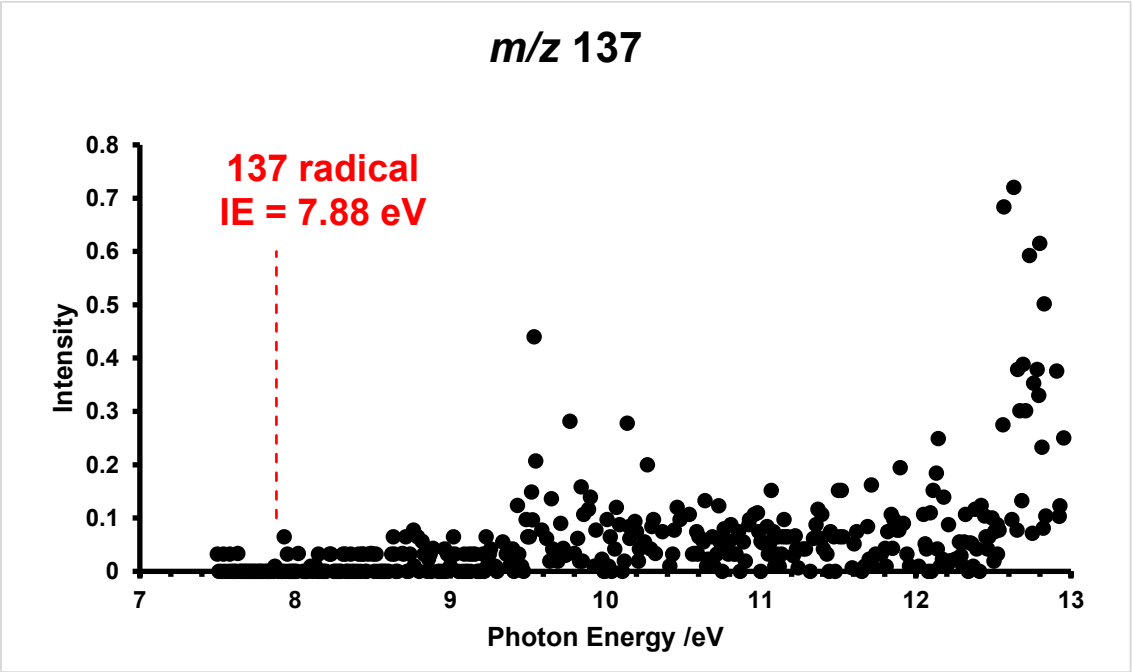

Figure 4-2. ms-TPES of *m*/*z* 137 from 4-ethylguaiacol.

We calculated the entire closed-shell pathway to acetone formation (**Figure 4-3**). Acetone formation is initiated by a 1,2-H shift from the methylene group of the ethyl side chain to the C atom on the ring, forming **INT1** (**Figure 4-3, 4-4**). From **INT1**, the methoxy O(–CH_3) binds to the C atom from which the initial 1,2-H shift occurred to form **INT2**. Loss of acetone from **INT2** can then proceed by either forming phenol (**PDT1**) first (red pathway) or 2,5-cyclohexadienone (**PDT3**, blue pathway). The phenol-forming pathway is energetically more favourable by 0.22 eV, a preference further supported by RRKM calculations of the competing rate constants k_{TS3} and k_{TS6} (**Figure 4-5**). It involves migration of the carbon group bearing the methoxy and methyl substituents to the vacant C on the ring, leading to **INT3**. A subsequent hydrogen transfer to the ring C *ortho* to the hydroxy group yields **INT4**, followed by a C–C pinch to form **INT5**, a phenol–acetone complex, and eventually losing acetone (**ACE**) to form phenol (**PDT1**, **Figure 4-6**). Conversely, the pathway involving the initial formation of 2,5-cyclohexadienone (**PDT3**, **Figure 4-6**) from **INT2** proceeds via a hydrogen transfer from the hydroxy group to the vacant C, yielding

INT6. From **INT6**, the subsequent reaction steps mirror the phenol-forming pathway except for the migration of the carbon group to the ring C in *para* position to the carbonyl group.

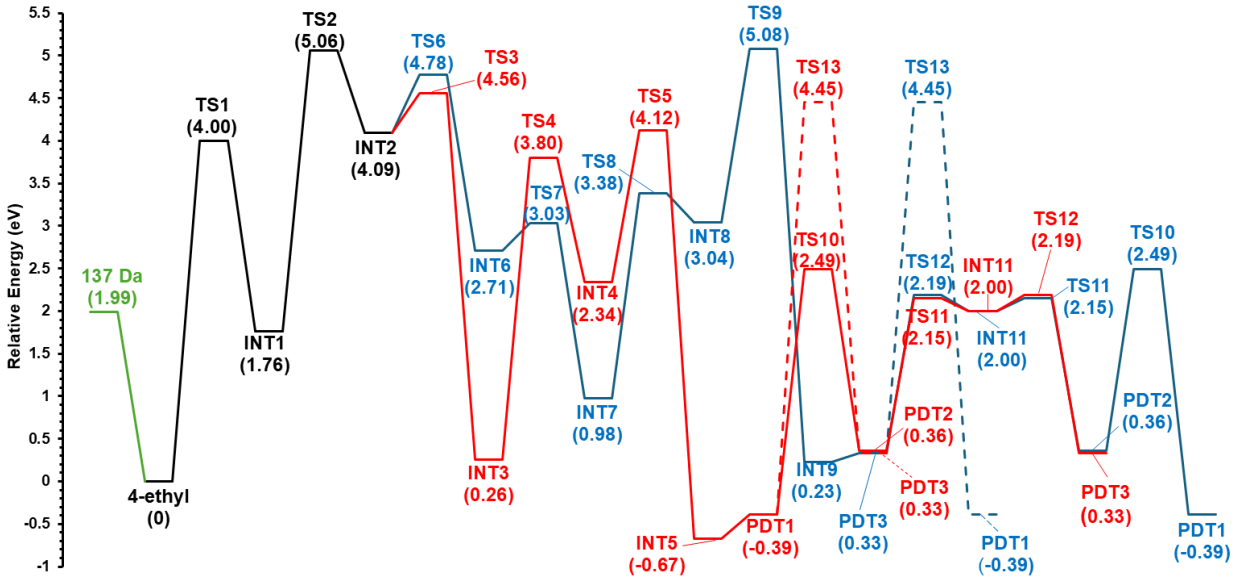

Figure 4-3. Calculated reaction pathways for the formation of 94 amu products from 4-ethylguaiacol at B3LYP/6-311+G(d,p) level of theory. Formation of **PDT1** (phenol), **PDT2** (2,4-cyclohexadienone) and **PDT3** (2,5-cyclohexadienone) is accompanied by acetone loss. The calculated energies of these products account for the presence of the acetone fragment and are relative to 4-ethylguaiacol. The initial process in black is expanded in **Figure 4-4.**

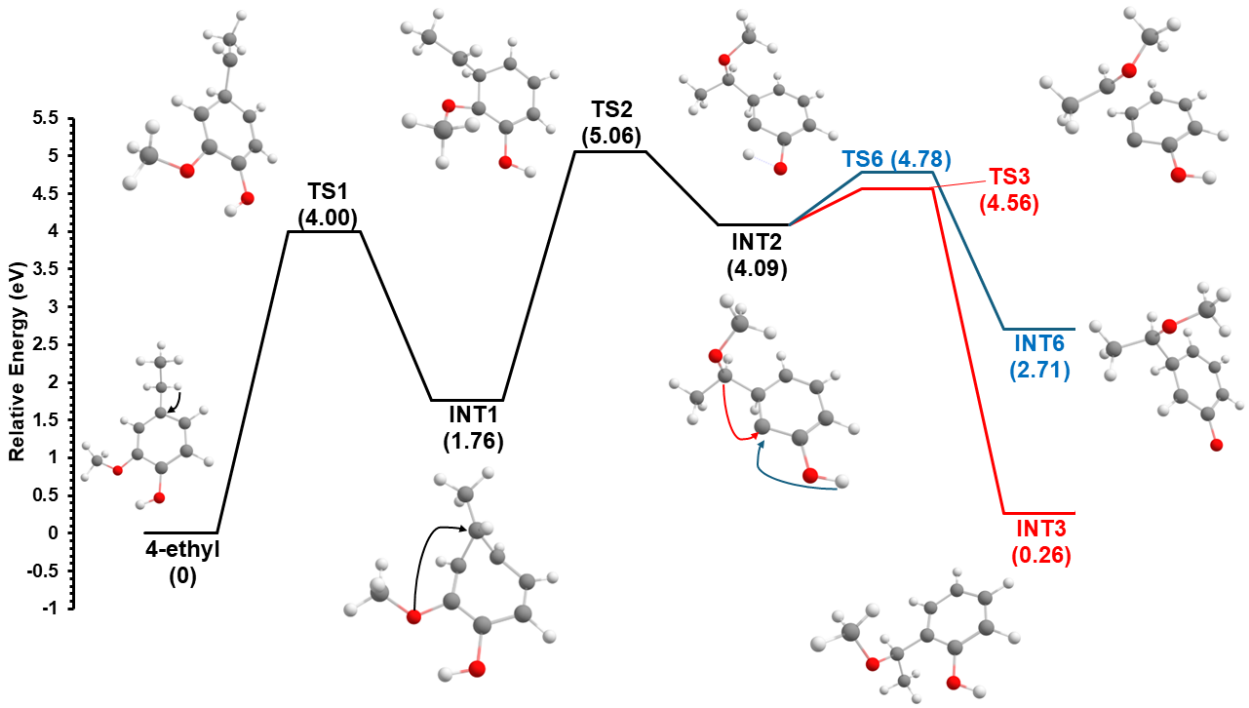

Figure 4-4. Initial steps in the formation of 94 amu products and acetone loss from 4-ethylguaiacol.

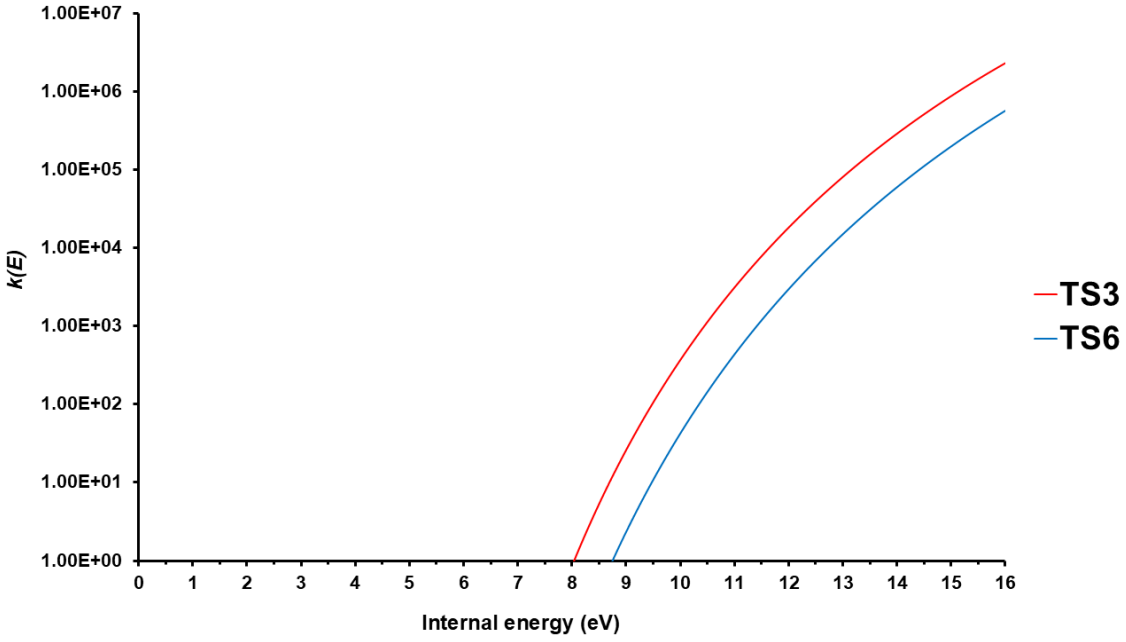

Figure 4-5. RRKM $k(E)$ vs E curves for phenol (**PDT1**) (red) vs 2,5-cyclohexadienone forming pathway (blue) over rate-determining transition states **TS3** and **TS6**, respectively.

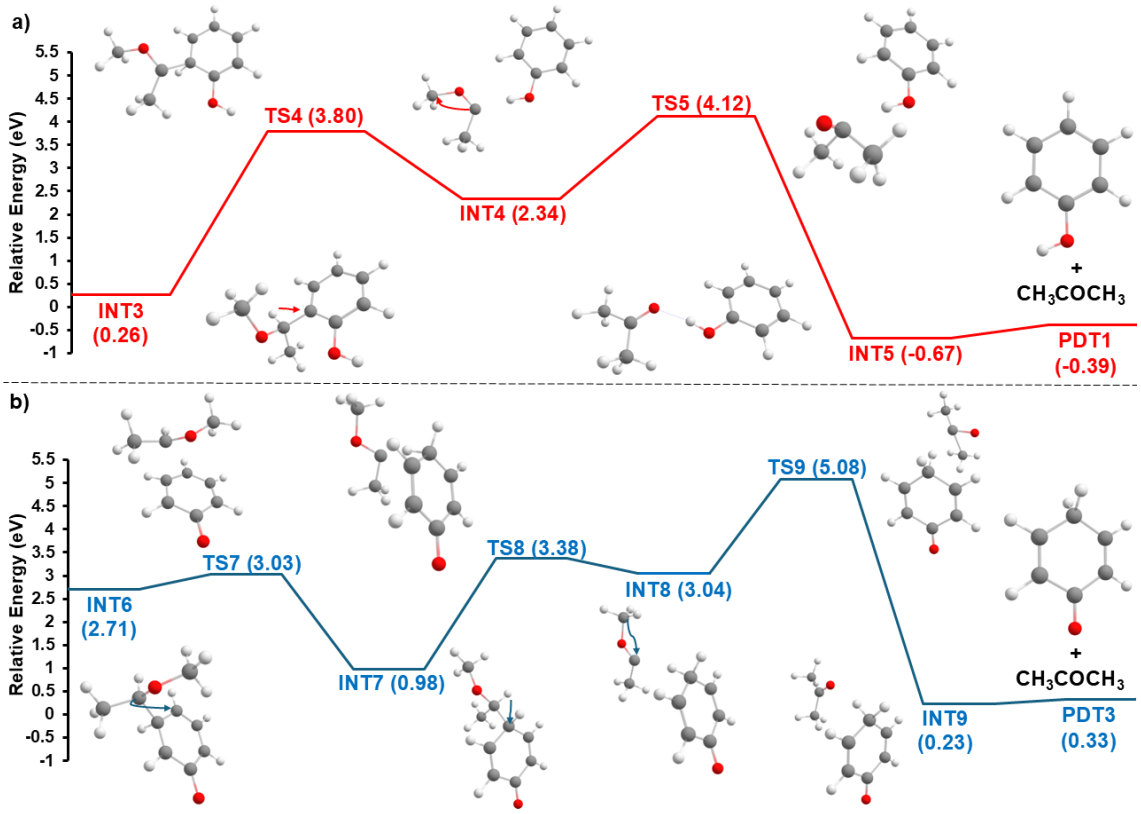

Figure 4-6. Pathways leading to a) phenol (**PDT1**), b) 2,5-cyclohexadienone (**PDT3**) via acetone loss in 4-ethylguaiacol. Energies of these products include acetone and are relative to 4-ethylguaiacol (0).

Phenol (**P**) and 2,5-cyclohexadienone (**p-cyc**) can interconvert (**Figure 4-7**) by a direct hydrogen transfer or by isomerizing into 2,4-cyclohexadienone (**o-cyc**) – energetically more favourable by 1.97 eV – via a series of hydrogen transfers. Although the pathway to phenol appears more favourable theoretically (**Figures 4-4, 4-5**), this is at odds with the low relative intensity of phenol in the ms-TPES (**Figure 4-1**), which suggests that cyclohexadienone isomers dominate. This discrepancy can be attributed to secondary degradation processes, as supported by previous phenol pyrolysis studies. Scheer et al.[195] reported the initial step of phenol degradation to be the enol/keto tautomerization to form 2,4-cyclohexadienone, which subsequently decomposes to cyclopentadiene by decarbonylation. Cyclopentadiene can then form the cyclopentadienyl radical, which further fragments to acetylene and propargyl radical. Similarly, Lovell et al.[165] identified benzene and cyclopentadiene as one of the major intermediates of phenol pyrolysis. These phenol pyrolysis products also appear as minor peaks in our study (**Figure 4-1**), suggesting that once

phenol is formed, either it primarily isomerizes to 2,4-cyclohexadienone and decomposes further, or alternatively dissociates directly into these lower-mass products. However, it is also plausible that some of these minor products originate directly from 4-ethylguaiacol degradation, as evidenced by the fast pyrolysis study conducted by Mullery et al.,[63] in which benzene was identified as one of the major products. Furthermore, Scheer et al.[195] noted that although the formation of 2,5-cyclohexadienone is energetically accessible, it lacks low-energy reaction channels. Hence, this could explain why the FC simulation of 2,5-cyclohexadienone aligns more closely with the ms-TPES than 2,4-cyclohexadienone.

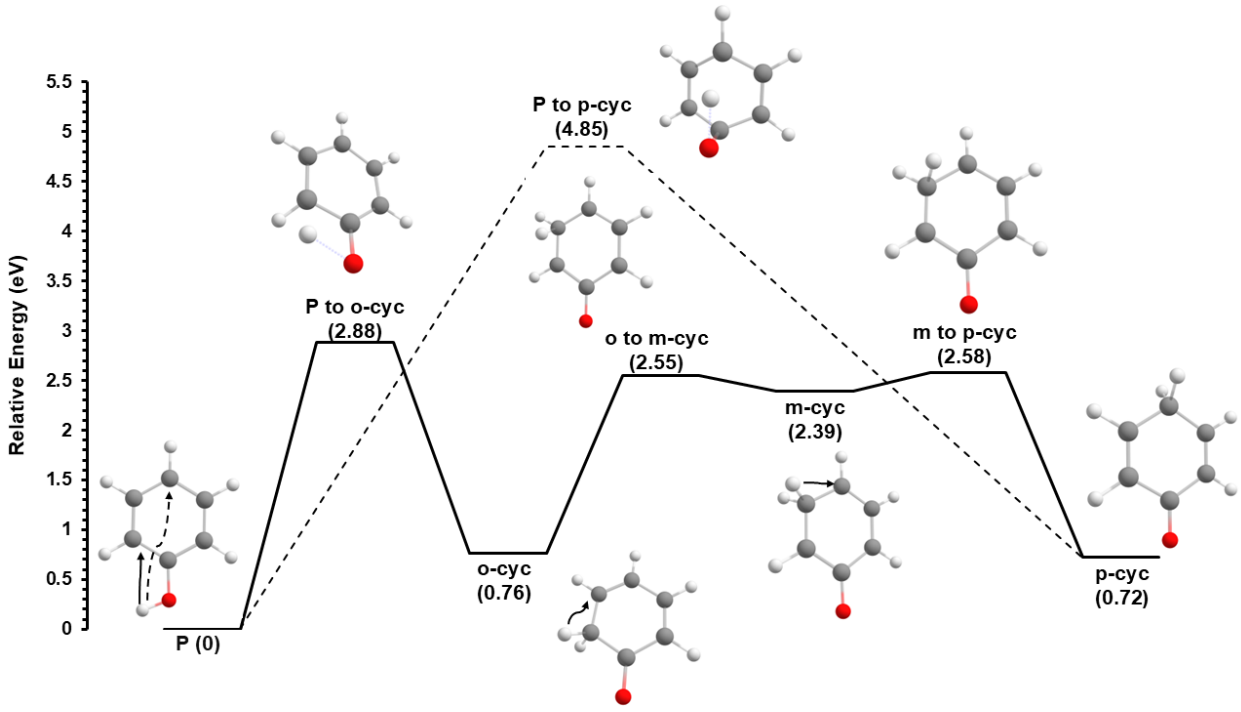

Figure 4-7. Interconversion of phenol (**P**) and 2,5-cyclohexadienone (**p-cyc**), involving isomerization to 2,4-cyclohexadienone (**o-cyc**). Energies of these products are relative to phenol.

We compared the initial steps to the free-radical-initiated path leading to the ethyl-substituted hydroxyphenoxyl radical (137 Da), **Figure 4-8**. As surmised by Mullery et al.,[63] the weak O−CH_3 bond means the rate constant for this entropically-favourable reaction is much greater than for the reactions leading to acetone formation, **Figure 4-9**.

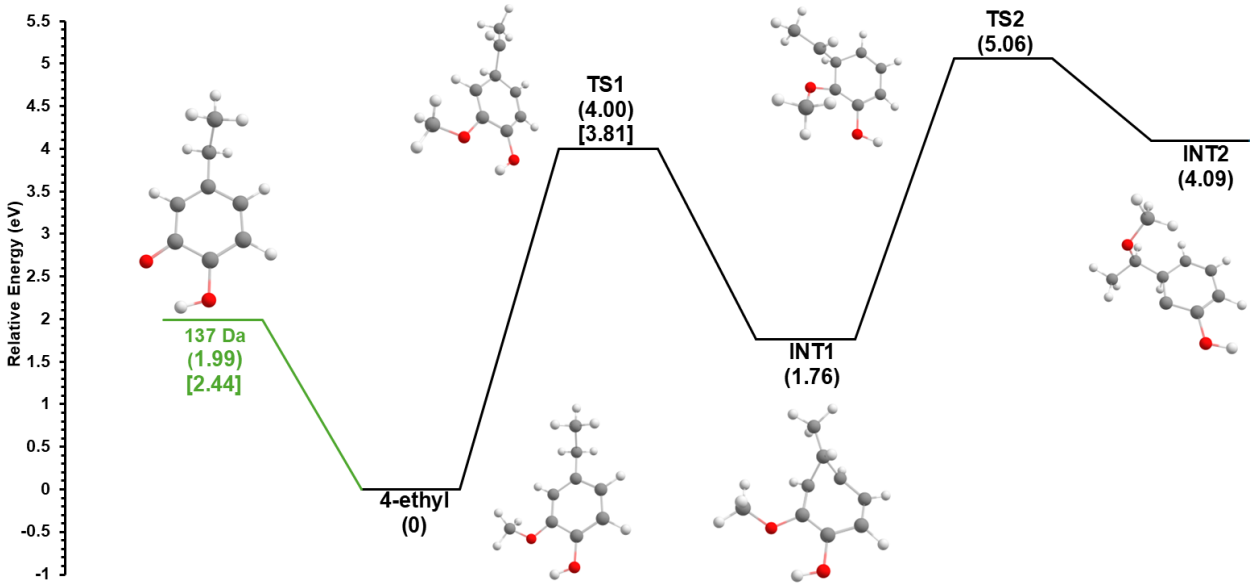

Figure 4-8. Calculated initial reaction pathways for the decomposition of 4-ethylguaiacol at the B3LYP/6-311+G(d,p) level of theory. The energies represented in the square brackets correspond to the CBS-QB3(sp)//B3LYP/6-311+G(d,p) calculated values. The green pathway denotes the O−CH_3 cleavage reaction leading to the formation of the ethyl-substituted hydroxyphenoxyl radical, and the black pathway represents the first key steps in the closed-shell pathway leading to acetone loss (the full pathway is presented in **Figure 4-3**).

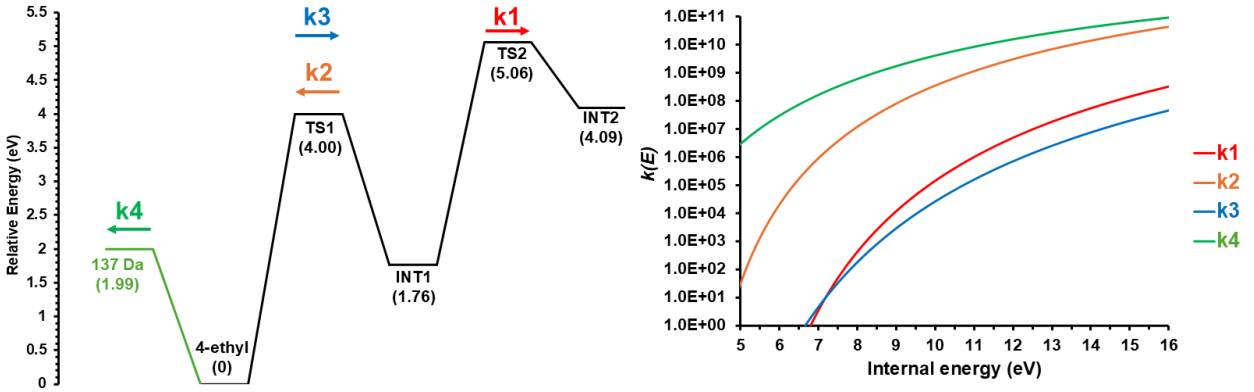

Figure 4-9. RRKM *k(E)* vs *E* curves for the green (ethyl-substituted hydroxyphenoxyl radical (*m/z* 137)) and black pathways (closed-shell unimolecular reaction) from 4-ethylguaiacol. Rate constants were calculated using DFT energies; although the two computational methods yield different absolute energies, it does not affect the overall kinetic picture.

The absence of an *m/z* 137 signal despite its favourable formation is suggestive of rapid secondary chemistry. A plausible rationale is that the ethyl-substituted hydroxyphenoxyl radical undergoes hydrogen abstraction to form an ethyl-substituted diol (138 Da). Structurally analogous to catechol (o-benzenediol), this ethyl-substituted diol could either undergo ethene loss to form catechol (**Figure 4-10**), which subsequently decomposes into the pyrolysis products identified in our experiment, or decompose itself into the identified products. We do not observe an ms-TPES for *m/z* 28, suggesting that the ethyl-substituted diol does not first form catechol prior to degradation. In addition, the loss of C_2H_4 from the ethyl-substituted diol goes over a 4.2 eV barrier (**Figure 4-10**), suggesting it should have been possible to observe the reactants and products of this reaction. Previous studies on the catalytic and thermal pyrolysis of catechol by Pan et al.[196] and Lomnicki et al.[197] identified phenol, benzene, and cyclopentadiene as primary products, all of which were observed in our study (**Figure 4-1**). This indicates that the elusive 137 Da radical may act as a short-lived precursor to a catechol-like degradation pathway. While Mullery et al.[63] suggested that the ethyl-substituted hydroxyphenoxyl radical intermediate may further react to form 4-ethylphenol (122 Da), our FC simulation of 4-ethylphenol does not match the experimental ms-TPES obtained for *m/z* 122, **Figure 4-1**.

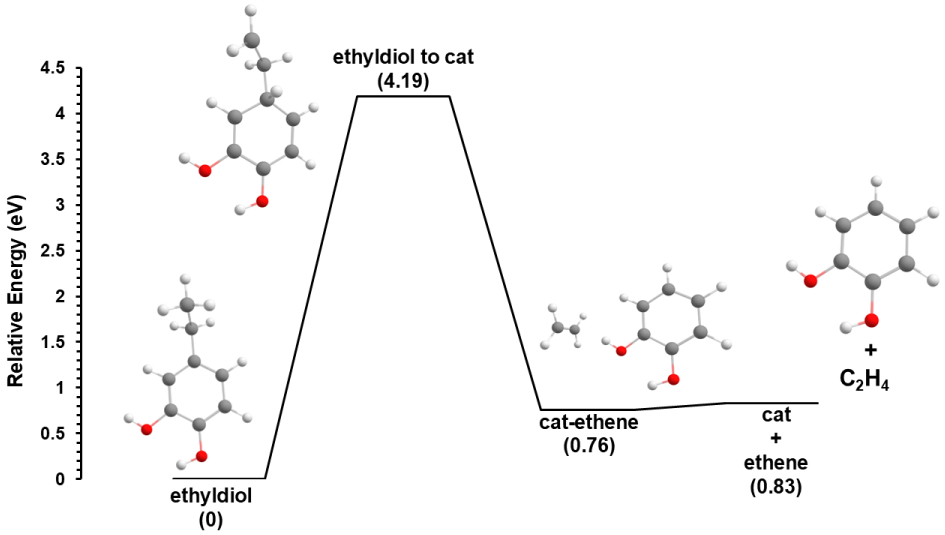

Figure 4-10. Calculated reaction pathway for catechol (110 Da) formation from ethyl-substituted diol (138 Da) via ethene loss at B3LYP/6-311+G(d,p) level of theory. Energies are related to the ethyl-substituted diol (0). Mechanistically, this reaction is initiated by a 1,3-H shift from the

terminal methyl of the side chain to the aromatic carbon, leading to an intermediate complex of catechol and ethene, and subsequently losing ethene to form catechol.

4.4.2 Eugenol

Figure 4-11 displays the ms-TPES and FC-simulations of the eugenol (*m/z* 164) pyrolysis products.

A predominant high-mass degradation product of eugenol is phenol (*m/z* 94) and its isomers 2,4-cyclohexadienone and 2,5-cyclohexadienone. The additional products identified through FC-simulations include *m/z* 120, benzene/fulvene (*m/z* 78), 1,3-cyclopentadiene (*m/z* 66), cyclopentadienyl radical (*m/z* 65), 1-buten-3-yne (*m/z* 52), propene (*m/z* 42), propargyl radical (*m/z* 39), ethylene (*m/z* 28), acetylene (*m/z* 26) and methyl radical (*m/z* 15). The FC-simulation for 1-phenylethenol appears to align with the ms-TPES at *m/z* 120, a product that may be formed through the sequential loss of acetylene and water from eugenol. By contrast, acetophenone, the ketone tautomer of 1-phenylethenol, does not reproduce the ms-TPES of *m/z* 120. Additionally, weak and scattered signals were observed at *m/z* 104 and 92, but their poor spectral quality precluded reliable assignments. Minor products may arise either directly from the primary decomposition of eugenol or from the secondary degradation of phenol.

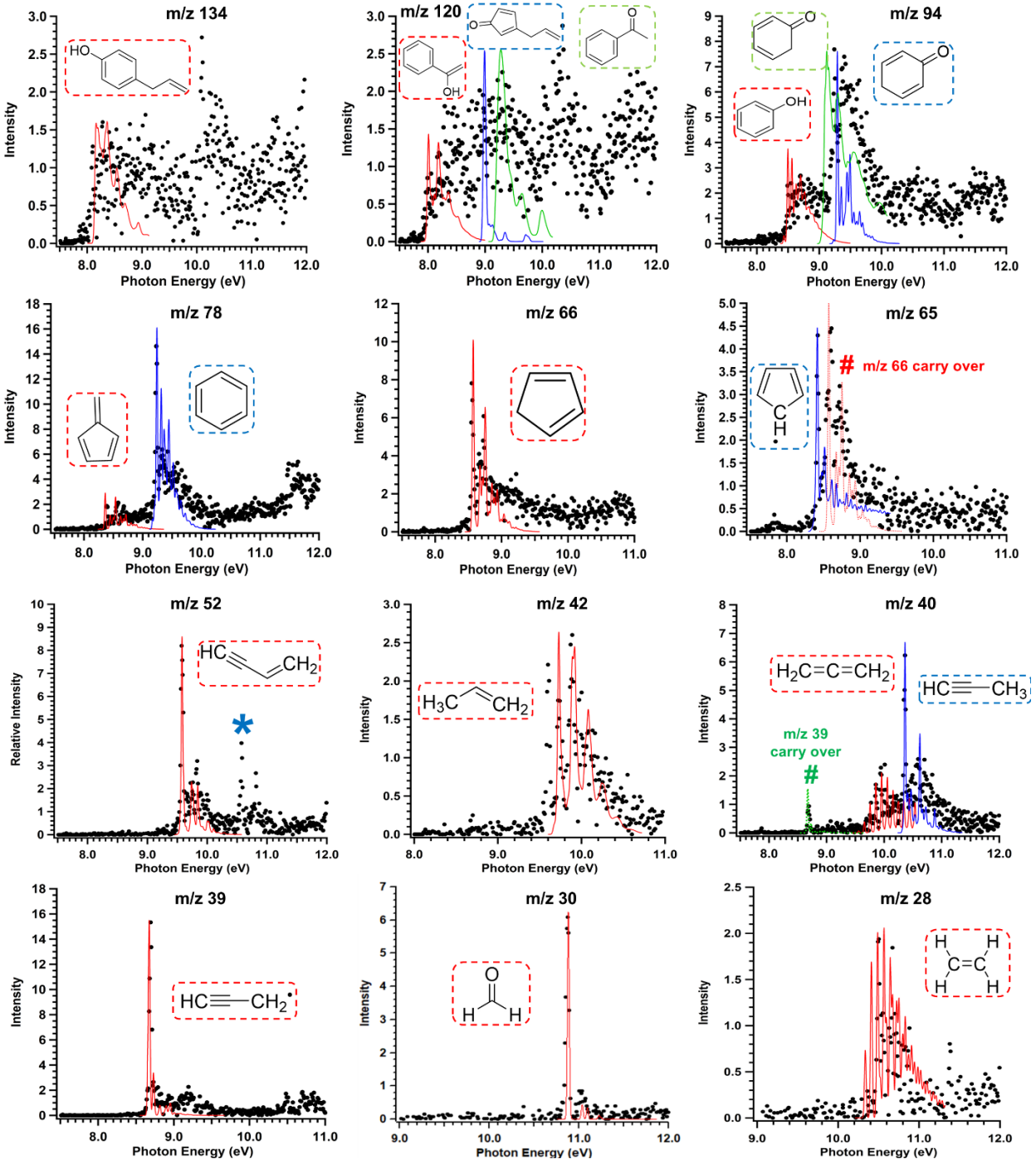
m/z 134
m/z 120
m/z 94
m/z 78
m/z 66
m/z 65
m/z 66 carry over
m/z 52
m/z 42
m/z 40
m/z 39 carry over
m/z 39
m/z 30
m/z 28
Intensity
Relative Intensity
Photon Energy (eV)

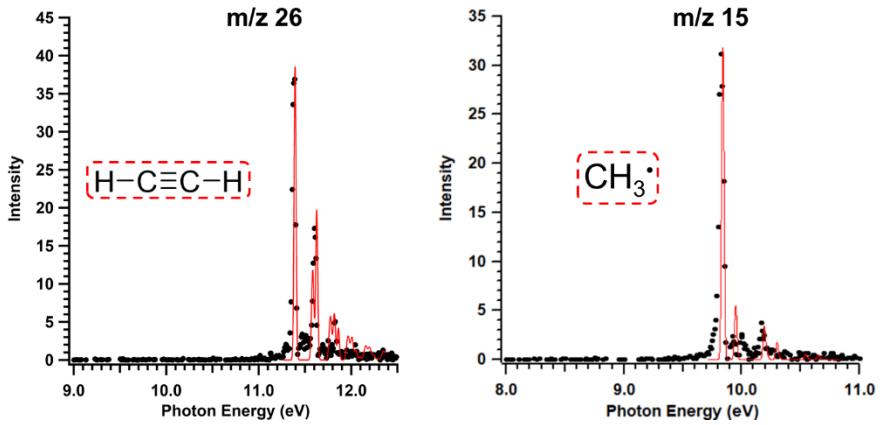

Figure 4-11. ms-TPES for all the products observed from eugenol pyrolysis. FC-simulations, overlaid in solid lines, have been adjusted to match the experimentally measured and computationally derived IEs listed in **Table A4-2** of the Appendix. The asterisk (*) denotes the excited-state feature of *m/z* 52 as reported by Buenger et al.[194]. The hash (#) represents signal carryover from neighbouring mass spectral peaks.

As with 4-ethylguaiacol, there are two possible routes to phenol production. One involves cleavage of the O−CH_3 bond to form the 5-allyl-2-hydroxyphenoxyl radical (149 Da), which then can go on to form phenol.[60,62,174] For instance, Shen et al.[62] reported the detection of *m/z* 149 in their mass spectra at 450 ºC, with molecular assignments based on IE values. However, the underlying photoionization spectra supporting this assignment exhibit a weak signal for *m/z* 149 (the mass spectrum was highly magnified and the parent eugenol peak truncated), raising the possibility that this feature could arise from dissociative photoionization rather than a stable radical product.[198,199] Conversely, in our study, no ms-TPES signal at *m/z* 149 was detected (**Figure 4-12**), which calls into question the presence or persistence of this radical under our experimental conditions. This discrepancy highlights the intrinsic difficulty of interpreting photoionization spectra when multiple species may contribute to the same *m/z* signal, or when fragment ions formed by dissociative ionization of larger precursors overlap with lower-mass peaks. Ledesma et al.[174] employed gas chromatography coupled with mass spectrometric detection in their study, which precludes the direct identification of the 149 Da radical. However, the observation of 4-(2-propenyl)-phenol (134 Da) and phenol (94 Da) in their product distribution is consistent with the products observed in the present work. In a separate study, Ledesma et al.[60] also proposed a radical-

based decomposition pathway for eugenol pyrolysis, based on experimental product distributions and energetic considerations. This pathway involved the initial formation of the 5-allyl-2-hydroxyphenoxyl radical (149 Da). However, the calculated energy requirements relative to eugenol were notably high, with several intermediates exceeding 6 eV and the highest activation barrier approaching 9 eV. Moreover, both Ledesma et al.[60] and Shen et al.[62] suggested that the 5-allyl-2-hydroxyphenoxyl radical (149 Da) dissociates into 3-allylcyclopentadienone (120 Da). However, in the present study, the FC simulation of 3-allylcyclopentadienone fails to reproduce the experimental ms-TPES of *m/z* 120 (**Figure 4-11**). Additionally, 3-allylcyclopentadienone was not reported as a product in the earlier work by Ledesma et al.[174], further calling into question its relevance in the dissociation mechanism.

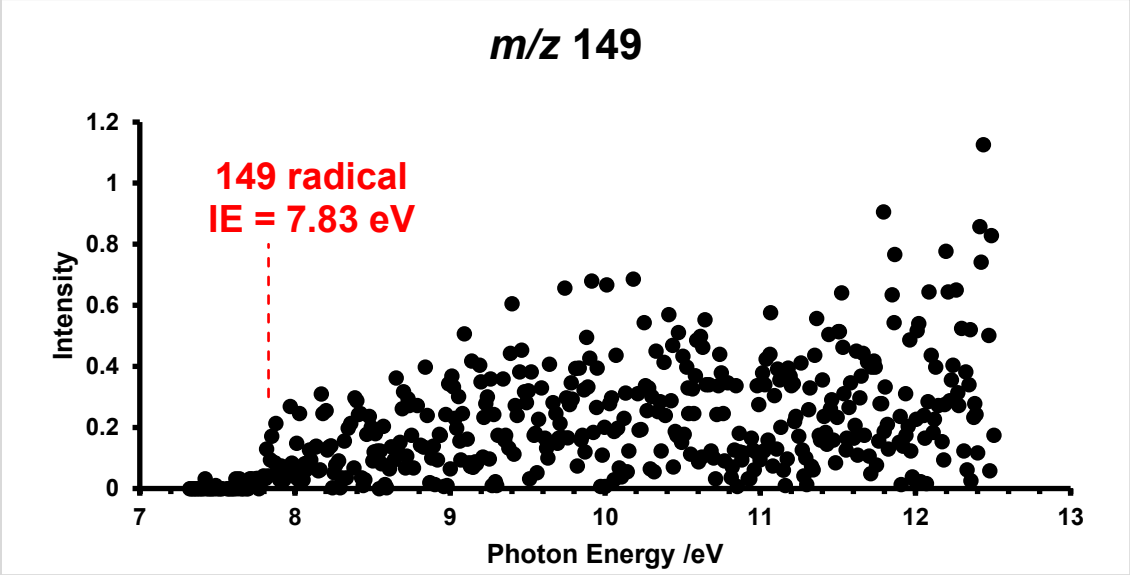

Figure 4-12. ms-TPES of *m/z* 149 from eugenol.

The second possible route to phenol and its isomers is via an initial loss of formaldehyde, yielding 4-(2-propenyl)-phenol (134 Da), **Figure 4-13**. This pathway is supported by the tentative agreement between the FC-simulation of the 4-(2-propenyl)-phenol photoelectron spectrum and the experimental ms-TPES for *m/z* 134 shown in **Figure 4-11**. Ledesma et al.[174] observed 4-(2-propenyl)-phenol among the pyrolysis products of eugenol, with maximum yield observed between 500 to 550 ºC. Subsequent loss of propyne (40 amu) from 4-(2-propenyl)-phenol provides a plausible route to phenol (**Figure 4-14**).

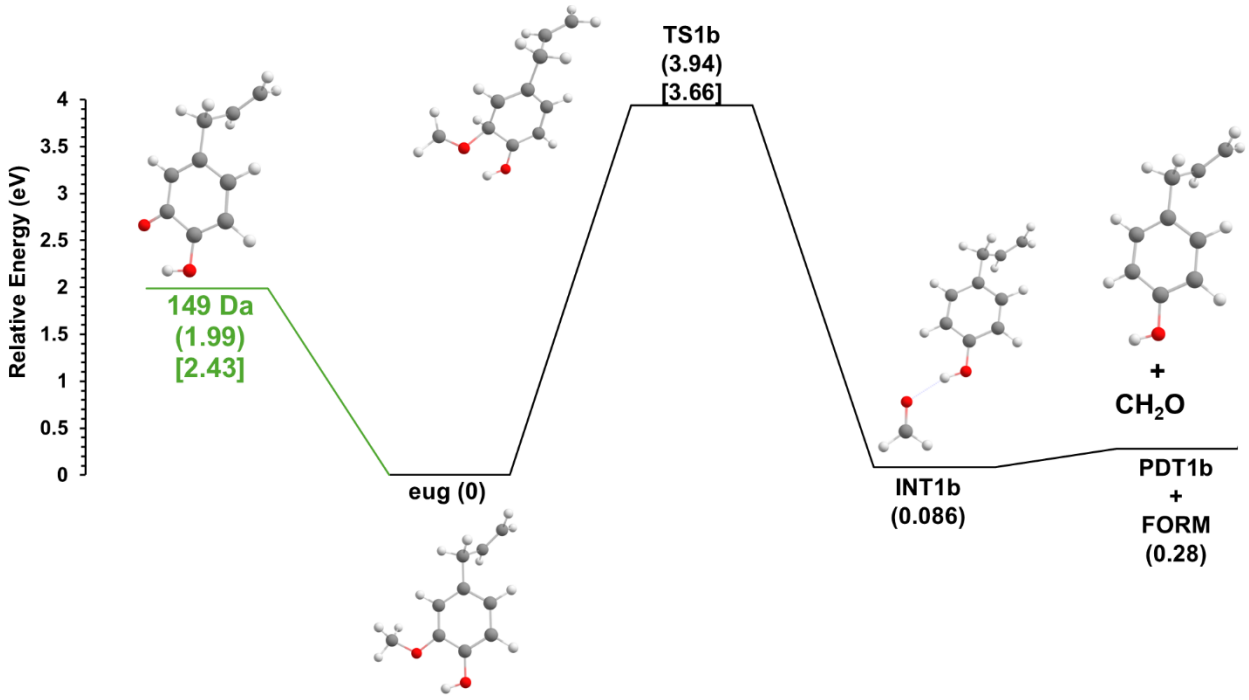

Figure 4-13. Calculated initial reaction pathways for the degradation of eugenol at the B3LYP/6-311+G(d,p) level of theory. The energies represented in the square brackets correspond to the CBS-QB3(sp)//B3LYP/6-311+G(d,p) calculated values. The green pathway denotes the O−CH_3 cleavage reaction forming the 5-allyl-2-hydroxyphenoxyl radical (149 Da), and the black pathway represents the closed-shell pathway forming 4-(2-propenyl)-phenol (134 Da, **PDT1b**) and formaldehyde. The sequential route to phenol (94 Da, **PDT2b**) and propyne are shown in **Figure 4-14**.

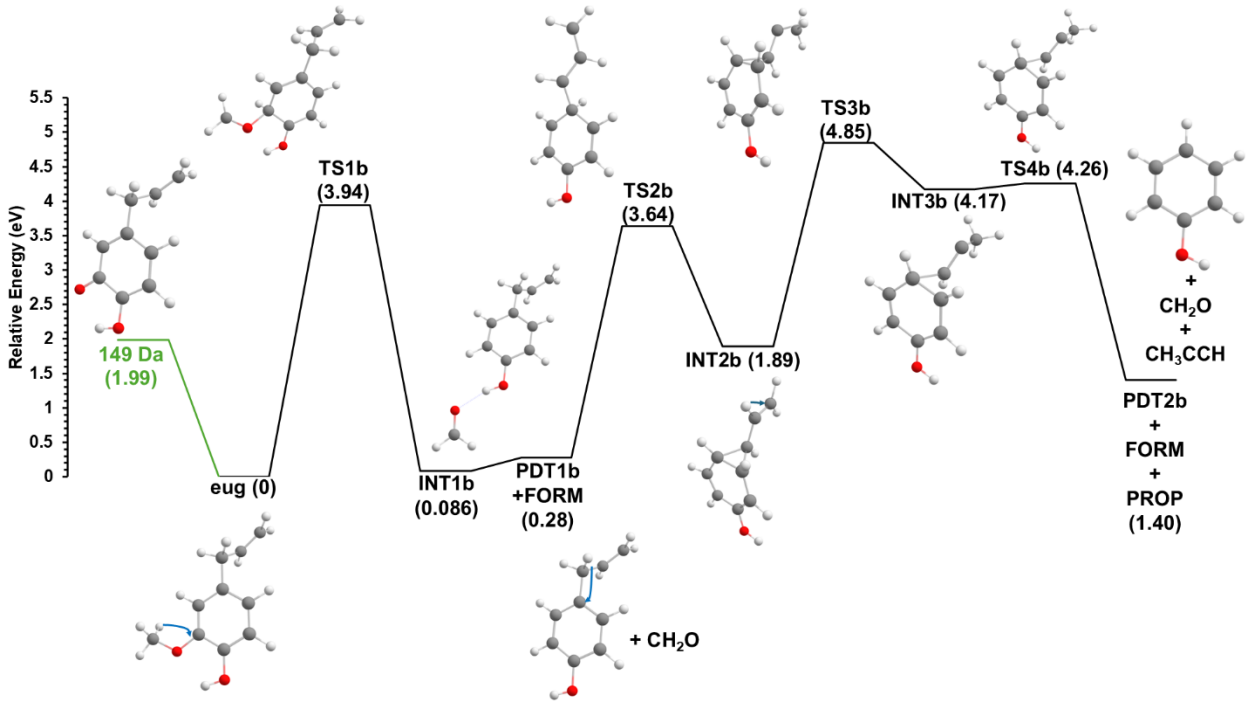

Figure 4-14. Calculated initial reaction pathways for the degradation of eugenol at the B3LYP/6-311+G(d,p) level of theory. The green pathway denotes the O−CH_3 cleavage reaction forming the 5-allyl-2-hydroxyphenoxyl radical (149 Da), and the black pathway represents the closed-shell pathway forming 4-(2-propenyl)-phenol (134 Da, **PDT1b**) and phenol (94 Da, **PDT2b**), following sequential loss of formaldehyde and propyne.

The calculated MERP (**Figure 4-14**) and the experimental ms-TPES suggest that *m*/*z* 40 is most likely propyne, which can isomerize to allene. The absence of an ms-TPES signal at *m*/*z* 70 further suggests that direct formation of phenol from eugenol is unlikely. As observed in 4-ethylguaiacol, phenol formed during the dissociation of eugenol may either isomerize to 2,4- or 2,5-cyclohexadienone or, alternatively, undergo direct fragmentation into lower-mass products (**Figure 4-11**). The proposed closed-shell mechanism for phenol formation from thermal decomposition of eugenol (**Figure 4-14**) proceeds by a 1,3-H shift from the methoxy group to an adjacent ring carbon, forming **INT1b** – a weakly bound complex of 4-(2-propenyl)-phenol and formaldehyde. Subsequent loss of formaldehyde (**FORM**) yields 4-(2-propenyl)-phenol (**PDT1b**). A 1,2-H transfer from the initial methylene group of the allyl side chain to the ring carbon results in the formation of **INT2b**. This is followed by another 1,2-H shift to the terminal methylene group within the side chain, yielding **INT3b**. Subsequent loss of propyne (**PROP**) from **INT3b** leads to

phenol (**PDT2b**). Phenol formation requires slightly less energy in eugenol than in 4-ethylguaiacol, with the highest transition state at 4.85 eV compared to 5.06 eV, respectively.

Analogous to 4-ethylguaiacol, energetic and RRKM (**Figure 4-15**) analyses indicate that homolytic O−CH_3 bond cleavage in eugenol is both kinetically and thermodynamically favourable relative to the closed-shell channel. Consequently, the detection of methyl radical, cyclopentadiene and benzene as pyrolysis products (**Figure 4-11**) suggests a degradation sequence that includes catechol formation. A plausible pathway is that the 5-allyl-2-hydroxyphenoxyl radical undergoes hydrogen abstraction to generate an allyl-substituted diol (150 Da), which subsequently undergoes allene loss to form catechol (**Figure 4-16**). Mechanistically, this mechanism parallels catechol formation in 4-ethylguaiacol, proceeding with a 1,3-H transfer from the allyl side chain to the ring carbon, followed by allene loss to produce catechol.

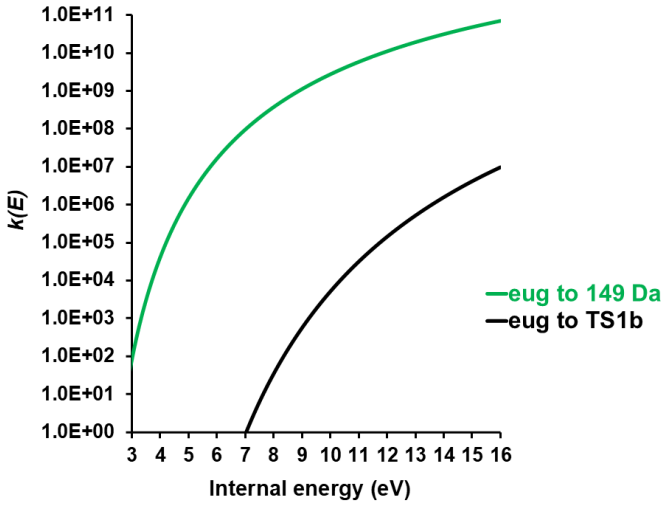

Figure 4-15. RRKM *k(E)* vs *E* curves for the green (5-allyl-2-hydroxyphenoxyl radical (149 Da)) and black (closed-shell unimolecular reaction) pathways from eugenol. Rate constants were calculated using DFT energies; although the two computational methods yield different absolute energies, it does not affect the overall kinetic picture.

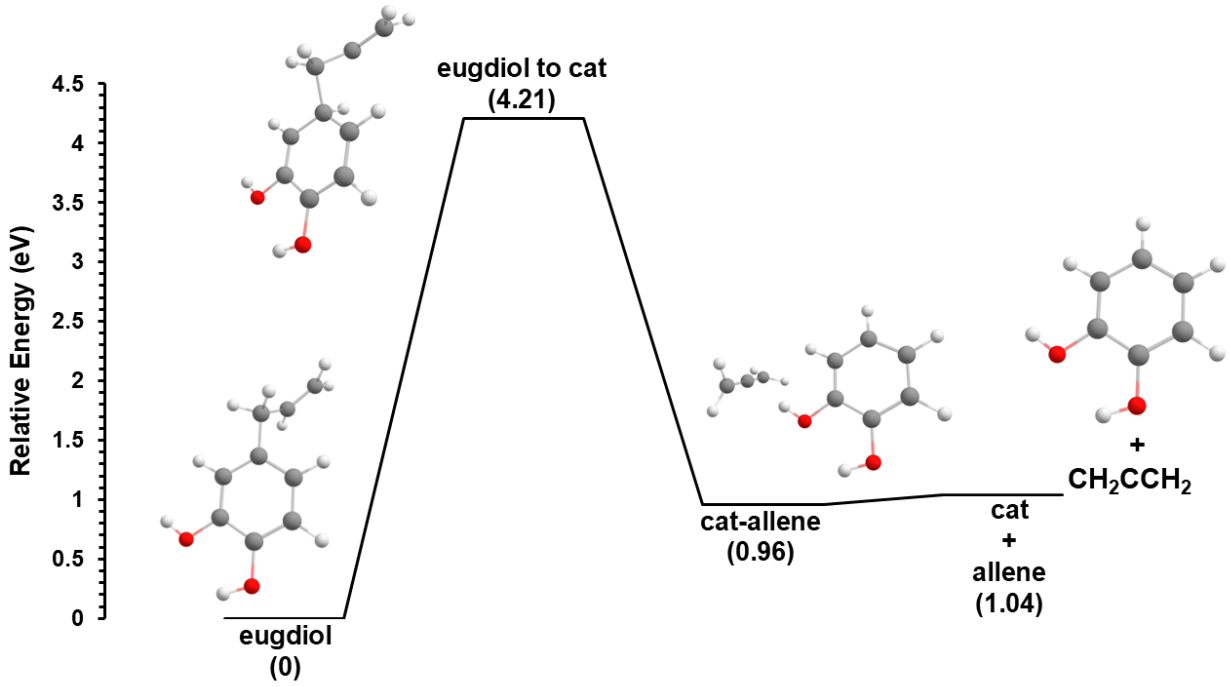

Figure 4-16. Calculated reaction pathway for catechol (*m/z* 110) formation from allyl-substituted diol (*m/z* 150) via allene loss at B3LYP/6-311+G(d,p) level of theory. Energies are related to the allyl-substituted diol (0).

4.5 Conclusion

A low-pressure SiC microreactor with imaging photoelectron photoion coincidence (iPEPICO) spectroscopy was employed to elucidate the thermal degradation products of 4-ethylguaiacol and eugenol in-vacuum flash pyrolysis by their ms-TPES and Franck–Condon simulations. Under the high temperature and low-pressure conditions studied, pyrolysis can proceed via either a closed-shell dissociation pathway or be initiated by CH_3 loss to form the corresponding radical. Although homolytic O–CH_3 bond breaking is both energetically and kinetically favourable for both substrates, the corresponding CH_3-loss radicals (when ionized, having *m/z* 137 and 149) were not detected as stable products in our ms-TPES measurements. The observation of methyl radical and product distributions consistent with catechol pyrolysis suggests that these radicals are short-lived and rapidly consumed by secondary reactions (for instance, hydrogen abstraction and diol formation) that ultimately feed into catechol-like degradation pathways. For comparison, we calculated the closed-shell reaction pathways to phenol and its isomers from 4-ethylguaiacol

(forming acetone) and eugenol (forming formaldehyde and propyne). Collectively, our results demonstrate that temperature and pressure are pivotal in modulating the thermal decomposition mechanisms of lignin model compounds, thereby offering a refined framework for optimizing product selectivity in sustainable lignin valorization. Furthermore, our findings pave the way for future developments in tailored pyrolysis processes that could significantly enhance the efficiency of biomass conversion technologies.

4.6 Appendix

Table A4-1. 4-Ethylguaiacol products ionization energies.

Da	Identity	IE/eV	Reference
122	4-Ethylphenol	Calc avg. 8.19	G2 – 8.25 G3 – 8.21 G4 – 8.11 CBS-QB3 – 8.20
	Bicyclo[2.2.2]oct-5-ene-2-one	8.60	Carnovale, F.; Gan, R.-H.; Peel, J.B.; Holmes, A.B., *Photoelectron spectroscopic studies of some 2-azabicyclo[2.2.2]octan-5-one and Bicyclo[2.2.2]octanone derivatives*, J. Chem. Soc. Perkin Trans. 2, 1981, 7, 991
	Benzoic acid	9.60	Meeks, J.; Wahlborg, A.; McGlynn, S.P., *Photoelectron spectroscopy of carbonyls: Benzoic acid and its derivatives*, J. Electron Spectrosc. Relat. Phenom., 1981, 22, 43.

94	Phenol	8.49	Fuke, K.; Yoshiuchi, H.; Kaya, K.; Achiba, Y.; Sato, K.; Kimura, K., *Multiphoton ionization photoelectron spectroscopy and two-color multiphoton ionization threshold spectroscopy on the hydrogen bonded phenol and 7-azaindole in a supersonic jet*, Chem. Phys. Lett., 1984, 108, 179.
	2,4-Cyclohexadienone	Calc avg. 9.12	G2 – 9.19 G3 – 9.17 G4 – 9.08 CBS-QB3 – 9.05
	2,5-Cyclohexadienone	Calc avg. 9.29	G2 – 9.35 G3 – 9.31 G4 – 9.21 CBS-QB3 – 9.30
78	Fulvene	8.36	Bieri, G.; Burger, F.; Heilbronner, E.; Maier, J.P., *Valence ionization energies of hydrocarbons*, Helv. Chim. Acta, 1977, 60, 2213.
	Benzene	9.24	Nemeth, G.I.; Selzle, H.L.; Schlag, E.W., *Magnetic ZEKE experiments with mass analysis*, Chem. Phys. Lett., 1993, 215, 151.
66	1,3-Cyclopentadiene	8.57	Derrick, P.J.; Asbrink, L.; Edqvist, O.; Jonsson, B.-O.; Lindholm, E., *Rydberg series in small molecules. XIII. Photoelectron spectroscopy and electronic structure of*

			cyclopentadiene, Intern. J. Mass Spectrom. Ion Phys., 1971, 6, 203.
65	Cyclopentadienyl radical	8.41	Lossing, F.P.; Traeger, J.C., *Stabilization in cyclopentadienyl, cyclopentenyl, and cyclopentyl cations*, J. Am. Chem. Soc., 1975, 97, 1579.
52	1-Buten-3-yne	9.58	Bieri, G.; Burger, F.; Heilbronner, E.; Maier, J.P., *Valence ionization energies of hydrocarbons*, Helv. Chim. Acta, 1977, 60, 2213.
39	Propargyl radical	8.67	Minsek, D.W.; Chen, P., *Photoelectron spectrum of the propargyl radical in a supersonic beam*, J. Phys. Chem., 1990, 94, 8399.
30	Formaldehyde	10.88	Niu, B.; Shirley, D.A.; Bai, Y., *High resolution photoelectron spectroscopy and femtosecond intramolecular dynamics of H_2CO^+ and D_2CO^+*, J. Chem. Phys., 1993, 98, 4377
15	Methyl radical	9.84	Houle, F.A.; Beauchamp, J.L., *Photoelectron spectroscopy of methyl, ethyl, isopropyl, and tert-butyl radicals. Implications for the thermochemistry and structures of the radicals and their corresponding carbonium ions*, J. Am. Chem. Soc., 1979, 101, 4067.

Table A4-2. Eugenol products ionizations energies.

Da	Identity	IE/eV	Reference
134	4-(2-Propenyl)-phenol	Calc avg. 8.17	G2 – 8.23 G3 – 8.18 G4 – 8.08 CBS-QB3 – 8.20
120	1-Phenylethenol	8.01	Turecek, F., *1-Phenylethenol: The enol form of acetophenone. Preparation, ionization energy, and the heat of formation in the gas phase*, Tetrahedron Lett., 1986, 27, 4219.
	3-allylcyclopentadienone	Calc. 8.99	CBS-QB3
94	Phenol	8.49	Fuke, K.; Yoshiuchi, H.; Kaya, K.; Achiba, Y.; Sato, K.; Kimura, K., *Multiphoton ionization photoelectron spectroscopy and two-color multiphoton ionization threshold spectroscopy on the hydrogen bonded phenol and 7-azaindole in a supersonic jet*, Chem. Phys. Lett., 1984, 108, 179.
	2,4-Cyclohexadienone	Calc avg. 9.12	G2 – 9.19 G3 – 9.17 G4 – 9.08 CBS-QB3 – 9.05
	2,5-Cyclohexadienone	Calc avg. 9.29	G2 – 9.35 G3 – 9.31 G4 – 9.21 CBS-QB3 – 9.30

78	Fulvene	8.36	Bieri, G.; Burger, F.; Heilbronner, E.; Maier, J.P., *Valence ionization energies of hydrocarbons*, Helv. Chim. Acta, 1977, 60, 2213.
	Benzene	9.24	Nemeth, G.I.; Selzle, H.L.; Schlag, E.W., *Magnetic ZEKE experiments with mass analysis*, Chem. Phys. Lett., 1993, 215, 151.
66	1,3-Cyclopentadiene	8.57	Derrick, P.J.; Asbrink, L.; Edqvist, O.; Jonsson, B.-O.; Lindholm, E., *Rydberg series in small molecules. XIII. Photoelectron spectroscopy and electronic structure of cyclopentadiene*, Intern. J. Mass Spectrom. Ion Phys., 1971, 6, 203.
65	Cyclopentadienyl radical	8.41	Lossing, F.P.; Traeger, J.C., *Stabilization in cyclopentadienyl, cyclopentenyl, and cyclopentyl cations*, J. Am. Chem. Soc., 1975, 97, 1579.
52	1-Buten-3-yne	9.58	Bieri, G.; Burger, F.; Heilbronner, E.; Maier, J.P., *Valence ionization energies of hydrocarbons*, Helv. Chim. Acta, 1977, 60, 2213.
42	Propene	9.73	Traeger, J.C., *A study of the allyl cation thermochemistry by photoionization mass spectrometry*, Int. J. Mass Spectrom. Ion Processes, 1984, 58, 259.
40	Allene	9.69	Yang, Z.Z.; Wang, L.S.; Lee, Y.T.; Shirley, D.A.; Huang, S.Y.; Lester, W.A., Jr., *Molecular beam*

			photoelectron spectroscopy of allene, Chem. Phys. Lett., 1990, 171, 9.
	Propyne	10.36	Carlier, P.; Dubois, J.E.; Masclet, P.; Mouvier, G., *Spectres de photoelectrons des alcynes*, J. Electron Spectrosc. Relat. Phenom., 1975, 7, 55.
39	Propargyl radical	8.67	Minsek, D.W.; Chen, P., *Photoelectron spectrum of the propargyl radical in a supersonic beam*, J. Phys. Chem., 1990, 94, 8399.
30	Formaldehyde	10.88	Niu, B.; Shirley, D.A.; Bai, Y., *High resolution photoelectron spectroscopy and femtosecond intramolecular dynamics of H_2CO^+ and D_2CO^+*, J. Chem. Phys., 1993, 98, 4377
28	Ethylene	10.51	Williams, B.A.; Cool, T.A., *Two-photon spectroscopy of Rydberg states of jet-cooled C_2H_4 and C_2D_4*, J. Am. Chem. Soc., 1991, 94, 6358.
26	Acetylene	11.40	Kimura, K.; Katsumata, S.; Achiba, Y.; Yamazaki, T.; Iwata, S., *Ionization energies, Ab initio assignments, and valence electronic structure for 200 molecules* in Handbook of HeI Photoelectron Spectra of Fundamental Organic Compounds, Japan Scientific Soc. Press, Tokyo, 1981.
15	Methyl radical	9.84	Houle, F.A.; Beauchamp, J.L., *Photoelectron spectroscopy of methyl, ethyl, isopropyl, and tert-butyl radicals. Implications for the*

			thermochemistry and structures of the radicals and their corresponding carbonium ions, J. Am. Chem. Soc., 1979, 101, 4067.

Chapter 5: The Fate of Protonated Guaiacol and Its Derivatives in the Gas Phase

The contents of Chapter 5 have been published as: Gondarry, S.; Mayer, P. M. The Fate of Protonated Guaiacol and Its Derivatives in the Gas Phase. J. Phys. Chem. A 2022, 126 (48), 9051–9058. https://doi.org/10.1021/acs.jpca.2c04692

Author contributions:
Sandesh Gondarry: Data curation, writing – original draft, DFT calculations.
Paul M. Mayer: Conceptualization, methodology, supervision, writing – review & editing.

5.1 Introduction

Biomass offers a renewable and sustainable source for generating fuels and chemicals.[200] Lignin, the second most abundant component in woody biomass (18-40 wt.%),[201] is a biopolymer consisting of phenylpropane units.[200] Pyrolysis of wood lignin primarily generates 2-methoxyphenol (guaiacol), 2,6-dimethoxyphenol, and their derivatives.[18,202–206] At standard ambient temperatures, guaiacol and its derivatives are predominantly distributed into the gas phase[202–204] and thus, these oxygenated aromatic molecules can undergo atmospheric degradation reactions.[207]

Studies dealing with the atmospheric reactions of guaiacol and its derivatives are rather scarce. Yang et al.[208] analyzed the gas-phase reactions of guaiacol and creosol with NO_3 radicals using a vacuum ultraviolet photoionization time-of-flight mass spectrometer and off-line GC-MS and determined the corresponding rate constants using the relative rate method. The primary degradation products identified for guaiacol were 4-nitroguaiacol, 6-nitroguaiacol and 4,6-dinitroguaiacol and 6-nitrocreosol for creosol. Furthermore, a rate constant value of 3.2×10^{-12} cm^3 $molecule^{-1}$ s^{-1} was determined for guaiacol and 2.4×10^{-13} cm^3 $molecule^{-1}$ s^{-1} for creosol at 298 K and 1 atm. Additionally, Khudoshin et al.[209] examined the main oxidation products for the reaction of guaiacol with ozone using HPLC (high-performance liquid chromatography) and proposed ozonation mechanisms. Nguyen et al.[210] determined the primary reaction pathways for the thermal

decomposition of guaiacol using the CBS-QB3 method and statistical mechanics calculations. The study showed that decomposition of guaiacol is predominantly initiated by homolytic cleavage of the methoxy group ($O-CH_3$), yielding the experimentally detected (obtained from literature) products carbon monoxide and hydroxy-cyclopentadienyl.

As guaiacol and its derivatives are primarily distributed in the gas phase, these molecules can interact with atmospheric water and form protonated molecules through proton transfer. In this study, a combination of tandem mass spectrometry and computational chemistry was employed to explore the trends in the unimolecular reactions of protonated guaiacol, creosol, 4-ethylguaiacol, 4-vinylguaiacol, eugenol and vanillin to explore any similarities between the dissociation of these species with the pyrolysis of the neutral molecules.

5.2 Experimental Procedures

Guaiacol (2-methoxyphenol), creosol (2-methoxy-4-methylphenol), 4-ethylguaiacol (4-ethyl-2-methoxyphenol), 4-vinylguaiacol (2-methoxy-4-vinylphenol), eugenol (2-methoxy-4-prop-2-enylphenol) and vanillin (4-hydroxy-3-methoxybenzaldehyde) were purchased from Sigma-Aldrich (>98%, Sigma-Aldrich, Oakville, Ontario, CA) and used without further purification.

Electrospray ionization mass spectrometry (ESI-MS) was performed on a Waters Micromass Quattro Ultima Pt triple quadrupole mass spectrometer. Solutions in methanol (1 mg/mL) were delivered to the source using a syringe pump with a flow rate of 27 $\mu L\ min^{-1}$. Capillary and cone voltages were set to approximately 4 kV and 110 V, respectively (but adjusted to maximize ion yield in each experiment). The desolvation gas (N_2) was set to a flow rate of 105 L/h. The generated ions were selected according to their m/z ratio with the first quadrupole and directed into the ion tunnel collision cell, where they were subjected to collision-induced dissociation (CID) with argon target gas (pressure reading of 1.00×10^{-4} bar). The resulting product ion mass spectra were recorded with the second quadrupole analyzer and detector. Breakdown curves were generated by plotting the relative abundance of the ions in the resulting CID mass spectra as a function of collision energy. To compare the breakdown of different ions, the laboratory-frame

collision energy (E_{lab}) was first converted to the center-of-mass frame (E_{com}) according to the following equation

$$E_{com} = E_{lab}\left(\frac{M_{Ar}}{M_{Ar} + M_I}\right)$$

where M_{Ar} is the mass of an argon atom and M_I is the mass of the ion.[94]

5.3 Computational Procedures

Equilibrium and transition state structures were optimized at the B3LYP/6-31G(d)[121,122] level of density functional theory (DFT) employing the GAUSSIAN 16 suite of programs.[112] In all cases, initial structures were manually built prior to optimization. Transition states were confirmed by the intrinsic reaction coordinate method. CBS-QB3 single-point energy calculations[129] (without geometry optimizations) were then employed on the DFT geometries to obtain more accurate energetics. An assessment was made of the suitability of the above level of theory for describing the minimum energy reaction pathways (MERPs) of protonated guaiacols. The MERP for protonated guaiacol was also optimized at the B3LYP/6-311+G(d,p) and M06/6-311+G(d,p) levels of theory (**Figure A5-1** in Appendix), and the results were found to be comparable to the CBS-QB3(sp)// B3LYP/6-31G(d) results.

Rice-Ramsperger-Kassel-Marcus (RRKM) theory was applied to calculate *k(E)* according to the following equation[108,157]

$$k(E) = \frac{\sigma N^{\ddagger}(E - E_0)}{h\rho(E)}$$

where σ represents the reaction degeneracy, h is Planck's constant, $N^{\ddagger}(E - E_0)$ is the number of internal states for the transition state at internal energy $(E - E_0)$ and $\rho(E)$ is the density of states for the reactant ion at internal energy (E) as calculated via the Beyer and Swinehart direct count algorithm.[109]

5.4 Results and Discussion

5.4.1 Protonated guaiacol and its derivatives

Figure 5-1 shows the global minimum structures for the different protonated guaiacols. The most stable protonated ion for guaiacol corresponds to protonation on the C atom para to the hydroxy group. In contrast, due to the presence of the substituent para to the OH group in creosol, 4-ethylguaiacol, 4-vinylguaiacol and eugenol, protonation is most favourable on the adjacent C atom, meta to the 1-hydroxy group. For vanillin, protonation on the aldehyde leads to the most stable protonated ion. The barriers between many of these structures can be found in the MERPs for each system.

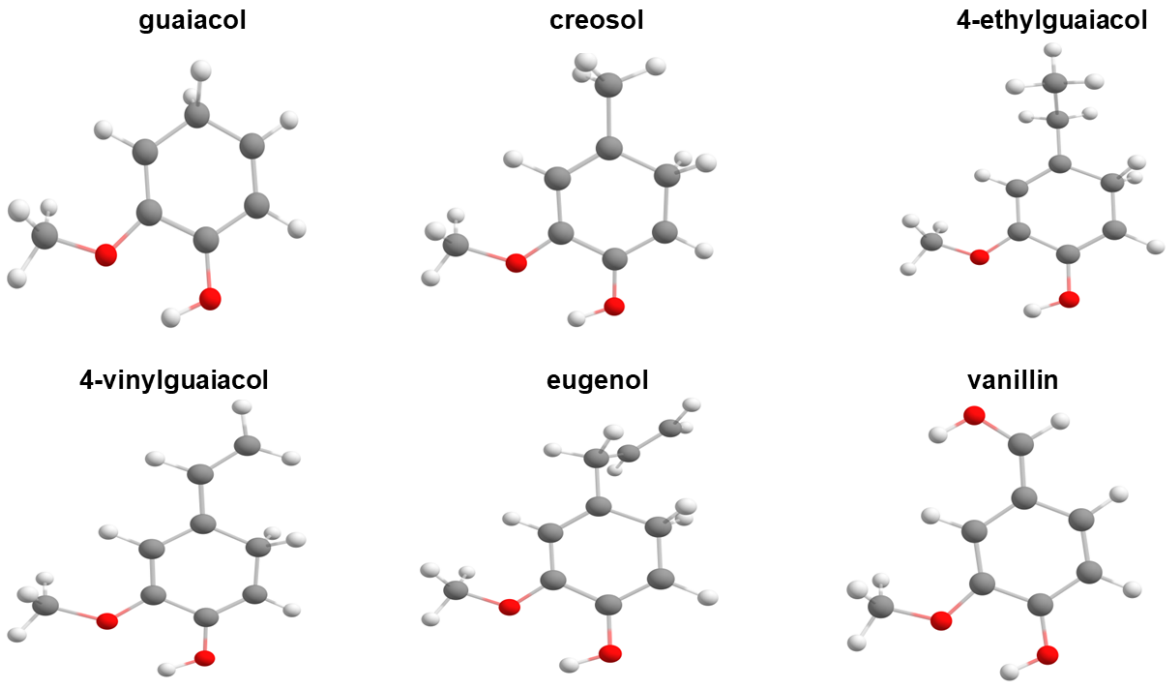

Figure 5-1. Global minimum protomers of guaiacol, creosol, 4-ethylguaiacol, 4-vinylguaiacol, eugenol and vanillin.

The energies relative to the global minimum of the various potential protonated guaiacols in each system were calculated and compared (**Figure 5-2**).

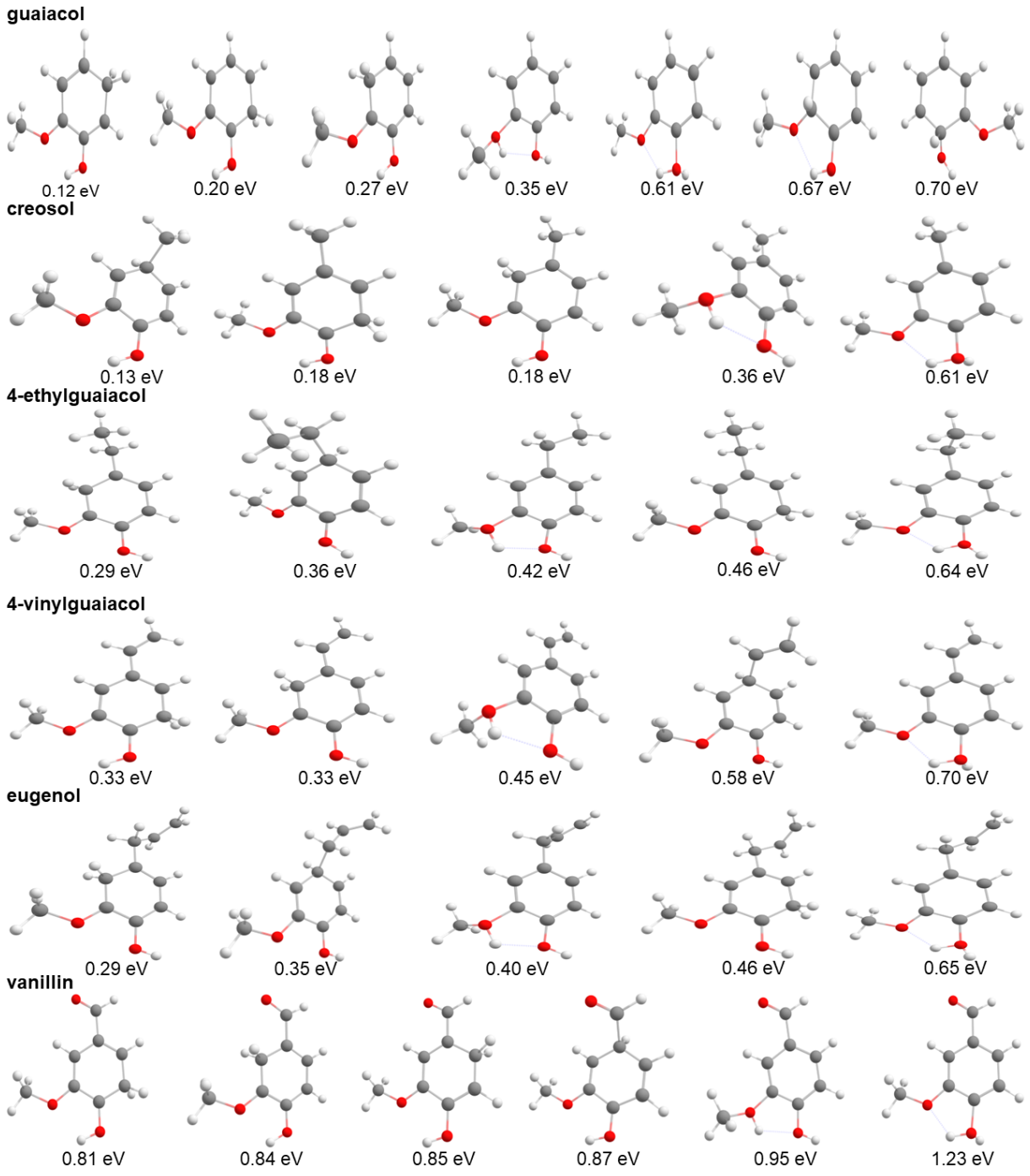

Figure 5-2. Protomers of guaiacol, creosol, 4-ethylguaiacol, 4-vinylguaiacol, eugenol and vanillin together with energy values relative to their global minimum structures (**Figure 5-1**).

Representative CID mass spectra for each protonated guaiacol derivative and their respective breakdown curves are shown in **Figures 5-3** and **5-4**. Protonated guaiacol (**1**) undergoes

dissociation by the loss of 32 Da (CH_3OH), leading to the formation of *m*/*z* 93. Evident from the breakdown curve is that this channel is in competition with the formation of *m*/*z* 111 (loss of CH_2). *m*/*z* 93 then dissociates by loss of 28 Da to form *m*/*z* 65. Evident from the breakdown curves is that protonated creosol (**2**), protonated 4-ethylguaiacol (**3**), protonated 4-vinylguaiacol (**4**), and protonated eugenol (**5**) all display the same major fragments and sequential loss of 32 and 28 Da. Additions include a methane loss channel for **3**, and several new channels for eugenol (**5**), which displays sequential loss of two 28 Da units (*m*/*z* 137 followed by *m*/*z* 109). There are also minor dissociation channels leading from *m*/*z* 165 to *m*/*z* 124, presumably by CH_2CHCH_2 loss, and to *m*/*z* 41 by $C_7H_8O_2$ loss.

Protonated vanillin (**6**) follows different dissociation pathways as compared to the other derivatives. The main fragmentation pathway starts with loss of 28 Da (*m*/*z* 125) followed by sequential losses of 32 Da (CH_3OH, *m*/*z* 93) and 28 Da (*m*/*z* 65). Evident from the breakdown curve is that this channel is in competition with the formation of *m*/*z* 110, following the loss of CH_3 from *m*/*z* 125, followed by sequential loss of 28 Da (*m*/*z* 82). Additionally, minor H loss peaks are observed for the different fragmented ions (*m*/*z* 137, 124 and 109), and the abundances of these peaks were all summed up with that of *m*/*z* 152 (highest H loss abundance) to obtain only one dissociation channel for H loss in the breakdown diagram. Moreover, there is a minor dissociation channel leading from *m*/*z* 153 to *m*/*z* 138 by CH_3 loss.

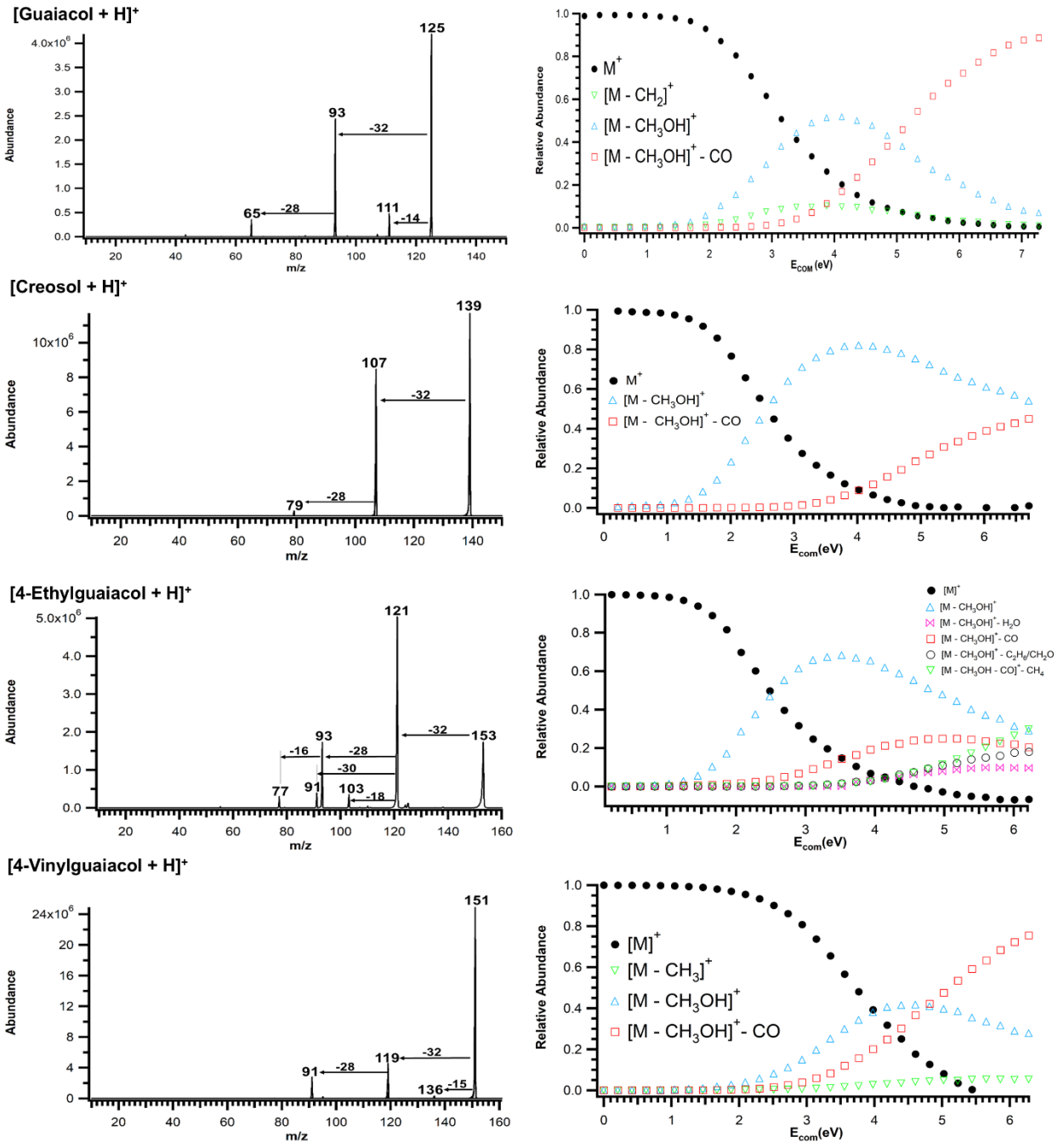

Figure 5-3. Representative CID mass spectra and breakdown diagrams for a) protonated guaiacol, b) creosol at 15 eV E_{lab}, c) protonated 4-ethylguaiacol, and d) 4-vinylguaiacol at 20 eV E_{lab}.

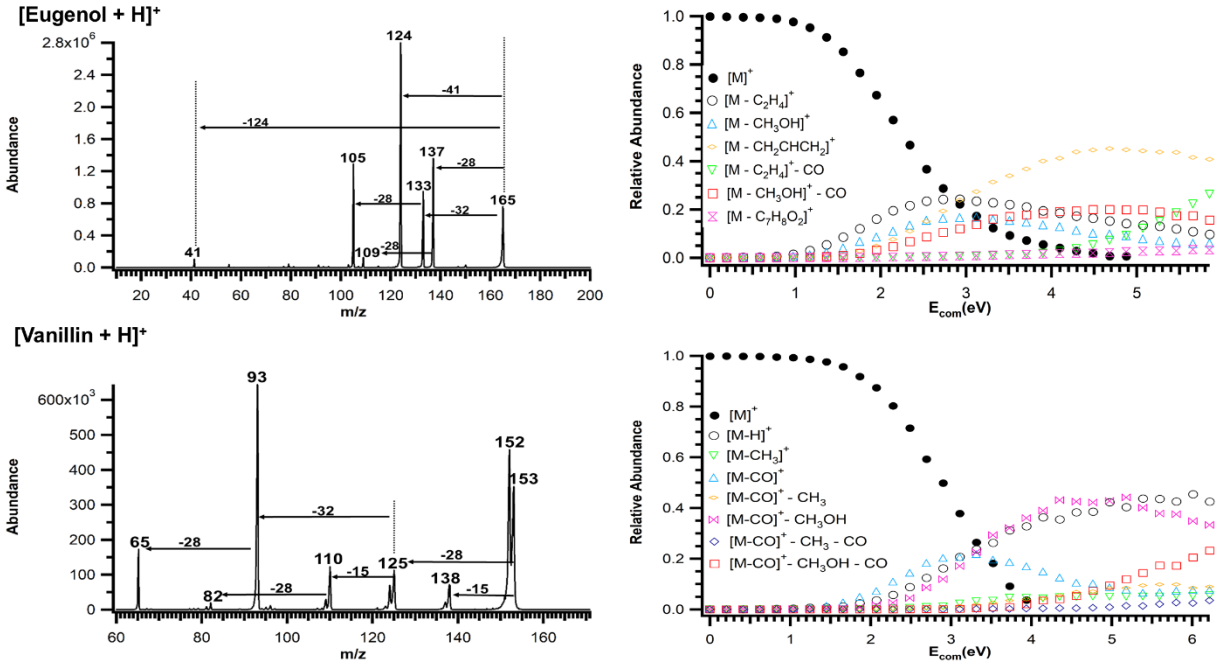

Figure 5-4. Representative CID mass spectra and breakdown diagrams for a) protonated eugenol at 20 eV E_{lab} and b) protonated vanillin at 25 eV E_{lab}.

5.4.2 Calculated minimum energy reaction pathways

We obtained minimum energy reaction pathways that were consistent with the data presented in the breakdown curves in **Figures 5-3** and **5-4**, **Figures 5-5** through **5-11**, with the transition states shown in **Figures A5-2** and **A5-3** of the Appendix.

The sequential loss of methanol and CO from protonated guaiacol (**1**) proceeds via hydrogen transfer from **1** to the adjacent C atom to form **1a** (**Figure 5-5**). Hydrogen transfer from **1a** to the adjacent O atom forms **1b**, from where methanol is lost, leading to *m*/*z* 93 via one of two pathways. The first is a concerted hydrogen transfer from the hydroxy group (OH) to the adjacent C atom coupled with dissociation of the methanol group to form **1d**. Alternatively, methanol cleaves directly from **1b** to form **1c**, which has a vacancy on a ring C-atom. The hydrogen transfer then occurs from the hydroxy group (OH) to the vacant C atom to form **1d**. The simple bond cleavage from **1b** to form **1c** is energetically favoured over the concerted pathway to **1d** by 0.5 eV. As the collision energy increases, the concerted reaction of **1b** to **1d** can occur, but only to a limited extent,

as evidenced from the RRKM calculation of the competing rate constants $k_{\mathbf{1b\text{-}1d}}$ and $k_{\mathbf{1b\text{-}1c}}$ (**Figure 5-6**). Loss of methanol likely dominates via the simple bond cleavage pathway (**1c** to **1d**), and **1d** then is the progenitor for CO loss. Ion **1d** undergoes a ring-pinching reaction that extrudes CO to form **1e**, followed by loss of CO to form **1f**, the cyclopentadiene cation. Interestingly, there is a competing channel due to the loss of CH_2 with low abundance in the breakdown curve. This channel starts with a 1,2-H shift from the methyl group in **1** to the adjacent O atom, the product of which ring closes to **1g**. Finally, there is the dissociation of CH_2 from **1g**, forming **1h**, *m*/*z* 111 (note that triplet CH_2 was used in the relative energy calculations).

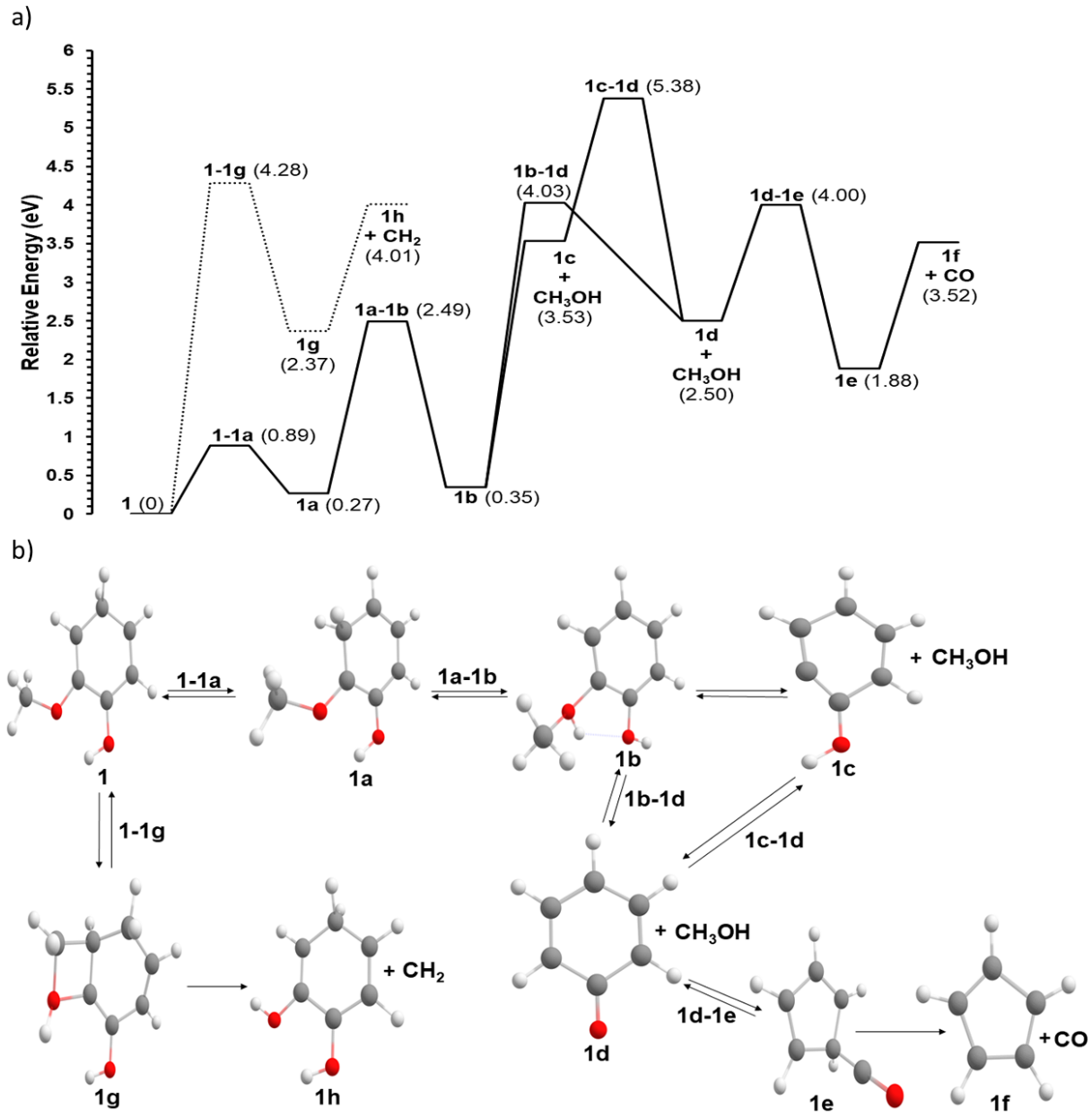

Figure 5-5. Calculated reaction pathways for protonated guaiacol **1** at the CBS-QB3(sp)//B3LYP/6-31G(d) level of theory. The oxygen atom is red.

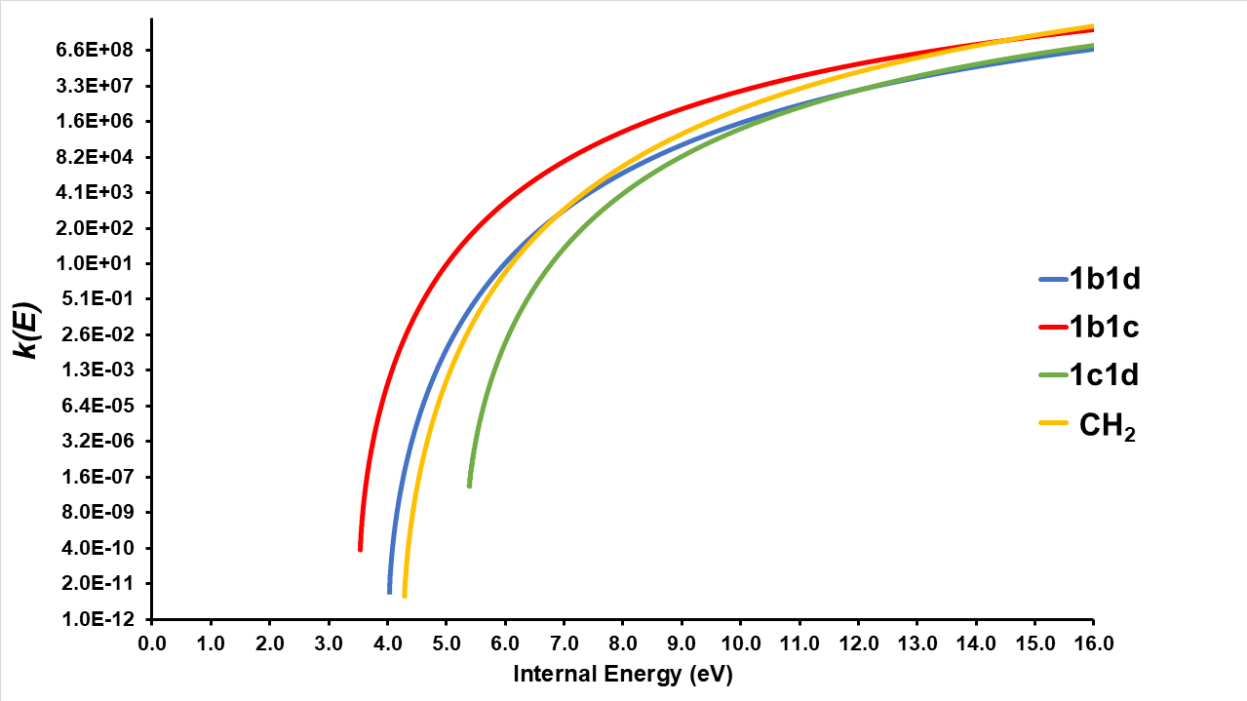

Figure 5-6. Illustrative RRKM *k(E)* vs *E* curves for the different pathways for the dissociation of protonated guaiacol.

Dissociation of **2** (**Figure 5-7**) proceeds via an analogous series of hydrogen transfers that sees the global minimum structure **2** converted to **2b** prior to a 1,2-H shift to form the O-protonated **2c**. As was seen with **1**, direct methanol loss from **2c** leads to **2d,** which then must isomerize to **2e** via a high-energy transition state. A concerted pathway from **2c** directly to **2e** is 1 eV lower in energy than this sequential path. Loss of CO then occurs by ring-pinching to a 5-member ring, extruding CO to form **2f** and then **2g**.

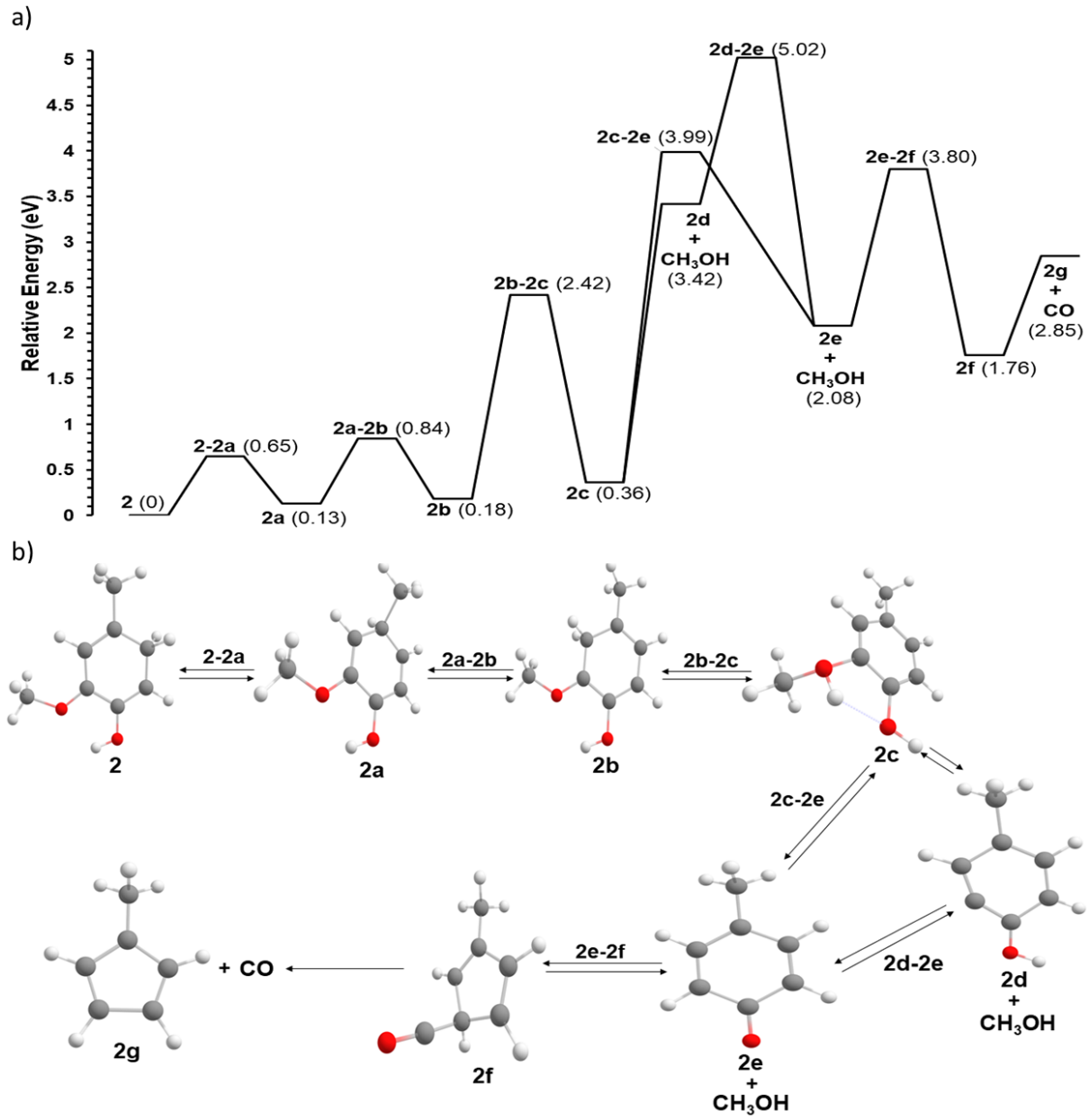

Figure 5-7. Calculated reaction pathways for CH_3OH and CO dissociation in protonated creosol **2** at the CBS-QB3//B3LYP/6-31G(d) level of theory. The oxygen atom is red.

Protonated 4-ethylguaiacol **3** (**Figure 5-8**) loses methanol followed by a loss of CO via a mechanism analogous to **1** and **2**, as are the subsequent concerted vs stepwise paths to **3e**. CO loss is mediated by a similar ring-pinching transition state to form **3f** and then **3g**, the ethylcyclopentadiene cation. Methane can then be formed from **3g** via a 1,4-H shift to form **3h**, which has an electrostatically bound CH_4 group. Given enough energy, **3h** can ring-expand to **3i**.

Two pathways resulting in loss of water were found. The first starts from **3d** where a hydrogen transfer to the hydroxy group leads to **3j**, which can directly cleave H_2O to form *m*/*z* 103, **3k**. A second path starting from **3e** involves a hydrogen transfer from the methylene group of the sidechain to the bare O atom to make **3L**, which then abstracts an H atom from the methyl group to form **3m**, which in turn cleaves water to make **3n**. **3n** is significantly lower in energy than **3k**, but a key transition state between **3L** and **3m** lies comparable in energy to that between **3d** and **3j**. We also explored C_2H_4 loss from **3d** and **3e** but found it to be 1-2 eV higher in energy. There is also a route to *m*/*z* 91 from **3d** or **3e**. We found that the products of CH_2O loss from **3d** and **3e** are preferred over those from C_2H_6 loss by 2.5 eV, and lie 0.25 eV above **TS 3e-3f**, which accounts for its low abundance.

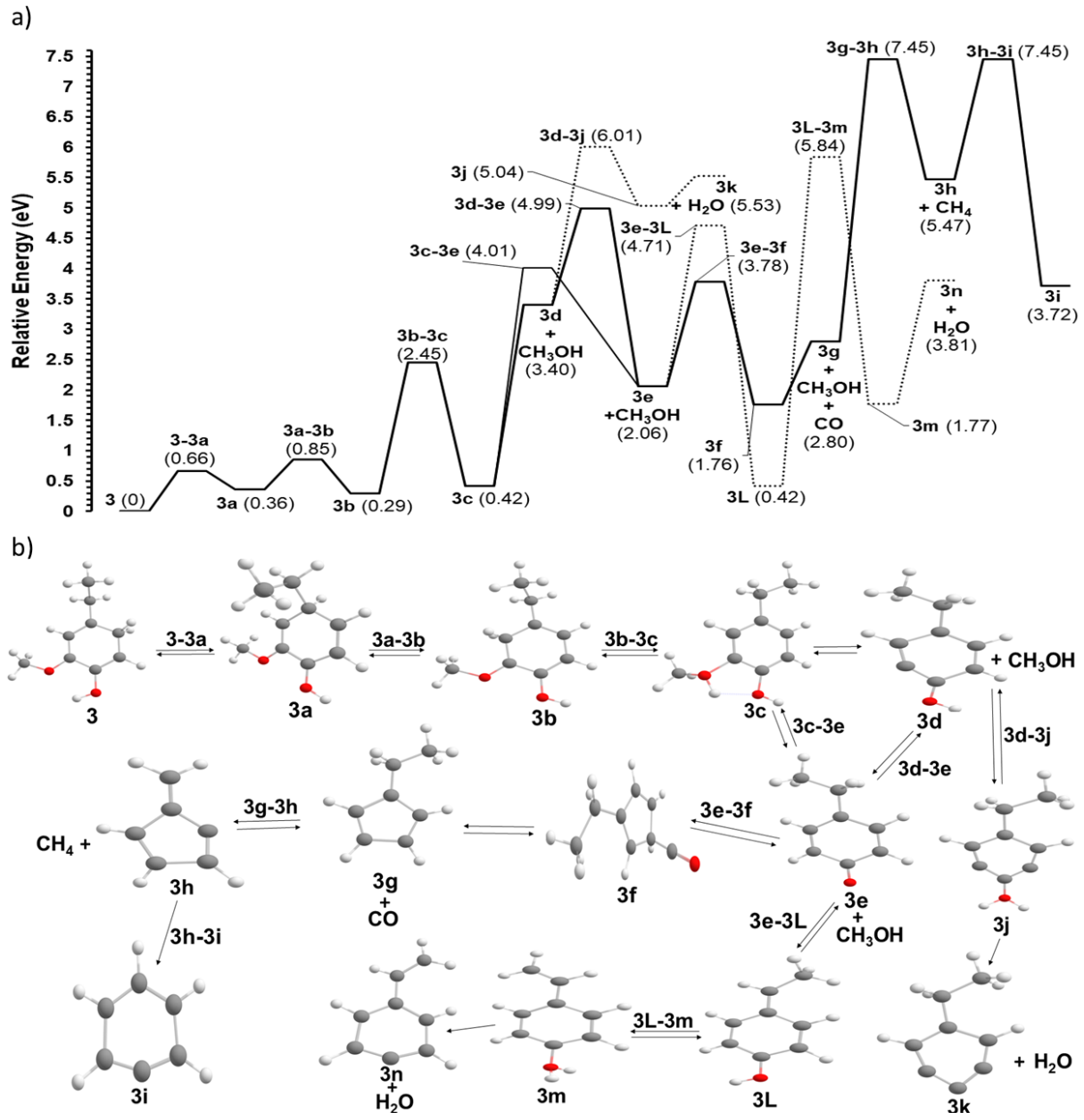

Figure 5-8. Calculated reaction pathways for CH_3OH, CO, CH_4 and H_2O formation from protonated 4-ethylguaiacol **3** at the CBS-QB3//B3LYP/6-31G(d) level of theory. The oxygen atom is red.

In addition to the now standard pathways to loss of CH_3OH and CO, methyl radical loss from **4** can occur either directly from **4** requiring an activation energy of 4.14 eV or from **4c**, the O-protonated isomer of **4** (**Figure 5-9**). This latter channel only requires 2.33 eV (relative to **4**) and

so is the kinetically favoured route. As with **3**, C_2H4 loss from **4d** and **4e** lies 4 - 4.5 eV higher in energy than CO loss.

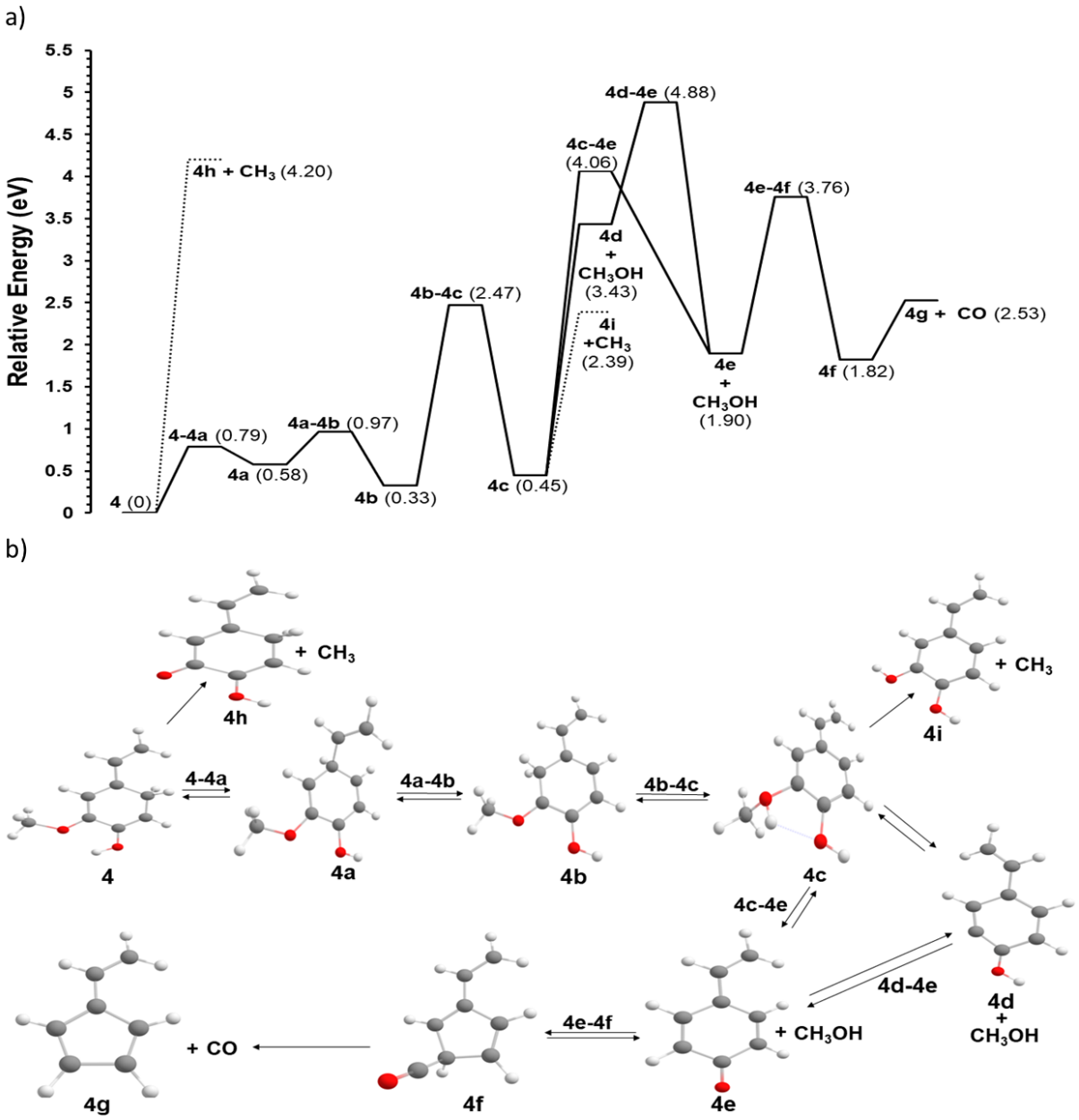

Figure 5-9. Calculated reaction pathways for CH_3OH, CO and CH_3 dissociation in protonated 4-vinylguaiacol **4** at the CBS-QB3//B3LYP/6-31G(d) level of theory. The oxygen atom is red.

For protonated eugenol (**Figure 5-10**), an additional hydrogen transfer from **5** to the prop-2-enyl group of the sidechain leads to the loss of C_2H_4 to form **5h**. Sequential loss of CO from **5h** proceeds

via a hydrogen transfer from the hydroxy group to the methylene group of the sidechain to form **5i**. **5i** then undergoes a ring-pinching reaction that extrudes CO to form **5j**, followed by loss of CO to form **5k.** Dissociation of the prop-2-enyl group of the sidechain from **5** forms **5L**, and a hydrogen transfer to the vacant C leads to the more stable **5m**. On the other hand, loss of the methoxy-phenol group ($C_7H_8O_2$) from **5** leads to **5n**, the prop-2-enyl ion. As with **3** and **4**, C_2H4 loss from **5d** lies 3.5 eV higher in energy than CO loss.

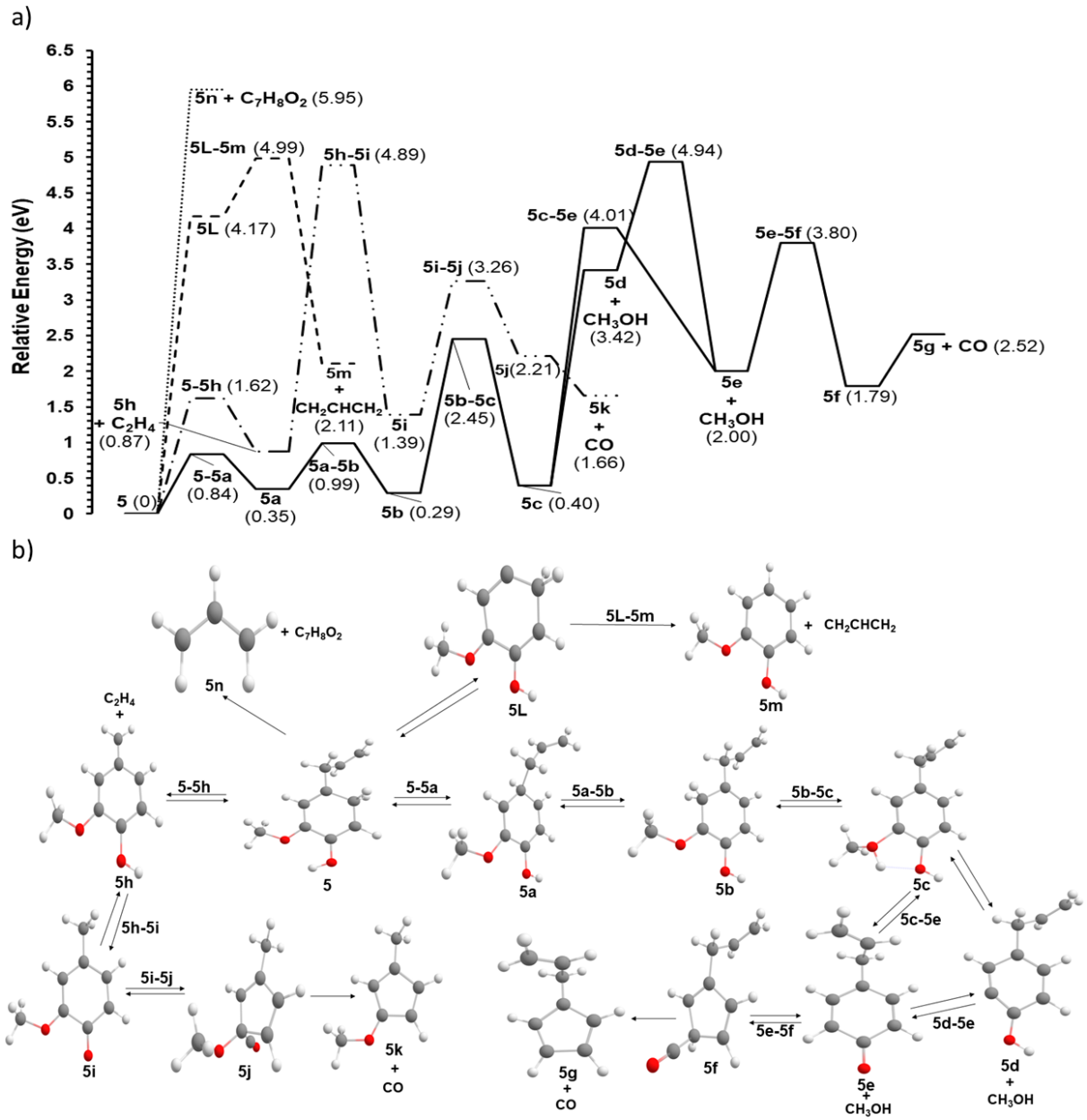

Figure 5-10. Calculated reaction pathways for CH_3OH, CO, C_2H_4, CH_2CHCH_2 and $C_7H_8O_2$ formation from protonated eugenol **5** at the CBS-QB3//B3LYP/6-31G(d) level of theory. The oxygen atom is red.

In contrast to the other derivatives, calculations for protonated vanillin **6** showed poor agreement between B3LYP/6-31G(d) level of theory and CBS-QB3//B3LYP/6-31G(d) level of theory (**Figure A5-4** in the Appendix). Thus, a higher level of theory was applied, namely CBS-QB3(sp)//B3LYP/6-311+G(d,p), **Figure 5-11**. The primary fragmentation channel of CO loss (*m*/*z*

125) followed by sequential losses of CH_3OH (*m*/*z* 93) and CO (*m*/*z* 65) proceeds via a 1,4-H shift from the O-protonated bound hydrogen in **6** to form **6a**. A 1,2-H shift from **6a** then leads to **6b**, followed by loss of CO to form **6c**. **6b** is simply **1a**, and the resulting chemistry follows that of protonated guaiacol. Hydrogen transfer from **6c** to the adjacent O atom forms **6d**, from where CH_3OH is lost leading to *m*/*z* 93, **6e**. Isomerization of **6e** via 1,3-H shift from the hydroxy group leads to **6f. 6f** then undergoes a ring-pinching reaction that extrudes CO to form **6g**, followed by loss of CO to form **6h**, a cyclopentadiene cation. The competing channel due to loss of CH_3 followed by sequential loss of CO starts via a methyl loss from **6c** leading to **6i**. Following this, loss of CO occurs by ring-pinching to a 5-member ring leading to **6j** (*m*/*z* 82). Additionally, there are two minor fragmentation channels originating from **6**. A loss of protonated-O-bound H leads to **6L**, while a methyl loss forms **6k**. H-atom loss from the phenolic OH group was also considered but found to lie 0.65 eV higher in energy than **6L**. We also explored the possibility that CH_3 loss occurs first by H atom loss to form **6L** followed by CH_2 loss (as was observed for guaiacol. However, this pathway was calculated to be 3 eV higher in energy than **6k** $+CH_3$.

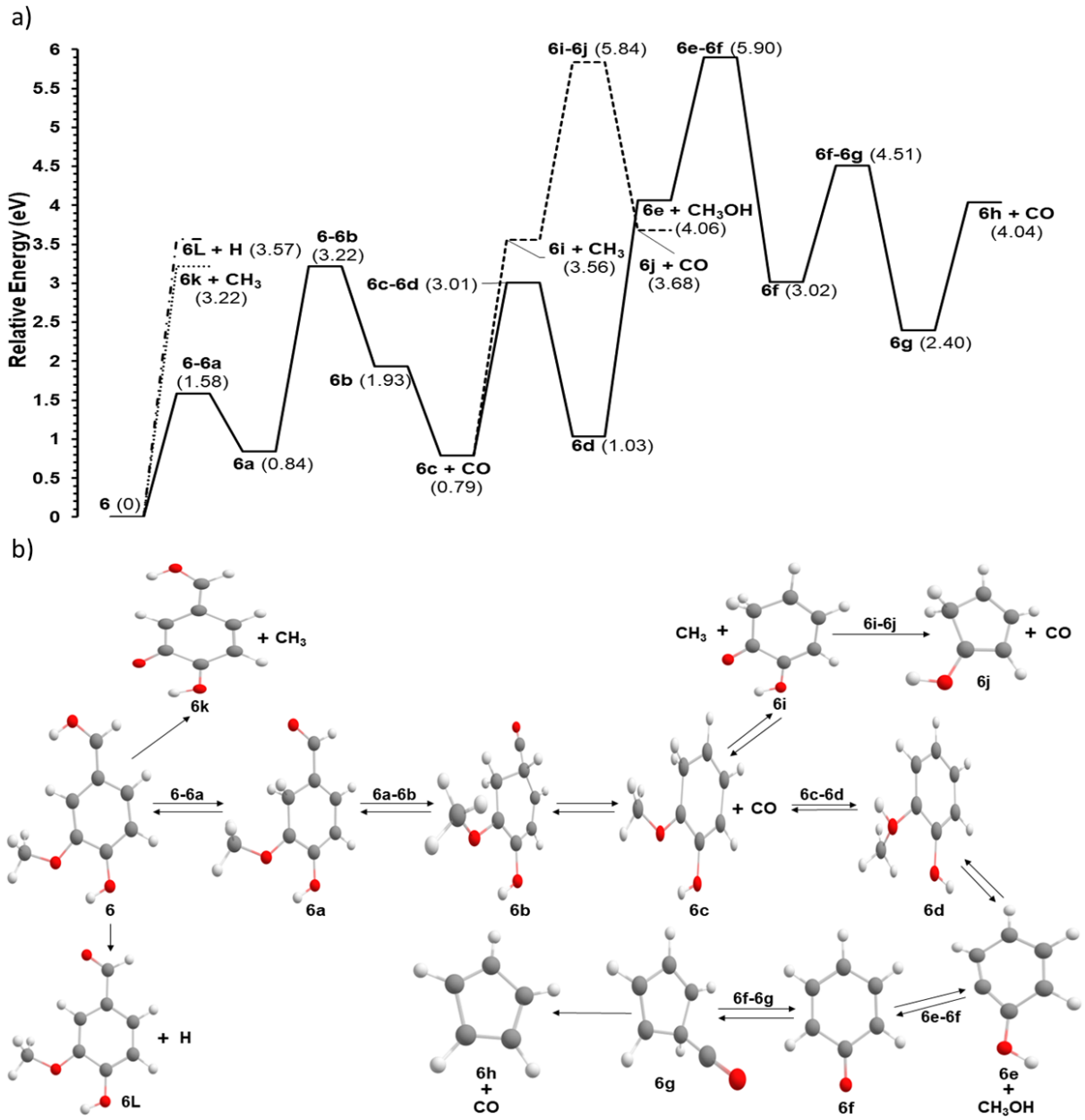

Figure 5-11. Calculated reaction pathways for H, CO, CH_3OH and CH_3 formation from protonated vanillin **6** at the CBS-QB3//B3LYP/6-311+G(d,p) level of theory. The oxygen atom is red.

The main differences between the observed reactions for the ions studied, with the exception of vanillin, occurred in minor channels. For example, protonated guaiacol shows a small CH_2 loss pathway which is absent for the other ions. We calculated this reaction for protonated creosol (starting from ion **2a**) and found the final energy requirement to be higher by 0.2 eV, which must be enough to lower the rate constant to the point where it becomes uncompetitive. Lowering the

relative rate constant by a factor of 2 would start to make it difficult to observe compared to the other reactions. The same was found for H_2O loss from ions other than protonated 4-ethylguaiacol. For example, the barrier to H_2O loss in creosol was calculated to be 2.6 eV above that required for loss of CH_3OH, while for 4-ethylguaiacol it is only 2 eV. For 4-vinylguaiacol and vanillin, methyl loss is a minor channel that barely competes with the other reactions. For guaiacol and creosol, methyl loss is calculated to be ~ 3.8 eV, but this must be high enough to slightly disfavour the reaction relative to the other pathways. A factor of 2 in the relative rate constant values would be enough to preclude its observation. Even small changes in the barrier heights can lead to the disappearance of minor fragmental channels.

5.5 Conclusion

The unimolecular reactions of protonated guaiacol and its derivatives were studied using tandem mass spectrometry and computational chemistry. A common dissociation pathway of CH_3OH loss followed by loss of CO was observed for protonated guaiacol, creosol, 4-ethylguaiacol, 4-vinylguaiacol and eugenol. Loss of CH_3OH via the simple bond cleavage pathway was favoured over the concerted pathway. On the other hand, protonated vanillin exhibited a different dissociation pathway, starting with loss of CO, followed by sequential losses of CH_3OH and CO. Altogether, all the protonated ions generate a cyclopentadienyl ion as the primary dissociation product. Minor dissociation channels were also observed for the protonated ions involving the loss of relatively small molecules such as H loss, CH_3 loss and others. These minor dissociation products varied in accordance with small changes in the energy requirements based on the identity of the specific substituents present in each ion.

Once formed in the atmosphere, all of these protonated ions can undergo loss of CO and CH_3OH upon activation by collision or photon absorption, leading to the formation of the R-cyclopentadiene cation (R=H or a substituent). The predominant neutral pyrolysis pathway in guaiacol also leads to a cyclopentenyl radical, although the mechanism is initiated by CH_3 loss followed by extrusion of CO. Indeed, Nguyen and co-workers[210] found that a number of cyclopentenyl products can be made depending on the temperature, so in this respect the dissociation of protonated guaiacol is analogous. The results are suggestive that there may be

similarities between neutral and protonated guaiacol derivative decomposition that could be explored further.

5.6 Appendix

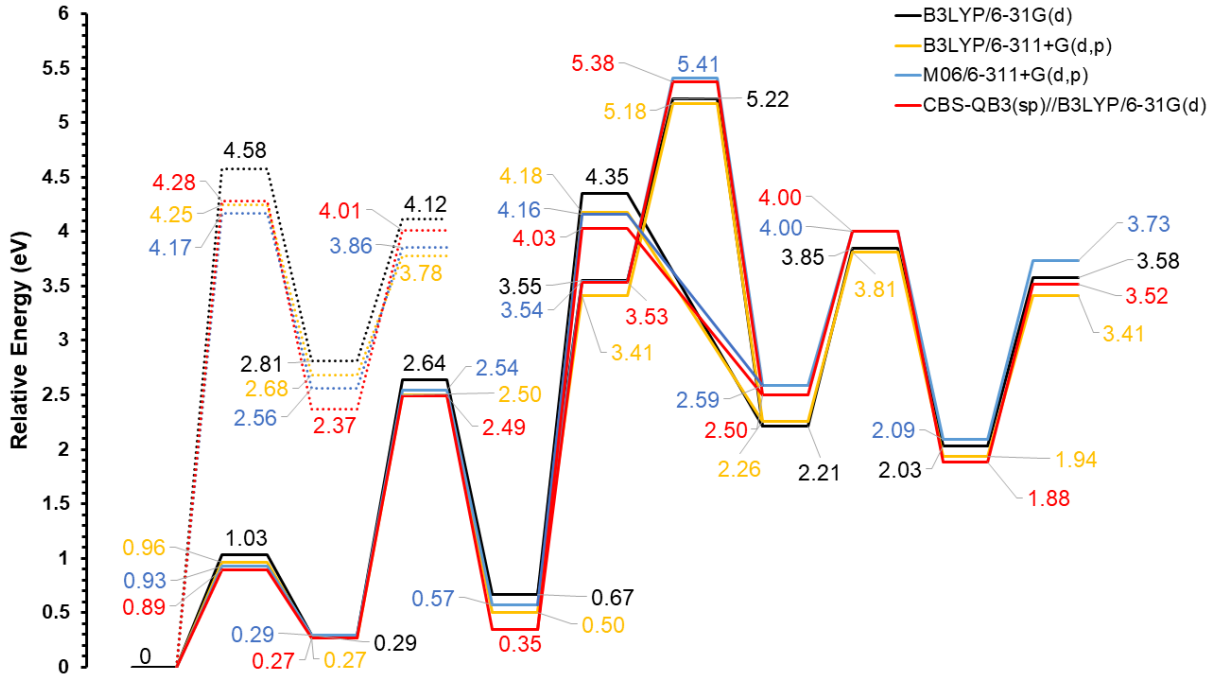

Figure A5-1. Comparison of the minimum energy reaction pathway for the dissociation of protonated guaiacol at the B3LYP/6-31G(d), B3LYP/6-311+G(d,p), M06/6-311+G(d,p) and CBS-QB3(sp)//B3LYP/6-31G(d) levels of theory.

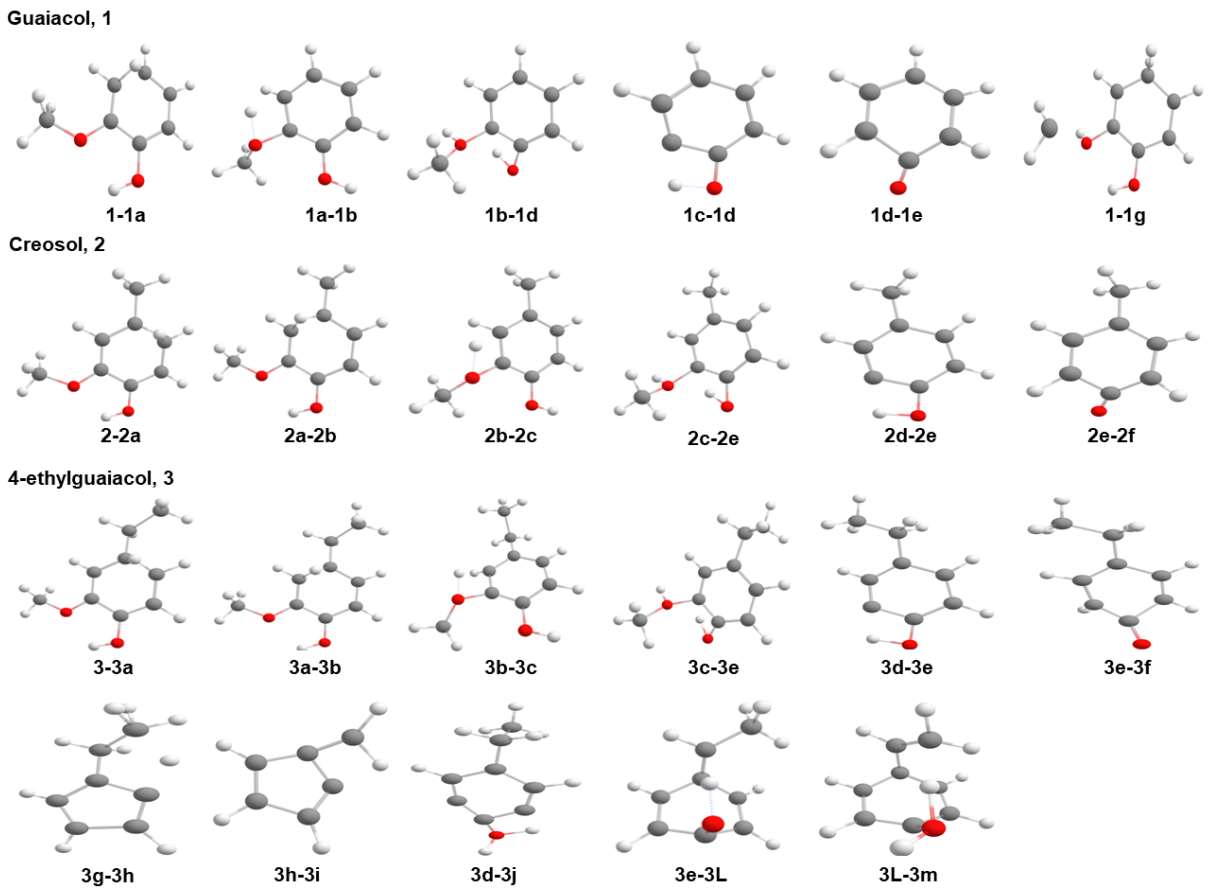

Figure A5-2. Transition states of the minimum energy reaction pathway for the dissociation of protonated guaiacol, creosol and 4-ethylguaiacol.

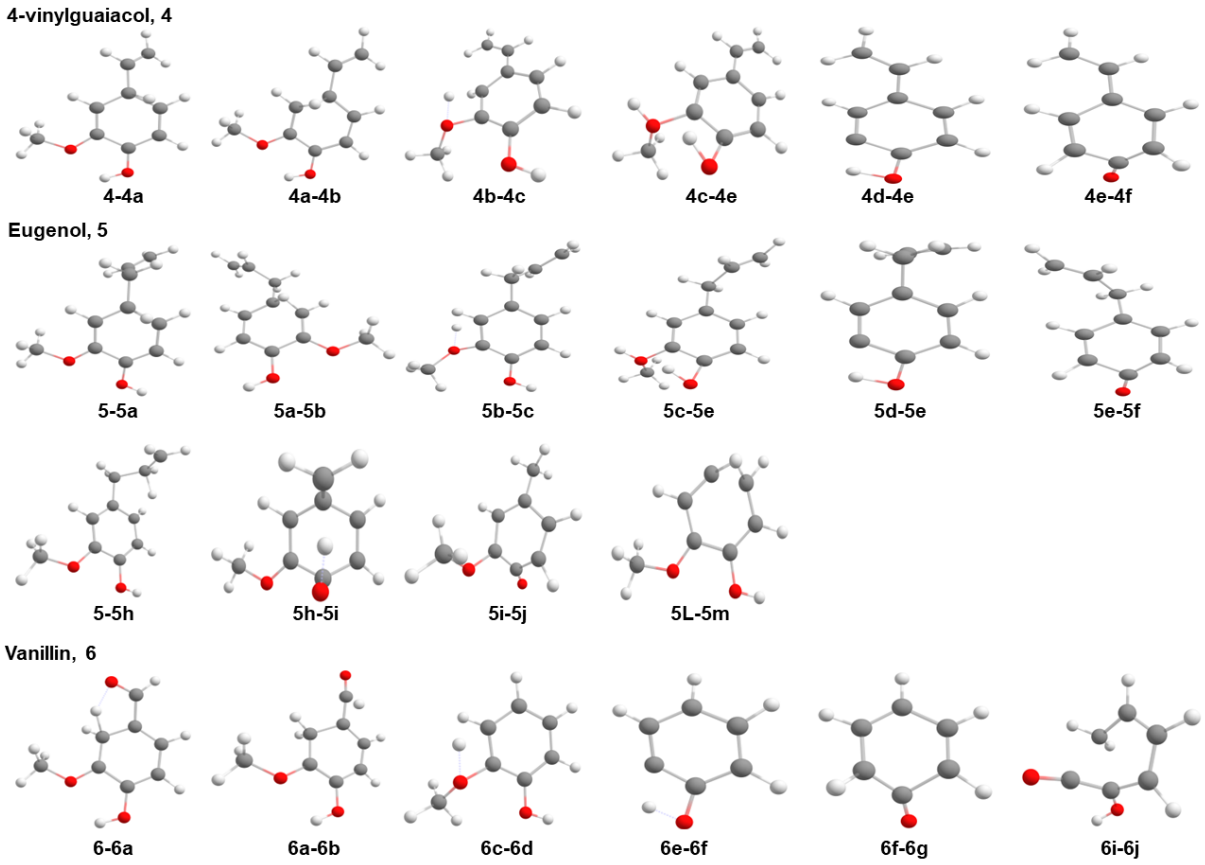

Figure A5-3. Transition states of the minimum energy reaction pathway for the dissociation of protonated 4-vinylguaiacol, eugenol and vanillin.

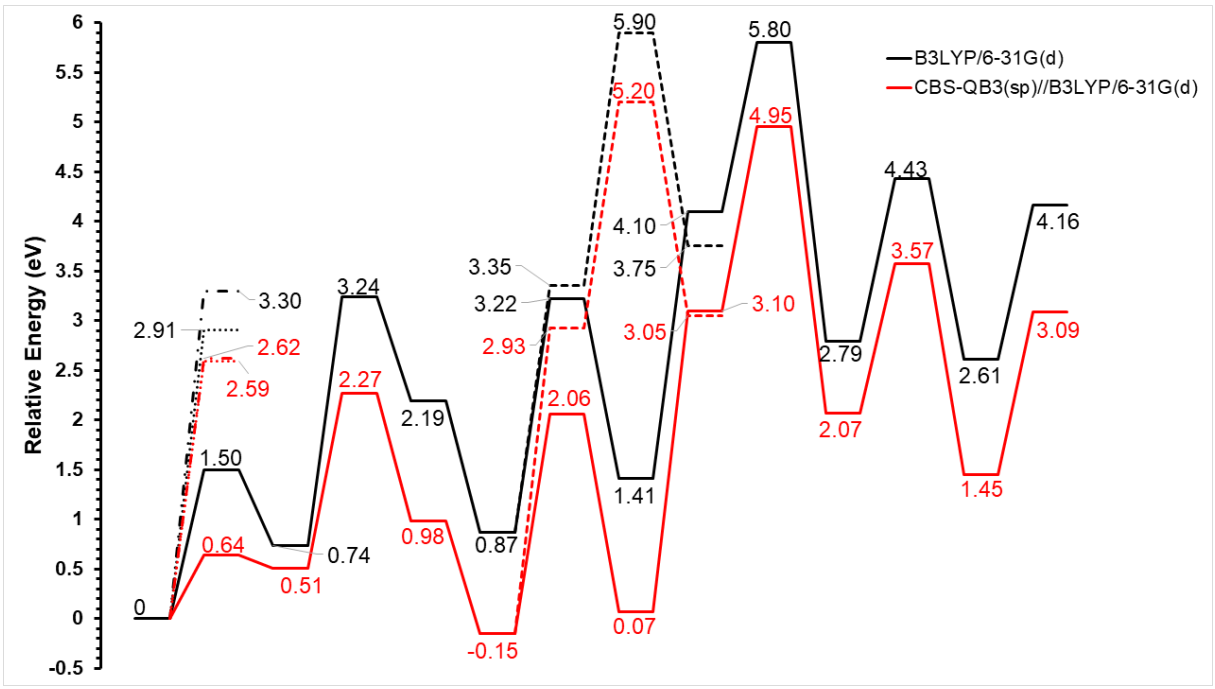

Figure A5-4. Comparison of the minimum energy reaction pathway for the dissociation of protonated vanillin at the B3LYP/6-31G(d) and CBS-QB3(sp)//B3LYP/6-31G(d) levels of theory.

Chapter 6: From guaiacol to benzene without hydrogenation: Acid anion-catalyzed deoxygenation in the gas phase

The contents of Chapter 6 have been accepted for publication in the Canadian Journal of Chemistry (special Canadian Society for Mass Spectrometry issue in honour of Jim Hager, Bob Boyd and Ray March).

Author contributions:
Sandesh Gondarry: Data curation, writing – original draft, DFT calculations.
Paul M. Mayer: Conceptualization, methodology, supervision, writing – review & editing.

6.1 Introduction

Lignocellulosic biomass, particularly lignin, represents an abundant and sustainable resource for renewable chemicals and fuels.[72] The resultant bio-oil from fast pyrolysis is severely limited by its high oxygen content, necessitating catalytic upgrading via hydrodeoxygenation (HDO) to yield stable bio-hydrocarbons.[72,211] Guaiacol (2-methoxyphenol), due to its dual oxygen functionalities (methoxy and hydroxyl substituents), is a primary representative model compound for the mechanistic study of this valorization process.[72]

Effective HDO commonly relies on bifunctional catalysis, combining metallic active sites with acidic functionality.[72,73] Metal sites are indispensable for activating hydrogen and facilitating ring saturation.[212,213] Experimental and computational studies have revealed that catalyst acidity, both Brønsted and Lewis character, plays a decisive role in facilitating $C_{(sp2)}$−O bond scission and steering pathways toward direct deoxygenation (DDO) versus hydrogenation–deoxygenation (HYD) routes.[72,214] Brønsted acid sites facilitate dehydration and proton-assisted deoxygenation by stabilizing key transition states and oxygenated intermediates,[215] and systematic studies show that tuning support acidity or adding acid promoters enhances DDO rates and reduces H_2 consumption by enabling protonation or stabilization before C−O bond cleavage.[73,214,216] Recent work has demonstrated that combining metal hydrogenation sites with proximate Brønsted acidity (for example, MoS_2 edge sites with -SH Brønsted character or Nb_2O_5-modified supports) increases

conversion and benzene selectivity in guaiacol HDO, linking physical changes in metal dispersion and surface acidity to catalytic performance.[217]

To elucidate the intrinsic, acid-mediated C−O cleavage pathway, a combination of tandem mass spectrometry and computational chemistry was employed to examine reactions of neutral guaiacol with bisulphate (HSO_4^-) and nitrate (NO_3^-) anions. In this gas-phase framework, the acid anion serves as a low-coordination, molecular analogue of a Brønsted acid site, permitting direct examination of intracluster proton and oxygen-transfer processes; the approach therefore tests whether acid-mediated rearrangements in the gas phase can extract oxygen as small oxygenates while leaving an aromatic hydrocarbon product.

6.2 Experimental Procedures

Guaiacol (2-methoxyphenol), water, deuterated water, sulphuric acid and nitric acid were purchased from Sigma-Aldrich (>98%, Sigma-Aldrich, Oakville, Ontario, CA) and used without further purification.

Electrospray ionization mass spectrometry (ESI-MS) was performed on a Waters Micromass Quattro Ultima Pt triple quadrupole mass spectrometer (Waters, Manchester, UK). For ion-molecule reactions, bisulphate anions, HSO_4^-, and nitrate anions, NO_3^-, were generated in the electrospray source by delivering acid solutions in water (1 mg/mL) with a syringe pump at a flow rate of 27 μL min^{-1}. Capillary and cone voltages were set to 3.90 kV and 35 V, respectively. The desolvation gas (N_2) was set to a flow rate of 30 L/h. The source and desolvation gas temperatures were held at 100 and 160 ºC, respectively. The acid anion was mass-selected with the first quadrupole and directed into the ion tunnel collision cell, where it reacted with guaiacol vapour introduced via a Granville-Phillips variable leak valve after three freeze-pump-thaw cycles to remove air. The voltage at the entrance and exit of the collision cell was set at 50 V to give an extraction voltage for the derived reaction products.[218] The resulting products were analyzed with the second quadrupole. The experiments were conducted at the lab-frame collision energies of 1, 3, and 5 eV to see the effect on the mass spectra as the energy is increased across the collision cell (**Figure 6-1**). Note that no CID gas (argon) was introduced.

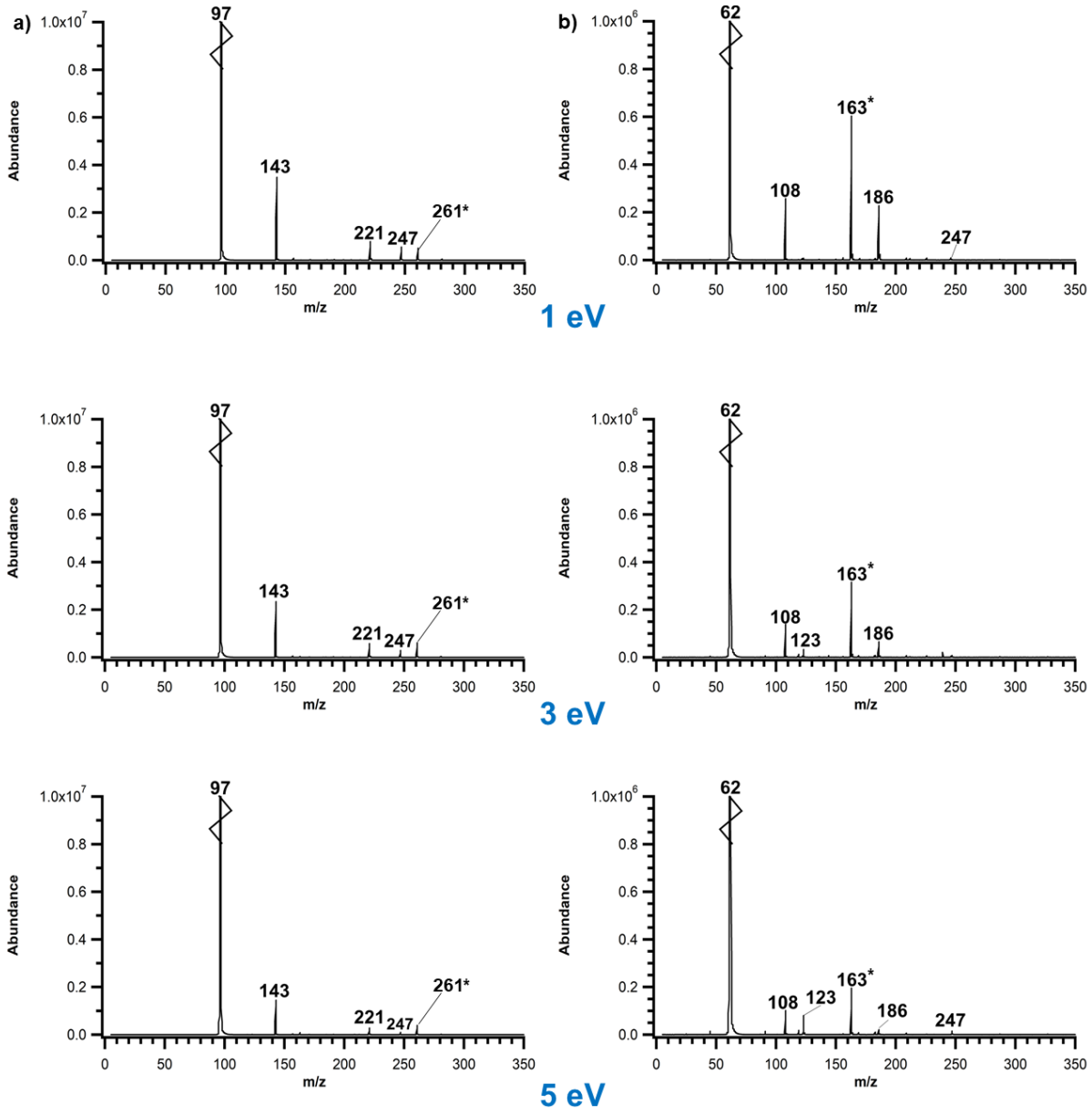

Figure 6-1. Reactions of guaiacol with a) HSO_4^- and b) NO_3^- at different collision energies. Artifacts are labelled with * (refer to section 6.4).

6.3 Computational Procedures

Equilibrium structures and harmonic vibrational frequencies were optimized at the M06/311++G(d,p)[121,122] level of density functional theory (DFT) employing the GAUSSIAN 16 suite of programs.[112]

6.4 Results and Discussion

Figure 6-2 shows the mass spectra derived from the reaction of HSO_4^- (*m*/*z* 97) and NO_3^- (*m*/*z* 62) with neutral guaiacol at 3 eV, with the whole set of data in **Figure 6-1**. In the former case, the major products observed are *m*/*z* 143, 221, and 247, while for the latter, they are *m*/*z* 108, 123, and 186. Note that *m*/*z* 163 is an artifact peak which is always present, and it is not a product resulting from the reaction between guaiacol and the acid anion. Moreover, *m*/*z* 261 is a reaction product involving the precursor to *m/z* 163, as confirmed through the reaction of HSO_4^- (*m/z* 97) from the source with background vapours in the collision cell (**Figure 6-3**).

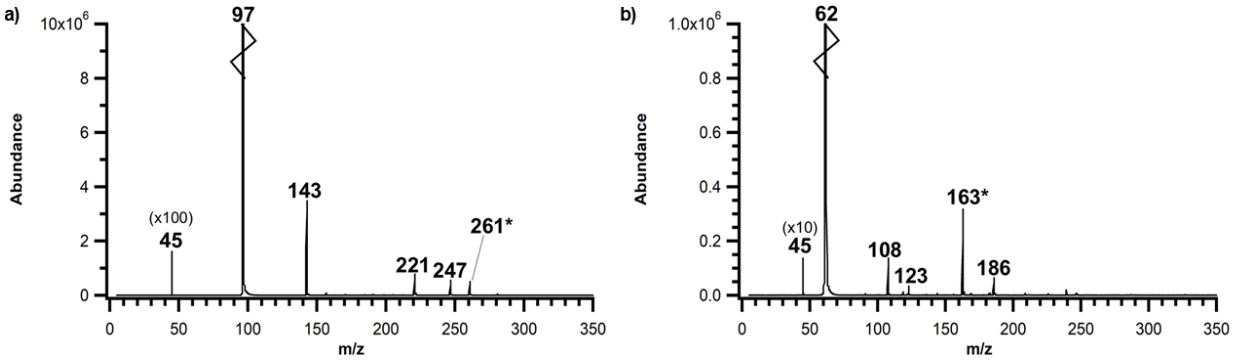

Figure 6-2. Main peaks obtained from the reaction of guaiacol with the a) bisulphate anion, and b) nitrate anion at a collision energy of 3 eV. The *m*/*z* 97 (HSO_4^-) and *m*/*z* 62 (NO_3^-) peaks were cut off, and the *m*/*z* 45 peaks were scaled for clarity. Peaks labelled with * are confirmed artifacts.

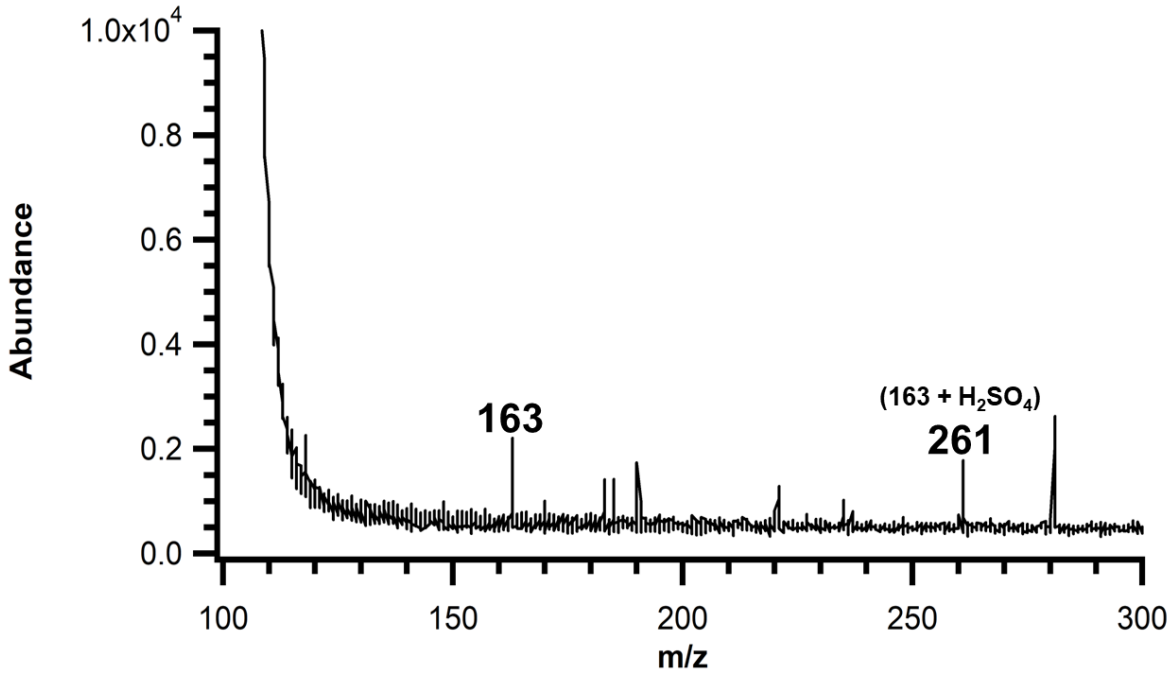

Figure 6-3. Mass spectrum of bisulphate anion (HSO_4^-) reacting with air from the source. *m/z* 163 and *m/z* 261 peaks are present as background noise and no guaiacol peak (*m/z* 123), which confirms *m/z* 163 to be an artifact peak.

Any reaction would involve the formation of an initial complex between the acid anion and neutral guaiacol, the observed ions *m/z* 221 (with HSO_4^-) and *m/z* 186 (with NO_3^-). The two product ions *m/z* 143 and *m/z* 108 correspond to $HSO_4(HCO_2H)^-$ and $NO_3(HCO_2H)^-$, complexes of the reacting acid with formic acid. These products would be due to the loss of a neutral molecule of benzene, following **Scheme 6-4**. This reaction is supported by the observation of formate anions, $HCOO^-$, in the mass spectra of both acids (**Figure 6-2**, expanded insets). To observe *m/z* 143 and 108, the loss of benzene must represent an overall exothermic reaction (or at least thermoneutral). For both acids HSO_4^- and NO_3^-, *m/z* 123 was observed corresponding to deprotonated guaiacol (**Figure 6-5**) and the deprotonated dimer of guaiacol, *m/z* 247 (**Figure 6-6**).

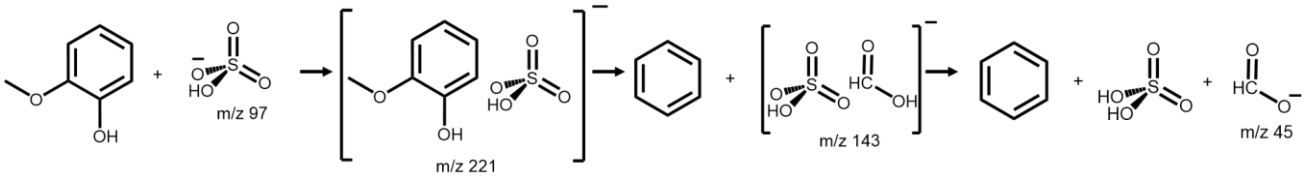

Scheme 6-4. Schematic representation of the overall reaction of guaiacol with HSO_4^-.

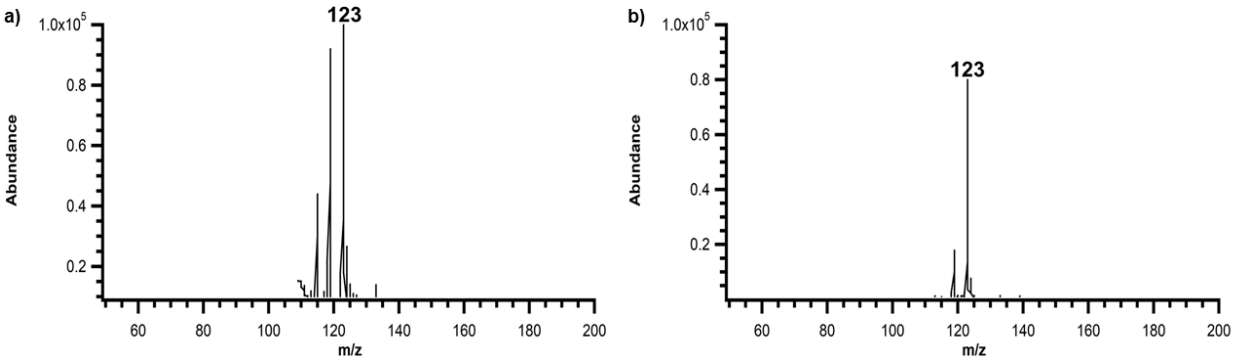

Figure 6-5. Deprotonated guaiacol, *m/z* 123, formed in the reaction with a) HSO_4^- and b) NO_3^-.

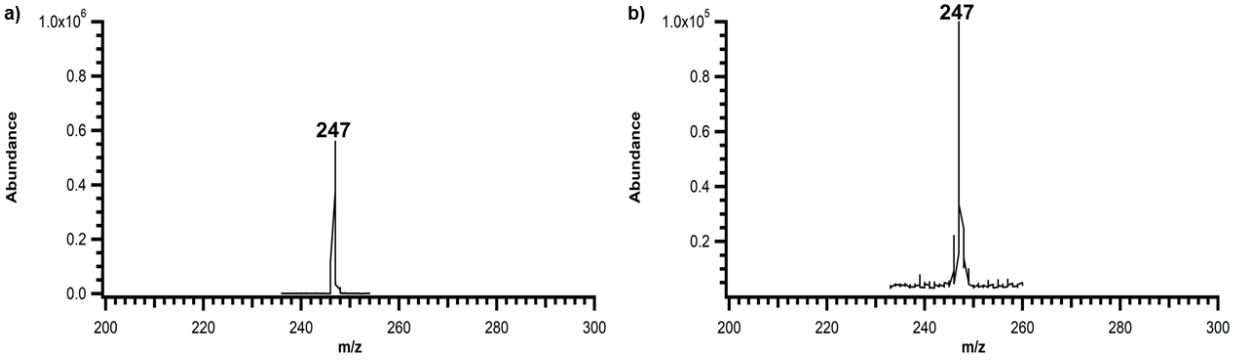

Figure 6-6. Guaiacol dimer peak *m/z* 247 with a) HSO_4^- and b) NO_3^-.

Additional insight into the encounter complex was obtained by forming DSO_4^- in the electrospray source (dissolving H_2SO_4 in D_2O). The reaction of DSO_4^- with neutral guaiacol revealed a reversible hydrogen transfer reaction that produced HSO_4^-. This experiment was carried out at the same collision energy of 3 eV but with the increasing pressure of guaiacol vapour. As the guaiacol pressure increased in the collision cell, there was a rise in the *m/z* 97 peak (HSO_4^-) and a drop in the *m/z* 98 peak (DSO_4^-), which is suggestive of an exchange reaction within a relatively long-lived complex (**Figure 6-7**).

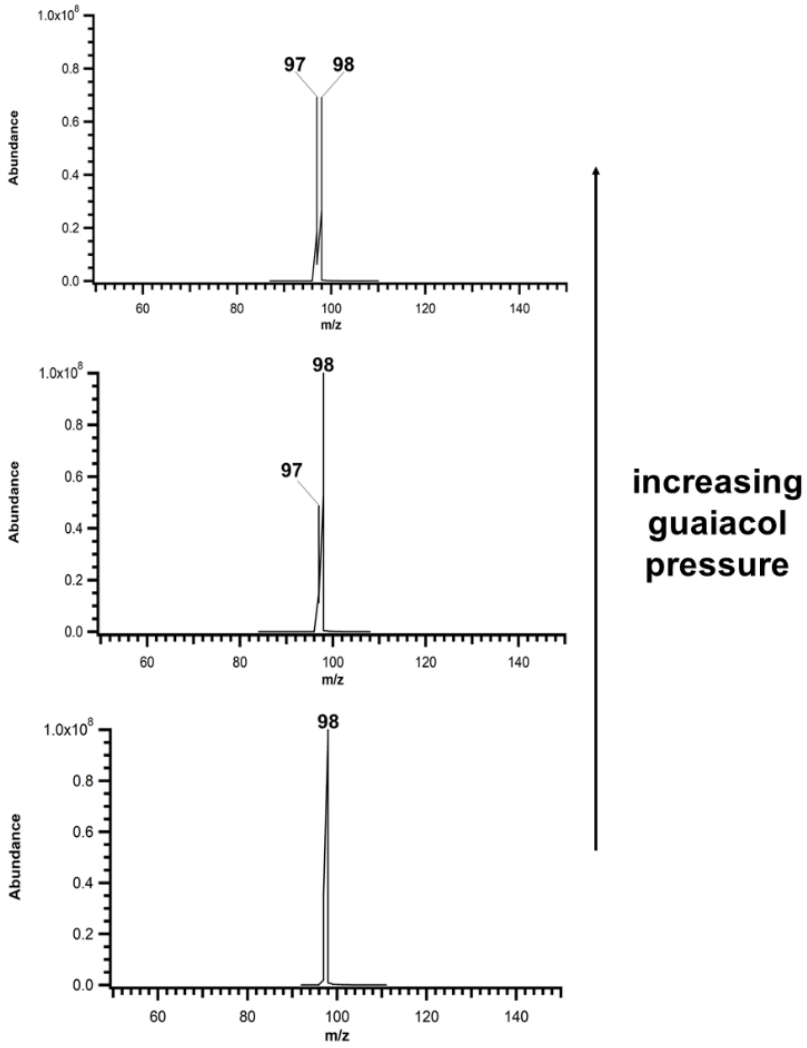

Figure 6-7. Mass spectra showing the exchange reaction between the anion and neutral guaiacol.

In addition, the reaction of DSO_4^- with guaiacol gave *m/z* 144 (**Figure 6-8**) corresponding to the $(DSO_4)(HCO_2H)^-$ analog of the main product in Figure **6-2a** (but the location of the D is undetermined). The presence of both *m/z* 143 and 144 indicates that deuterated benzene is being formed as a neutral. The observation of *m/z* 221 and 222 suggests that a deuterium swap can occur independent of the formation of a long-lived complex. *m/z* 248 corresponds to a deuterated guaiacol dimer.

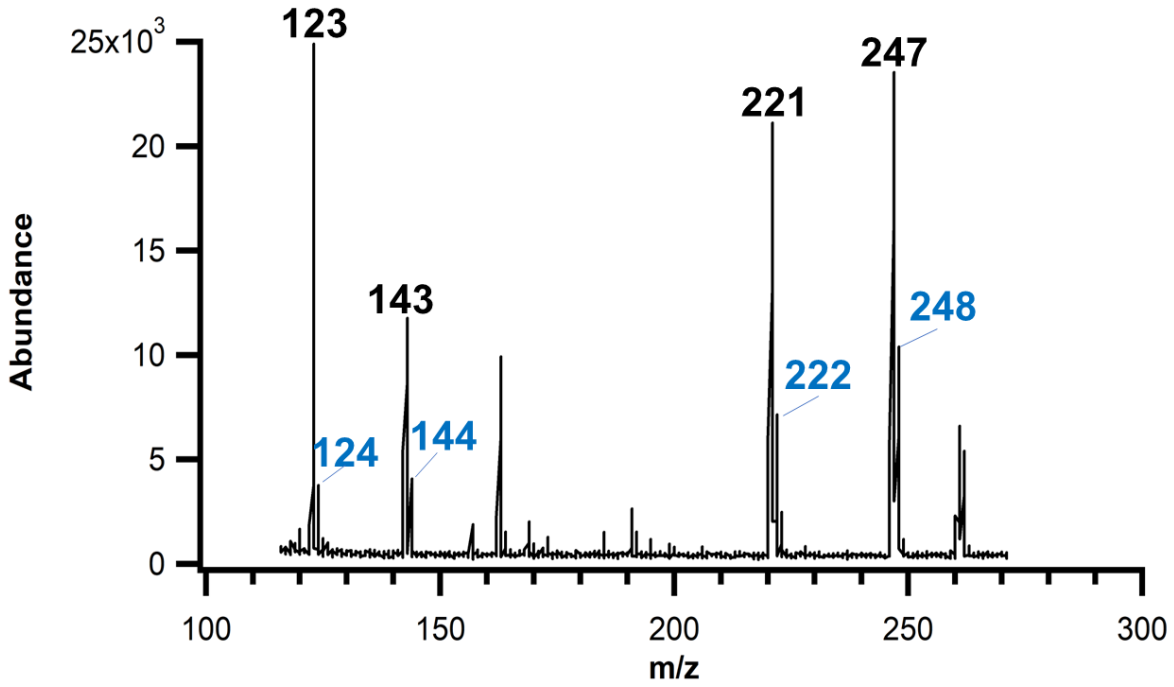

Figure 6-8. Mass spectrum for the reaction of DSO_4^- (*m/z* 98, not shown) with guaiacol. The peaks in blue correspond to the reaction products observed in **Figure 6-2**, but with a D atom replacing an H atom.

It appears that the main reaction of the acid anions with neutral guaiacol is the production of neutral benzene and formic acid. We explored these reactions computationally with density functional theory (**Figure 6-9**). Using the reaction with HSO_4^- as an example, the reaction proceeds by the formation of the collision complex lying 76 kJ mol^{-1} below the reactants. Proton abstraction to form the guaiacol anion is endothermic from here by around 237 kJ mol^{-1} due to the large difference in gas-phase acidity between guaiacol and H_2SO_4 of 168 kJ mol^{-1}.[219] From the encounter complex, the system proceeds to a complex consisting of benzene, HSO_4^- and formic acid, exothermic from the initial collision complex by 84 kJ mol^{-1}. Due to the low quadrupole moment of benzene, this complex is bound by only 73 kJ mol^{-1}, dissociating into the experimentally observed products $HSO_4(HCOOH)^-$, *m/z* 143. A similar reaction holds for the NO_3^- reaction (**Figure 6-9b**). Both overall reactions are exothermic with respect to the initial reactants.

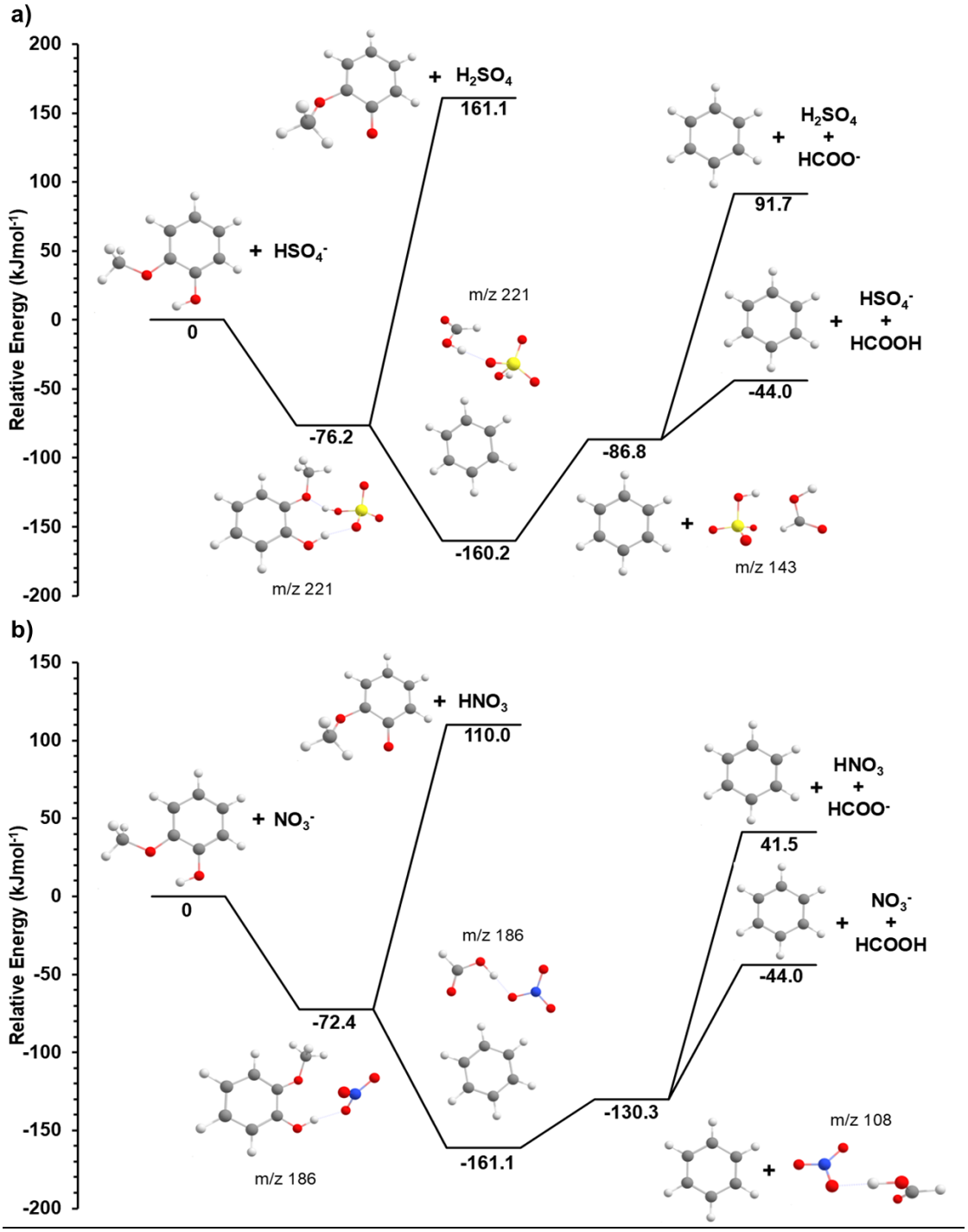

Figure 6-9. Reaction minima leading from reactants to products for the reaction of a) HSO_4^- and b) NO_3^- with neutral guaiacol.

It was not possible to elucidate a complete minimum energy reaction pathway due to the inherent complexity and variety of H-transfer reactions that can occur in the long-lived reaction complexes. A detailed mechanism thus, must await a further study.

6.5 Conclusion

In this study, gas-phase ion-molecule reaction has been explored to establish a fundamentally important catalytic degradation pathway for guaiacol, mimicking the function of Brønsted acid sites in heterogeneous catalysts. The acid anion drives a rearrangement in the initial encounter complex that leads to the extraction of formic acid from guaiacol, leaving neutral benzene. Crucially, the process is inherently catalytic: the acid anion facilitates the reaction and is recovered in a complexed form ($HSO_4(HCOOH)^-$ and $NO_3(HCOOH)^-$), essentially acting as a recovered catalyst. These results provide a molecular-level demonstration that strong acid centres can mediate C−O bond cleavage of methoxyphenols without requiring extensive solvation or conventional metal hydrogenation steps, rationalizing why catalysts that combine proximate acid and metal functionalities perform well in guaiacol HDO studies. While the experimental setup (collision-cell energies, vacuum environment, and ion-guided encounters) differ from practical catalytic reactors, the mechanistic structures identified - encounter complex formation, intracluster hydrogen transfer, and acid-stabilized loss of small oxygenates - are directly relevant to interpreting the role of surface Brønsted acidity on solid catalysts and for designing bifunctional materials that optimize direct deoxygenation versus hydrogenation–deoxygenation pathways.

Chapter 7: Does the dissociation of guaiacol family radical cations mimic their thermal decomposition?

The contents of Chapter 7 have been published as: Gondarry, S.; Mayer, P. M. Does the Dissociation of Guaiacol Family Radical Cations Mimic Their Thermal Decomposition? *Comput. Theor. Chem.* 2023, *1229* (May), 114323. https://doi.org/10.1016/j.comptc.2023.114323.

Author contributions:
Sandesh Gondarry: Data curation, writing – original draft, DFT calculations.
Paul M. Mayer: Conceptualization, methodology, supervision, writing – review & editing.

7.1 Introduction

Lignin, one of the main components of woody biomass (accounting for 18-40 wt %),[201] provides an alternative eco-friendly source of aromatic polymers and oxygenated hydrocarbons that can be transformed into valuable fuels and chemicals.[220] Experimental and theoretical studies on lignin pyrolysis illustrated that primarily syringol- and guaiacol-related products are formed at the preliminary pyrolysis process, with guaiacol being the predominant product.[210,220]

To date, guaiacol has been primarily considered as a model lignin compound in numerous experimental and theoretical studies on lignin pyrolysis.[77,221] Scheer et al.[77] analyzed the pyrolysis of guaiacol using a heated SiC microtubular reactor, and a combination of photoionization time-of-flight mass spectroscopy (PIMS) and matrix isolation infrared spectroscopy (IR) techniques was utilized for decomposition product detection. The initial decomposition step identified was the loss of a methyl radical ($^{\bullet}CH_3$), forming the hydroxy-substituted phenoxy radical, $HO{-}C_6H_4O^{\bullet}$, followed by decarbonylation to produce hydroxycyclopentadienyl radicals, $HOC_5H_4^{\bullet}$. Moreover, Asmadi et al.[221] examined the thermal reactions of guaiacol using a closed ampoule reactor (N_2 /400-600 ^{0}C / 40-600 s) and proposed that the homolytic cleavage of the methoxy group ($RO{-}CH_3$) is the primary pathway for pyrolytic guaiacol decomposition. Wu et al.[222] explored the thermal decomposition of vanillin in an in-vacuum flash pyrolysis microreactor by photoelectron photoion coincidence spectroscopy. Mass-selected threshold photoelectron spectra (ms-TPES) were utilized

for isomer-selective intermediate and product detection. Methyl loss through C−O bond fission was found to be the preliminary unimolecular decomposition step yielding $^{\bullet}CH_3$ and the primary intermediate, the 2-hydroxy-5-formyl-phenoxy radical, which can undergo several decarbonylation steps and sequential hydrogen loss to ultimately form but-2-ene-3-yne.

Various studies have been performed exhibiting the similarities and differences in the thermal degradation of neutral molecules and their corresponding radical cations. Lowe et al.[186,187] investigated the pyrolysis of methyl formate and ethyl formate using synchrotron radiation and theory and discovered identical dissociation products for both the neutral and radical cations of methyl formate and ethyl formate. To the best of our knowledge, no studies have been carried out on the degradation of the radical cations of guaiacol and its derivatives. In this study, a combination of mass spectrometry and computational chemistry was applied to explore the trends in the unimolecular reactions of radical cations of guaiacol (**1**), creosol (**2**), 4-ethylguaiacol (**3**), 4-vinylguaiacol (**4**), eugenol (**5**) and vanillin (**6**) to examine any similarities between the dissociation of these radical species with the pyrolysis of the neutral molecules.

7.2 Experimental Procedures

Guaiacol (2-methoxyphenol), creosol (2-methoxy-4-methylphenol), 4-ethylguaiacol (4-ethyl-2-methoxyphenol), 4-vinylguaiacol (2-methoxy-4-vinylphenol), eugenol (2-methoxy-4-prop-2-enylphenol) and vanillin (4-hydroxy-3-methoxybenzaldehyde) were purchased from Sigma-Aldrich (>98%, Sigma-Aldrich, Oakville, Ontario, CA) and used without further purification.

Mass-analyzed ion kinetic energy (MIKE) spectrometry was performed on a VG ZAB mass spectrometer (Manchester)[223,224]. Guaiacols were introduced into the ion source of the instrument by mild thermal desorption. The ion source pressure was read externally using an ion gauge and the pressure was kept at ~1.0×10^{-5} Torr. The radical cations were generated by electron ionization with 80 eV electrons. The resulting ions were accelerated to 8 kV toward the magnetic sector, where the precursor ion of interest (the molecular ion in each case) was momentum selected and transmitted to the second field-free region. Ions that spontaneously dissociate in this region are coined “metastable ions”. Due to the conservation of energy and momentum, product ions from

unimolecular dissociation (F^+) have a fraction of the precursor ion's (P^+) translational energy, T, according to the equation:

$$T_{F^+} = T_{P^+}\left(\frac{M_{F^+}}{M_{P^+}}\right)$$

Where M_{F^+} and M_{P^+} are the m/z ratios of the product and precursor ion, respectively (and for singly-charged ions correspond to the ion masses).

7.3 Computational Procedures

Equilibrium and transition state structures were optimized at the B3LYP/6-311+G(d,p)[121,122] level of density functional theory (DFT) employing the GAUSSIAN 16 suite of programs[112]. Transition states were confirmed by the intrinsic reaction coordinate method. CBS-QB3 single-point energy calculations[129] (without geometry optimizations) were then employed on the DFT geometries to obtain more accurate energetics. Rice-Ramsperger-Kassel-Marcus (RRKM) theory was applied to calculate *k(E)* according to the following equation[108,157]

$$k(E) = \frac{\sigma N^{\ddagger}(E - E_0)}{h\rho(E)}$$

where σ represents the reaction degeneracy, h is Planck's constant, $N^{\ddagger}(E - E_0)$ is the number of internal states for the transition state at internal energy $(E - E_0)$ and $\rho(E)$ is the density of states for the reactant ion at internal energy (E) as calculated via the Beyer and Swinehart direct count algorithm.[109] B3LYP/6-311+G(d,p) calculated rotational constants and harmonic vibrational frequencies of the reactant ion and transition states were employed in the direct count algorithm to obtain sums and densities of states for the RRKM calculation.

7.4 Results and Discussion

7.4.1 Mike spectra

The MIKE spectra for guaiacol and its derivatives are shown in **Figure 7-1**. With the exception of vanillin (**6**), guaiacol (**1**) and its derivatives share a common fragmentation pathway, the loss of a methyl radical ($^{\bullet}CH_3$). Methanol (CH_3OH) loss was also observed in creosol (**2**), 4-ethylguaiacol (**3**) and eugenol (**5**). The relative intensities of the methanol-loss fragment ions in **2** and **3** were much lower than those for methyl loss, whereas for eugenol, the opposite was true. Ionized vanillin (**6**) was unique by displaying only loss of CO.

$$\frac{7060.2\ eV}{7999.5\ eV}\ X\ 124_{(precursor\ ion)} = 109_{(fragment\ ion,-CH_3)}$$

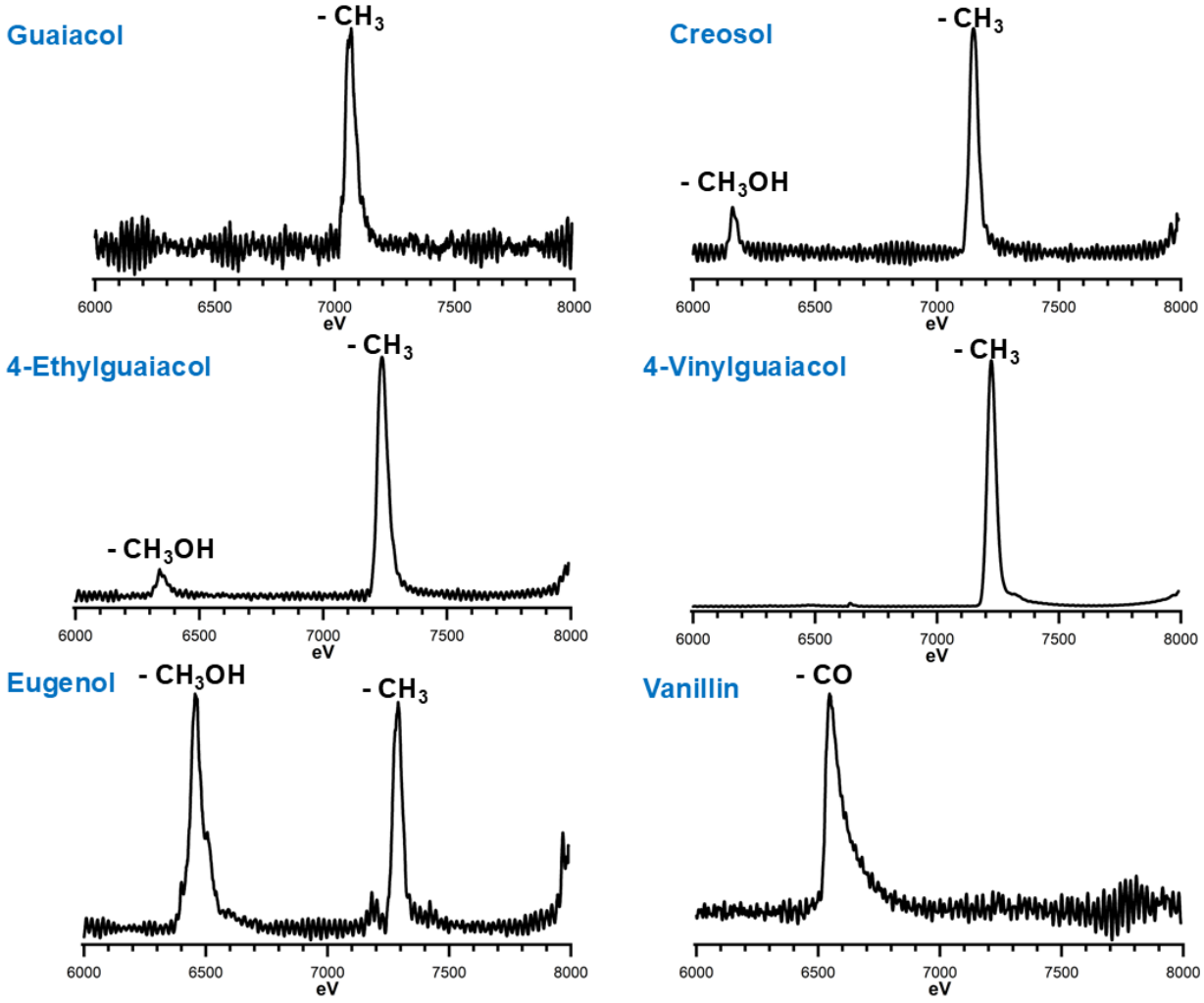

Figure 7-1. MIKE spectra of ionized guaiacol, creosol, 4-ethylguaiacol, 4-vinylguaiacol, eugenol and vanillin. The peak at 8000 eV for eugenol corresponds to the tail of the precursor ion and not a fragment ion. In vanillin, the tail on the peak is due to the high amplifier gain needed to acquire the signal. An example of the calculation of the product ion *m/z* ratio is provided in guaiacol. In each case, the precursor ion, which is 1000x more intense than the observed fragments, is omitted from the plots for clarity.

The dissociating metastable ions do so over a very narrow internal energy window. **Figure 7-2** presents an example for **1**, but the result is very similar for all of the ions studied here. Based on the geometry of the instrument and the accelerating potential, the residence time of the ions in the field-free region can be calculated and the fraction of ions, dn/n_o, having a particular

microcanonical rate constant *k(E)* that dissociate in the region is calculated. This is plotted in **Figure 7-2** against the total observed dissociation rate constant of **1**. The MIKE spectra correspond to the dissociation of ions primarily between 4 and 5 eV of internal energy. Lower internal energy ions largely survive to reach the detector intact (and are displayed as precursor ions in the MIKE spectra – a signal that is so large that it is excluded from the spectra in **Figure 7-1**), while higher internal energy ions will dissociate prior to the magnetic sector and not be selected. This will be significant when comparing to the calculated minimum energy reaction pathways for each system.

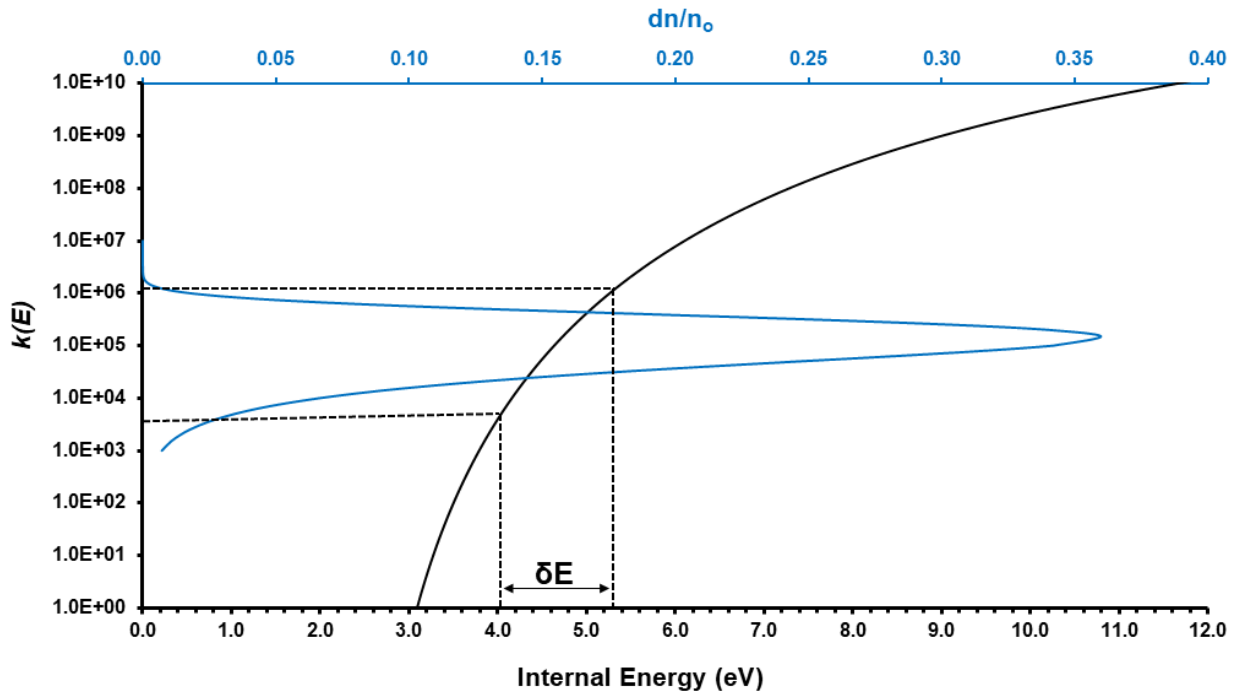

Figure 7-2. RRKM *k(E)* vs *E* curve (left and bottom axis - black) generated by combining the rate constants for CH_3 and CH_3OH losses for the dissociation of guaiacol. Superimposed on the left side of the graph is a plot of the distribution of rate constants that contribute to metastable ion dissociation (left and top axis – blue). The approximate energy window for the metastable dissociations is denoted by δE, which was obtained from the limits of the plotted distribution.

7.4.2 Guaiacol, 1

The loss of $^{\bullet}CH_3$ from **1** proceeds via a simple bond cleavage to form **1a** (**Figure 7-3**). While this is the only reaction observed, we have also calculated the pathway for methanol loss to compare

it to the other ions in this study. Loss of methanol proceeds via a 1,3-H shift to form **1b**. From **1b**, methanol cleaves from the ring and forms an intermediate structure **1c**, from which methanol is lost to form **1d**. We tried moving the OH hydrogen atom to the methoxy O-atom, but the resulting intermediate was not an equilibrium structure and the H-atom returned to form the OH group in a barrierless reaction. The higher energy demand for methanol loss is also apparent when the *k(E)* curves for the two reactions are compared (**Figure 7-4**). In the 4-5 eV internal energy range, the rate constant for $^{\bullet}CH_3$ loss is over six orders of magnitude greater and thus only this channel is experimentally observed. Furthermore, we explored the simple bond cleavage reactions in the ion that generate OH and CH_3O radicals. These were found to require 5.35 and 5.15 eV of energy, respectively, far more than that required for the observed reaction. Similar conclusions could be drawn for the other derivatives discussed below.

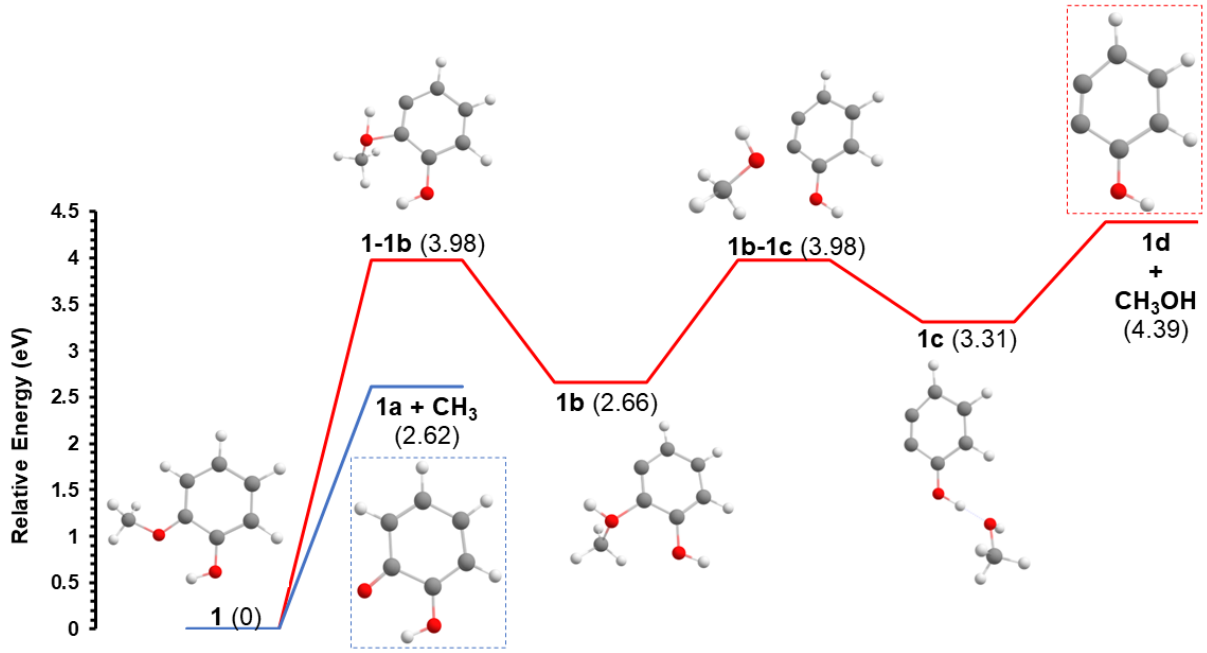

Figure 7-3. Calculated reaction pathways for CH_3 and CH_3OH losses from guaiacol (**1**) at the CBS-QB3(sp)// B3LYP/6-311+G(d,p) level of theory. The oxygen atom is red.

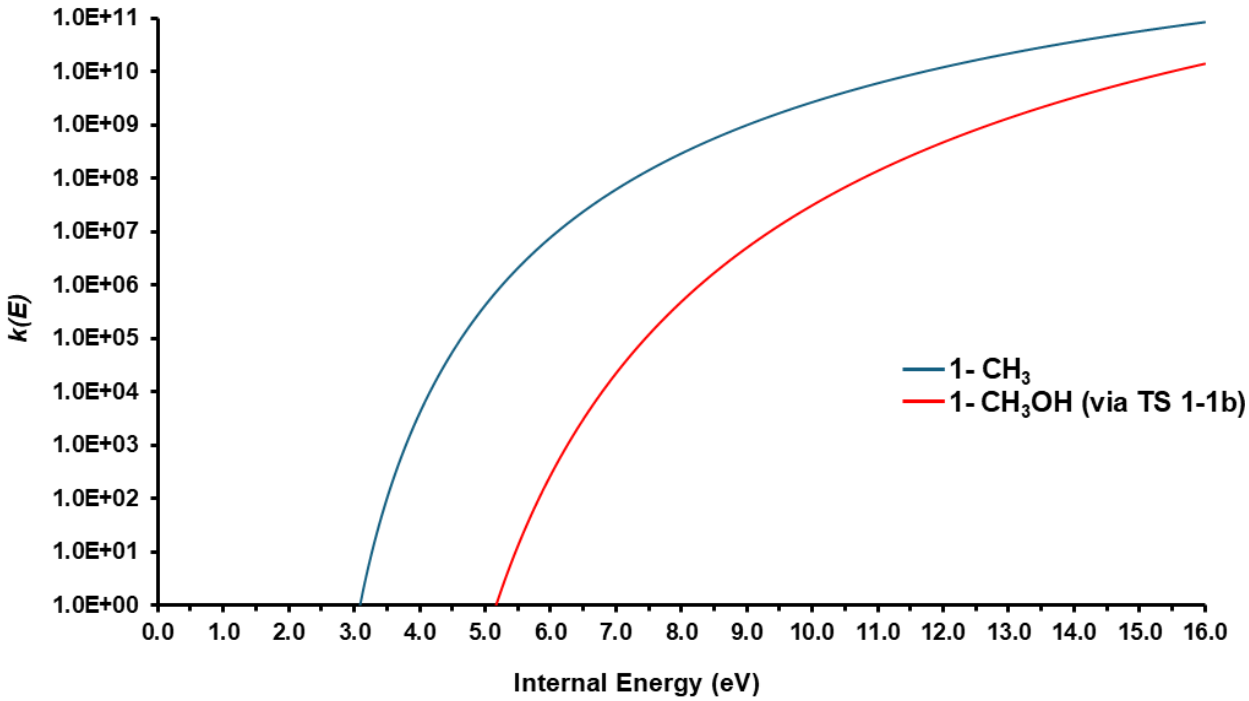

Figure 7-4. RRKM *k(E)* vs *E* curves for the losses of $^{\bullet}CH_3$ (**1a**) and CH_3OH (**1-1b**) from **1**.

7.4.3 Creosol, 2

Creosol undergoes $^{\bullet}CH_3$ loss through bond cleavage either from the methoxy group or from the ring (**Figure 7-5**). Methyl loss from the methoxy group (**2** to **2a**) is energetically favoured over loss from the ring (**2** to **2b**) by 2.19 eV.

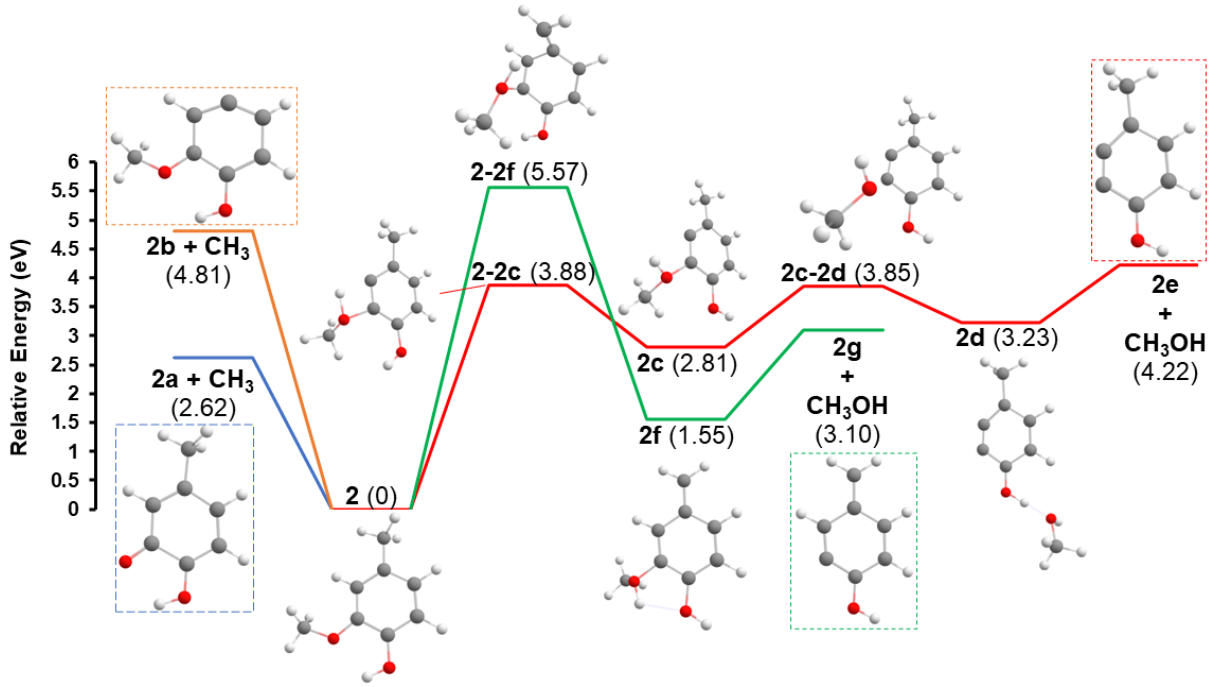

Figure 7-5. Calculated reaction pathways for $^{\bullet}CH_3$ and CH_3OH losses loss from creosol (**2**) at the CBS-QB3(sp)// B3LYP/6-311+G(d,p) level of theory. The oxygen atom is red.

The loss of methanol from **2** can proceed via two pathways. The first is analogous to the reaction in **1**, starting with a 1,3-H shift to form **2c**, followed by formation of the intermediate hydrogen-bonded complex **2d,** which then loses methanol to make **2e**. Alternatively, hydrogen transfer from the para-methyl group to the methoxy group oxygen atom leads to **2f**, followed by methanol loss to form **2g**. The 1,3-H shift pathway from **2** to form **2c** is energetically favoured over the methyl group hydrogen transfer pathway to **2f** by 1.69 eV. A comparison of the $^{\bullet}CH_3$ and CH_3OH loss *k(E)* curves are presented in **Figure 7-6**. The curves, as is, suggest that CH_3OH loss should not compete with $^{\bullet}CH_3$ loss in the metastable window for creosol. Clearly they do, which highlights the sensitivity of the RRKM calculations to the computed reaction surface. For example, employing a full CBS-QB3 treatment (not a single-point calculation) for **2a** + $^{\bullet}CH_3$ leads to a relative energy for this channel of 2.34 eV compared to the 2.62 eV in **Figure 7-5**. This uncertainty, combined with the unknown internal energy distribution of the ions generated by electron ionization could be the reason for the discrepancy between the observation and the theoretical prediction.

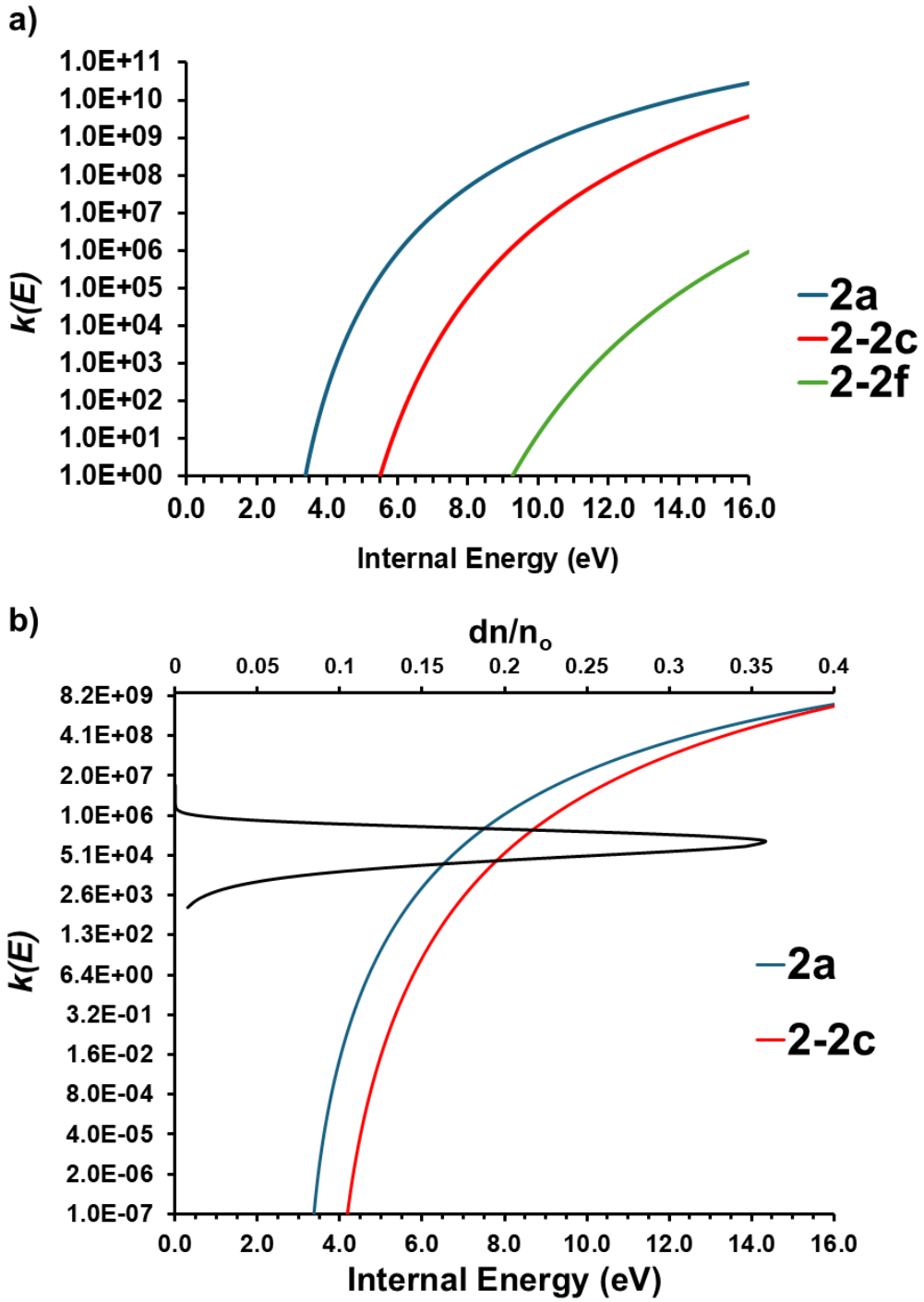

Figure 7-6. a) RRKM *k(E)* vs *E* curves for the different pathways for the dissociation of creosol radical cations, b) RRKM *k(E)* vs *E* curves with a 0.6 eV change in the relative E_0 values for the two main reactions, for comparison.

7.4.4 4-ethylguaiacol, 3

Methyl loss from **3** can occur from the methoxy (**3** to **3a**) or ethyl (**3** to **3b**) groups, with the latter being energetically favoured by 0.46 eV (**Figure 7-7**).

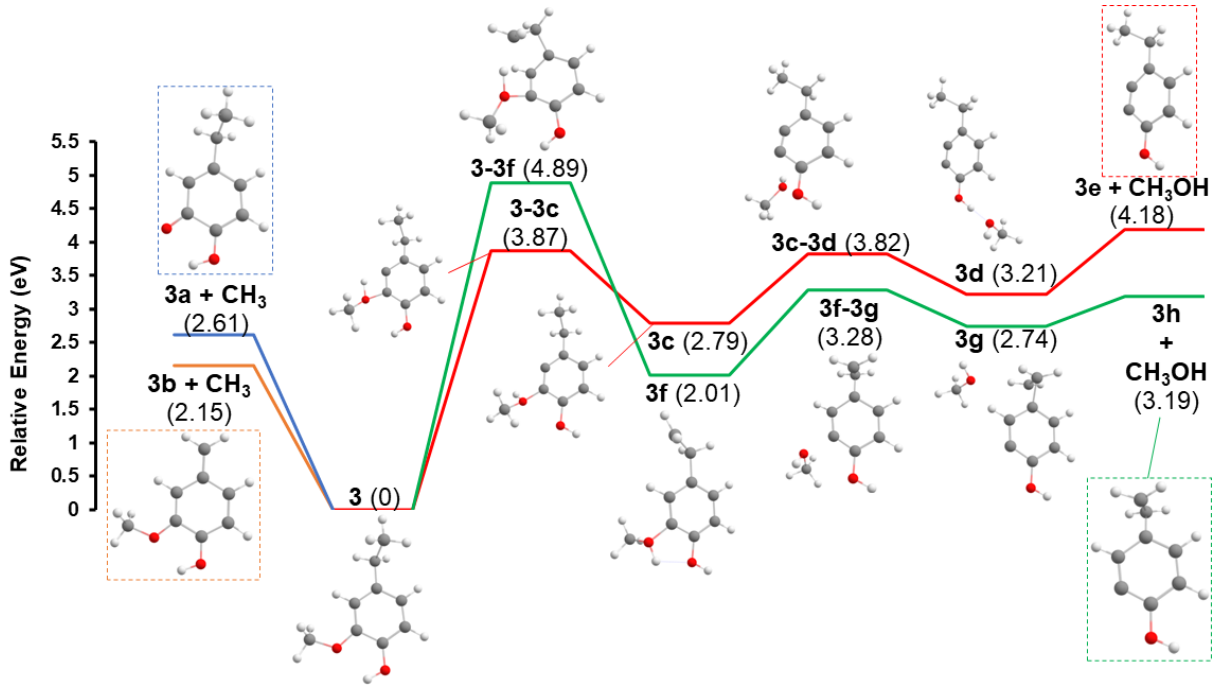

Figure 7-7. Calculated reaction pathways for $^{\bullet}CH_3$ and CH_3OH losses from 4-ethylguaiacol (**3**) at the CBS-QB3(sp)// B3LYP/6-311+G(d,p) level of theory. The oxygen atom is red.

Two different pathways are possible for the loss of methanol. The first involves a 1,3-H shift (analogous to methanol loss from **1**) to form **3c**, followed by formation of the intermediate **3d** and subsequent loss of methanol to form **3e**. The second possible pathway proceeds via a hydrogen transfer from the ethyl group to the methoxy oxygen atom, forming **3f**, which then proceeds to make the ion-molecular complex **3g**. The 1,3-H shift pathway is energetically favoured over the ethyl group hydrogen transfer pathway by 1.02 eV. A comparison of the $^{\bullet}CH_3$ and CH_3OH loss *k(E)* curves are presented in **Figure A7-1** of the Appendix.

7.4.5 4-vinylguaiacol, 4

The kinetically favoured $^{\bullet}CH_3$ loss route in **4** is via bond cleavage from the methoxy group (**4** to **4a**) which only requires 2.75 eV (**Figure 7-8**). **4** can also undergo methyl loss via two additional pathways which are initiated by a hydrogen shift either from the ring or from the hydroxy group. The ring pathway proceeds via a hydrogen transfer from the ring to the methylene group (CH_2) of the side chain leading to **4b**, followed by loss of $^{\bullet}CH_3$ to form **4c**. Conversely, a hydrogen transfer from the hydroxy group to the methylene group of the side chain leads to **4d**, which loses $^{\bullet}CH_3$ to form **4e**. Both these latter two pathways lie 3.09-3.62 eV higher in energy than cleavage of the methoxy methyl group.

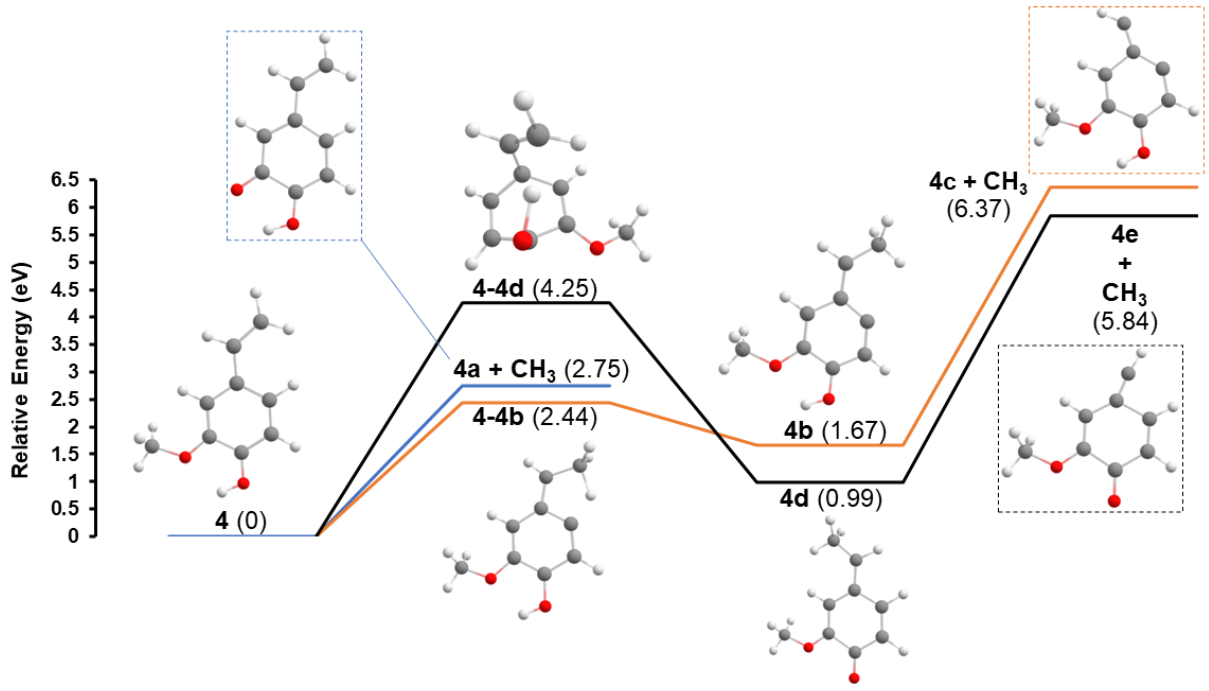

Figure 7-8. Calculated reaction pathways for $^{\bullet}$CH3 loss from 4-vinylguaiacol (**4**) at the CBS-QB3(sp)// B3LYP/6-311+G(d,p) level of theory. The oxygen atom is red.

The kinetically favoured methanol loss pathway in **4** is analogous to that seen from **2**, starting with a 1,3-H shift to form **4f**, followed by methanol cleavage to form the intermediate structure **4g** and ultimately methanol dissociation to form **4h** (red path in **Figure 7-9**). Methanol loss can also proceed via an H shift from the methylene group (CH_2) of the side chain to the methoxy oxygen atom to form **4j** (green path in **Figure 7-9**), a process requiring an additional 0.58 eV than the 1,3-

H shift pathway. A third pathway (purple path in **Figure 7-9**) involves a hydrogen transfer from the CH group of the side chain to the oxygen atom of the methoxy group to form **4m,** which lies 2.2 eV higher than the lowest energy methanol loss pathway. Methanol cleavage from **4m** leads to the intermediate structure **4n**. From **4n**, the cleaved methanol group is attracted to the hydrogen atom of the hydroxy group to form a second intermediate structure **4o**, which dissociates to form **4p**. Evident from the RRKM calculation of the competing rate constants k_{4-4f} and k_{4-4j} (**Figure A7-2** in the Appendix) is that the 1,3-H shift pathway is the favoured methanol loss pathway. Notably, this path produces the least thermodynamically-stable product ion **4h** in a kinetically-controlled reaction.

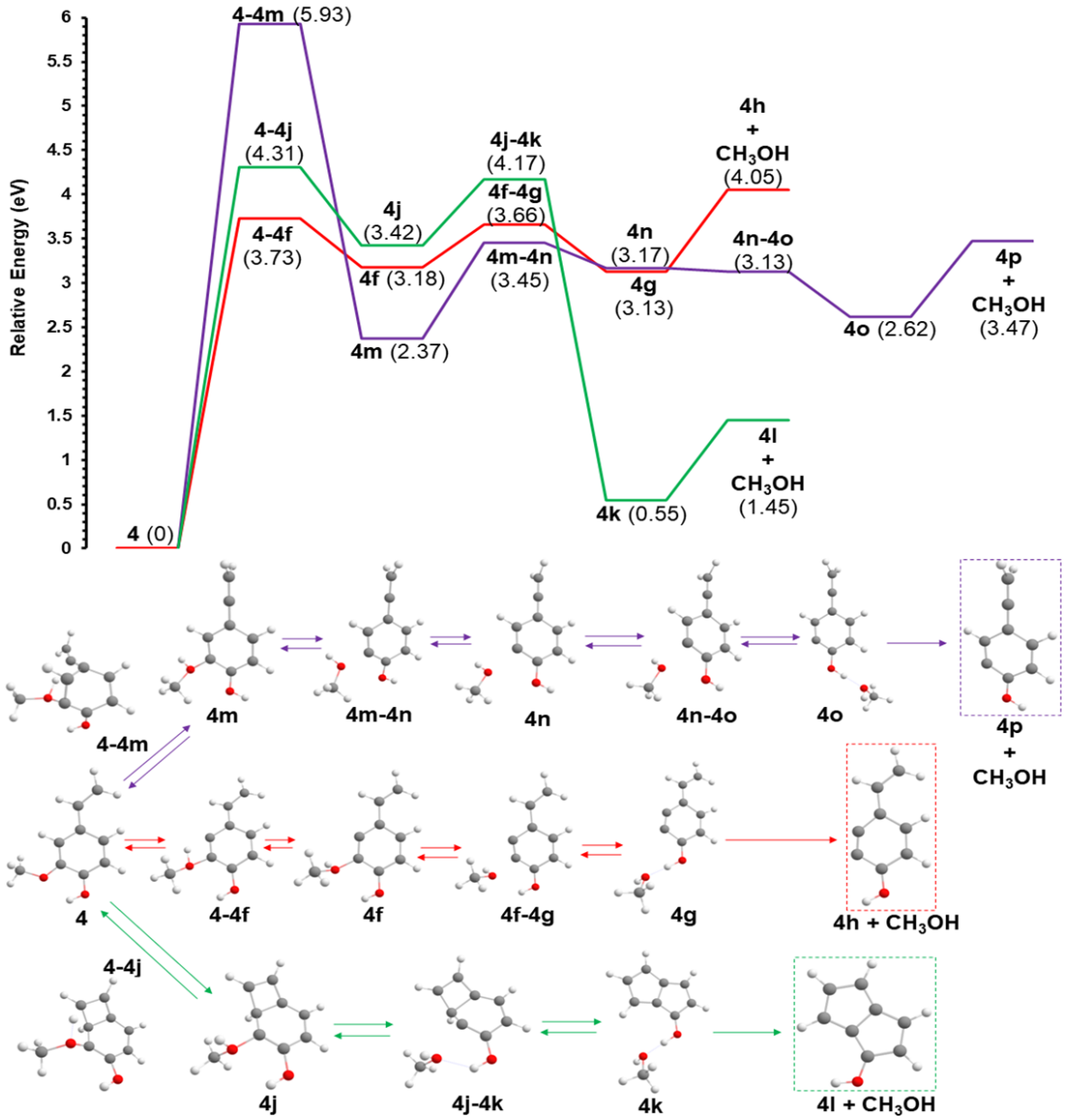

Figure 7-9. Calculated reaction pathways for CH_3OH loss from 4-vinylguaiacol (**4**) at the CBS-QB3(sp)// B3LYP/6-311+G(d,p) level of theory. The oxygen atom is red.

7.4.6 Eugenol, 5

Methyl loss in eugenol can occur via bond cleavage from the methoxy group leading to **5a** or via a hydrogen transfer from the ring to the methylene group (CH_2) of the side chain forming **5b** followed by **5c** (**Figure 7-10**). Although the initial step for the hydrogen transfer pathway is

energetically lower than the direct bond cleavage from the methoxy group pathway by 0.07 eV, RRKM calculation of the competing rate constants $k_{5\text{-}5b}$ and k_{5a} (**Figure A7-3** in the Appendix) show that these two channels can compete in the metastable internal energy window of 4-5 eV, and thus a mixture of product ions is likely formed.

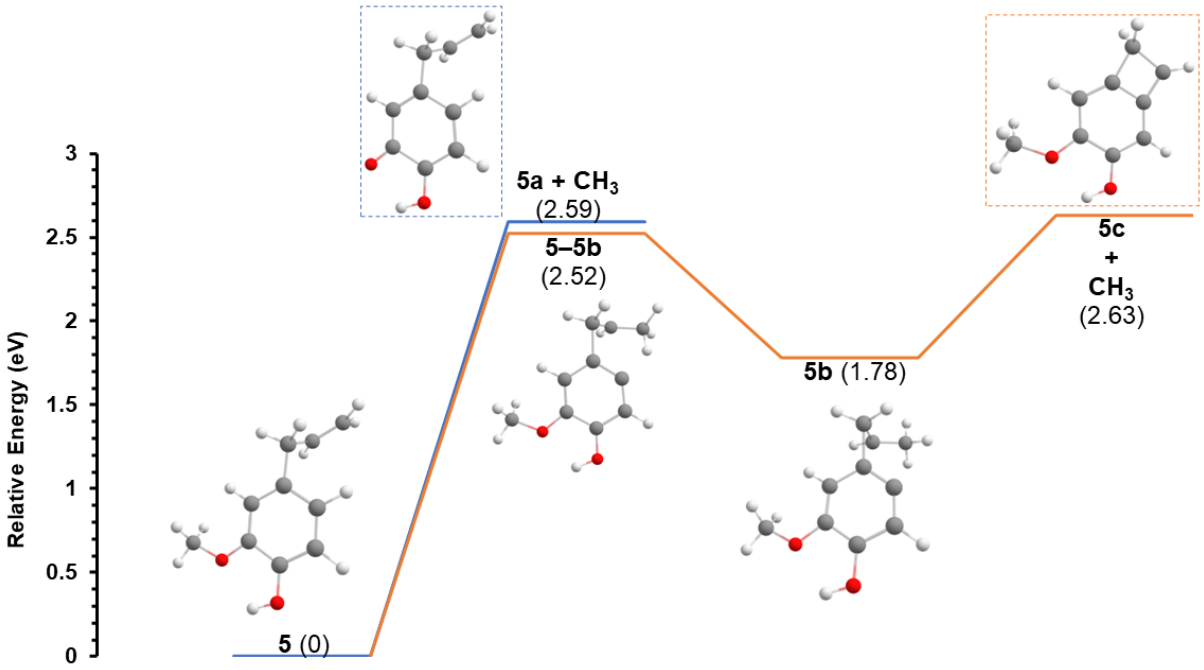

Figure 7-10. Calculated reaction pathways for CH_3 loss from eugenol (**5**) at the CBS-QB3(sp)// B3LYP/6-311+G(d,p) level of theory. The oxygen atom is red.

Four different pathways can lead to methanol loss from **5** (**Figure 7-11**). The kinetically favoured pathway is analogous to that in **2**, which starts with a 1,3-H shift to form **5g**, proceeds to **5h** and ultimately leads to **5j**. Alternatively, a hydrogen transfer from the terminal methylene group of the allyl side chain leads to **5d**, which proceeds via **5e** to **5f**. Even though the **5**→**5d** pathway is lower in energy than the **5**→**5g** pathway (1,3-H shift), RRKM calculations of the competing rate constants $k_{5\text{-}5d}$ and $k_{5\text{-}5g}$ (**Figure A7-3** in Appendix) show that the favoured methanol loss pathway is through the 1,3-H shift pathway. The third pathway proceeds via H shift from the CH of the allyl side chain forming **5k**, eventually forming **5m**. The fourth pathway involves a hydrogen transfer from the initial methylene group of the allyl side chain forming **5n**, followed by methanol loss leading to **5o**. The methanol loss peak is composite (**Figure 7-12**) which consists of a narrow

Gaussian peak with $T_{0.5}$ (half-width kinetic energy release)[223] of 60 meV, overlapping a dish-shaped peak with $T_{0.5}$ of 429 meV. This latter reaction is indicative of a process that involves a very large translational energy release, which is often associated with forming a product over a high reverse-energy barrier, making products with a wide distribution of internal and translational energies. Consequently, this suggests that methanol dissociation may also proceed via the fourth pathway (**5**-**5n**) as well, given that this pathway leads to a lower energy product (**5o**) via a high reverse-energy barrier compared to the kinetically favoured pathway (**5**-**5g**).

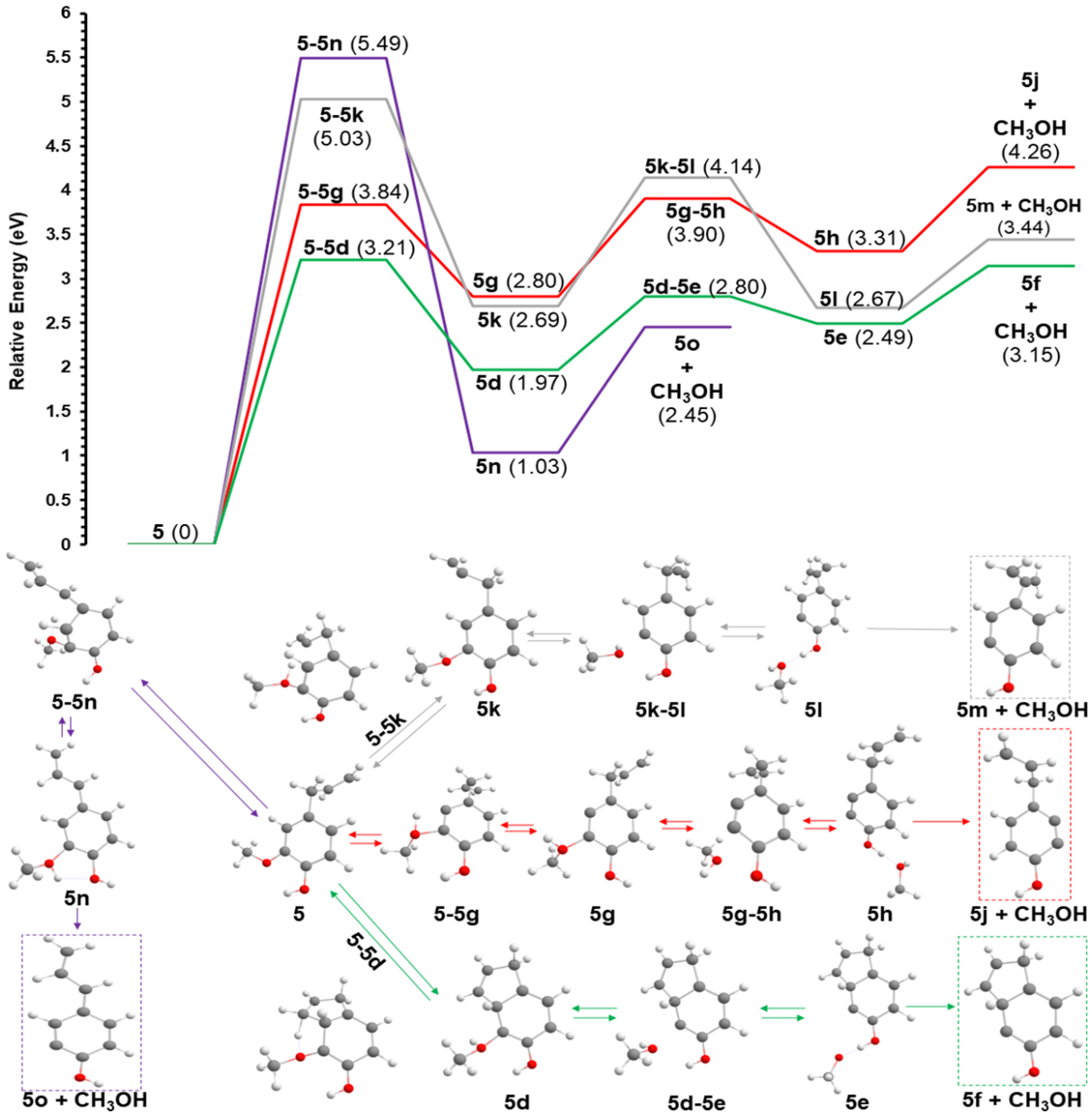

Figure 7-11. Calculated reaction pathways for CH_3OH loss from eugenol (**5**) at the CBS-QB3(sp)// B3LYP/6-311+G(d,p) level of theory. The oxygen atom is red.

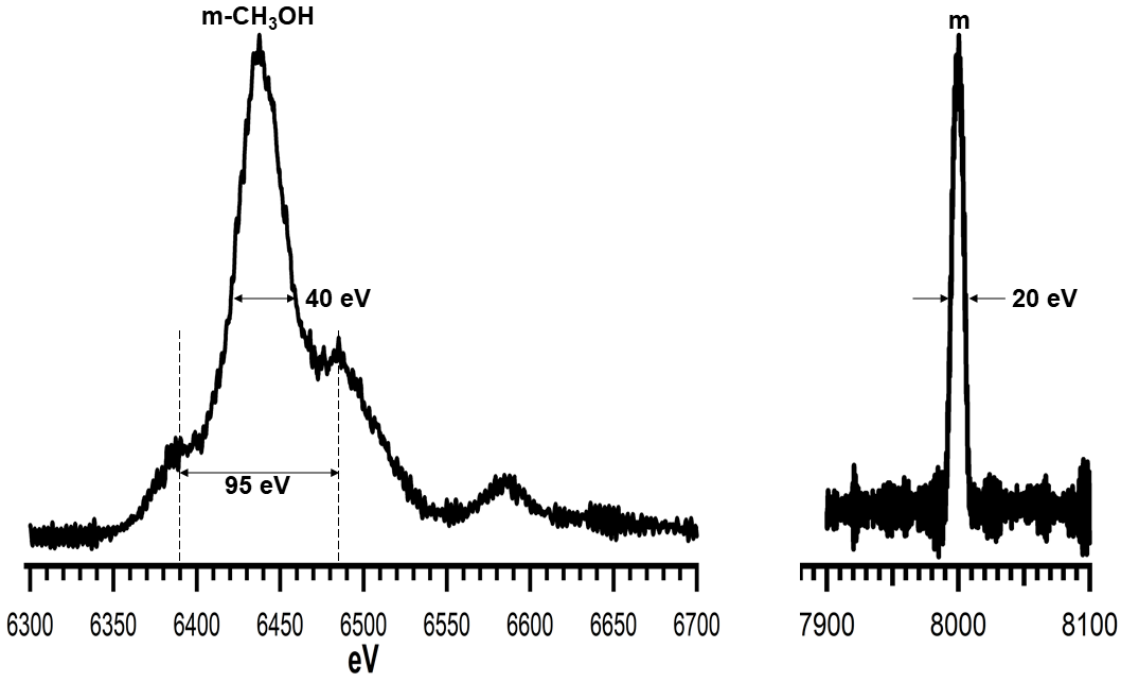

Figure 7-12. The presence of a narrow Gaussian peak overlapping a dish-shaped peak for the dissociation of eugenol radical cation is indicative of a large translational energy release. The main beam (precursor ion) profile is shown to the right for comparison. The reported peak widths were converted to kinetic energy release values calculated from the half-height widths, $T_{0.5}$, according to the following equation:

$$T_h = \frac{(m_1^2)(W_h^2 - W_m^2)}{16 m_2 m_3 V_{acc}}$$

Where h is the height, expressed as a fraction of the total height (h_0) at which the peak width (W_h) is measured, W_m is the corresponding width of the main ion beam, and m_1, m_2, m_3 are the masses of the precursor ion and reaction products, respectively, and V_{acc} is the translational kinetic energy (8 kV). [223]

7.4.7 Vanillin, 6

The loss of CO from **6** can occur via two pathways (**Figure 7-13**). The kinetically favoured pathway proceeds via a 1,2-H shift from the formyl group to form **6a**, followed by CO dissociation leading to **6b**. Conversely, hydrogen transfer from the phenolic hydrogen of **6** to the formyl oxygen leads to **6c**, followed by a ring-pinching reaction that extrudes CO to form **6d**, and subsequent CO

loss leads to **6e**. This reaction is reminiscent of the loss of CO from protonated vanillin[225]. The 1,2-H shift pathway from **6** to form **6a** lies 1.56 eV lower in energy than the phenolic hydrogen transfer pathway to form **6c**. While this is the only reaction observed, we have also calculated the pathways for methyl and methanol losses to compare with the other ions in this study. $^{\bullet}CH_3$ loss from **6** proceeds via a simple bond cleavage to form **6f,** and methanol loss is analogous to that seen from **2**, starting with a 1,3-H shift to form **6g,** which leads to the ion-molecule complex **6h** and finally methanol cleavage to form **6j.** In the 4-5 eV internal energy range, the rate constant for CO loss is over 2 orders of magnitude greater and thus only this channel is experimentally observed (**Figure 7-14**).

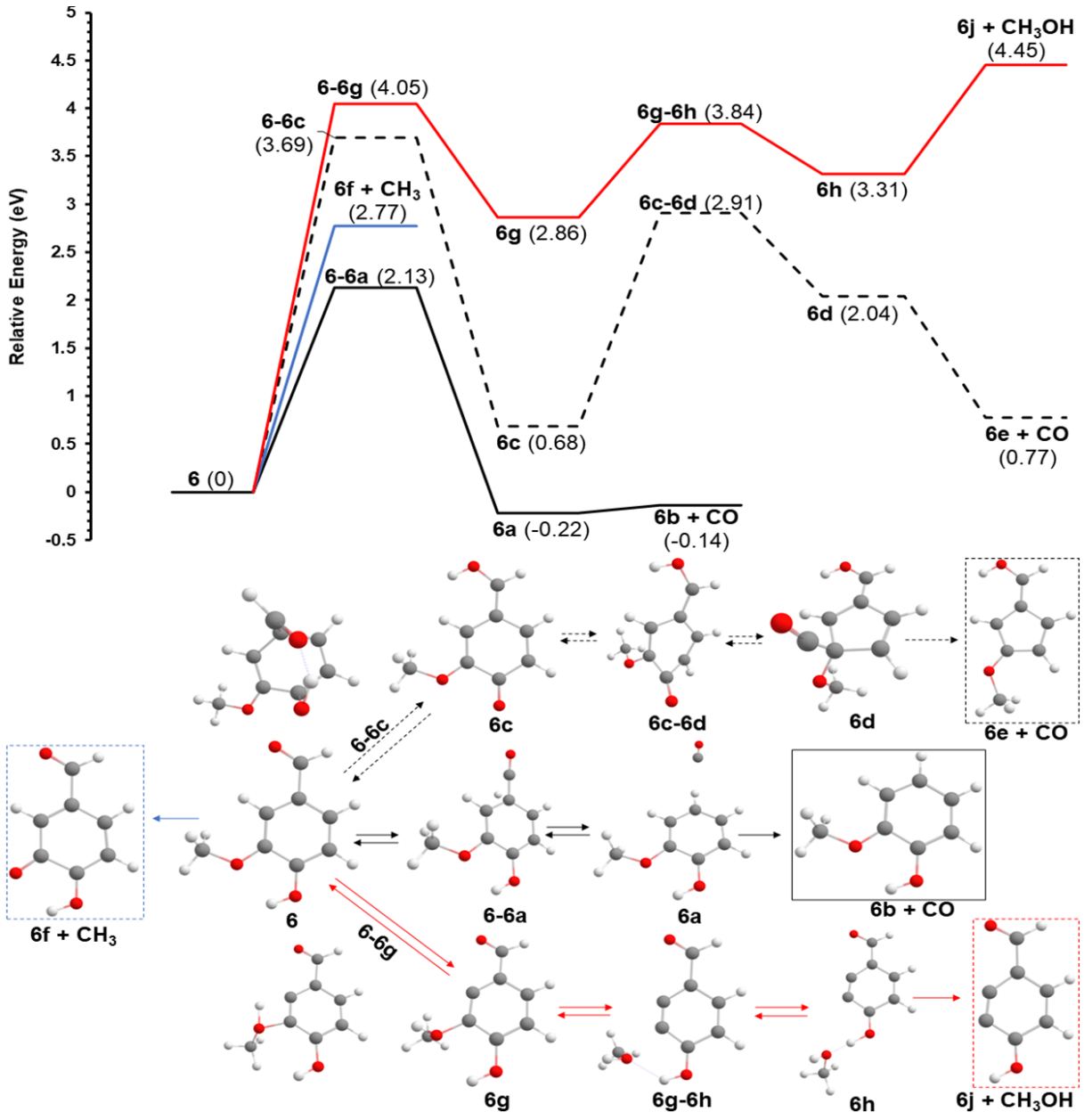

Figure 7-13. Calculated reaction pathways for CO and CH_3 and CH_3OH losses from vanillin (**6**) at the CBS-QB3(sp)// B3LYP/6-311+G(d,p) level of theory. The oxygen atom is red.

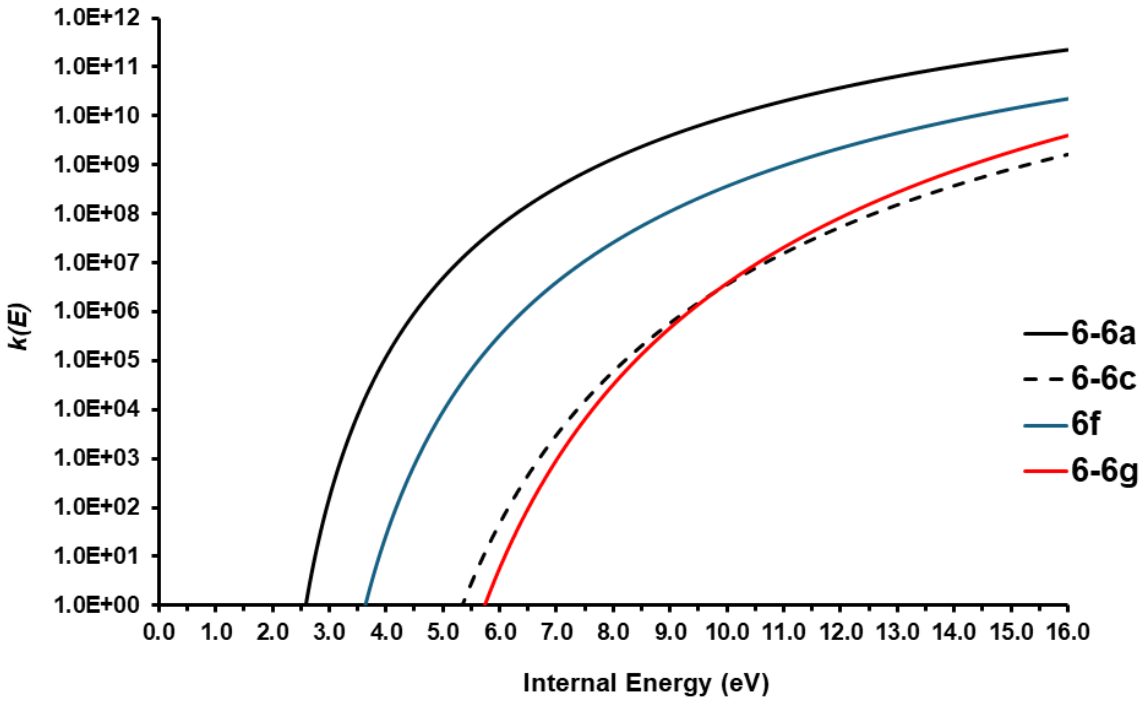

Figure 7-14. Illustrative RRKM *k(E)* vs *E* curves for the different pathways for the dissociation of vanillin.

7.5 Conclusion

The unimolecular reactions of the radical cations of guaiacol and its derivatives were studied using tandem mass spectrometry and computational chemistry. Besides vanillin, all the ions studied exhibited the loss of a methyl radical ($^{\bullet}CH_3$). For guaiacol (**1**), creosol (**2**) and 4-vinylguaiacol (**4**), the favoured $^{\bullet}CH_3$ loss pathway is via bond cleavage from the methoxy group. $^{\bullet}CH_3$ dissociation from the ethyl group is kinetically favoured over dissociation from the methoxy group for 4-ethylguaiacol (**3**). Two energetically very similar pathways are observed (bond cleavage from the methoxy group and hydrogen transfer) for eugenol (**5**), and RRKM calculations revealed that both pathways are equally possible, likely resulting in a mixture of product ions. For all ions (**2**, **3** and **5**) that exhibited methanol loss, the favoured methyl radical pathways are energetically lower than that of the favoured methanol loss pathways, and this is also evident from the RRKM calculation of the competing rate constants. On the other hand, vanillin radical cation exhibits a different dissociation pathway which proceeds via the loss of CO.

Methyl loss from the guaiacol family of radical cations is consistent with the thermal degradation of neutral guaiacol observed by Scheer et al.[77] and Asmadi et al.[221]. Therefore, in accordance with the results obtained for the radical cations of the derivatives, this leads us to speculate that the thermal degradation of neutral creosol, 4-ethylguaiacol, 4-vinylguaiacol or eugenol might lead to the formation of methanol as well. Conversely, vanillin radical cation dissociation is initiated via CO loss, while thermal degradation of vanillin as studied by Wu et al.[222] revealed the occurrence of CO loss only after the initial loss of a methyl radical. The results are suggestive that there may be similarities between the decomposition of neutral and radical cation guaiacol derivatives that could be explored further.

7.6 Appendix

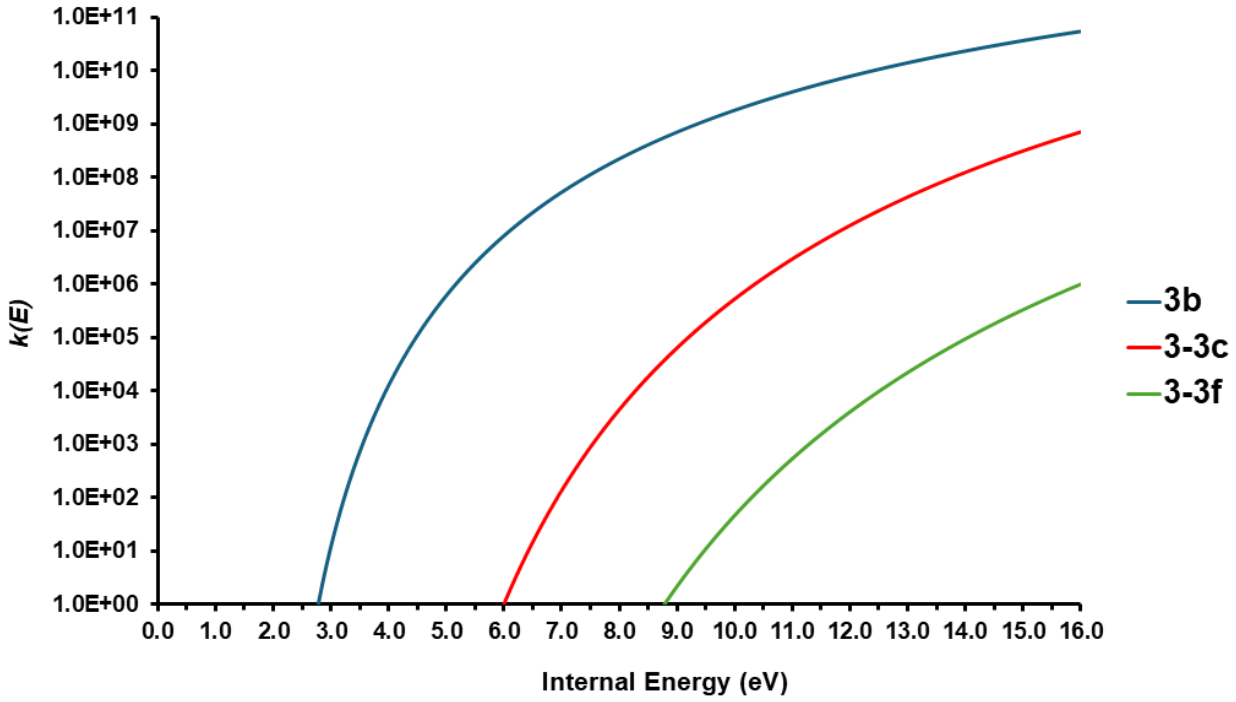

Figure A7-1. RRKM *k(E)* vs *E* curves for the different pathways for the dissociation of 4-ethylguaiacol radical cations.

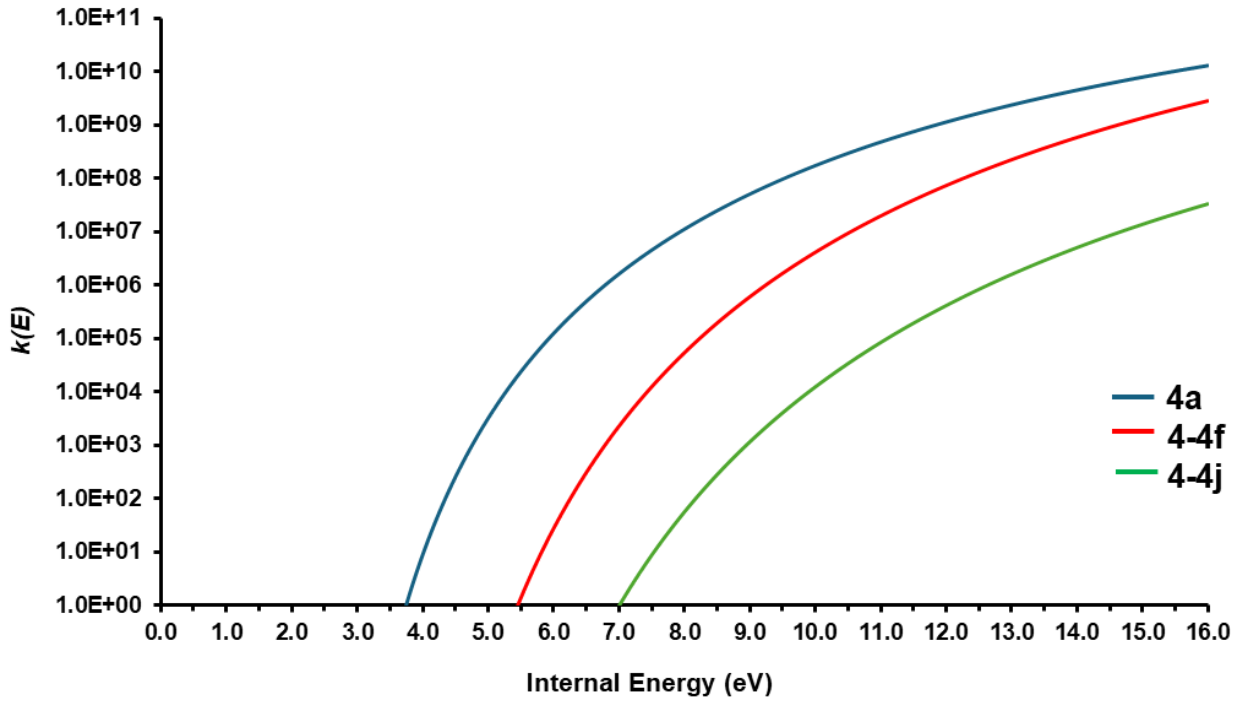

Figure A7-2. RRKM *k(E)* vs *E* curves for the different pathways for the dissociation of 4-vinylguaiacol radical cations.

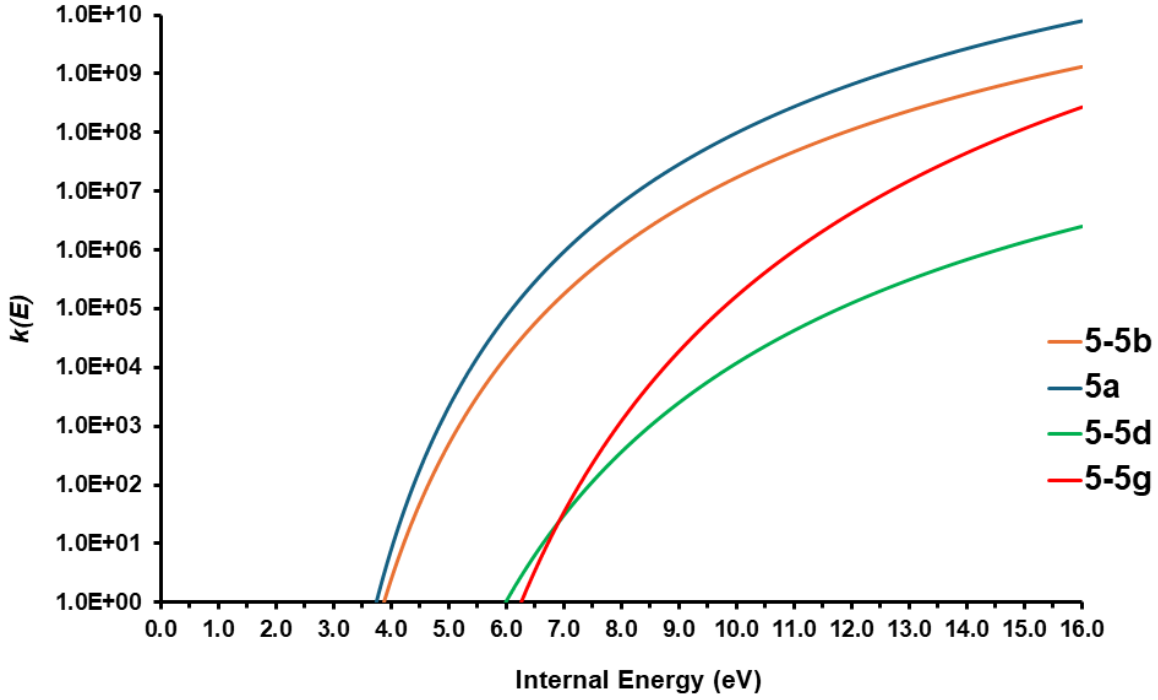

Figure A7-3. RRKM *k(E)* vs *E* curves for the different pathways for the dissociation of eugenol radical cations.

Chapter 8: Bridging Experiment and Computation: Unveiling Novel Dissociation Pathways of 4-Ethylguaiacol and Eugenol Radical Cations Using iPEPICO Spectroscopy

The contents of Chapter 8 have been published as: Gondarry, S.; Bodi, A.; Mayer, P. M. Bridging Experiment and Computation: Unveiling Novel Dissociation Pathways of 4-Ethylguaiacol and Eugenol Radical Cations Using IPEPICO Spectroscopy. *J. Phys. Chem. A* 2026, *130* (3), 661–669. https://doi.org/10.1021/acs.jpca.5c07784.

Author contributions:
Sandesh Gondarry: Writing – original draft, experimental data processing for the iPEPICO data, DFT calculations.
Paul M. Mayer: Conceptualization, methodology, supervision, experimental work at Swiss Light Source (SLS), writing – review & editing.
Andras Bodi: assisted experimental work at SLS, writing – review & editing.

8.1 Introduction

Lignin, a key structural polymer in plant biomass, represents a significant source of renewable aromatic compounds.[160] Lignin depolymerization, often achieved through thermal or catalytic processes, yields a variety of phenolic compounds, including guaiacol derivatives such as 4-ethylguaiacol and eugenol.[52,210,220,226] While the fragmentation pathways of these derivatives are essential for understanding their stability and reactivity, experimental studies on their radical cations, which form the basis for their analytical detection by mass spectrometry, remain limited.[227–232] Universal, multiplexed, selective, and sensitive analytical tools, such as imaging photoelectron photoion coincidence (iPEPICO) spectroscopy,[233] are needed to identify trace intermediates and products in pyrolysis,[234] catalytic pyrolysis[235] or catalytic conversion[236] studies. For instance, the previously postulated quinone methide intermediates in catalytic lignin moiety conversion[237] could recently be detected experimentally thanks to iPEPICO spectroscopy.[235] Besides reference photoion mass-selected threshold photoelectron spectra,[238] iPEPICO also offers quantitative data on dissociative photoionization reaction energy thresholds. The former is

routinely used together with Franck–Condon simulations to identify even trace components of reaction mixtures, while the latter can be used to assign photoionization mass spectrum peaks of fragment ions to their parent. The present study investigates the unimolecular dissociation of 4-ethylguaiacol and eugenol radical cations using iPEPICO spectroscopy, revealing novel fragmentation pathways for methyl loss in both and for methanol loss in the eugenol radical cation.

In previous work from our laboratory, the ion chemistry of the 4-ethylguaiacol and eugenol radical cations was explored with mass-analyzed ion kinetic energy (MIKE) spectrometry and density functional theory and composite method calculations (refer to chapter 7).[199] The 4-ethylguaiacol radical cation was found to be metastable at low energies and exhibited a single fragmentation reaction, the loss of $^{\bullet}CH_3$, which, when resulting from homolytic bond breaking in the ethyl group, was computed to have an energy threshold of 2.15 eV at the CBS-QB3(sp)//B3LYP/6-311+G(d,p) level of theory; the barrier to $^{\bullet}CH_3$ loss from the methoxy group was calculated to be 0.46 eV higher.[199] Eugenol radical cations were found to dissociate by two competing reactions, loss of $^{\bullet}CH_3$ or CH_3OH. Methyl radical loss from the methoxy group was calculated to have an energy requirement of 2.59 eV. Alternatively, H-transfer from the aromatic ring to the sidechain vinyl group over a 2.52 eV transition state resulted in methyl loss with a product energy of 2.63 eV. Four methanol loss routes were evaluated, and the most favourable involved H-transfer from the vinyl group to the methoxy-oxygen, forming a bicyclic ring system and a methanol molecule hydrogen-bonded to the hydroxy group, prior to methanol loss. The highest energy transition state for this reaction was calculated to be 3.21 eV above the cation minimum.[199]

However, MIKE spectrometry is not an energy-resolved technique. Rather, precursor ions generated by electron ionization, having a broad and ill-defined internal energy distribution, are momentum selected and those dissociating in a certain, instrument-defined time window are studied. There is no quantitative way to directly link the experimental observations with the derived calculated reaction energetics. We decided to revisit the unimolecular dissociation of these two radical cations, this time with iPEPICO spectroscopy, with a view to obtaining experimental confirmation of the proposed reaction mechanisms. Our results highlight the necessity of integrating quantitative experimental data with computational approaches to uncover new reaction

pathways and demonstrate that iPEPICO spectroscopy remains indispensable in elucidating complex unimolecular dissociation mechanisms.

8.2 Experimental Procedures

4-Ethylguaiacol and eugenol (both >98%) were purchased from Sigma-Aldrich, Oakville, Ontario, CA, and used without further purification. The experiment involved the previously described double imaging CRF-PEPICO endstation at the VUV beamline of the Swiss Light Source (Paul Scherrer Institute).[100,175] Synchrotron radiation from a bending magnet was collimated and monochromatized using a 600 lines/mm laminar grating before being focused onto a 200 μm exit slit within a differentially pumped rare gas filter.[239] The photon beam achieved a resolution of 2–4 meV, depending on the photon energy, which was calibrated by measuring the 11 s′–14 s′ argon autoionization lines in first and second order.[240] 4-Ethylguaiacol and eugenol were soaked onto glass wool and placed inside a molecular beam source with ca. 4 mm internal diameter and an internal 200 μm orifice, followed by a 1 mm internal diameter tube with an open aperture to vacuum. The temperature of the tube was raised to 350 K to increase the vapour pressure. Argon carrier gas was passed over the sample and directed through a 2 mm diameter skimmer into the interaction region of the instrument. Due to the smooth pressure drop in the source and limited collisional cooling in vacuum, the source can be considered as effusive[241] and was used primarily to ensure comparable experimental conditions to in-vacuum flash pyrolysis experiments during the same beamtime. Photoions and photoelectrons were extracted by a continuous, weak, 218 V cm^{-1} electric field. Electrons were velocity map imaged on a RoentDek delay line detector, where their time and position were captured, and the corresponding photoions were measured in delayed coincidence using a time-of-flight mass spectrometer. The low draw-out potential enables ions to dissociate on the microsecond time scale while being accelerated, leading to asymmetric time-of-flight peaks for product ions that can be modelled to determine unimolecular decay rate constants in the $10^3 < k / s^{-1} < 10^7$ range as a function of photon energy. Threshold electrons were mapped at the center of the imaging detector, while non-zero kinetic energy ("hot") electrons were detected off-axis based on their momentum in the detection plane. Hot electrons without an off-axis momentum component are also imaged in the centre. The resulting hot electron contamination of the centre signal is represented based on a ring-shaped region around the centre spot and subtracted

from the centre signal to obtain the corrected threshold signal.[102] The threshold photoelectron spectra (TPES) were recorded from 7.5 to 10.5 eV with 0.005 eV step size and 30 s accumulation time for 4-ethylguaiacol and from 7.6 to 8 eV (0.007 eV step size, 30 s accumulation time), then from 8 to 9.6 eV (15 s accumulation time), and from 9.6 to 10 eV (0.02 eV step size and 60 s accumulation time) for eugenol. The breakdown diagram was recorded from 10.5 to 12.5 eV (0.1 eV step size and 300 s accumulation time) for 4-ethylguaiacol, and from 10.4 to 12.7 eV (0.1 eV step size and 300 s accumulation time) for eugenol.

8.3 Computational Procedures

Geometry optimizations for minima and transition states and harmonic vibrational frequency calculations were performed at the B3LYP/6-311+G(d,p)[121,122] level of density functional theory (DFT) employing the GAUSSIAN 16 suite of programs.[112] Transition states were confirmed to connect the intended minima by the intrinsic reaction coordinate method. Excited-state geometry optimizations were carried out using time-dependent density functional theory (TD-DFT) with the same functional and basis set. CBS-QB3[129] single-point energy calculations at the B3LYP/6-311+G(d,p) geometries yielded accurate reaction energetics as well as adiabatic and vertical ionization energies (IE_a/IE_v). For simplicity, we will refer to these energies as CBS-QB3* to distinguish them from the standard CBS-QB3 composite method, with the only difference being that the latter uses a slightly smaller basis set without diffuse functions on 2nd row atoms. Franck–Condon simulations in the double harmonic approximation but beyond the parallel approximation, *i.e.,* including the Duschinsky rotations, were carried out in GAUSSIAN 16 using unscaled frequencies to model and interpret the threshold photoelectron spectral structure. The Outer-Valence Green's function (OVGF) method, combined with the cc-pVTZ basis set, was used to calculate vertical outer valence orbital ionization energies.

Breakdown curves and threshold ionization time-of-flight distributions were fitted using the minimalPEPICO program.[107] Based on physical parameters of the ion optics in the iPEPICO experiment, the internal energy distribution of the parent ion (obtained by shifting the thermal energy distribution of the neutral by the photon energy less the adiabatic ionization energy), and the statistical rate constants for each reaction, the program calculates theoretical branching ratios

and time-of-flight distributions, which are compared to experimental data. Rice–Ramsperger–Kassel–Marcus (RRKM) theory was applied to calculate $k(E)$ according to the equation[108,157]

$$k(E) = \frac{\sigma N^{\ddagger}(E - E_0)}{h\rho(E)}$$

where σ represents the reaction degeneracy, h is Planck's constant, $N^{\ddagger}(E - E_0)$ is the number of internal states for the transition state at internal energy $(E - E_0)$ and $\rho(E)$ is the density of states for the reactant ion at internal energy (E) as calculated via the Beyer and Swinehart direct count algorithm.[109] B3LYP/6-311+G(d,p) calculated harmonic vibrational frequencies were employed in the direct count algorithm to obtain sums and densities of vibrational states for the RRKM calculation. Due to the large kinetic shifts, *i.e.,* fragmentation requiring more than 2 eV excess energy to become observable on the experimental time scale, the rate curves had to be extrapolated from a relatively flat region to the onset E_0. Together with the use of harmonic state functions at high internal energies and the treatment of multi-step fragmentation as an effective single-well dissociation, the derived E_0 values for the major channels are expected to carry an uncertainty of 0.2–0.3 eV. Accordingly, we approximated the transition state vibrational frequencies either by the highest-lying transition state frequencies or, in the absence of such, by those of the precursor ion removing one mode to represent the reaction coordinate, and scaled the lowest five modes to adjust the effective activation entropy, $\Delta^{\ddagger}S$, to reproduce the experimental data.

8.4 Results and Discussion

8.4.1 4-Ethylguaiacol

The threshold photoelectron spectrum of 4-ethylguaiacol is shown in **Figure 8-1** together with the CBS-QB3* calculated ionization energy and the OVGF vertical ionization energies to the ground and first excited electronic states of the cation. The molecular orbitals of the neutral, ionization from which corresponds to these states, are also illustrated. The experimental ionization energy, 7.65 ± 0.05 eV, has been determined by matching the experimental spectrum to the simulated Franck–Condon profile of the ground-state band at the ionization onset in **Figure 8-1**. The

calculated CBS-QB3* adiabatic IE is slightly higher at 7.73 eV. OVGF calculations are in agreement with the band structure of the TPES. They underestimate the ground state experimental vertical ionization energy IE_v (7.87 eV), by about 0.28 eV (while the computed IE_v is 7.78 eV at the CBS-QB3* level). Molecular orbital **30**, responsible for ionization into this state, corresponds to a π-orbital of the benzene ring that also includes the oxygen lone pair. The OVGF IE_v for ionization from orbital **29** is in reasonable agreement with the experimental data, and MO (molecular orbital) **29** is also π in character. Overlaid in blue and green are Franck–Condon (FC) simulations of the 4-ethylguaiacol ground and first excited states, respectively, at 350 K, which agree very well with the experimental TPES. Overall, the experimental data are critical for determining the ionization energy values for the ground and excited states; together with the FC-simulation, it allows for the origin transition to be located in the spectrum, illuminating the adiabatic IEs.

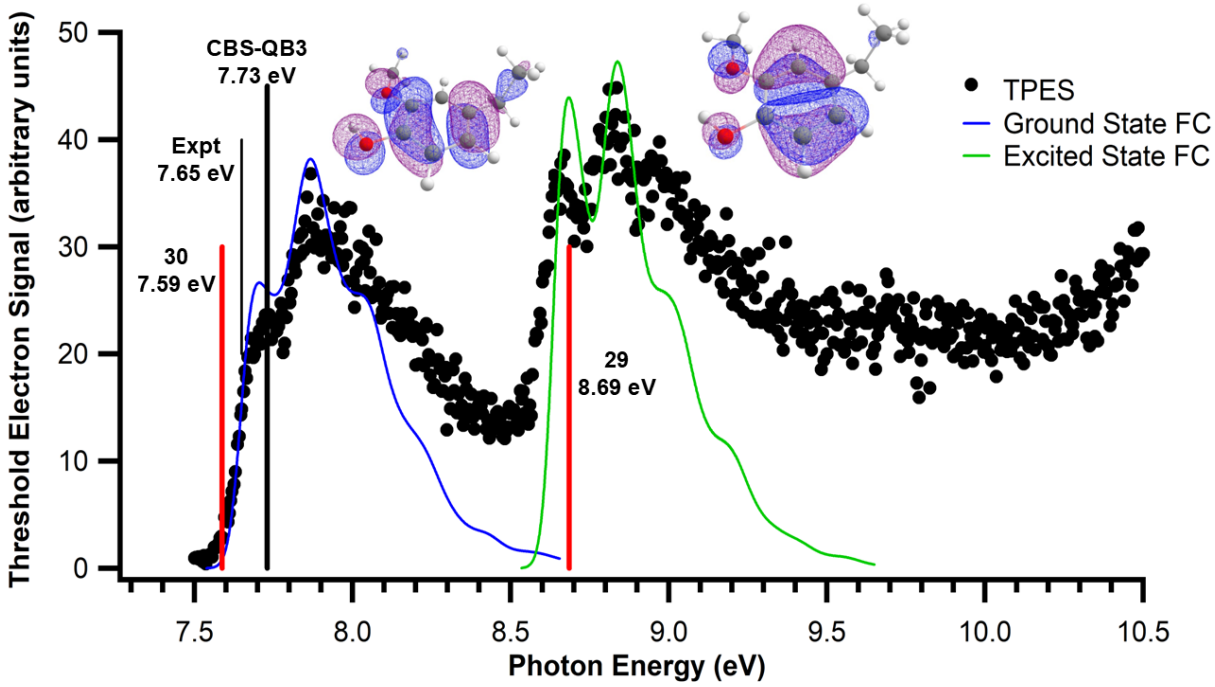

Figure 8-1. TPES for 4-ethylguaiacol. Red vertical lines correspond to OVGF calculated vertical ionization energies (molecular orbital numbers from the OVGF calculation correspond to the outer valence MOs). The blue and green lines represent the 350 K FC simulations of the ground state and first excited state, respectively. Both vibrational line spectra were convolved with a Gaussian with a full width at half maximum (FWHM) of 0.075 eV.

The breakdown diagram of 4-ethylguaiacol (**Figure 8-2a**) and selected time-of-flight distributions with asymmetric *m*/*z* 137 peak shapes (**Figure 8-2b)**, indicative of a metastable parent ion, were modelled using statistical theory. Similar to previous results,[199] the primary dissociation channel of the 4-ethylguaiacol radical cation was found to be the loss of $^{\bullet}CH_3$, although a weak methanol-loss signal was also observed here. The minuscule methanol loss branching ratio means that its appearance energy and activation entropy are poorly constrained experimentally. The measured 4-ethylguaiacol ionization energy of 7.65 eV was used to convert photon energy to ion internal energy for the RRKM analysis. The reaction leading to $^{\bullet}CH_3$ loss was modelled to have an E_0 of 1.88 eV, assuming a single rate-determining transition state. For a complex reaction mechanism with multiple transition states, this value best represents the rate-determining transition state, i.e., the minimum reaction energy requirement. From our previous work,[199] we found that direct methyl loss can occur from the methoxy group or from the ethyl group, at energies of 2.61 and 2.15 eV, respectively (**Figure 8-3**). Even the lower one of these is too high compared to the RRKM model result of 1.88 eV. This discrepancy between the previously calculated and the current E_0 values led to the search for and the discovery of a new reaction pathway for $^{\bullet}CH_3$ loss in the 4-ethylguaiacol radical cation (**Figure 8-3**).

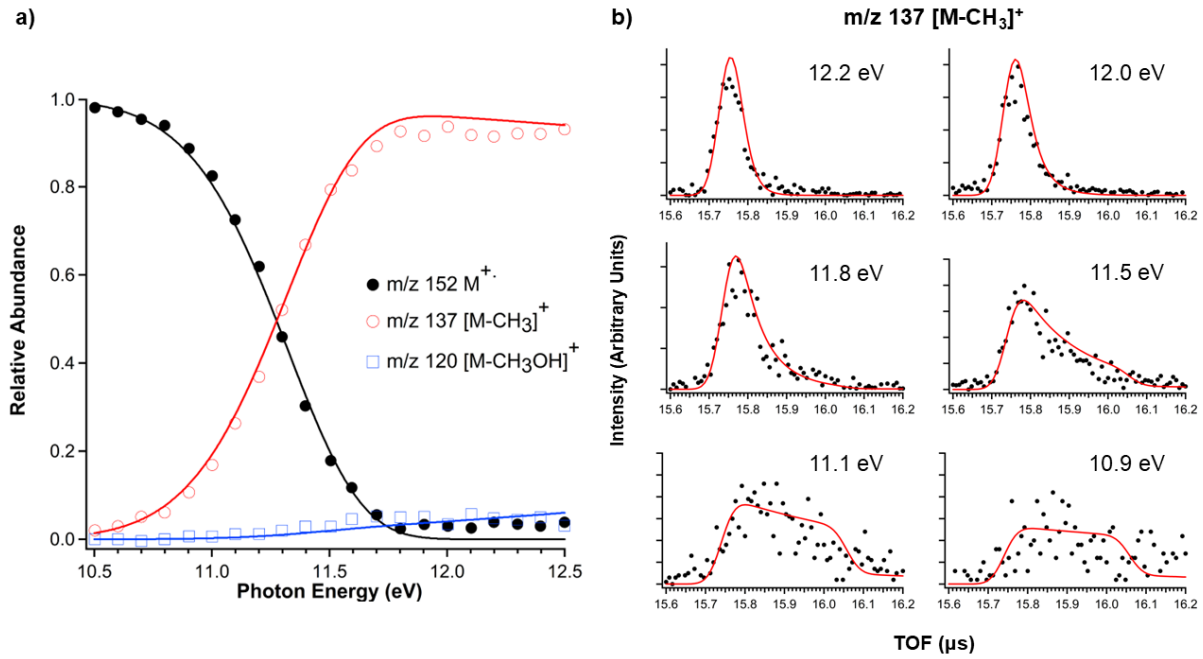

Figure 8-2. (a) Experimental 4-ethylguaiacol [$M^{+\bullet}$] breakdown diagram (points) with RRKM fit (solid lines). (b) Representative *m*/*z* 137 time-of-flight distributions (points) and the RRKM fit (solid lines) as a function of photon energy.

The reaction proceeds via hydrogen transfer from the methylene group to the vicinal ring carbon atom of the 4-ethylguaiacol cation, forming **INT1**, followed by a 1,2-H shift leading to **INT2**. From **INT2**, a subsequent 1,2-H shift proceeds to **INT3**, or C–C bond breaking leads to methyl loss and the formation of the fragment ion **PDT1**. The B3LYP threshold to **PDT1** agrees with the RRKM E_0 value to within 0.05 eV. However, the CBS-QB3* result is around 0.39 eV higher, leading to the formation of **INT3** from **INT2** being energetically more favourable, albeit over a tighter transition state, than releasing a methyl radical and forming **PDT1**. From **INT3**, methyl loss leads to the second methyl loss product, **PDT2**, which is the energetically favoured methyl-loss product. Alternatively, hydrogen transfer from the hydroxy group to the methoxy oxygen atom forms **INT4**, which subsequently loses methanol to yield product **PDT3**. Here also, the B3LYP-computed thresholds are lower than CBS-QB3*, while the **TS4** energy is lower than **PDT3** according to CBS-QB3* calculations. Considering the **TS2** and **TS3** critical frequencies of 1102 and 1025 *i*cm^{-1}, respectively, together with the fact that quantum tunnelling can shift the apparent onset below even broader H-loss barriers by ca. 0.1 eV,[242] the most likely conclusion is that **PDT2**

is the primary low-energy methyl loss fragment ion of 4-ethylguaiacol, and, at higher energies, late branching over **TS4** is responsible for the methanol-loss channel leading to **PDT3**.

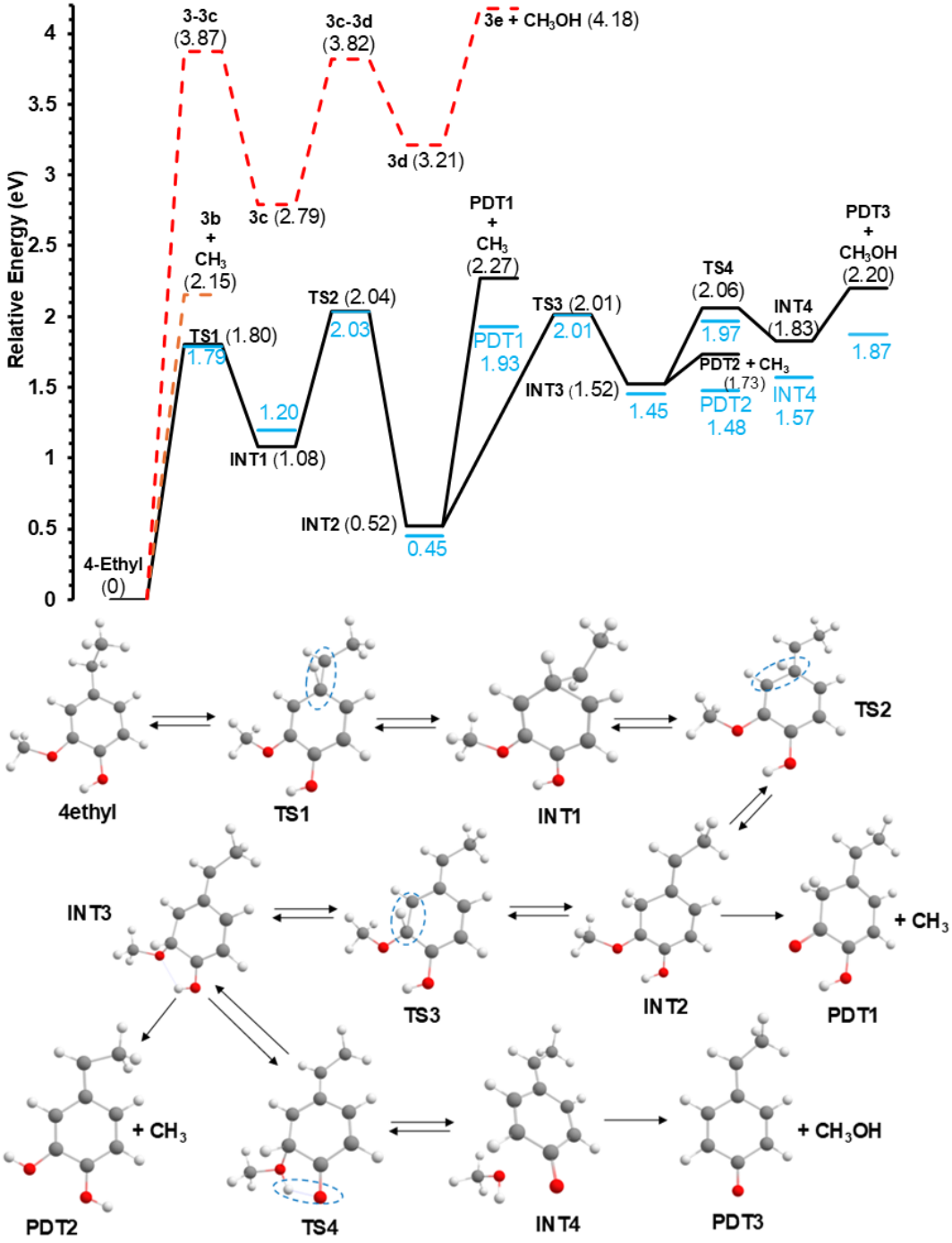

Figure 8-3. Calculated reaction pathways for CH_3 and CH_3OH losses from 4-ethylguaiacol at B3LYP/6-311+G(d,p) (solid blue lines) and CBS-QB3* (solid black line) level of theory. Oxygen atoms are red, and the blue dashed line highlights the hydrogen migration steps. For comparison,

the reaction pathways for $^{\bullet}CH_3$ and CH_3OH losses from 4-ethylguaiacol at CBS-QB3* level of theory as reported in our previous study[199] are overlaid as orange and red dashed lines. The nomenclature is the same as in ref. 199.[199] A schematic representation of the reactions can be found in **Figure A8-1** in the Appendix.

8.4.2 Eugenol

The TPES of eugenol is shown in **Figure 8-4** along with the CBS-QB3* calculated ionization energy and the OVGF results for vertical ionization to the first three electronic states of the cation. The neutral molecular orbitals, ionization from which corresponds to these states, are also illustrated. The calculated CBS-QB3* adiabatic IE at 7.72 eV is close to the experimentally derived ionization energy of 7.67 eV ± 0.05 eV, based on matching the onset of the simulated Franck–Condon envelope with the experimental spectrum (**Figure 8-4**). Longarte et al.[243] reported the experimental IE of eugenol at 7.76 eV using REMPI (resonance-enhanced multiphoton ionization) spectroscopy, which differs by less than 0.09 eV from our experimental result. Our experimental resolution is insufficient to decide whether the conformational richness of eugenol and its cation or discrepancies in the shape of the simulated Franck–Condon envelope lead to this minor discrepancy. At 7.60 eV, OVGF underestimates the ground-state vertical ionization energy (IE_v = 7.88 eV experimentally and 7.77 eV using CBS-QB3* level of theory). The small gap between the IE_a and IE_v is indicative of small geometry change upon ionization. The HOMO of the neutral, MO **32**, is, here again, an aromatic ring π-orbital with oxygen lone-pair contributions. The OVGF-calculated ionization energies from molecular orbitals **31** and **30** align qualitatively with the TPES bands. While the former is also a predominantly aromatic ring π MO, the latter is localized on the substituent and is described as a π bond in the vinyl group. Overlaid in blue, green, and pink are 350 K Franck–Condon (FC) simulations of the eugenol ground, first and second excited states, respectively, which were aligned with the experimental data to have the best match. The ground and second excited state FC simulations (blue and pink) match most closely with the experimental TPES, while the TPES data for the first excited state appears to be broadened with respect to the simulation. It was difficult to optimize the first excited state, and thus, it is possible that the TD-DFT calculations did not find the real minimum for this structure due to the low barrier for rotation of the C3 side-chain.

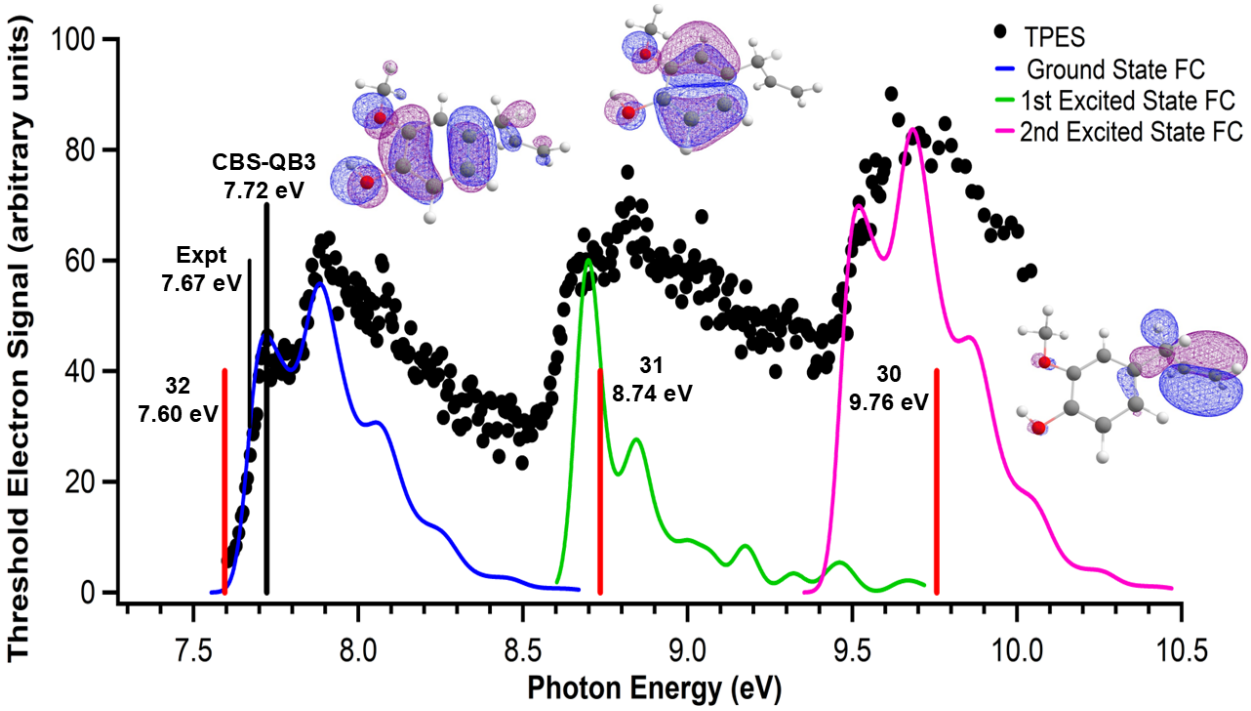

Figure 8-4. TPES for eugenol. Red vertical lines correspond to OVGF calculated vertical orbital ionization energies (molecular orbital numbers from the OVGF calculation correspond to the outer valence MOs). The blue, green, and pink lines represent the 350 K FC simulations of the ground state, first and second excited states, respectively. Vibrational line spectra were convolved with a Gaussian with a FWHM of 0.075 eV.

Consistent with the MIKE results,[199] the eugenol radical cation (*m*/*z* 164) exhibits the loss of a methyl radical (yielding *m*/*z* 149) and methanol (to *m*/*z* 132) as primary degradation channels at low internal energies (**Figure 8-5a**). Furthermore, *m*/*z* 104 is a significant fragment ion that was not previously observed. This is presumably due to the narrow internal energy window accessed in the MIKES experiment, likely below 11.5 eV, relative to the neutral. The experimental ionization energy of 7.67 eV was used to convert the photon energy to ion internal energy for the RRKM analysis. Methyl- and methanol-loss channels are competitive, with the methanol-loss channel being favoured at lower photon energies. The reactions leading to $^{\bullet}CH_3$ and CH_3OH loss were modelled to have an E_0 of 1.60 eV and 1.52 eV, respectively. Given that these estimates are for single transition state mechanisms and the potential complexity of the dissociation reactions, it is challenging to assign meaningful uncertainties to these values. However, the uncertainty of the

RRKM rate curve extrapolation could be as high as 0.30 eV, *i.e.,* 10% of the ca. 3 eV kinetic shift. Thus, the model results are, here again, "effective" reaction barriers approximating the lowest energies required for the two reactions to proceed. The previously calculated $^{\bullet}CH_3$- and CH_3OH-loss thresholds[199] were, nevertheless, significantly higher than these E_0 values. The bond cleavage energy in the methoxy group for $^{\bullet}CH_3$ loss or the hydrogen transfer transition state energy from the ring to the methylene group were computed to be at least 0.92 eV higher than the RRKM extrapolation results herein. The 1,3-H shift pathway, the first step of the previously described CH_3OH-loss channel, is even 2.32 eV higher in energy than the RRKM model onset. This discrepancy between the previously calculated and the current E_0 values prompted us to find lower energy reaction pathways for $^{\bullet}CH_3$ and CH_3OH loss in the eugenol radical cation, the results of which are shown in **Figure 8-6**.

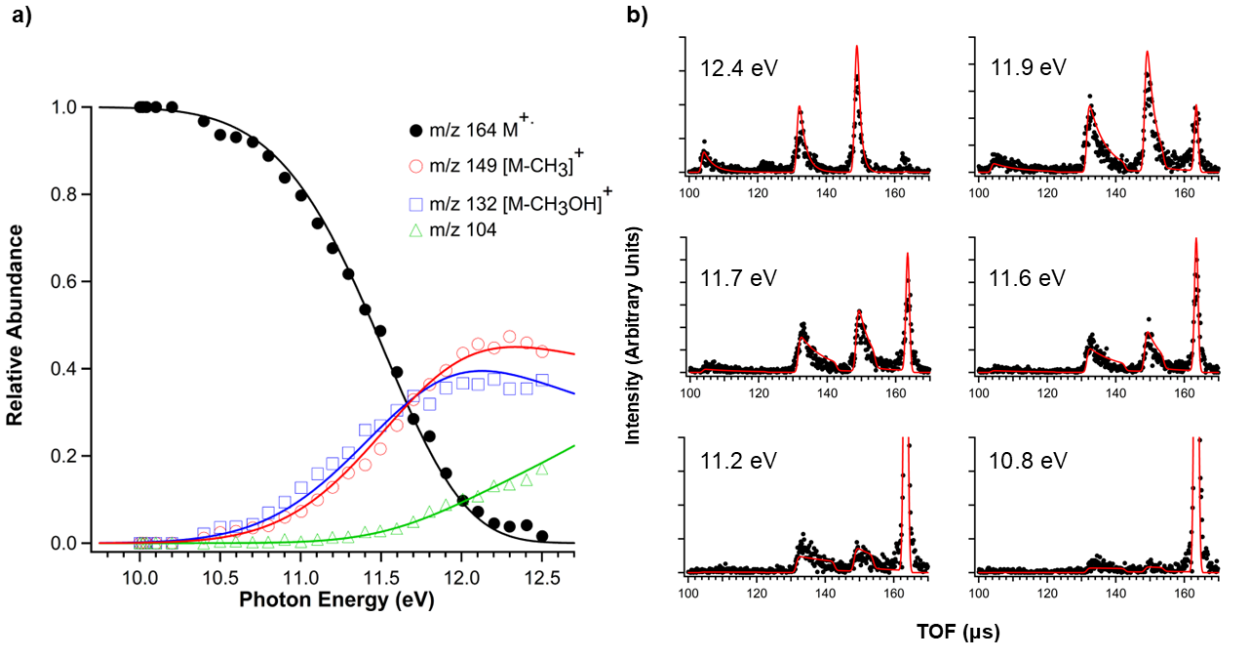

Figure 8-5. (a) Experimental eugenol $M^{+\bullet}$ breakdown diagram (points) with RRKM fit (solid lines), (b) representative *m/z* 164, *m/z* 149, *m/z* 132 and *m/z* 104 time-of-flight distributions (points) and the RRKM fit (solid lines) as a function of photon energy. The *m/z* 164 peak was cut off at 10.8 and 11.2 eV for clarity.

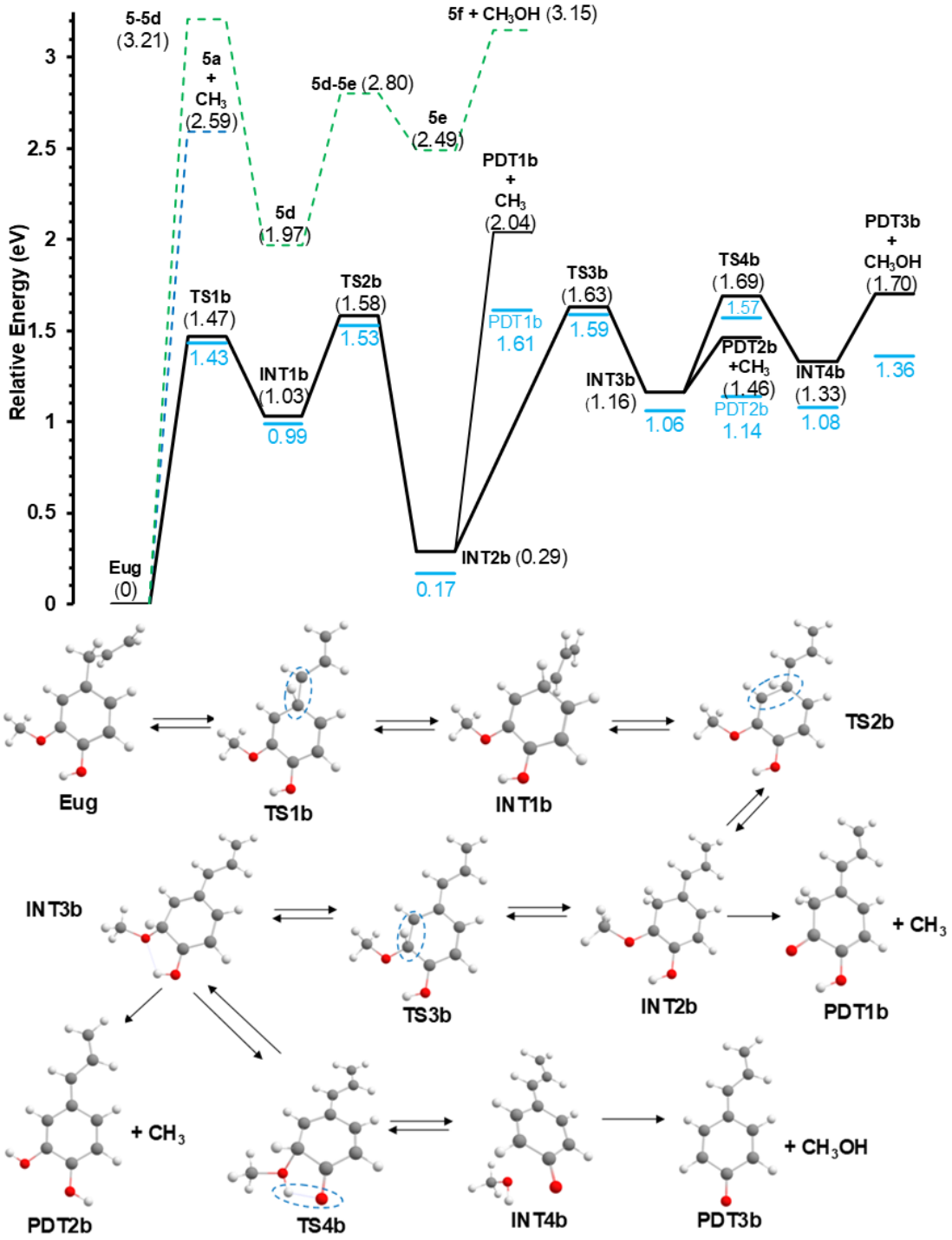

Figure 8-6. Calculated reaction pathways for CH_3 and CH_3OH losses from eugenol at B3LYP/6–311+G(d,p) (solid blue lines) and CBS-QB3* (solid black line) level of theory. Oxygen atoms are red, and the blue dashed line highlights the hydrogen migration steps. For comparison, the previously reported minimum energy reaction pathways at the CBS-QB3* level of theory[199] are

overlaid as blue and green dashed lines using the original structural indices. A schematic representation of the reactions can be found in **Figure A8-2** in the Appendix.

The new, lower-energy reaction fragmentation pathway is analogous to that found for the 4-ethylguaiacol cation. In the eugenol cation, the B3LYP threshold to **PDT1b** agrees with the RRKM E_0 value within 0.01 eV, and the CBS-QB3* result is around 0.44 eV higher. Both DFT and CBS-QB3* results suggest that forming **INT3b** from **INT2b** is energetically more favourable than direct formation of **PDT1b**. For the methanol loss product **PDT3b**, the B3LYP-derived threshold energies remain lower than those obtained at the CBS-QB3* level. Moreover, CBS-QB3* calculations indicate that the **TS4b** energy is lower than the energy of **PDT3b**. Overall, the eugenol ion dissociation pathway proceeds at lower energies than that of 4-ethylguaiacol. The most stable methyl- and methanol-loss fragment ions, **PDT2b** and **PDT3b** also correspond to the methyl-loss quinone methide pathways observed in the catalytic fast pyrolysis of eugenol.[235] Thus, the relative ease of H transfer steps in the cation leads to analogous decomposition steps as observed for the neutral over a zeolite catalyst with abundant Brønsted acid sites.

The identity of *m*/*z* 104 could be ionized styrene or 1,4-dihydropentalene**,** accompanied by the aggregate loss of neutral acetic acid or methylformate. While breakdown diagram modelling can sometimes reveal sequential and parallel channels contributing to the same mass channel,[244] unfortunately, our breakdown diagram energy range is too limited to decide whether the *m*/*z* 104 fragment ion is a sequential product, in which case its precursor would vanish at higher energies, or if it is a parallel fragmentation product from the parent ion, in which case its branching ratio would likely level off. That being said, when we attempted to model the data using a sequential origin for *m*/*z* 104, the RRKM estimate for its E_0 from *m*/*z* 149 or 132 was less than 0.3 eV, while the calculated lowest energy products (relative to ionized eugenol) were at a relative energy of over 3.5 eV, far beyond anything that could compete in this experiment. These results suggest *m*/*z* 104 is indeed formed in a parallel reaction to *m*/*z* 149 and 132. In this parallel model, the reaction leading to *m*/*z* 104 was estimated to have an E_0 of 2.01 eV (employing an estimated transition state, refer to section 8.3 Computational Procedures). In light of the experimental data, we can only speculate about the identity of the cationic and neutral fragments. A comprehensive calculation of

these obviously complex reaction pathways is outside the scope of this study, in which we focus on the synergies between experiment and quantum chemistry to reveal unimolecular mechanisms.

A note about the relationship between the B3LYP and CBS-QB3* results. In both cases, as the reaction coordinate passes **INT2/2b**, the agreement between the two levels of theory gets poorer. This can be traced to spin contamination in the wave function theory Hartree–Fock reference functions in the energy computation steps of the CBS-QB3 calculation. The value of the Hartree–Fock $\langle S^2 \rangle$ climbs from ~ 1 early on in the reaction scheme to over 1.5 as products are formed (as opposed to the pure-doublet value of 0.75). We recently discussed the cation chemistry of dibenzofuran and dibenz[b,f]oxepin and found single-reference wave function theory (WFT) based composite methods unusable to describe the reaction pathways due to spin-contamination, while DFT yielded results that were physically meaningful and broadly congruent with experiment.[245] While the methyl-loss product energies will not be affected, because the fragment ions are singlets and the leaving methyl is known to be well-described by CBS-QB3, an ancillary insight of the potential energy surface exploration is that in these highly delocalized systems, as well, the DFT and the WFT-based composite method results are inconsistent: they agree best when the WFT reference functions are not significantly affected by spin contamination. As multireference approaches are not routinely applicable to systems of such size, the inescapable conclusion seems to be that reaction mechanism exploration must always be based on experiment until cheaper quantum chemical approaches become available to describe such doublet systems consistently.

8.5 Conclusion

Threshold photoelectron spectra of 4-ethylguaiacol and eugenol have provided experimental ground and excited state IE values for comparisons to CBS-QB3, OVGF, and TD-DFT calculations, with the ground-state IE of 4-ethylguaiacol being determined here for the first time at 7.65 eV. We also highlight the importance of experiments in elucidating unimolecular dissociation mechanisms of radical cations. Quantitative imaging photoelectron photoion coincidence (iPEPICO) spectroscopy and statistical modelling provided novel insights and pointed to new pathways for the dissociative photoionization of 4-ethylguaiacol and eugenol radical cations, which could then be found computationally. This demonstrates how experimental findings

serve as critical benchmarks for computational modelling. For 4-ethylguaiacol, the dominant fragmentation pathway was confirmed to be $^{\bullet}CH_3$ loss. However, a notable deviation between the RRKM-derived reaction energy and previous theoretical calculations prompted the discovery of an alternative dissociation mechanism involving sequential hydrogen shifts and structural rearrangements. It was clear from the failure of the more direct routes to $^{\bullet}CH_3$ and CH_3OH loss that hydrogen migration had to be involved in the reactions. The only H atom easily available is from the CH_2 group in the side-chain. Moving one of these H atoms to facilitate $^{\bullet}CH_3$ loss, for example, requires multiple 1,2-H shift reactions due to the rigidity of the benzene group and the availability of p-orbitals along the route.

In the case of the eugenol radical cation, the primary fragmentation channels were confirmed to be the loss of $^{\bullet}CH_3$ and CH_3OH, with the methanol loss pathway being energetically favoured at lower photon energies. However, the experimental energy barriers derived from RRKM analysis were significantly lower than previous theoretical predictions, revealing an analogous dissociation mechanism to that of 4-ethylguaiacol. In the end, the fragmentation pathways of the cation showed remarkable similarities to the catalytic pyrolysis mechanism of the neutral, which can be rationalized in facile H migration in the cation mimicking the effect of ample Brønsted acid sites on the zeolite catalyst. Additionally, a fragment ion at *m*/*z* 104 was also detected, although, without trajectory calculations and further experimental insights, its structural assignment remains elusive. Computational analysis revealed a significant inconsistency between the B3LYP and CBS-QB3 theoretical methods, particularly as the reaction progresses past **INT2/2b** toward products, traced to severe spin contamination ($\langle S^2 \rangle > 1.5$) in the reference wave functions of the wave function theory steps of CBS-QB3, highlighting the unreliability of single-reference composite methods for describing these highly delocalized doublet reaction pathways. The significant disparity between experimental and computationally predicted energy barriers underscores the limitations of theoretical models in fully capturing radical cation reactivity. This finding reinforces the necessity of experimental validation, demonstrating that computational approaches, while powerful, require empirical confirmation to ensure mechanistic accuracy. By providing new insights into the dissociation behaviour of guaiacol derivatives, these findings contribute to the broader understanding of lignin-derived radical cations and their potential applications in sustainable biorefinery processes and fine chemical synthesis.[246,247]

8.6 Appendix

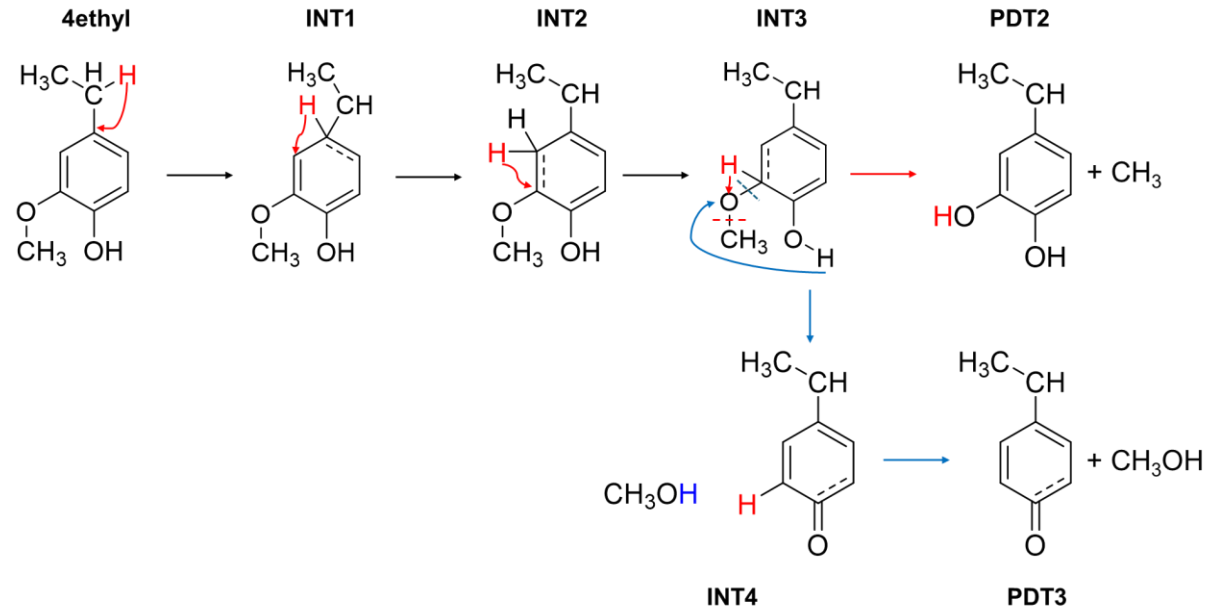

Figure A8-1. Schematic representation of the reactions leading to CH_3 and CH_3OH loss from 4-ethylguaiacol ions.

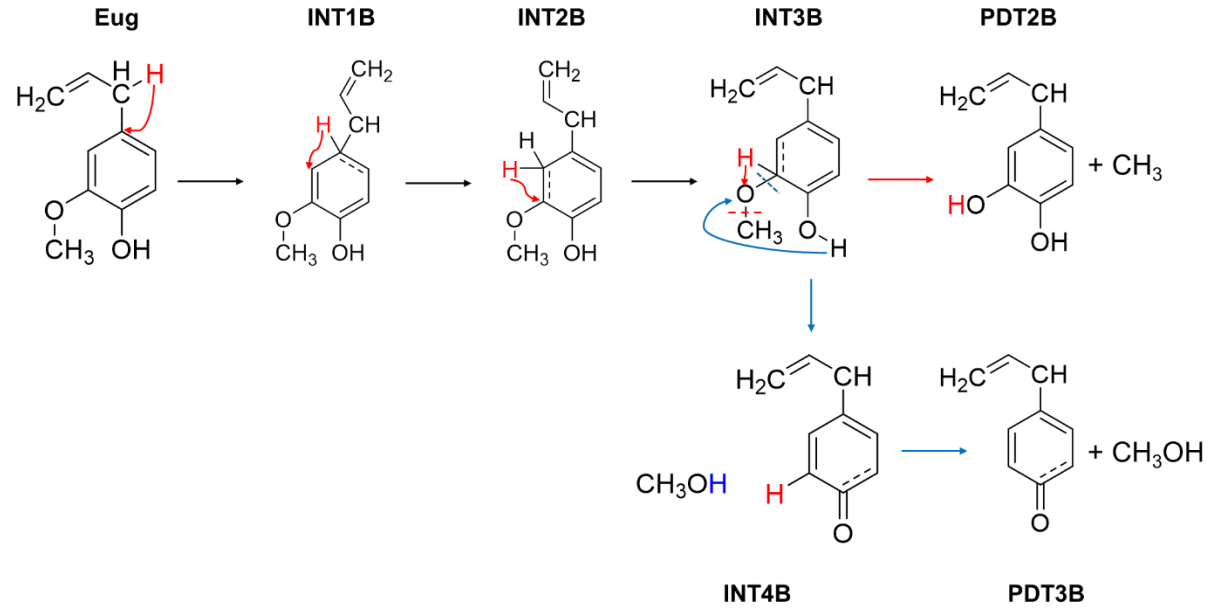

Figure A8-2. Schematic representation of the reactions leading to CH_3 and CH_3OH loss from eugenol ions.

CHAPTER 9: CONCLUSION

The research presented in this thesis establishes a definitive molecular-level framework for understanding the thermal and atmospheric degradation of methoxyphenols, a critical class of biomass combustion markers and precursors to secondary pollutants. By integrating high-resolution iPEPICO spectroscopy, MIKE spectrometry and ESI-MS with advanced computational and statistical modelling, this multifaceted approach has enabled the precise determination of appearance energies, rate constants and mechanistic pathways for the complex reaction landscapes of guaiacol and its substituted derivatives – creosol, 4-ethylguaiacol, 4-vinylguaiacol, eugenol and vanillin. These findings both advance the fundamental understanding of the unimolecular chemistry of guaiacols and provide critical parameters for atmospheric and combustion models, with direct implications for SOA and BrC formation, atmospheric lifetimes and environmental policy.

9.1 Neutral thermal pyrolysis

The investigation into the neutral pyrolysis of 4-ethylguaiacol and eugenol via a low-pressure SiC microreactor at temperatures exceeding 1000 ºC elucidates the complex mechanistic bifurcation between homolytic radical scission and concerted closed-shell rearrangements during the thermal decomposition of substituted guaiacols at elevated temperatures. A key finding reported in Chapter 4 is that, under flash pyrolysis conditions, the loss of a methyl radical ($^{\bullet}CH_3$) from the methoxy group is both kinetically and thermodynamically favourable over closed-shell pathways leading to aldehydes or ketones.

A notable discrepancy was observed between the calculated energetic favourability of these radical intermediates and their experimental detectability. For 4-ethylguaiacol, although computationally predicted on energetic grounds, the ethyl-substituted hydroxyphenoxyl radical (*m*/*z* 137) was not observed in the ms-TPES, despite a strong methyl radical signal. Analysis of the potential energy surface suggests that these transient radicals are highly reactive precursors that rapidly undergo secondary transformations. It is proposed that these intermediates participate in hydrogen abstraction reactions to generate substituted diol species (catechol analogs), which subsequently degrade into cyclopentadiene and benzene.

Comparative analysis with eugenol further supports this radical-driven cascade. While previous literature suggested the persistence of the *m*/*z* 149 radical, the current iPEPICO data indicate that this species is likely consumed via hydrogen abstraction to generate an allyl-substituted diol, which subsequently undergoes allene loss to form catechol.

Collectively, these findings demonstrate that the effective temperature and pressure regimes within the microreactor facilitate a hybrid of unimolecular and bimolecular processes. By identifying these short-lived intermediates and their subsequent degradation products, this research provides a more nuanced understanding of the "catechol-like" pathway in lignin pyrolysis. Such insights are critical for the rational design of catalysts and reactor conditions intended to optimize product selectivity in the sustainable valorization of lignin-derived biomass.

9.2 Protonated guaiacols

Chapter 5 shifts the focus to aqueous-phase atmospheric processing, examining the behaviour of protonated methoxyphenols formed by proton transfer in acidic cloud and fog droplets. Experimental CID and breakdown curves demonstrate that a consistent fragmentation motif exists across the majority of the guaiacol family. With the exception of vanillin, all studied protonated derivatives – guaiacol, creosol, 4-ethylguaiacol, 4-vinylguaiacol and eugenol – exhibit a sequential loss of methanol (CH_3OH, 32 Da) and carbon monoxide (CO, 28 Da). Protonated vanillin undergoes an initial CO loss, followed by sequential cleavage of CH_3OH and a second CO unit.

Computational calculations reveal that the dissociation pathways are strictly dictated by the relative thermodynamic stability of competing protomers and specific hydrogen-transfer mechanisms. In guaiacol, the global minimum corresponds to protonation at the carbon atom para to the hydroxy group. In contrast, substituted derivatives (creosol, 4-ethylguaiacol, 4-vinylguaiacol, and eugenol) preferentially protonate at the meta position. For vanillin, the formyl group serves as a highly basic protonation site and directs the initial fragmentation.

The study concludes that all investigated protonated guaiacols ultimately converge on the formation of the cyclopentadienyl ion (or its substituted analogs). This finding is particularly

significant as it parallels the products of neutral pyrolysis, suggesting that protonation in the atmosphere provides distinct, low-energy pathways to these reactive intermediates. The formation of such ions likely influences the chemical evolution of SOA, potentially affecting their chemical composition and long-term radiative properties.

9.3 Radical cations

The comparative study of radical cations using MIKES and iPEPICO spectroscopy, presented in Chapters 7 and 8, revealed novel, low-energy dissociation pathways for 4-ethylguaiacol and eugenol radical cations. While preliminary metastable ion analysis via MIKES provided a qualitative overview of fragmentation, the high-energy resolution and threshold photoionization capabilities of iPEPICO enabled a quantitative determination of appearance energies (E_0).

In Chapter 7, MIKES analysis of metastable ions suggested that the radical cations primarily mimic neutral pyrolysis by losing methyl radical ($^{\bullet}CH_3$) via simple bond cleavage. However, the subsequent iPEPICO investigation in Chapter 8 revealed that the 0 K appearance energy (E_0) for methyl loss in 4-ethylguaiacol (1.88 eV) is significantly lower than the calculated thresholds for direct O−CH_3 or ethyl-side-chain cleavage (2.15 & 2.61 eV, respectively). This discrepancy prompted a search for more complex reaction mechanisms, leading to the discovery of a sequence of intramolecular hydrogen shifts that ultimately facilitates methyl loss. Similar mechanistic complexity was observed in the eugenol radical cation, where analogous structural isomerizations were found to drive the loss of neutral fragments at energies significantly below those predicted by simple bond-fission models.

The identification of these low-energy, rearrangement-driven pathways provides a critical mechanistic link to condensed-phase lignin upgrading. The observed H shift sequences closely mirror the catalytic deoxygenation pathways found in acid-catalyzed lignin conversion over zeolite catalysts. Furthermore, as radical cations are ubiquitous in high-energy environments (combustion zones and biomass pyrolysis reactors), characterizing these non-intuitive dissociation channels is essential for improving predictive models of thermal biomass processing and atmospheric chemical evolution. This study underscores the necessity of combining high-resolution

coincidence spectroscopy with high-level theory to accurately describe the complex chemistry of lignin-derived aromatics.

9.4 Cross-state comparison: Influence of charge state on reaction topographies

The results presented in Chapters 4 through 8 show that the electronic charge state fundamentally modulates the reaction pathways available to the guaiacol molecular core. A primary unifying mechanistic thread across all the studied states is the dominance of methyl group transformations, which manifest as methyl radical loss ($^{\bullet}CH_3$) in the neutral and radical cationic states, but transition to neutral methanol loss (CH_3OH) in the protonated state. While neutral pyrolysis proceeds predominantly via direct homolytic bond scission, the introduction of charge – either through the addition of a proton or removal of an electron – facilitates complex, charge-directed hydrogen-migration pathways that bypass simple bond scission in favour of lower energy rearrangements. This charge-dependent reconfiguration of the energy landscape implies that biomass-derived molecular tracers may follow divergent chemical fates depending on their specific environmental context, such as the transition from gas-phase thermal zones to acidic aqueous droplets.

9.5 Broad significance and impact

A comprehensive investigation of the unimolecular degradation of guaiacol and its derivatives across their various molecular forms is a significant endeavour that bridges molecular-level chemistry and large-scale environmental processes. The high-quality kinetic and thermodynamic data produced in this thesis will enable more accurate atmospheric simulations by supplying experimentally constrained parameters for elementary steps – such as branching ratios, appearance energies, and rate constants. These data will support refinement of atmospheric chemical-transport models and improve predictions of SOA mass yields, atmospheric lifetimes of methoxyphenols, and the contribution of these compounds to secondary pollutants, including BrC and tropospheric ozone precursors.[17,248]

Beyond atmospheric modelling, elucidating degradation pathways has direct practical applications in pollution mitigation and thermal processing.[249,250] Detailed mechanistic information on thermal decomposition across various molecular states can inform the design and operation of biomass pyrolysis and gasification reactors to enhance conversion efficiency and minimize the formation of undesirable byproducts, including high-molecular-weight tars and soot precursors implicated in polycyclic aromatic hydrocarbon (PAH) formation.[251,252]

9.6 Concluding statement

This thesis bridges the gap between small-scale laboratory measurements and large-scale environmental processes by providing experimentally validated, charge-resolved kinetic and thermodynamic data for guaiacol and its derivatives. The results demonstrate that thermal and high-energy environments (combustion and pyrolysis) readily access the radical-driven channels, while aqueous protonation and condensed-phase chemistry open distinct low-energy routes to SOA and BrC precursors – pathways that are feasible under realistic atmospheric multiphase conditions and that potentially may influence air quality and climate forcing. By supplying quantitative elementary-step parameters required by atmospheric and process models, this work supports improved prediction, targeted monitoring and practical mitigation of the environmental and health impacts associated with biomass-derived methoxyphenols.

REFERENCES

(1) *Five ways to jump-start the renewable energy transition now*. https://www.un.org/en/climatechange/raising-ambition/renewable-energy-transition.

(2) Delbeke, J.; Runge-Metzger, A.; Slingenberg, Y.; Werksman, J. The Paris Agreement. *Towar. a Clim. Eur. Curbing Trend* **2019**, 24–45. https://doi.org/10.4324/9789276082569-2.

(3) Energy Transitions Commision. Fossil Fuels in Transition: Committing to the Phase-down of All Fossil Fuels. **2023**, No. November.

(4) Welsby, D.; Price, J.; Pye, S.; Ekins, P. Unextractable Fossil Fuels in a 1.5 °C World. *Nature* **2021**, *597* (7875), 230–234. https://doi.org/10.1038/s41586-021-03821-8.

(5) *'If you ignore emissions, we did great': Germany's challenging fight to go green*. https://www.theguardian.com/environment/2025/nov/02/germans-challenging-fight-to-go-green-climate-net-zero.

(6) *The Climate-neutral Federal Administration Coordination Office (KKB)*. https://www.bundeswirtschaftsministerium.de/Redaktion/EN/Dossier/kkb.html.

(7) *Net-zero emissions by 2050*. https://www.canada.ca/en/services/environment/weather/climatechange/climate-plan/net-zero-emissions-2050.html.

(8) *Bioenergy*. https://www.iea.org/energy-system/renewables/bioenergy#overview.

(9) Dioxide, C.; Gases, O. G.; Biofuels, O.; Table, S.; Agency, E. P.; Dioxide, C.; From, E.; Energy, B.; Tables, M. E. R.; Table, M. E. R.; Panel, I.; Change, C.; Guidelines, I.; Greenhouse, N.; Inventories, G. Section 11 Methodology and Sources. **2025**, No. October, 223–226.

(10) *Biomass explained*. https://www.eia.gov/energyexplained/biomass/biomass-and-the-environment.php.

(11) Kent, R. Renewables 2023 Analysis and Forecast to 2028. *Plast. Eng.* **2018**, *74* (9), 56–57.

(12) *IEA: Bioenergy to lead growth in renewables over next five years*. https://www.carbonbrief.org/iea-bioenergy-lead-growth-renewables-over-next-five-years/.

(13) Fang, Z.; Lai, A.; Dongmei Cai, N.; Chunlin Li, N.; Carmieli, R.; Chen, J.; Wang, X.; Rudich, Y. Secondary Organic Aerosol Generated from Biomass Burning Emitted

Phenolic Compounds: Oxidative Potential, Reactive Oxygen Species, and Cytotoxicity. *Environ. Sci. Technol.* **2024**, *58* (19), 8194–8206. https://doi.org/10.1021/acs.est.3c09903.

(14) Carreras-Sospedra, M.; Williams, R.; Dabdub, D. Assessment of the Emissions and Air Quality Impacts of Biomass and Biogas Use in California. *J. Air Waste Manag. Assoc.* **2016**, *66* (2), 134–150. https://doi.org/10.1080/10962247.2015.1087892.

(15) Tran, H.; Juno, E.; Arunachalam, S. Emissions of Wood Pelletization and Bioenergy Use in the United States. *Renew. Energy* **2023**, *219* (P2), 119536. https://doi.org/10.1016/j.renene.2023.119536.

(16) Tomlin, A. S. Air Quality and Climate Impacts of Biomass Use as an Energy Source: A Review. *Energy and Fuels* **2021**, *35* (18), 14213–14240. https://doi.org/10.1021/acs.energyfuels.1c01523.

(17) Yee, L. D.; Kautzman, K. E.; Loza, C. L.; Schilling, K. A.; Coggon, M. M.; Chhabra, P. S.; Chan, M. N.; Chan, A. W. H.; Hersey, S. P.; Crounse, J. D.; Wennberg, P. O.; Flagan, R. C.; Seinfeld, J. H. Secondary Organic Aerosol Formation from Biomass Burning Intermediates: Phenol and Methoxyphenols. *Atmos. Chem. Phys.* **2013**, *13* (16), 8019–8043. https://doi.org/10.5194/acp-13-8019-2013.

(18) Simpson, C. D.; Paulsen, M.; Dills, R. L.; Liu, L. J. S.; Kalman, D. A. Determination of Methoxyphenols in Ambient Atmospheric Particulate Matter: Tracers for Wood Combustion. *Environ. Sci. Technol.* **2005**, *39* (2), 631–637. https://doi.org/10.1021/es0486871.

(19) Zhang, X.; Lei, H.; Chen, S.; Wu, J. Catalytic Co-Pyrolysis of Lignocellulosic Biomass with Polymers: A Critical Review. *Green Chem.* **2016**, *18* (15), 4145–4169. https://doi.org/10.1039/c6gc00911e.

(20) Kakroodi, A. R.; Sain, M. *Lignin-Reinforced Rubber Composites*; Elsevier Inc., 2016. https://doi.org/10.1016/B978-0-323-35565-0.00010-2.

(21) Doherty, W. O. S.; Mousavioun, P.; Fellows, C. M. Value-Adding to Cellulosic Ethanol: Lignin Polymers. *Ind. Crops Prod.* **2011**, *33* (2), 259–276. https://doi.org/10.1016/j.indcrop.2010.10.022.

(22) Creteanu, A.; Lungu, C. N.; Lungu, M. Lignin: An Adaptable Biodegradable Polymer Used in Different Formulation Processes. *Pharmaceuticals* **2024**, *17* (10). https://doi.org/10.3390/ph17101406.

(23) Kitanovski, Z.; Čusak, A.; Grgić, I.; Claeys, M. Chemical Characterization of the Main Products Formed through Aqueous-Phase Photonitration of Guaiacol. *Atmos. Meas. Tech.* **2014**, *7* (8), 2457–2470. https://doi.org/10.5194/amt-7-2457-2014.

(24) Dong, S.; Feng, G. A Comprehensive Review of Catalytic Hydrodeoxygenation of Lignin-Derived Phenolics to Aromatics. *Molecules* **2025**, *30* (10), 2225. https://doi.org/10.3390/molecules30102225.

(25) Chen, C.; Liu, P.; Xia, H.; Zhou, M.; Zhao, J.; Sharma, B. K.; Jiang, J. Photocatalytic Cleavage of β-O-4 Ether Bonds in Lignin over Ni/TiO2. *Molecules* **2020**, *25* (9), 2109. https://doi.org/10.3390/molecules25092109.

(26) Zhou, M.; Chen, C.; Liu, P.; Xia, H.; Li, J.; Sharma, B. K.; Jiang, J. Catalytic Hydrotreatment of β-O-4 Ether in Lignin: Cleavage of the C–O Bond and Hydrodeoxygenation of Lignin-Derived Phenols in One Pot. *ACS Sustain. Chem. Eng.* **2020**, *8* (38), 14511–14523. https://doi.org/10.1021/acssuschemeng.0c04941.

(27) Supriyanto; Usino, D. O.; Ylitervo, P.; Dou, J.; Sipponen, M. H.; Richards, T. Identifying the Primary Reactions and Products of Fast Pyrolysis of Alkali Lignin. *J. Anal. Appl. Pyrolysis* **2020**, *151* (June). https://doi.org/10.1016/j.jaap.2020.104917.

(28) Kjällstrand, J.; Ramnäs, O.; Petersson, G. Methoxyphenols from Burning of Scandinavian Forest Plant Materials. *Chemosphere* **2000**, *41* (5), 735–741. https://doi.org/10.1016/S0045-6535(99)00427-0.

(29) Adamek, M.; Kavčič, A.; Debeljak, M.; Šala, M.; Grdadolnik, J.; Vogel-Mikuš, K.; Kroflič, A. Toxicity of Nitrophenolic Pollutant 4-Nitroguaiacol to Terrestrial Plants and Comparison with Its Non-Nitro Analogue Guaiacol (2-Methoxyphenol). *Sci. Rep.* **2024**, *14* (1), 1–11. https://doi.org/10.1038/s41598-024-52610-6.

(30) Zhang, B.; Shen, Z.; He, K.; Sun, J.; Huang, S.; Xu, H.; Li, J.; Ho, S. S. H.; Cao, J. J. Insight into the Primary and Secondary Particle-Bound Methoxyphenols and Nitroaromatic Compound Emissions from Solid Fuel Combustion and the Updated Source Tracers. *Environ. Sci. Technol.* **2023**, *57* (38), 14280–14288. https://doi.org/10.1021/acs.est.3c04370.

(31) Cubison, M. J.; Ortega, A. M.; Hayes, P. L.; Farmer, D. K.; Day, D.; Lechner, M. J.; Brune, W. H.; Apel, E.; Diskin, G. S.; Fisher, J. A.; Fuelberg, H. E.; Hecobian, A.; Knapp, D. J.; Mikoviny, T.; Riemer, D.; Sachse, G. W.; Sessions, W.; Weber, R. J.; Weinheimer,

A. J.; Wisthaler, A.; Jimenez, J. L. Effects of Aging on Organic Aerosol from Open Biomass Burning Smoke in Aircraft and Laboratory Studies. *Atmos. Chem. Phys.* **2011**, *11* (23), 12049–12064. https://doi.org/10.5194/acp-11-12049-2011.

(32) Zhang, J.; Shrivastava, M.; Ma, L.; Jiang, W.; Anastasio, C.; Zhang, Q.; Zelenyuk, A. Modeling Novel Aqueous Particle and Cloud Chemistry Processes of Biomass Burning Phenols and Their Potential to Form Secondary Organic Aerosols. *Environ. Sci. Technol.* **2024**, *58* (8), 3776–3786. https://doi.org/10.1021/acs.est.3c07762.

(33) Pye, H. O. T.; Ward-Caviness, C. K.; Murphy, B. N.; Appel, K. W.; Seltzer, K. M. Secondary Organic Aerosol Association with Cardiorespiratory Disease Mortality in the United States. *Nat. Commun.* **2021**, *12* (1), 1–8. https://doi.org/10.1038/s41467-021-27484-1.

(34) Padhi, A.; Chandran P.R, S.; Fadnavis, S. Seasonality, Trends, and SOA Formation Potential of Anthropogenic Volatile Organic Compounds: Implications for Pollution. *Atmos. Pollut. Res.* **2025**, No. September, 102765. https://doi.org/10.1016/j.apr.2025.102765.

(35) Lauraguais, A.; Coeur-Tourneur, C.; Cassez, A.; Deboudt, K.; Fourmentin, M.; Choël, M. Atmospheric Reactivity of Hydroxyl Radicals with Guaiacol (2-Methoxyphenol), a Biomass Burning Emitted Compound: Secondary Organic Aerosol Formation and Gas-Phase Oxidation Products. *Atmos. Environ.* **2014**, *86*, 155–163. https://doi.org/10.1016/j.atmosenv.2013.11.074.

(36) Sun, Y.; Chen, X.; Liu, L.; Xu, F.; Zhang, X. Mechanisms and Kinetics Studies of the Atmospheric Oxidation of Eugenol by Hydroxyl Radicals and Ozone Molecules. *Sci. Total Environ.* **2021**, *770*, 145203. https://doi.org/10.1016/j.scitotenv.2021.145203.

(37) Zhang, X.; Liu, H.; Cheng, J.; Song, W.; Wang, H.; Zhang, Y.; Wang, X. Gas-Phase Oxidation of Guaiacol by NO 3 Radicals: Kinetic Measurements and Implications . *ACS ES&T Air* **2025**, *2* (5), 903–910. https://doi.org/10.1021/acsestair.4c00353.

(38) Schauer, J. J.; Kleeman, M. J.; Cass, G. R.; Simoneit, B. R. T. Measurement of Emissions from Air Pollution Sources. 5. C 1 −C 32 Organic Compounds from Gasoline-Powered Motor Vehicles. *Environ. Sci. Technol.* **2002**, *36* (6), 1169–1180. https://doi.org/10.1021/es0108077.

(39) Simpson, C. D.; Paulsen, M.; Dills, R. L.; Liu, L.-J. S.; Kalman, D. A. Determination of

Methoxyphenols in Ambient Atmospheric Particulate Matter: Tracers for Wood Combustion. *Environ. Sci. Technol.* **2005**, *39* (2), 631–637. https://doi.org/10.1021/es0486871.

(40) Jiang, W.; Yu, L.; Yee, L.; Chhabra, P.; Seinfeld, J.; Anastasio, C.; Zhang, Q. Chemical Differences between Phenolic Secondary Organic Aerosol Formed through Gas-Phase and Aqueous-Phase Reactions. *ACS Earth Sp. Chem.* **2024**, *8* (11), 2270–2283. https://doi.org/10.1021/acsearthspacechem.4c00204.

(41) Ma, L.; Guzman, C.; Niedek, C.; Tran, T.; Zhang, Q.; Anastasio, C. Kinetics and Mass Yields of Aqueous Secondary Organic Aerosol from Highly Substituted Phenols Reacting with a Triplet Excited State. *Environ. Sci. Technol.* **2021**, *55* (9), 5772–5781. https://doi.org/10.1021/acs.est.1c00575.

(42) Smith, J. D.; Sio, V.; Yu, L.; Zhang, Q.; Anastasio, C. Secondary Organic Aerosol Production from Aqueous Reactions of Atmospheric Phenols with an Organic Triplet Excited State. *Environ. Sci. Technol.* **2014**, *48* (2), 1049–1057. https://doi.org/10.1021/es4045715.

(43) Arciva, S.; Niedek, C.; Mavis, C.; Yoon, M.; Sanchez, M. E.; Zhang, Q.; Anastasio, C. Aqueous · OH Oxidation of Highly Substituted Phenols as a Source of Secondary Organic Aerosol. *Environ. Sci. Technol.* **2022**, *56* (14), 9959–9967. https://doi.org/10.1021/acs.est.2c02225.

(44) Ervens, B.; Turpin, B. J.; Weber, R. J. Secondary Organic Aerosol Formation in Cloud Droplets and Aqueous Particles (AqSOA): A Review of Laboratory, Field and Model Studies. *Atmos. Chem. Phys.* **2011**, *11* (21), 11069–11102. https://doi.org/10.5194/acp-11-11069-2011.

(45) Yang, J.; Au, W. C.; Law, H.; Lam, C. H.; Nah, T. Formation and Evolution of Brown Carbon during Aqueous-Phase Nitrate-Mediated Photooxidation of Guaiacol and 5-Nitroguaiacol. *Atmos. Environ.* **2021**, *254* (January), 118401. https://doi.org/10.1016/j.atmosenv.2021.118401.

(46) Laskin, A.; Laskin, J.; Nizkorodov, S. A. Chemistry of Atmospheric Brown Carbon. *Chem. Rev.* **2015**, *115* (10), 4335–4382. https://doi.org/10.1021/cr5006167.

(47) Ramanathan, V.; Carmichael, G. Global and Regional Climate Changes Due to Black Carbon. *Nat. Geosci.* **2008**, *1* (4), 221–227. https://doi.org/10.1038/ngeo156.

(48) Laskin, A.; West, C. P.; Hettiyadura, A. P. S. Molecular Insights into the Composition, Sources, and Aging of Atmospheric Brown Carbon. *Chem. Soc. Rev.* **2025**, *54* (3), 1583–1612. https://doi.org/10.1039/d3cs00609c.

(49) Rowell, A.; Brean, J.; Beddows, D. C. S.; Shi, Z.; Kumar, A.; Rissanen, M.; Dal Maso, M.; Mettke, P.; Weinhold, K.; Merkel, M.; Harrison, R. M. The Behaviour of Charged Particles (Ions) during New Particle Formation Events in Urban Leipzig, Germany. *Atmos. Chem. Phys.* **2024**, *24* (18), 10349–10361. https://doi.org/10.5194/acp-24-10349-2024.

(50) Kong, X.; Ammann, M.; George, C.; Knopf, D. Atomic and Molecular Ions in Atmospheric Chemistry: Interfacial Reactivity, Emerging Mechanisms, and Future Perspectives. *J. Geophys. Res. Atmos.* **2025**, *130* (20). https://doi.org/10.1029/2025JD044379.

(51) Hirsikko, A.; Nieminen, T.; Gagné, S.; Lehtipalo, K.; Manninen, H. E.; Ehn, M.; Hõrrak, U.; Kerminen, V. M.; Laakso, L.; McMurry, P. H.; Mirme, A.; Mirme, S.; Petäjä, T.; Tammet, H.; Vakkari, V.; Vana, M.; Kulmala, M. Atmospheric Ions and Nucleation: A Review of Observations. *Atmos. Chem. Phys.* **2011**, *11* (2), 767–798. https://doi.org/10.5194/acp-11-767-2011.

(52) Nowakowska, M.; Herbinet, O.; Dufour, A.; Glaude, P. A. Kinetic Study of the Pyrolysis and Oxidation of Guaiacol. *J. Phys. Chem. A* **2018**, *122* (39), 7894–7909. https://doi.org/10.1021/acs.jpca.8b06301.

(53) Wu, X.; Salionov, D.; Hemberger, P.; Vogel, F.; Bodi, A.; Bjelić, S. Beyond Vanilla: The Dissociation Mechanism of Vanillin in Four Charge States. *Comput. Theor. Chem.* **2023**, *1229* (June). https://doi.org/10.1016/j.comptc.2023.114340.

(54) Glowacki, D. R.; Pilling, M. J. Unimolecular Reactions of Peroxy Radicals in Atmospheric Chemistry and Combustion. *ChemPhysChem* **2010**, *11* (18), 3836–3843. https://doi.org/10.1002/cphc.201000469.

(55) Stephenson, T. A.; Lester, M. I. Unimolecular Decay Dynamics of Criegee Intermediates: Energy-Resolved Rates, Thermal Rates, and Their Atmospheric Impact. *Int. Rev. Phys. Chem.* **2020**, *39* (1), 1–33. https://doi.org/10.1080/0144235X.2020.1688530.

(56) Yerrayya, A.; Natarajan, U.; Vinu, R. Fast Pyrolysis of Guaiacol to Simple Phenols: Experiments, Theory and Kinetic Model. *Chem. Eng. Sci.* **2019**, *207*, 619–630. https://doi.org/10.1016/j.ces.2019.06.025.

(57) Delort, N.; Meziane, I.; Framinet, M.; Bounaceur, R.; Bourgalais, J.; Battin-Leclerc, F.; Herbinet, O. An Experimental and Modeling Investigation of the Combustion of Anisole and Guaiacol. *Fuel* **2024**, *362*, 130832. https://doi.org/10.1016/j.fuel.2023.130832.

(58) Nguyen, T. T. P.; Mai, T. V.-T.; Huynh, L. K. Detailed Kinetic Modeling of Thermal Decomposition of Guaiacol – A Model Compound for Biomass Lignin. *Biomass and Bioenergy* **2018**, *112*, 45–60. https://doi.org/10.1016/j.biombioe.2018.02.006.

(59) Furutani, Y.; Dohara, Y.; Kudo, S.; Hayashi, J.; Norinaga, K. Theoretical Study on the Kinetics of Thermal Decomposition of Guaiacol and Catechol. *J. Phys. Chem. A* **2017**, *121* (44), 8495–8503. https://doi.org/10.1021/acs.jpca.7b08112.

(60) Ledesma, E. B.; Hoang, J. N.; Nguyen, Q.; Hernandez, V.; Nguyen, M. P.; Batamo, S.; Fortune, C. K. Unimolecular Decomposition Pathway for the Vapor-Phase Cracking of Eugenol, a Biomass Tar Compound. *Energy and Fuels* **2013**, *27* (11), 6839–6846. https://doi.org/10.1021/ef401760c.

(61) Kroflič, A.; Anders, J.; Drventić, I.; Mettke, P.; Böge, O.; Mutzel, A.; Kleffmann, J.; Herrmann, H. Guaiacol Nitration in a Simulated Atmospheric Aerosol with an Emphasis on Atmospheric Nitrophenol Formation Mechanisms. *ACS Earth Sp. Chem.* **2021**, *5* (5), 1083–1093. https://doi.org/10.1021/acsearthspacechem.1c00014.

(62) Shen, Y.; Liu, X.; Ren, H.; Xiao, X.; Sun, R.; Liu, H.; Lu, J.; Huang, C.; Zhao, L.; Zhou, Z.; Qi, F. Unveiling Radical Pathways in the Pyrolysis of Eugenol: Experimental and Computational Insights. *J. Anal. Appl. Pyrolysis* **2024**, *177* (October 2023), 106317. https://doi.org/10.1016/j.jaap.2023.106317.

(63) Mullery, A. A.; Hoang, J. N.; Nguyen, A. T.; Luong, C. D.; Ledesma, E. B. Thermal Decomposition Pathways of 4-Ethylguaiacol under Fast Pyrolysis and Gasification Conditions. *J. Anal. Appl. Pyrolysis* **2017**, *123*, 83–91. https://doi.org/10.1016/j.jaap.2016.12.023.

(64) Chen, X.; Sun, Y.; Qi, Y.; Liu, L.; Xu, F.; Zhao, Y. Mechanistic and Kinetic Investigations on the Ozonolysis of Biomass Burning Products: Guaiacol, Syringol and Creosol. *Int. J. Mol. Sci.* **2019**, *20* (18), 4492. https://doi.org/10.3390/ijms20184492.

(65) Delić, A.; Skube, U.; Šala, M.; Kroflič, A. Kinetics and Product Identification of Water-Dissolved Nitroguaiacol Photolysis under Artificial Sunlight. *Front. Chem.* **2023**, *11* (July), 1–12. https://doi.org/10.3389/fchem.2023.1211061.

(66) Buenger, E. W.; Mayer, P. M. Where You Protonate Matters: Deciphering the Unimolecular Chemistry of Protonated Myrcene and Linalool. *J. Mass Spectrom.* **2024**, *59* (10). https://doi.org/10.1002/jms.5096.

(67) Almatarneh, M. H.; Elayan, I. A.; Al-Sulaibi, M.; Al Khawaldeh, A.; Saber, S. O. W.; Al-Qaralleh, M.; Altarawneh, M. Unimolecular Decomposition Reactions of Propylamine and Protonated Propylamine. *ACS Omega* **2019**, *4* (2), 3306–3313. https://doi.org/10.1021/acsomega.8b02792.

(68) Jacob, J. . *Introduction to Atmospheric Chemistry*; Princeton University Press Princeton, New Jersey, 1999.

(69) Longsworth, O. M.; Bready, C. J.; Joines, M. S.; Shields, G. C. The Driving Effects of Common Atmospheric Molecules for Formation of Clusters: The Case of Sulfuric Acid, Nitric Acid, Hydrochloric Acid, Ammonia, and Dimethylamine. *Environ. Sci. Atmos.* **2023**, *3* (11), 1585–1600. https://doi.org/10.1039/d3ea00118k.

(70) Liu, L.; Li, H.; Zhang, H.; Zhong, J.; Bai, Y.; Ge, M.; Li, Z.; Chen, Y.; Zhang, X. The Role of Nitric Acid in Atmospheric New Particle Formation. *Phys. Chem. Chem. Phys.* **2018**, *20* (25), 17406–17414. https://doi.org/10.1039/c8cp02719f.

(71) Tilgner, A.; Schaefer, T.; Alexander, B.; Barth, M.; Collett, J. L.; Fahey, K. M.; Nenes, A.; Pye, H. O. T.; Herrmann, H.; McNeill, V. F. Acidity and the Multiphase Chemistry of Atmospheric Aqueous Particles and Clouds. *Atmos. Chem. Phys.* **2021**, *21* (17), 13483–13536. https://doi.org/10.5194/acp-21-13483-2021.

(72) Morteo-Flores, F.; Roldan, A. Mechanisms and Trends of Guaiacol Hydrodeoxygenation on Transition Metal Catalysts. *Front. Catal.* **2022**, *2* (May), 1–12. https://doi.org/10.3389/fctls.2022.861364.

(73) Robinson, A. M.; Hensley, J. E.; Will Medlin, J. Bifunctional Catalysts for Upgrading of Biomass-Derived Oxygenates: A Review. *ACS Catal.* **2016**, *6* (8), 5026–5043. https://doi.org/10.1021/acscatal.6b00923.

(74) Siuzdak, G.; North, S.; BelBruno, J. J. Multiphoton Ionization of Phenol in Nonaqueous Solutions: Characterization of the Cation and Ion-Molecule Chemistry. *J. Phys. Chem.* **1991**, *95* (13), 5186–5190. https://doi.org/10.1021/j100166a050.

(75) Tureček, F.; Julian, R. R. Peptide Radicals and Cation Radicals in the Gas Phase. *Chem. Rev.* **2013**, *113* (8), 6691–6733. https://doi.org/10.1021/cr400043s.

(76) Li, G.; Luo, Z.; Wang, W.; Cen, J. A Study of the Mechanisms of Guaiacol Pyrolysis Based on Free Radicals Detection Technology. *Catalysts* **2020**, *10* (3), 295. https://doi.org/10.3390/catal10030295.

(77) Scheer, A. M.; Mukarakate, C.; Robichaud, D. A.; Nimlos, M. R.; Ellison, B. Thermal Decomposition Mechanisms of the Methoxyphenols: Formation of Phenol, Cyclopentadieneone, Vinylacetylene and Acetylene. *ACS Natl. Meet. B. Abstr.* **2011**, 13381–13389.

(78) Axson, J. L.; Takahashi, K.; De Haan, D. O.; Vaida, V. Gas-Phase Water-Mediated Equilibrium between Methylglyoxal and Its Geminal Diol. *Proc. Natl. Acad. Sci.* **2010**, *107* (15), 6687–6692. https://doi.org/10.1073/pnas.0912121107.

(79) Delić, A.; Skube, U.; Šala, M.; Kroflič, A. Kinetics and Product Identification of Water-Dissolved Nitroguaiacol Photolysis under Artificial Sunlight. *Front. Chem.* **2023**, *11*. https://doi.org/10.3389/fchem.2023.1211061.

(80) Kitanovski, Z.; Čusak, A.; Grgić, I.; Claeys, M. Chemical Characterization of the Main Products Formed through Aqueous-Phase Photonitration of Guaiacol. *Atmos. Meas. Tech.* **2014**, *7* (8), 2457–2470. https://doi.org/10.5194/amt-7-2457-2014.

(81) Curchod, B. F. E.; Orr-Ewing, A. J. Perspective on Theoretical and Experimental Advances in Atmospheric Photochemistry. *J. Phys. Chem. A* **2024**, *128* (32), 6613–6635. https://doi.org/10.1021/acs.jpca.4c03481.

(82) Morris, M.; Bateman, B.; Riley, T.; Nicolaysen, L.; Brooks, V. *The History of Magnetic Sector Mass Spectrometry at VG - Micromass - Waters*. https://www.asms.org/docs/default-source/history-posters/vendor_vg-sectors_36x18.pdf?sfvrsn=e63576c3_0.

(83) Jean H. Futrell. *Gaseous Ion Chemistry and Mass Spectrometry.*; John Wiley & Sons, Inc., 1986.

(84) Gross, J. H. *Mass Spectrometry*; Springer International Publishing: Cham, 2017. https://doi.org/10.1007/978-3-319-54398-7.

(85) John H. Moore, N. D. S. *Encyclopedia of Chemical Physics and Physical Chemistry - 3 Volume Set*; CRC Press, 2001. https://doi.org/https://doi.org/10.1201/9780429143755.

(86) Ekman, R.; Silberring, J.; Westman-Brinkmalm, A.; Kraj, A. *Mass Spectrometry*; Wiley & Sons, Inc., 2009.

(87) Waters Corporatiioin. Micromass Quattro Ultima Pt Mass Spectrometer: Operator's Guide. *71500066502* **2003**, 1–282.

(88) Konermann, L.; Ahadi, E.; Rodriguez, A. D.; Vahidi, S. Unraveling the Mechanism of Electrospray Ionization. *Anal. Chem.* **2013**, *85* (1), 2–9. https://doi.org/10.1021/ac302789c.

(89) CS Ho, CWK Lam, MHM Chan, RCK Cheung, LK Law, LCW Lit, KF Ng, MWM Suen, and H. T. Electrospray Ionisation Mass Spectrometry: Principles and Clinical Applications. *Clin Biochem Rev* **2003**.

(90) March, R. E. Ion Trap Mass Spectrometers. *Encycl. Spectrosc. Spectrom.* **2016**, 330–337. https://doi.org/10.1016/B978-0-12-409547-2.12675-7.

(91) Mathieu, E. Memoire Sur Le Mouvement Vibratoire d'une Membrane de Forme Elliptique. Journal de Mathématiques Pures et Appliquées. *J. Math. Pure Appl.* **1986**, *13*, 137–203.

(92) Shimadzu. *Introduction to mass analyzers*. https://www.shimadzu.com/an/service-support/technical-support/analysis-basics/fundamental/mass_analyzers.html.

(93) Overton, S. PRIMARY FRAGMENTATION PATHWAYS AND THEIR ION MOBILITY, 2021.

(94) Cooks, R. G. No Title. *Collision-induced dissociation Polyat. ions* **1978**, No. Plenum Press: New York, 357–446.

(95) Harvey, J. *Modelling the Dissociation Dynamics and Threshold Photoelectron Spectroscopy of Small Halogenated Molecules*; 2014.

(96) Baer, T. Photoelectron–Photoion Coincidence Methods in Mass Spectrometry (PEPICO). *Encycl. Spectrosc. Spectrom.* **1999**, *3*, 1831–1839. https://doi.org/10.1006/rwsp.2000.0238.

(97) Softley, T. P. Applications of Molecular Rydberg States in Chemical Dynamics and Spectroscopy. *Int. Rev. Phys. Chem.* **2004**, *23* (1), 1–78. https://doi.org/10.1080/01442350310001652940.

(98) Guyon, P. M.; Baer, T.; Nenner, I. Interactions between Neutral Dissociation and Ionization Continua in N 2O. *J. Chem. Phys.* **1983**, *78* (6), 3665–3672. https://doi.org/10.1063/1.445141.

(99) Bodi, A.; Johnson, M.; Gerber, T.; Gengeliczki, Z.; Sztáray, B.; Baer, T. Imaging

Photoelectron Photoion Coincidence Spectroscopy with Velocity Focusing Electron Optics. *Rev. Sci. Instrum.* **2009**, *80* (3). https://doi.org/10.1063/1.3082016.

(100) Sztáray, B.; Voronova, K.; Torma, K. G.; Covert, K. J.; Bodi, A.; Hemberger, P.; Gerber, T.; Osborn, D. L. CRF-PEPICO: Double Velocity Map Imaging Photoelectron Photoion Coincidence Spectroscopy for Reaction Kinetics Studies. *J. Chem. Phys.* **2017**, *147* (1). https://doi.org/10.1063/1.4984304.

(101) Eppink, A. T. J. B.; Parker, D. H. Velocity Map Imaging of Ions and Electrons Using Electrostatic Lenses: Application in Photoelectron and Photofragment Ion Imaging of Molecular Oxygen. *Rev. Sci. Instrum.* **1997**, *68* (9), 3477–3484. https://doi.org/10.1063/1.1148310.

(102) Sztáray, B.; Baer, T. Suppression of Hot Electrons in Threshold Photoelectron Photoion Coincidence Spectroscopy Using Velocity Focusing Optics. *Rev. Sci. Instrum.* **2003**, *74* (8), 3763–3768. https://doi.org/10.1063/1.1593788.

(103) Wiley, Ï. W. C.; Mclaren, I. H.; Karas, M. SPECIAL FEATURE : " Time-of-Flight Mass Spectrometer with Improved. *Chem. Commun.* **1997**, *32*, 1–3.

(104) Eland, J. H. D. Photoelectron-Photoion Coincidence Spectroscopy. *Int. J. Mass Spectrom. Ion Phys.* **1972**, *8* (2), 143–151. https://doi.org/10.1016/0020-7381(72)80004-4.

(105) Atkins, P., & Friedman, R. *Molecular Quantum Mechanics*, Fifth Edit.; OUP Oxford, Ed.; Oxford Univeristy Press, 2010.

(106) Hollas, J. M. *High Resolution Spectroscopy*, 2nd ed.; Chichester ; New York : J. Wiley, 1998.

(107) Sztáray, B.; Bodi, A.; Baer, T. Modeling Unimolecular Reactions in Photoelectron Photoion Coincidence Experiments. *J. Mass Spectrom.* **2010**, *45* (11), 1233–1245. https://doi.org/10.1002/jms.1813.

(108) Baer, T.; Hase, W. L. *Unimolecular Reaction Dynamics: Theory and Experiments*, Vol. 31.; Oxford University Press on Demand, New York, 1996.

(109) Beyer, T.; Swinehart, D. F. Algorithm 448: Number of Multiply-Restricted Partitions. *Commun. ACM* **1973**, *16* (6), 379. https://doi.org/10.1145/362248.362275.

(110) Borkar, S.; Sztáray, B. Self-Consistent Heats of Formation for the Ethyl Cation, Ethyl Bromide, and Ethyl Iodide from Threshold Photoelectron Photoion Coincidence Spectroscopy. *J. Phys. Chem. A* **2010**, *114* (20), 6117–6123.

https://doi.org/10.1021/jp102162f.

(111) Kercher, J. P.; Stevens, W.; Gengeliczki, Z.; Baer, T. Modeling Ionic Unimolecular Dissociations from a Temperature Controlled TPEPICO Study on 1-C4H9I Ions. *Int. J. Mass Spectrom.* **2007**, *267* (1–3), 159–166. https://doi.org/10.1016/j.ijms.2007.02.035.

(112) Frisch, M. J.; Trucks, G. W.; Schlegel, H. B.; Scuseria, G. E.; Robb, M. A.; Cheeseman, J. R.; Scalmani, G.; Barone, V.; Petersson, G. A.; Nakatsuji, H.; et Al. Gaussian 16, Rev. B.01; Gaussian Inc.: Wallingford, CT, 2016.

(113) Fiedler, L.; Modine, N. A.; Schmerler, S.; Vogel, D. J.; Popoola, G. A.; Thompson, A. P.; Rajamanickam, S.; Cangi, A. Predicting Electronic Structures at Any Length Scale with Machine Learning. *npj Comput. Mater.* **2023**, *9* (1), 1–10. https://doi.org/10.1038/s41524-023-01070-z.

(114) Bretonnet, J.-L. Basics of the Density Functional Theory. *AIMS Mater. Sci.* **2017**, *4* (6), 1372–1405. https://doi.org/10.3934/matersci.2017.6.1372.

(115) Lewars, E. G. Density Functional Calculations. In *Computational Chemistry*; Springer International Publishing: Cham, 2016; pp 483–563. https://doi.org/10.1007/978-3-319-30916-3_7.

(116) Hohenberg, P.; Kohn, W. Inhomogeneous Electron Gas. *Phys. Rev.* **1964**, *136* (3B), B864–B871. https://doi.org/10.1103/PhysRev.136.B864.

(117) Kohn, W.; Sham, L. J. Self-Consistent Equations Including Exchange and Correlation Effects. *Phys. Rev.* **1965**, *140* (4A), A1133–A1138. https://doi.org/10.1103/PhysRev.140.A1133.

(118) Runge, E.; Gross, E. K. U. Density-Functional Theory for Time-Dependent Systems. *Phys. Rev. Lett.* **1984**, *52* (12), 997–1000. https://doi.org/10.1103/PhysRevLett.52.997.

(119) Stratmann, R. E.; Scuseria, G. E.; Frisch, M. J. An Efficient Implementation of Time-Dependent Density-Functional Theory for the Calculation of Excitation Energies of Large Molecules. *J. Chem. Phys.* **1998**, *109* (19), 8218–8224. https://doi.org/10.1063/1.477483.

(120) Raghavachari, K. Perspective on "Density Functional Thermochemistry. III. The Role of Exact Exchange." *Theor. Chem. Accounts Theory, Comput. Model. (Theoretica Chim. Acta)* **2000**, *103* (3–4), 361–363. https://doi.org/10.1007/s002149900065.

(121) Becke, A. D. Density-Functional Thermochemistry. III. The Role of Exact Exchange. *J. Chem. Phys.* **1993**, *98* (7), 5648–5652. https://doi.org/10.1063/1.464913.

(122) Lee, C.; Yang, W.; Parr, R. G. Development of the Colle-Salvetti Correlation-Energy Formula into a Functional of the Electron Density. *Phys. Rev. B* **1988**, *37* (2), 785–789. https://doi.org/10.1103/PhysRevB.37.785.

(123) Zhao, Y.; Truhlar, D. G. The M06 Suite of Density Functionals for Main Group Thermochemistry, Thermochemical Kinetics, Noncovalent Interactions, Excited States, and Transition Elements: Two New Functionals and Systematic Testing of Four M06-Class Functionals and 12 Other Function. *Theor. Chem. Acc.* **2008**, *120* (1–3), 215–241. https://doi.org/10.1007/s00214-007-0310-x.

(124) Hehre, W. J.; Ditchfield, R.; Pople, J. A. Self—Consistent Molecular Orbital Methods. XII. Further Extensions of Gaussian—Type Basis Sets for Use in Molecular Orbital Studies of Organic Molecules. *J. Chem. Phys.* **1972**, *56* (5), 2257–2261. https://doi.org/10.1063/1.1677527.

(125) McLean, A. D.; Chandler, G. S. Contracted Gaussian Basis Sets for Molecular Calculations. I. Second Row Atoms, Z =11–18. *J. Chem. Phys.* **1980**, *72* (10), 5639–5648. https://doi.org/10.1063/1.438980.

(126) Krishnan, R.; Binkley, J. S.; Seeger, R.; Pople, J. A. Self-Consistent Molecular Orbital Methods. XX. A Basis Set for Correlated Wave Functions. *J. Chem. Phys.* **1980**, *72* (1), 650–654. https://doi.org/10.1063/1.438955.

(127) Clark, T.; Chandrasekhar, J.; Spitznagel, G. W.; Schleyer, P. V. R. Efficient Diffuse Function-augmented Basis Sets for Anion Calculations. III. The 3-21+G Basis Set for First-row Elements, Li–F. *J. Comput. Chem.* **1983**, *4* (3), 294–301. https://doi.org/10.1002/jcc.540040303.

(128) Frisch, M. J.; Pople, J. A.; Binkley, J. S. Self-Consistent Molecular Orbital Methods 25. Supplementary Functions for Gaussian Basis Sets. *J. Chem. Phys.* **1984**, *80* (7), 3265–3269. https://doi.org/10.1063/1.447079.

(129) Montgomery, J. A.; Frisch, M. J.; Ochterski, J. W.; Petersson, G. A. A Complete Basis Set Model Chemistry. VI. Use of Density Functional Geometries and Frequencies. *J. Chem. Phys.* **1999**, *110* (2–12), 2822–2827. https://doi.org/10.1063/1.477924.

(130) Montgomery, J. A.; Frisch, M. J.; Ochterski, J. W.; Petersson, G. A. A Complete Basis Set Model Chemistry. VII. Use of the Minimum Population Localization Method. *J. Chem. Phys.* **2000**, *112* (15), 6532–6542. https://doi.org/10.1063/1.481224.

(131) Ochterski, J. W.; Petersson, G. A.; Montgomery, J. A. A Complete Basis Set Model Chemistry. V. Extensions to Six or More Heavy Atoms. *J. Chem. Phys.* **1996**, *104* (7), 2598–2619. https://doi.org/10.1063/1.470985.

(132) Cramer, C. J. *Essentials of Computational Chemistry : Theories and Models*, 2nd ed.; Chichester, West Sussex, England ; Hoboken, NJ : Wiley, 2004.

(133) Jensen, F. *Introduction to Computational Chemistry*, 3rd ed.; John Wiley & Sons: Chichester, 2017.

(134) Møller, C.; Plesset, M. S. Note on an Approximation Treatment for Many-Electron Systems. *Phys. Rev.* **1934**, *46* (7), 618–622. https://doi.org/10.1103/PhysRev.46.618.

(135) Krishnan, R.; Schlegel, H. B.; Pople, J. A. Derivative Studies in Configuration–Interaction Theory. *J. Chem. Phys.* **1980**, *72* (8), 4654–4655. https://doi.org/10.1063/1.439708.

(136) Raghavachari, K.; Trucks, G. W.; Pople, J. A.; Head-Gordon, M. A Fifth-Order Perturbation Comparison of Electron Correlation Theories. *Chem. Phys. Lett.* **1989**, *157* (6), 479–483. https://doi.org/10.1016/S0009-2614(89)87395-6.

(137) Nyden, M. R.; Petersson, G. A. Complete Basis Set Correlation Energies. I. The Asymptotic Convergence of Pair Natural Orbital Expansions. *J. Chem. Phys.* **1981**, *75* (4), 1843–1862. https://doi.org/10.1063/1.442208.

(138) Curtiss, L. A.; Raghavachari, K.; Trucks, G. W.; Pople, J. A. Gaussian-2 Theory for Molecular Energies of First- and Second-Row Compounds. *J. Chem. Phys.* **1991**, *94* (11), 7221–7230. https://doi.org/10.1063/1.460205.

(139) Curtiss, L. A.; Raghavachari, K.; Redfern, P. C.; Rassolov, V.; Pople, J. A. Gaussian-3 (G3) Theory for Molecules Containing First and Second-Row Atoms. *J. Chem. Phys.* **1998**, *109* (18), 7764–7776. https://doi.org/10.1063/1.477422.

(140) Curtiss, L. A.; Redfern, P. C.; Raghavachari, K. Gaussian-4 Theory. *J. Chem. Phys.* **2007**, *126* (8). https://doi.org/10.1063/1.2436888.

(141) Cederbaum, L. S. One-Body Green's Function for Atoms and Molecules: Theory and Application. *J. Phys. B At. Mol. Phys.* **1975**, *8* (2), 290–303. https://doi.org/10.1088/0022-3700/8/2/018.

(142) Cederbaum, L. S.; Schirmer, J. Green's Functions for Open-Shell Atoms and Molecules. *Zeitschrift für Phys.* **1974**, *271* (3), 221–227. https://doi.org/10.1007/BF01677927.

(143) Ortiz, J. V. The Electron Propagator Picture of Molecular Electronic Structure. In

Computational Chemistry: Reviews of Current Trends; Leszczynski, J., Ed.; World Scientific , Singapore, 1997; pp 1–61. https://doi.org/10.1142/9789812812148_0001.

(144) von Niessen, W.; Schirmer, J.; Cederbaum, L. S. Computational Methods for the One-Particle Green's Function. *Comput. Phys. Reports* **1984**, *1* (2), 57–125. https://doi.org/10.1016/0167-7977(84)90002-9.

(145) DeYonker, N. J.; Peterson, K. A.; Wilson, A. K. Systematically Convergent Correlation Consistent Basis Sets for Molecular Core−Valence Correlation Effects: The Third-Row Atoms Gallium through Krypton. *J. Phys. Chem. A* **2007**, *111* (44), 11383–11393. https://doi.org/10.1021/jp0747757.

(146) Christopher J. Cramer. *Essentials of Computational Chemistry: Theories and Models, 2nd Edition*; Wiley, 2004.

(147) Rabah Ali Khalil. *A Simple Approach to Quantum Chemistry*; Nova Science Publishers, Inc., 2020.

(148) Peng, C.; Bernhard Schlegel, H. Combining Synchronous Transit and Quasi-Newton Methods to Find Transition States. *Isr. J. Chem.* **1993**, *33* (4), 449–454. https://doi.org/10.1002/ijch.199300051.

(149) Peng, C.; Ayala, P. Y.; Schlegel, H. B.; Frisch, M. J. Using Redundant Internal Coordinates to Optimize Equilibrium Geometries and Transition States. *J. Comput. Chem.* **1996**, *17* (1), 49–56. https://doi.org/10.1002/(SICI)1096-987X(19960115)17:1<49::AID-JCC5>3.0.CO;2-0.

(150) Deng, L.; Ziegler, T.; Fan, L. A Combined Density Functional and Intrinsic Reaction Coordinate Study on the Ground State Energy Surface of H2CO. *J. Chem. Phys.* **1993**, *99* (5), 3823–3835. https://doi.org/10.1063/1.466129.

(151) Deng, L.; Ziegler, T. The Determination of Intrinsic Reaction Coordinates by Density Functional Theory. *Int. J. Quantum Chem.* **1994**, *52* (4), 731–765. https://doi.org/10.1002/qua.560520406.

(152) Johnson, R. D.; Irikura, K. K.; Kacker, R. N.; Kessel, R. Scaling Factors and Uncertainties for Ab Initio Anharmonic Vibrational Frequencies. *J. Chem. Theory Comput.* **2010**, *6* (9), 2822–2828. https://doi.org/10.1021/ct100244d.

(153) NIST Standard Reference Database Number 101. *NIST Computational Chemistry Comparison and Benchmark Database*; Russell D. Johnson III, Ed.; 2022.

https://doi.org/10.18434/T47C7Z.

(154) Baer, T.; Hase, W. L. *Unimolecular Reaction Dynamics : Theory and Experiments*; New York : Oxford University Press, 1996.

(155) Marcus, R. A. Unimolecular Dissociations and Free Radical Recombination Reactions. *J. Chem. Phys.* **1952**, *20* (3), 359–364. https://doi.org/10.1063/1.1700424.

(156) Robinson, P. J.; Holbrook, K. A. *Unimolecular Reactions*; New York : Wiley-Interscience ; London, 1972.

(157) Baer, T.; Mayer, P. M. Statistical RRKM/QET Calculations in Mass Spectrometry. *J. Am. Soc. Mass Spectrom.* **1997**, *8* (96), 103–115.

(158) Nesbitt, D. J.; Field, R. W. Vibrational Energy Flow in Highly Excited Molecules: Role of Intramolecular Vibrational Redistribution. *J. Phys. Chem.* **1996**, *100* (31), 12735–12756. https://doi.org/10.1021/jp960698w.

(159) Wang, H.; Male, J.; Wang, Y. Recent Advances in Hydrotreating of Pyrolysis Bio-Oil and Its Oxygen-Containing Model Compounds. *ACS Catal.* **2013**, *3* (5), 1047–1070. https://doi.org/10.1021/cs400069z.

(160) Alherech, M.; Omolabake, S.; Holland, C. M.; Klinger, G. E.; Hegg, E. L.; Stahl, S. S. From Lignin to Valuable Aromatic Chemicals: Lignin Depolymerization and Monomer Separation via Centrifugal Partition Chromatography. *ACS Cent. Sci.* **2021**, *7* (11), 1831–1837. https://doi.org/10.1021/acscentsci.1c00729.

(161) Brown, R. C. Thermochemical Processing of Biomass: Conversion into Fuels, Chemicals and Power: Second Edition. *Thermochem. Process. Biomass Convers. into Fuels, Chem. Power* **2019**, 1–386. https://doi.org/10.1002/9781119417637.

(162) Huber, G. W.; Corma, A. Synergies between Bio- and Oil Refineries for the Production of Fuels from Biomass. *Angew. Chemie - Int. Ed.* **2007**, *46* (38), 7184–7201. https://doi.org/10.1002/anie.200604504.

(163) Erickson, E.; Bleem, A.; Kuatsjah, E.; Werner, A. Z.; DuBois, J. L.; McGeehan, J. E.; Eltis, L. D.; Beckham, G. T. Critical Enzyme Reactions in Aromatic Catabolism for Microbial Lignin Conversion. *Nat. Catal.* **2022**, *5* (2), 86–98. https://doi.org/10.1038/s41929-022-00747-w.

(164) Becker, J.; Wittmann, C. A Field of Dreams: Lignin Valorization into Chemicals, Materials, Fuels, and Health-Care Products. *Biotechnol. Adv.* **2019**, *37* (6), 107360.

https://doi.org/10.1016/j.biotechadv.2019.02.016.

(165) Lovell, A. B.; Brezinsky, K.; Glassman, I. The Gas Phase Pyrolysis of Phenol. *Int. J. Chem. Kinet.* **1989**, *21* (7), 547–560. https://doi.org/10.1002/kin.550210706.

(166) Horn, C.; Roy, K.; Frank, P.; Just, T. Shock-Tube Study on the High-Temperature Pyrolysis of Phenol. *Symp. Combust.* **1998**, *27* (1), 321–328. https://doi.org/10.1016/S0082-0784(98)80419-0.

(167) Brezinsky, K.; Pecullan, M.; Glassman, I. Pyrolysis and Oxidation of Phenol. *J. Phys. Chem. A* **1998**, *102* (44), 8614–8619. https://doi.org/10.1021/jp982177+.

(168) Liu, C.; Ye, L.; Yuan, W.; Zhang, Y.; Zou, J.; Yang, J.; Wang, Y.; Qi, F.; Zhou, Z. Investigation on Pyrolysis Mechanism of Guaiacol as Lignin Model Compound at Atmospheric Pressure. *Fuel* **2018**, *232* (June), 632–638. https://doi.org/10.1016/j.fuel.2018.05.162.

(169) Jegers, H. E.; Klein, M. T. Primary and Secondary Lignin Pyrolysis Reaction Pathways. *Ind. Eng. Chem. Process Des. Dev.* **1985**, *24* (1), 173–183. https://doi.org/10.1021/i200028a030.

(170) Evans, R. J.; Milne, T. A. Molecular Characterization of the Pyrolysis of Biomass. 2. Applications. *Energy & Fuels* **1987**, *1* (4), 311–319. https://doi.org/10.1021/ef00004a001.

(171) Mullen, C. A.; Boateng, A. A. Chemical Composition of Bio-Oils Produced by Fast Pyrolysis of Two Energy Crops. *Energy & Fuels* **2008**, *22* (3), 2104–2109. https://doi.org/10.1021/ef700776w.

(172) Stiles, H. N.; Kandiyoti, R. Secondary Reactions of Flash Pyrolysis Tars Measured in a Fluidized Bed Pyrolysis Reactor with Some Novel Design Features. *Fuel* **1989**, *68* (3), 275–282. https://doi.org/10.1016/0016-2361(89)90087-2.

(173) Rath, J.; Staudinger, G. Cracking Reactions of Tar from Pyrolysis of Spruce Wood. *Fuel* **2001**, *80* (10), 1379–1389. https://doi.org/10.1016/S0016-2361(01)00016-3.

(174) Ledesma, E. B.; Campos, C.; Cranmer, D. J.; Foytik, B. L.; Ton, M. N.; Dixon, E. A.; Chirino, C.; Batamo, S.; Roy, P. Vapor-Phase Cracking of Eugenol: Distribution of Tar Products as Functions of Temperature and Residence Time. *Energy and Fuels* **2013**, *27* (2), 868–878. https://doi.org/10.1021/ef3018332.

(175) Bodi, A.; Hemberger, P.; Gerber, T.; Sztáray, B. A New Double Imaging Velocity Focusing Coincidence Experiment: I 2PEPICO. *Rev. Sci. Instrum.* **2012**, *83* (8).

https://doi.org/10.1063/1.4742769.

(176) Bodi, A.; Hemberger, P.; Pérez-Ramírez, J. Photoionization Reveals Catalytic Mechanisms. *Nat. Catal.* **2022**, *5* (10), 850–851. https://doi.org/10.1038/s41929-022-00847-7.

(177) Hemberger, P.; Custodis, V. B. F.; Bodi, A.; Gerber, T.; Van Bokhoven, J. A. Understanding the Mechanism of Catalytic Fast Pyrolysis by Unveiling Reactive Intermediates in Heterogeneous Catalysis. *Nat. Commun.* **2017**, *8* (May), 1–9. https://doi.org/10.1038/ncomms15946.

(178) Hemberger, P.; Bodi, A.; Bierkandt, T.; Köhler, M.; Kaczmarek, D.; Kasper, T. Photoelectron Photoion Coincidence Spectroscopy Provides Mechanistic Insights in Fuel Synthesis and Conversion. *Energy and Fuels* **2021**, *35* (20), 16265–16302. https://doi.org/10.1021/acs.energyfuels.1c01712.

(179) Guan, Q.; Urness, K. N.; Ormond, T. K.; David, D. E.; Barney Ellison, G.; Daily, J. W. The Properties of a Micro-Reactor for the Study of the Unimolecular Decomposition of Large Molecules. *Int. Rev. Phys. Chem.* **2014**, *33* (4), 447–487. https://doi.org/10.1080/0144235X.2014.967951.

(180) Grimm, S.; Baik, S. J.; Hemberger, P.; Bodi, A.; Kempf, A. M.; Kasper, T.; Atakan, B. Gas-Phase Aluminium Acetylacetonate Decomposition: Revision of the Current Mechanism by VUV Synchrotron Radiation. *Phys. Chem. Chem. Phys.* **2021**, *23* (28), 15059–15075. https://doi.org/10.1039/d1cp00720c.

(181) Hemberger, P.; Wu, X.; Pan, Z.; Bodi, A. Continuous Pyrolysis Microreactors: Hot Sources with Little Cooling? New Insights Utilizing Cation Velocity Map Imaging and Threshold Photoelectron Spectroscopy. *J. Phys. Chem. A* **2022**, *126* (14), 2196–2210. https://doi.org/10.1021/acs.jpca.2c00766.

(182) McCabe, M. N.; Hemberger, P.; Reusch, E.; Bodi, A.; Bouwman, J. Off the Beaten Path: Almost Clean Formation of Indene from the Ortho -Benzyne + Allyl Reaction. *J. Phys. Chem. Lett.* **2020**, *11* (8), 2859–2863. https://doi.org/10.1021/acs.jpclett.0c00374.

(183) Rogers, C. O.; Lockwood, K. S.; Nguyen, Q. L. D.; Labbe, N. J. Diol Isomer Revealed as a Source of Methyl Ketene from Propionic Acid Unimolecular Decomposition. *Int. J. Chem. Kinet.* **2021**, *53* (12), 1272–1284. https://doi.org/10.1002/kin.21532.

(184) Vasiliou, A. K.; Kim, J. H.; Ormond, T. K.; Piech, K. M.; Urness, K. N.; Scheer, A. M.;

Robichaud, D. J.; Mukarakate, C.; Nimlos, M. R.; Daily, J. W.; Guan, Q.; Carstensen, H. H.; Ellison, G. B. Biomass Pyrolysis: Thermal Decomposition Mechanisms of Furfural and Benzaldehyde. *J. Chem. Phys.* **2013**, *139* (10). https://doi.org/10.1063/1.4819788.

(185) Zaleski, D. P.; Sivaramakrishnan, R.; Weller, H. R.; Seifert, N. A.; Bross, D. H.; Ruscic, B.; Moore, K. B.; Elliott, S. N.; Copan, A. V.; Harding, L. B.; Klippenstein, S. J.; Field, R. W.; Prozument, K. Substitution Reactions in the Pyrolysis of Acetone Revealed through a Modeling, Experiment, Theory Paradigm. *J. Am. Chem. Soc.* **2021**, *143* (8), 3124–3142. https://doi.org/10.1021/jacs.0c11677.

(186) Lowe, B.; Cardona, A. L.; Salas, J.; Bodi, A.; Mayer, P. M.; Burgos Paci, M. A. Probing the Pyrolysis of Ethyl Formate in the Dilute Gas Phase by Synchrotron Radiation and Theory. *J. Mass Spectrom.* **2023**, *58* (1), 1–12. https://doi.org/10.1002/jms.4901.

(187) Lowe, B.; Cardona, A. L.; Salas, J.; Bodi, A.; Burgos Paci, M. A.; Mayer, P. M. Probing the Pyrolysis of Methyl Formate in the Dilute Gas Phase by Synchrotron Radiation and Theory. *J. Mass Spectrom.* **2022**, *57* (6), 1–11. https://doi.org/10.1002/jms.4868.

(188) Lowe, B.; Cardona, A. L.; Bodi, A.; Mayer, P. M.; Burgos Paci, M. A. The Unimolecular Chemistry of Methyl Chloroformate Ions and Neutrals: A Story of Near-Threshold Decomposition. *J. Am. Soc. Mass Spectrom.* **2023**, *34* (12), 2831–2839. https://doi.org/10.1021/jasms.3c00334.

(189) Pan, Z.; Puente-Urbina, A.; Bodi, A.; van Bokhoven, J. A.; Hemberger, P. Isomer-Dependent Catalytic Pyrolysis Mechanism of the Lignin Model Compounds Catechol, Resorcinol and Hydroquinone. *Chem. Sci.* **2021**, *12* (9), 3161–3169. https://doi.org/10.1039/D1SC00654A.

(190) Robin, M. B. Handbook of He(I) Photoelectron Spectra of Fundamental Organic Molecules. *J. Electron Spectros. Relat. Phenomena* **1982**, *28* (2), 225. https://doi.org/10.1016/0368-2048(82)85046-9.

(191) Sharon G. Lias, John E. Bartmess, Joel F. Liebman, John L. Holmes, Rhoda D. Levin, W. Gary Mallard, S. A. K. Ion Energetics Data. In *NIST Chemistry WebBook, NIST Standard Reference Database Number 69*; National Institute of Standards and Technology, Gaithersburg MD, 2025; p 20899. https://doi.org/https://doi.org/10.18434/T4D303.

(192) S.G. Lias, J.E. Bartmess, J.F. Liebman, J.L. Holmes, R. D.; Levin, and W. G. M. Gas-Phase Ion and Neutral Thermochemistry. *J. Phys. Chem. Ref. Data* **1988**, *17* (1).

(193) Venkatesan, T. S.; Mahapatra, S. Exploring the Jahn-Teller and Pseudo-Jahn-Teller Conical Intersections in the Ethane Radical Cation. *J. Chem. Phys.* **2005**, *123* (11). https://doi.org/10.1063/1.2032927.

(194) Buenger, E. W.; Bodi, A.; Burgos-Paci, M. A.; Mayer, P. M. Cyclopentene and Cyclopentadiene Formation in Isoprene Pyrolysis. *Phys. Chem. Chem. Phys.* **2024**, *26* (36), 23971–23978. https://doi.org/10.1039/d4cp02798a.

(195) Scheer, A. M.; Mukarakate, C.; Robichaud, D. J.; Nimlos, M. R.; Carstensen, H. H.; Barney Ellison, G. Unimolecular Thermal Decomposition of Phenol and d 5-Phenol: Direct Observation of Cyclopentadiene Formation via Cyclohexadienone. *J. Chem. Phys.* **2012**, *136* (4). https://doi.org/10.1063/1.3675902.

(196) Pan, Z.; Puente-Urbina, A.; Bodi, A.; van Bokhoven, J. A.; Hemberger, P. Isomer-Dependent Catalytic Pyrolysis Mechanism of the Lignin Model Compounds Catechol, Resorcinol and Hydroquinone. *Chem. Sci.* **2021**, *12* (9), 3161–3169. https://doi.org/10.1039/d1sc00654a.

(197) Lomnicki, S.; Truong, H.; Dellinger, B. Mechanisms of Product Formation from the Pyrolytic Thermal Degradation of Catechol. *Chemosphere* **2008**, *73* (4), 629–633. https://doi.org/10.1016/j.chemosphere.2008.03.064.

(198) Bridging Experiment and Computation: Unveiling Novel Dissociation Pathways of 4-Ethylguaiacol and Eugenol Radical Cations Using IPEPICO Spectroscopy. *J. Phys. Chem. A*.

(199) Gondarry, S.; Mayer, P. M. Does the Dissociation of Guaiacol Family Radical Cations Mimic Their Thermal Decomposition? *Comput. Theor. Chem.* **2023**, *1229* (May), 114323. https://doi.org/10.1016/j.comptc.2023.114323.

(200) Amen-Chen, C.; Pakdel, H.; Roy, C. Production of Monomeric Phenols by Thermochemical Conversion of Biomass: A Review. *Bioresour. Technol.* **2001**, *79* (3), 277–299. https://doi.org/10.1016/S0960-8524(00)00180-2.

(201) D. Fengel and G. Wegener. *Wood-Chemistry, Ultrastructure, Reactions*; Walter de Gruyter, Berlin, 1984.

(202) Schauer, J. J.; Kleeman, M. J.; Cass, G. R.; Simoneit, B. R. T. Measurement of Emissions from Air Pollution Sources. 3. C1-C29 Organic Compounds from Fireplace Combustion of Wood. *Environ. Sci. Technol.* **2001**, *35* (9), 1716–1728.

https://doi.org/10.1021/es001331e.

(203) Mazzoleni, L. R.; Zielinska, B.; Moosmüller, H. Emissions of Levoglucosan, Methoxy Phenols, and Organic Acids from Prescribed Burns, Laboratory Combustion of Wildland Fuels, and Residential Wood Combustion. *Environ. Sci. Technol.* **2007**, *41* (7), 2115–2122. https://doi.org/10.1021/es061702c.

(204) Hays, M. D.; Geron, C. D.; Linna, K. J.; Smith, N. D.; Schauer, J. J. Speciation of Gas-Phase and Fine Particle Emissions from Burning of Foliar Fuels. *Environ. Sci. Technol.* **2002**, *36* (11), 2281–2295. https://doi.org/10.1021/es0111683.

(205) Liu, C.; Zhang, P.; Wang, Y.; Yang, B.; Shu, J. Heterogeneous Reactions of Particulate Methoxyphenols with NO3 Radicals: Kinetics, Products, and Mechanisms. *Environ. Sci. Technol.* **2012**, *46* (24), 13262–13269. https://doi.org/10.1021/es303889z.

(206) Mcdonald, J. D.; Zielinska, B.; Fujita, E. M.; Sagebiel, J. C.; Chow, J. C.; Watson, J. G. Fine Particle and Gaseous Emission Rates from Residential Wood Combustion. *Environ. Sci. Technol.* **2000**, *34* (11), 2080–2091. https://doi.org/10.1021/es9909632.

(207) Coeur-Tourneur, C.; Cassez, A.; Wenger, J. C. Rate Coefficients for the Gas-Phase Reaction of Hydroxyl Radicals with 2-Methoxyphenol (Guaiacol) and Related Compounds. *J. Phys. Chem. A* **2010**, *114* (43), 11645–11650. https://doi.org/10.1021/jp1071023.

(208) Yang, B.; Zhang, H.; Wang, Y.; Zhang, P.; Shu, J.; Sun, W.; Ma, P. Experimental and Theoretical Studies on Gas-Phase Reactions of NO3 Radicals with Three Methoxyphenols: Guaiacol, Creosol, and Syringol. *Atmos. Environ.* **2016**, *125* (3), 243–251. https://doi.org/10.1016/j.atmosenv.2015.11.028.

(209) Khudoshin, A. G.; Mitrofanova, A. N.; Lunin, V. V. Kinetics and Mechanism of the Reactions of Ozone with Guaiacol, Veratrol, and Veratrol Derivatives. *Russ. Chem. Bull.* **2008**, *57* (2), 283–288. https://doi.org/10.1007/s11172-008-0043-6.

(210) Nguyen, T. T. P.; Mai, T. V. T.; Huynh, L. K. Detailed Kinetic Modeling of Thermal Decomposition of Guaiacol – A Model Compound for Biomass Lignin. *Biomass and Bioenergy* **2018**, *112* (June 2016), 45–60. https://doi.org/10.1016/j.biombioe.2018.02.006.

(211) de Miguel Mercader, F.; Groeneveld, M. J.; Kersten, S. R. A.; Venderbosch, R. H.; Hogendoorn, J. A. Pyrolysis Oil Upgrading by High Pressure Thermal Treatment. *Fuel* **2010**, *89* (10), 2829–2837. https://doi.org/10.1016/j.fuel.2010.01.026.

(212) Xu, Y.; Liu, Z.; Liu, B.; Dong, B.; Li, Y.; Li, Y.; Guo, H.; Chai, Y.; Liu, C. Hydrodeoxygenation of Guaiacol to Bio-Hydrocarbons over Ni Catalyst Supported on Activated Coconut Carbon in Alkaline Condition. *Biomass and Bioenergy* **2022**, *163* (January), 106506. https://doi.org/10.1016/j.biombioe.2022.106506.

(213) Wang, X.; Zhang, Z.; Yan, Z.; Li, Q.; Zhang, Y. Catalysts with Metal-Acid Dual Sites for Selective Hydrodeoxygenation of Lignin Derivatives: Progress in Regulation Strategies and Applications. *Appl. Catal. A Gen.* **2023**, *662* (March), 119266. https://doi.org/10.1016/j.apcata.2023.119266.

(214) Yan, P.; Li, M. M. J.; Kennedy, E.; Adesina, A.; Zhao, G.; Setiawan, A.; Stockenhuber, M. The Role of Acid and Metal Sites in Hydrodeoxygenation of Guaiacol over Ni/Beta Catalysts. *Catal. Sci. Technol.* **2020**, *10* (3), 810–825. https://doi.org/10.1039/c9cy01970g.

(215) Mercader, F. de M.; Groeneveld, M. J.; Kersten, S. R. A.; Venderbosch, R. H.; Hogendoorn, J. A. Pyrolysis Oil Upgrading by High Pressure Thermal Treatment. *Fuel* **2010**, *89* (10), 2829–2837. https://doi.org/10.1016/j.fuel.2010.01.026.

(216) Quintero-Arroyo, G.; Rueda, A. C.; Granados-Reyes, J.; Fals, J.; Cesteros, Y. Effect of Acid Properties of Fluorinated Beta and ZSM-5 Zeolites Used as Supports of Ni Catalysts for the Catalytic Hydrodeoxygenation of Guaiacol. *Catalysts* **2024**, *14* (9). https://doi.org/10.3390/catal14090586.

(217) Xu, Y.; Wang, W.; Liu, B.; Pan, Y.; Dong, B.; Li, Y.; Li, Y.; Guo, H.; Chai, Y.; Liu, C. The Role of Nb2O5 in Controlling Metal-Acid Sites of CoMoS/γ-Al2O3 Catalyst for the Enhanced Hydrodeoxygenation of Guaiacol into Hydrocarbons. *J. Catal.* **2022**, *407*, 19–28. https://doi.org/10.1016/j.jcat.2022.01.027.

(218) Curtis, S.; Dimuzio, J.; Mungham, A.; Roy, J.; Hassan, D.; Renaud, J.; Mayer, P. M. Reactions of Atomic Metal Anions in the Gas Phase: Competition between Electron Transfer, Proton Abstraction and Bond Activation. *J. Phys. Chem. A* **2011**, *115* (48), 14006–14012. https://doi.org/10.1021/jp2086736.

(219) Bartmess, J. E. Negative Ion Energetics Data. In *NIST Chemistry WebBook, NIST Standard Reference Database Number 69*; P.J. Linstrom and W.G. Mallard, Ed.; National Institute of Standards and Technology, Gaithersburg MD, 2024; p 20899. https://doi.org/https://doi.org/10.18434/T4D303.

(220) Liu, C.; Zhang, Y.; Huang, X. Study of Guaiacol Pyrolysis Mechanism Based on Density

Function Theory. *Fuel Process. Technol.* **2014**, *123*, 159–165. https://doi.org/10.1016/j.fuproc.2014.01.002.

(221) Asmadi, M.; Kawamoto, H.; Saka, S. Thermal Reactions of Guaiacol and Syringol as Lignin Model Aromatic Nuclei. *J. Anal. Appl. Pyrolysis* **2011**, *92* (1), 88–98. https://doi.org/10.1016/j.jaap.2011.04.011.

(222) Wu, X.; Pan, Z.; Bjelić, S.; Hemberger, P.; Bodi, A. Unimolecular Thermal Decarbonylation of Vanillin Stifled by the Bimolecular Reactivity of Methyl-Loss Intermediate. *J. Anal. Appl. Pyrolysis* **2022**, *161*. https://doi.org/10.1016/j.jaap.2021.105410.

(223) Holmes, J. L.; Christiane, A.; Mayer, P. M. *Assigning Structures to Ions in Mass Spectrometry*; CRC Press: Boca Raton, 2007.

(224) Cooks, R. G.; Beynon, J. H.; Caprioli, R. M.; Lester, G. R. *Metastable Ions*; Company, E. S. P., Ed.; Amsterdam, 1973.

(225) Gondarry, S.; Mayer, P. M. The Fate of Protonated Guaiacol and Its Derivatives in the Gas Phase. *J. Phys. Chem. A* **2022**, *126* (48), 9051–9058. https://doi.org/10.1021/acs.jpca.2c04692.

(226) Kumar, M. M.; Prabhudesai, V. S.; Vinu, R. Lignin Depolymerization to Guaiacol and Vanillin Derivatives via Catalytic Transfer Hydrogenolysis Using Pd-Lewis Metal Oxide Supported on Activated Carbon Catalysts. *Mol. Catal.* **2023**, *549* (March), 113474. https://doi.org/10.1016/j.mcat.2023.113474.

(227) Shen, X.; Meng, Q.; Mei, Q.; Liu, H.; Yan, J.; Song, J.; Tan, D.; Chen, B.; Zhang, Z.; Yang, G.; Han, B. Selective Catalytic Transformation of Lignin with Guaiacol as the Only Liquid Product. *Chem. Sci.* **2020**, *11* (5), 1347–1352. https://doi.org/10.1039/c9sc05892c.

(228) Milheiro, J.; Filipe-Ribeiro, L.; Vilela, A.; Cosme, F.; Nunes, F. M. 4-Ethylphenol, 4-Ethylguaiacol and 4-Ethylcatechol in Red Wines: Microbial Formation, Prevention, Remediation and Overview of Analytical Approaches. *Crit. Rev. Food Sci. Nutr.* **2019**, *59* (9), 1367–1391. https://doi.org/10.1080/10408398.2017.1408563.

(229) Wille, U. Reaction Mechanisms: Radical and Radical Ion Reactions. *Annu. Reports Prog. Chem. - Sect. B* **2012**, *108*, 228–250. https://doi.org/10.1039/c2oc90015g.

(230) Yan, M.; Lo, J. C.; Edwards, J. T.; Baran, P. S. Radicals: Reactive Intermediates with Translational Potential. *J. Am. Chem. Soc.* **2016**, *138* (39), 12692–12714.

https://doi.org/10.1021/jacs.6b08856.

(231) Anouar, E.; Calliste, C. A.; Košinová, P.; Di Meo, F.; Duroux, J. L.; Champavier, Y.; Marakchi, K.; Trouillas, P. Free Radical Scavenging Properties of Guaiacol Oligomers: A Combined Experimental and Quantum Study of the Guaiacyl-Moiety Role. *J. Phys. Chem. A* **2009**, *113* (50), 13881–13891. https://doi.org/10.1021/jp906285b.

(232) Li, G.; Luo, Z.; Wang, W.; Cen, J. A Study of the Mechanisms of Guaiacol Pyrolysis Based on Free Radicals Detection Technology. *Catalysts* **2020**, *10* (3). https://doi.org/10.3390/catal10030295.

(233) Baer, T.; Tuckett, R. P. Advances in Threshold Photoelectron Spectroscopy (TPES) and Threshold Photoelectron Photoion Coincidence (TPEPICO). *Phys. Chem. Chem. Phys.* **2017**, *19* (15), 9698–9723. https://doi.org/10.1039/c7cp00144d.

(234) Wu, X.; Pan, Z.; Bjelić, S.; Hemberger, P.; Bodi, A. Unimolecular Thermal Decarbonylation of Vanillin Stifled by the Bimolecular Reactivity of Methyl-Loss Intermediate. *J. Anal. Appl. Pyrolysis* **2022**, *161*, 105410. https://doi.org/10.1016/j.jaap.2021.105410.

(235) Pan, Z.; Wu, X.; Bodi, A.; van Bokhoven, J. A.; Hemberger, P. Catalytic Pyrolysis Mechanism of Lignin Moieties Driven by Aldehyde, Hydroxyl, Methoxy, and Allyl Functionalization: The Role of Reactive Quinone Methide and Ketene Intermediates. *Green Chem.* **2024**, *26* (18), 9899–9910. https://doi.org/10.1039/D4GC03143A.

(236) Zhang, Z.; Li, Q.; Wu, X.; Bourmaud, C.; Vlachos, D. G.; Luterbacher, J.; Bodi, A.; Hemberger, P. A Solution for 4-Propylguaiacol Hydrodeoxygenation without Ring Saturation. *Nat. Commun.* **2024**, *15* (1), 6330. https://doi.org/10.1038/s41467-024-50724-z.

(237) Kotake, T.; Kawamoto, H.; Saka, S. Pyrolysis Reactions of Coniferyl Alcohol as a Model of the Primary Structure Formed during Lignin Pyrolysis. *J. Anal. Appl. Pyrolysis* **2013**, *104*, 573–584. https://doi.org/10.1016/j.jaap.2013.05.011.

(238) Hemberger, P.; Pan, Z.; Wu, X.; Zhang, Z.; Kanayama, K.; Bodi, A. Photoion Mass-Selected Threshold Photoelectron Spectroscopy to Detect Reactive Intermediates in Catalysis: From Instrumentation and Examples to Peculiarities and a Database. *J. Phys. Chem. C* **2023**, *127* (34), 16751–16763. https://doi.org/10.1021/acs.jpcc.3c03120.

(239) Johnson, M.; Bodi, A.; Schulz, L.; Gerber, T. Vacuum Ultraviolet Beamline at the Swiss

Light Source for Chemical Dynamics Studies. *Nucl. Instruments Methods Phys. Res. Sect. A Accel. Spectrometers, Detect. Assoc. Equip.* **2009**, *610* (2), 597–603. https://doi.org/10.1016/j.nima.2009.08.069.

(240) Y. Ralchenku, A.E. Kramida, J. Reader, N. A. T. *NIST Atomic Spectra Database,National Institute of Standards and Technology, Gaithersburg, MD*; 2008. https://doi.org/https://dx.doi.org/10.18434/T4W30F.

(241) Hemberger, P.; Wu, X.; Pan, Z.; Bodi, A. Continuous Pyrolysis Microreactors: Hot Sources with Little Cooling? New Insights Utilizing Cation Velocity Map Imaging and Threshold Photoelectron Spectroscopy. *J. Phys. Chem. A* **2022**, *126* (14), 2196–2210. https://doi.org/10.1021/acs.jpca.2c00766.

(242) Bodi, A.; Daniel Brannock, M.; Sztáray, B.; Baer, T. Tunneling in H Loss from Energy Selected Ethanol Ions. *Phys. Chem. Chem. Phys.* **2012**, *14* (46), 16047. https://doi.org/10.1039/c2cp43255b.

(243) Longarte, A.; Unamuno, I.; Fernández, J. A.; Castaño, F.; Redondo, C. Experimental and Theoretical Study of the Structures and Binding Energies of Eugenol (H2O)n, N=0-2. *J. Chem. Phys.* **2004**, *121* (1), 209–219. https://doi.org/10.1063/1.1738646.

(244) Weidner, P.; Voronova, K.; Bodi, A.; Sztáray, B. Dissociative Photoionization of 1,3-dioxolane: We Need Six Channels to Fit the Elephant. *J. Mass Spectrom.* **2020**, *55* (9). https://doi.org/10.1002/jms.4522.

(245) Zinck, N.; Bodi, A.; Mayer, P. M. Can OPAH Ions Be a Source of CO and HCO in the Interstellar Medium? Lessons Learned from the Unimolecular Dissociation of Dibenzofuran and Dibenz[b,f]Oxepin Radical Cations. *Int. J. Mass Spectrom.* **2025**, *507*, 117366. https://doi.org/10.1016/j.ijms.2024.117366.

(246) Zhou, N.; Thilakarathna, W. P. D. W.; He, Q. S.; Rupasinghe, H. P. V. A Review: Depolymerization of Lignin to Generate High-Value Bio-Products: Opportunities, Challenges, and Prospects. *Front. Energy Res.* **2022**, *9* (January), 1–18. https://doi.org/10.3389/fenrg.2021.758744.

(247) Luo, J.; Liu, T. L. Electrochemical Valorization of Lignin: Status, Challenges, and Prospects. *J. Bioresour. Bioprod.* **2023**, *8* (1), 1–14. https://doi.org/10.1016/j.jobab.2022.11.003.

(248) Dai, J.; Zhang, K.; Feng, Y.; Yi, X.; Li, R.; Xue, J.; Li, Q.; Shi, L.; Liao, J.; Yi, Y.; Wang,

F.; Yang, L.; Chen, H.; Huang, L.; Tan, J.; Wang, Y.; Li, L. Significant Influence of Oxygenated Volatile Organic Compounds on Atmospheric Chemistry: A Case Study in a Typical Industrial City in China. *Atmos. Chem. Phys.* **2025**, *25* (13), 7467–7484. https://doi.org/10.5194/acp-25-7467-2025.

(249) Gao, Y.; Dias Da Silva, P.; Alvarez, P. J. J.; Zygourakis, K. Integrating Thermal Analysis and Reaction Modeling for Rational Design of Pyrolytic Processes to Remediate Soils Contaminated with Heavy Crude Oil. *Environ. Sci. Technol.* **2021**, *55* (17), 11987–11996. https://doi.org/10.1021/acs.est.1c03607.

(250) Liu, Z.; Gao, S.; Yuan, Z.; Yang, R.; Zhang, X.; El-Mesery, H. S.; Dai, X.; Lu, W.; Xu, R. Exploring Formation and Control of Hazards in Thermal Processing for Food Safety. *Foods* **2025**, *14* (13), 2168. https://doi.org/10.3390/foods14132168.

(251) Vuppaladadiyam, A. K.; Varsha Vuppaladadiyam, S. S.; Sikarwar, V. S.; Ahmad, E.; Pant, K. K.; S, M.; Pandey, A.; Bhattacharya, S.; Sarmah, A.; Leu, S.-Y. A Critical Review on Biomass Pyrolysis: Reaction Mechanisms, Process Modeling and Potential Challenges. *J. Energy Inst.* **2023**, *108*, 101236. https://doi.org/10.1016/j.joei.2023.101236.

(252) Nowakowska, M.; Herbinet, O.; Dufour, A.; Glaude, P. A. Kinetic Study of the Pyrolysis and Oxidation of Guaiacol. *J. Phys. Chem. A* **2018**, *122* (39), 7894–7909. https://doi.org/10.1021/acs.jpca.8b06301.